Optical Resonance Sensors Based on Whispering-Gallery-Mode Technique

Sirirat Panich

A thesis submitted in partial fulfilment of the requirement for the degree of doctor of Philosophy

Department of Chemistry, Imperial College London

May 2016

Declaration of Originality

I hereby declare that this thesis is entirely my own original work. All other sources of information presented which are not part of my own work have been properly cited in the bibliography. No part of this thesis has been submitted for any degree at any other university or academic institution.

Sirirat Panich

Copyright Declaration

The copyright of this thesis rests with the author and is made available under a Creative Commons Attribution Non-Commercial No Derivatives licence. Researchers are free to copy, distribute or transmit the thesis on the condition that they attribute it, that they do not use it for commercial purposes and that they do not alter, transform or build upon it. For any reuse or redistribution, researchers must make clear to others the licence terms of this work.

Abstract

In recent years, the whispering gallery mode (WGM) technique has received considerable attention as a novel and extremely sensitive technique for use in sensors. The technique is able to detect target molecules at very low levels and in real time, a capability which cannot be matched by any other detection technique currently in use. With this potential rarely found in common sensors, WGM is becoming one of the most widely used. The WGM set-up is simple and inexpensive. Light generated by a tunable laser, circumnavigates the surface of a resonator through a tapered waveguide. This light is strongly confined inside the microresonator by total internal reflection (TIR). Energy is extracted from the fibre, resulting in a negative peak. The surface of the resonator needs to be functionalised for reacting with the target molecule. If a chemical or biological analyte is to be bound on the surface of the resonator, the negative peak must be shifted. This shift can be used for measuring the amount of the analyte. In view of its exciting potential, it is not surprising that WGM is establishing itself as the detection method of choice, especially in chemical and biomedical applications. The work reported in this thesis is in two sections. In the first part, the use of the WGM technique integrated self-assembled glutathione (GSH) modified gold nanoparticles (Au NPs) on an optical microsphere resonator in an ultrasensitive chemical detection assay for Pb(II) (down to 10 ppt or 0.05 nM) is described. This satisfies the demanding sensitivity required for monitoring the maximum Pb(II) exposure limits set by both International Agency for Research on Cancer (IARC) and the United States Environmental Protection Agency (EPA). The second section presents an example of the use of WGM in a biosensor to study the interactions between small molecules and G-quadruplex DNA which is well known to be active targets for anticancer treatments. Currently methods typically used to study such systems have proven to be valuable; however, they have limitations, such as low sensitivity, time-consuming monitoring and lack of real time analysis. To circumvent these problems, a novel platform based around WGM is developed. The sensor offers a real time, fast and sensitive analysis. In addition, kinetic data such as dissociation equilibrium constant (K_D) as well as association and dissociation constant (k_{on} and k_{off}, respectively) can be easily obtained.

Acknowledgement

I would like to express my gratitude to the following people, without whose help this thesis could not have been complete. Dr. Joshua B Edel, my supervisor, whose constant guidance and sympathetic encouragements has been indispensable. Dr. Sylvain Ladame, my co-supervior, who made valuable suggestions during my work on G-quadruplex. Dr. Kerry Wilson, my mentor in Edel group, whose patient explanation of the WGM technique was vital at the start of my project. Dr. Mazen Sleiman, who helped me to set up the G-quadruplex DNA experiment. Dr. Jame Redman and Dr. Ramon Vilar for their valuable comments during my viva. Isobel Steer, Jame Million, Dr. Binoy Nadappuram and Dr. Collin Click, for their help with proof-reading. Faculty of Science and Technology, Rajamangala University of Technology Phanakorn (RMUTP), my work place in Thailand, for the opportunity to do my Ph.D. aboard. The Royal Thai Government for my Ph.D. scholarship. My colleagues in the Edel group especially Dr. Aleksandar Ivanov, Dr. Kristelle Bougot-Robin, Dr. Agnieszka Rutkowska for their advices and helping me during my experiment in the lab.

My sincere thanks also go to Yuwadee Sundarasaradula, Chaipat Lapinee and Nuchutha Thamsumet for their supporting me during living in London. Thanks are also due to many personal friends I have made while working at Imperial College. I would like to mention especially the kindness and support I have received from Christopher Wood, Jasmine Sze and Cadinu Paolo. Finally, I want to acknowledge my indebtedness to my family, whose understanding and love have sustained me at times when living in foreign country far from home has proven difficult.

Sirirat Panich

Table of Contents

Declaration of Originality....2

Copyright Declaration....3

Abstract....4

Acknowledgements....5

List of Abbreviations....10

List of Symbols....13

Chapter 1 | Introduction....15

1.1 Sensors....16

1.1.1 Advantages and disadvantages of WGM sensing compared with other sensing techniques....19

1.2 Theories of optical WGM....22

1.2.1 Gallery of whispers....22

1.2.2 From the whispering gallery to a chemical and a biological sensor....22

1.2.3 Resonant mode and total internal reflection effect....23

1.2.4 The operating principles of WGM....24

1.2.5 WGM microresonators....30

1.2.6 Microresonator surface modification....30

1.2.7 Light coupling into a microresonator....31

1.2.8 Cavity Q-factor....32

1.3 WGM based sensing and applications....34

1.3.1 Chemical WGM based sensing....34

1.3.2 Biological WGM based sensing....34

1.3.3 Other sensing....36

1.4 Project aims and objectives....38

1.4.1 Chapter 3: Pb(II) sensor experiment....38

1.4.2 Chapter 4: G-quadruplex experiment....38

1.4.3 Chapter 5: thrombin experiment....38

1.4.4 Chapter 6: conclusion....38

1.5 References....39

Chapter 2 | Instrumentation and Methodology 49
2.1 WGM experiment set-up 50
2.1.1 Instrumentations and devices 50
2.1.1.1. Devices 51
2.1.1.2 Consumable fibre cables 52
2.1.1.3. Instruments 53
2.1.2 Fabrication process 54
2.1.2.1 Glass spherical microresonator 54
2.1.2.2 Fibre tapered waveguides 55
2.1.2.3. Fluidic cell designs and fabrication 56
2.1.3 Experimental set up for resonant wavelength shift detection 57
2.1.4 Parameters for resonant-shift recording 59
2.2 Data analysis 60
2.2.1 Microsphere Q-factor calculation 60
2.2.2 Programme and software for wavelength-shift analysis 61
2.3 References 62
Chapter 3 | Optical-Resonator-Based Chemical sensing: Heavy metal detection Pb(II) by optical microcavity 64
3.1 Introduction 65
3.2 Experimental methods 67
3.2.1 Chemical and Materials 67
3.2.2 Preparation and characterization of the Au NPs 68
3.2.3 Modification of the Au NP surface with GSH 68
3.2.4 Decoration of the GSH-Au NPs onto the modified silanized microresonator surface 69
3.2.5 Detection of Pb(II) by WGM resonance shift 69
3.3 Results and discussions 70
3.3.1 Characterization of Au NPs and GSH-modified Au NPs 70
3.3.2 Attaching GSH modified Au NP complex on the resonator surface 77
3.3.3 Quality or Q-factor 79
3.3.4 Characterization of the functionalized resonator surface 84
3.3.5 WGM resonance shift measurements 88
3.3.6 Quantification of Pb(II) using WGM sensing 90
3.3.7 Kinetic study 93
3.3.8 Noise and detection limit 95

3.3.9 Interference, sensitivity and selectivity study of the sensor 97
3.4 Conclusion 102
3.5 Outlook and future work 103
3.6 References.... 103
Chapter 4 | Optical-Resonator-Based Biosensing: G-quadruplex (G4) structure and ligand study....108
4.1 Introduction 109
4.1.1 Background and introduction to G-quadruplexes....109
4.1.2 Human telomeric G-Quadruplexes 110
4.1.3 Folding and topology of quadruplexes 110
4.1.4 Characterization of G-quadruplex structure....111
4.1.5 Methods for investigating G-quadruplex DNA/ligand interaction 112
4.1.6 Binding mode of ligand to G-Quadruplex....115
4.2 Experimental methods.... 119
4.2.1 Chemical and materials....119
4.2.2 Circular dichroism (CD) experiment....119
4.2.3 Attenuated total reflection spectroscopy (ATR) experiment 120
4.2.4 Fluorescence experiment....120
4.2.5 Fabrication and functionalization of the microsphere resonator....120
4.2.6. WGM assay for interrogating G4 structure/function....122
4.2.7. WGM assay for ligands interaction with G4 structure....123
4.3 Results and discussions 123
4.3.1 Characterization of G-quadruplex structure in solution 123
4.3.2 Immobilization of DNAs onto the resonator surface and discriminate between folded and unfolded states of G4 region of the c-myc promoter 125
4.3.3 Characterization of functionalized and immobilized DNAs on the resonator surface 129
4.3.4. Kinetic of G-quadruplex binding from the WGM signal 134
4.3.5 Mass transported limitation (MTL)....135
4.3.6 Interpreting kinetic fingerprints from ligand binding to G-quadruplex or duplex DNA 136
4.3.7 Binding affinities for selected five ligands....143
4.3.8 Control and competition experiment....144
4.3.9 Discriminate different forms of c-myc by WGM....147
4.3.10 Attempting to fold and unfold G-quadruplex on the resonator surface....148
4.3.11 Hybridization c-myc and pre-folded c-myc with complementary strand on the resonator surface 152

4.4 Conclusion 155
4.5 Outlook and future work 156
4.6 References 157
Chapter 5 | Thrombin (TB) detection by WGM 165
5.1 Introduction to blood clotting 166
5.1.1 TB and FB protein 166
5.1.2 Conversion of FB to F clot by TB 168
5.2 Motivation and challenging in TB-based WGM sensor 169
5.3 Reviews of TB-sensor 169
5.4 Experimental methods 171
5.4.1 Chemical and materials 171
5.4.2 Fabrication and functionalization of the microresonator and WGM resonance shift measurements for TB-sensor 171
5.4.3 Quantification of TB using TB-based WGM sensing 171
5.4.3.1 Method: 1 FB-Au NPs and TB 172
5.4.3.2 Method: 2 Biotin-FB and TB 172
5.4.3.3 Method: 3 MPTMS-FB and TB 173
5.5 Results and discussions 173
5.5.1 Method: 1 FB-Au NPs and TB 173
5.5.2 Method: 2 Biotin-FB and TB 175
5.5.3 Method: 3 MPTMS-FB and TB 178
5.5.3 Conclusion from TB-based WGM sensor 180
5.6 Possible future outlook 180
5.7 References 180
Chapter 6 | Conclusions and future outlooks 183
6.1 Conclusions 184
6.2 Future outlook 187
Appendices 188

List of Abbreviations

A

AAS	Atomic absorption spectrometry
AFM	Atomic-force microscopy
a.k.a	As known as
APTES	(3-aminopropyl) triethoxysilane
APTMS	Aminopropyltrimethoxysilane
ATR	Attenuated total reflection spectroscopy
AuNPs	Gold nanoparticles

B

BSA	Bovine serum albumin

C

ca.	Circa (around)
CE	Capillary electrophoresis

D

DVT	Deep vein thrombosis

E

EDC	1-ethyl-3-(3dimethylaminopropyl) -carbodiimide
EPA	Environmental Protection Agency
Eq	Equation

G

GSH	Glutathione
G4	G-quadruplex

F

13F	Tridecafluoro-1,1,2,2-tetrahydrooc-tyl)-l-ldimethylchlorosilane

F	Fibrin
FB	Fibrinogen
FIR	Fluorescence intensity ratio
FWHM	Full width at half maximum

I

IARC	International Agency for Research on Cancer
ICP	Inductively coupled plasma spectroscopy
i.e.	Exempli gratia (for example)
IR	Infrared
IUPAC	International Union of Pure and Applied Chemistry
IU	International Units

M

MBT	Mercaptobenzothiazole
MPTMS	3-mercaptopropyl-trimethoxy-silane

N

NHS	N-hydroxysuccinimide

P

PE	Pulmonary embolism
ppb	Part per billion
ppm	Part per million
ppt	Part per trillion
PS	Polystyrene
PVC	Polyvinyl chloride

W

WGM	Whispering gallery mode

R

RIU	Refractive index unit
RLS	Resonance light scattering

S

SEM	Scanning electron microscopy
SER	Surface-enhanced Raman spectroscopy
SiPEG	Silane-polyethylene glycol
SPR	Surface plasmon resonance

T

TB	Thrombin
TBA	Thrombin binding aptamer
TIR	Total internal reflection

U

UV	Ultraviolet

V

VTE	Venous thromboembolism

W

WHO	World Health Organization

Q

Q-factor	Quality factor

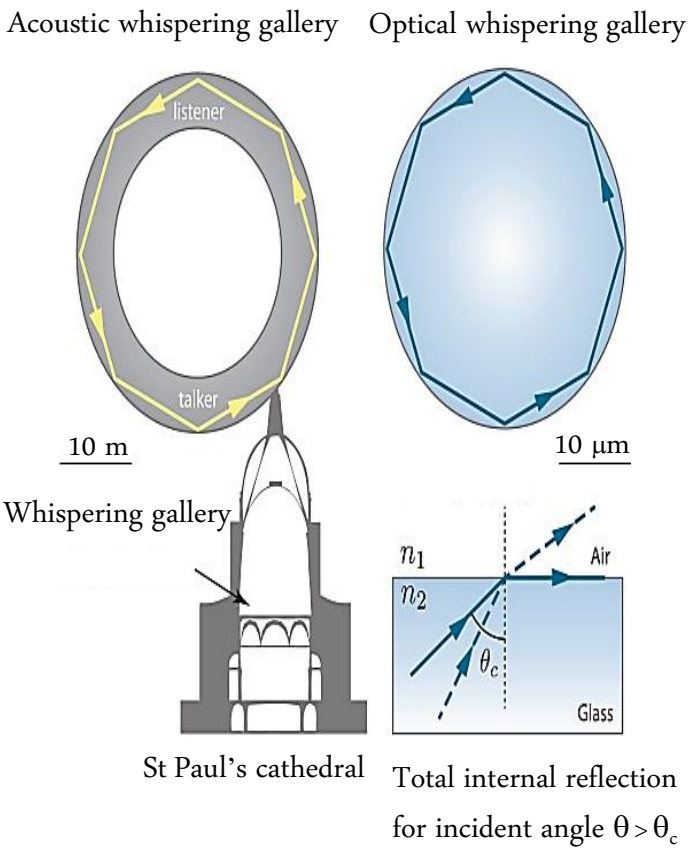
List of Symbols

A	Absorbance
θ	Angle at which total internal reflection takes place
θ_1	Angle of light incident
k_1, k_{on}	Association rate constant
N	Average number of gold nanoparticle
D	Average core diameter of the particle
M	Atomic weight of gold
σ	Average surface density
N_A	Avogadro's constant
θ_c	Critical angle of light
k_{-1},k_{off}	Dissociation rate constant
d	Decay constant
ρ	Density for FCC
n_{eff}	Effective refractive index of the surrounding sphere
α_{ex}	Excess polarizability
δλ	Full width at half-maximum of the attenuation peak
fM	Femto molar
N_{total}	Initial amount of gold salt
m	Integer
K	Kelvin
µL	Micro litre
µM	Micro molar

mL	Milli litre
ε	Molar extinction coefficient
C	Molar concentration of nanoparticles solution
nm	Nano metre
nM	Nano molar
k_{obs}	Observed rate constant
π	Pi
R	Radius
n	Refractive index
λ_r	Resonance wavelength
n_s	Refractive indices of the sphere
n_m	Refractive indices of the exterior medium
$\Delta\lambda_r$	Resonance wavelength shift
α	Total optical loss coefficient
V	Volume of the reaction solution

Chapter 1 | Introduction





St Paul's cathedral

Total internal reflection for incident angle $\theta > \theta_c$

The whispering gallery phenomenon was first witnessed in a rounded architectural feature – the dome of St Paul's Cathedral, London, is shown in the left picture. The term refers to the principle that when one person whispers, the sound is clearly audible by a total internal reflection (TIR) effect to a remote listener who places their ear close to the wall at any position of the gallery. The whispering gallery mode (WGM) technique is a novel optical technique integrated into a sensor. It applies the same principle as St Paul's whispering gallery but instead of sound, light waves are utilised, so specific molecules down to even a single molecule in samples can be detected. It is only in the last two decades that the technique has been integrated to quantify specific molecules in chemical and/or biological sensors, although the WGM principle was described more than a hundred years ago [1-4]. The right picture is adapted with permission from [5, 6].

WGM optical resonator sensors (sometimes referred to as optical cavity sensors, or resonance evanescent wave sensors) are one of the most fascinating and outstanding optical sensors due to their highly sensitive, label-free, rapid, selective and multiplexed detection capabilities. The technique is becoming more prevalent due to the numerous advantages it offers. This research project aims to develop WGM further to detect specific analytes in order to solve some key problems in chemical/biosensor research, such as difficulties in the label free monitoring of specific analytes in real-time. As part of this thesis, applications such as the Pb(II) sensor in Chapter 3, the G-quadruplex–ligand interaction sensor in Chapter 4 and the thrombin (TB) sensor in Chapter 5 will be demonstrated. To better understand the work in this project, some physical operating principles of WGM sensing relevant to all the experiments will be presented. Moreover, the up-to-date literature from the WGM field will be reviewed. Research project aims and goals are likewise discussed.

1.1 Sensors

A sensor is a device made in order to obtain qualitative and/or quantitative information. This information may be from the surrounding environment or from inside the human body and it can affect our daily lives: pollutant molecules, toxic elements and biomarkers are all of interest. These can exist in a complicated mixture that contains other substances which interfere with measurements made by the sensor [7]. Separation of a molecule of interest from the interference, its recognition, and the determination of the target molecule's concentration are the key aims of sensor research and development [2]. The signals from the sensor devices depend on characteristics of the analytes, the transducer and other factors. To date, many sensing techniques have emerged and therefore many problems have been addressed with varying degrees of success. Several test kits have been developed for different purposes in the hospital or even the home. A pregnancy test can give results with 99% accuracy from a small test kit in a few minutes. Another example is a gas detector used to detect a gas leak or hazardous gases in a residence for safety purposes. In chemical and biomedical research, many types of sensors have been published and produced commercially, such as toxic chemicals or cancer biomarker sensor sensors.

In this work, the WGM technique was developed for both chemical and biological sensors. To fulfil these aims, the definition of chemical and biological sensors should necessarily be mentioned. Many classifications and definitions of a chemical sensor can be found in the literature. Among them, the International Union of Pure and Applied Chemistry (IUPAC) defines chemical sensors as follows.

"A chemical sensor is a device that transforms chemical information, ranging from the concentration of a specific sample component to total composition analysis, into an analytically useful signal. The chemical information, mentioned above, may originate from a chemical reaction of the analyte or from a physical property of the system investigated" [8].

In terms of biosensors, there are also many definitions. The following definition, from a review by T. Daniel *et al.* [9], is well-suited here.

"A biosensor is an integrated receptor-transducer device, which is capable of providing selective quantitative or semi-quantitative analytical information using a biological recognition element" [9].

Herein, a WGM sensor can be defined as a sensor which monitors optical resonances occurring in microresonators, the surface of which is functionalised with chemical-recognition elements and/or bio-recognition elements.

Currently in chemical, biological and medicinal sensor research there are numerous advanced techniques that have been reported and integrated into devices. There is still, however, plenty of room for developments to address issues such as high costs, complexity and a lack of real-time analysis which is highly specific to the target analyte. Therefore, there is a pressing requirement for the development of label-free sensing technologies with high sensitivity and selectivity for target molecules. Indeed, the growing field of optical detection techniques is being paid increasing attention recently [2, 10].

Optical sensing methods such as fluorescence, Raman, ultraviolet (UV) absorption and surface-enhanced Raman spectroscopy (SERS) have become a basic technology in chemical and biosensor research. The popularity of these techniques can be attributed to their speed, flexibility and low cost. Moreover, some optic sensors such as surface plasmon resonance (SPR) can support optical technology such as wave guides, photodiodes, optical fibres and light sources, especially lasers [11]. WGM cavities, in which light is trapped inside a cavity, are one type of optical sensor. They are one of the most fascinating types of optical sensor since they afford an extreme level of sensitivity down to single molecule detection, as well as real-time analysis often without the need for labels, multiplexed sensing ability and cost-effective integration with fibre optics. By utilising light rays from a laser source, many benefits were gained from this sensor such as high speed and low cost [5, 12]. The classification, advantages and disadvantages of optical sensors can be seen in the Table 1.1.

Table 1.1 Classification, advantage and disadvantage of optical sensor

Optical sensor [13]					
Absorption-based UV-Visible, Infrared (IR) spectroscopy		**Emission-based fluorescence, phosphorescence, luminescence**		**Refractometric/Interferometric SPR, WGM**	
Advantage	**Disadvantage**	**Advantage**	**Disadvantage**	**Advantage**	**Disadvantage**
-The instrumentation is simple and cheap -Already present in portable and commercial devices	-Relatively low sensitivity and specificity to the target molecule	-Sensitivity and specificity -Sensitivity of luminescence is about 1000 times greater than that of most spectrophotometric techniques -Lower limits of detection -The instrumentation is simple and cheap	-The sample is excited only by a pulse rather than by continuous illumination -The precision and accuracy are affected by fluctuations in the light-source's intensity, detector sensitivity, filter effects, reagent concentration, sample turbidity, and sensing layer thickness -In the case of measuring luminescence lifetimes instead of intensities, instrumentation complexity and high costs are drawbacks, along with a limited number of indicator dyes available that show significant analyte-dependent changes in the lifetime	-Label-free: no need for time-consuming labelling steps-High sensitivity and selectivity toward the target analtye-Small sample sizes achieved by integration with microfluidics-Real-time monitoring within a couple minute-The binding kinetics of interactions can be achieved -Multiplexed detection	-Surface fouling -Discriminating between specific and non-specific interactions is sometimes not easy -Reference material or control samples are needed in order to correct for non-specific binding -Low molecular weight compounds are more difficult to detect [14]

1.1.1 Advantages and disadvantages of WGM sensing compared with other sensing techniques

In light of all that has been mentioned so far, one may suppose that WGM sensors have established superior sensitivity levels and have revealed a plethora of applications. The table below will summarise both advantages and disadvantages of WGM sensors.

Table 1.2 Comparison of the advantages and disadvantages of WGM sensors

	Topic
Advantages	**Setup** -By utilising optical technology such as photodiodes and optical fibres, the WGM sensor can be developed as a flexibile and low-cost sensor [5]. -By integrating with miniaturised nanotechnology [15], the size of the resonator can be reduced to the micro or nano scale, such as microring [16], microgloblet [17] and microdisk [18] resonators, as a result a size of the sensor can be miniaturised.
	Specificity towards a target molecule -Any surface modification which is already in use on glass surfaces can be easily applied.
	Running cost -A home-built benchtop machine costs less than £5,000 and the cost of each experiment is small (not including the chemical reagent)
	Sensitivity -The technique is well known to be extremely sensitive and can detect the target molecule down to a single molecule [19-21].
	Multiplexing, real-time monitoring and label-free detection -Possible to modify as a multiplexed detection sensor by using mode splitting [22], a parallel goblet resonator [17], or by combination with fluorescence techniques [23]. -The sensor can be applied as a label-free detection technique [2, 24, 25]
	Applications -A variety of sensor applications has already been published, providing the extraordinary versatility of the WGM sensing technique [5]. -The technique is compatible with many other techniques in order to improve the quality of the sensor such as Raman spectroscopy, microdroplet [26] and fluorescence techniques [23].

Table 1.2 Comparison of the advantages and disadvantages of WGM sensors (Continued)

Topic	
Disadvantages	**Setup** -The WGM sensor is sensitive to temperature so for field work a temperature controller is required [27]. -Conducting measurements in solution is challenging, as this reduces the Q-factor and poses serious technical limitations [26]. -Improving the setup to be used in as a portable device is also challenging. For example, the microsphere coupled with the tapered wave-guide is the simplest set-up but the WGM measurement will be very sensitive to the alignment of the tapered fibre optic next to the resonator. Small changes in the gap or position along the taper can affect the Q-factor and can reduce the robustness of the approach for high throughput applications.

Table 1.3 Comparison of WGM with the SPR technique [13]

Topic	WGM	SPR
Surface functionalisation	Functionalisation of the WGM resonator can be achieved by applying many surface functionalisation protocols as the material of the resonator is silica so glass surface functionalisation, which is well-established, can be applied.	Functionalisation of a SPR chip is already commercial and well-established i.e. Biacore SPR. However, the process is restricted to only the metal based-SPR chip, even if reusable sensor chips be achieved, it is not as flexible as in WGM.
Fabricated in several geometries	The geometry of the resonator can be varied: sphere, cylinder, ring, goblet and disk are all possible.	SPR chips are limited to a planar geometry.
Label-free	Can be applied to label free sensing.	Can be applied to label free sensing.
Multiplex detection	Possible using many resonators	Possible from multi-channels in a SPR chip.
Sensitivity	Can detect down to a single molecule.	Can detect down to a single molecule.

Table 1.3 Comparison of WGM with the SPR technique (Continued)

Commercial platforms	Not fully in commercial use.	Already in commercial platforms such as Biacore.
Cost effective	A home-built benchtop WGM setup costs less than £5,000, and the cost of each WGM sensor is small.	Costly in terms of hardware (£270,000 for the T200 Biacore instrument), software (£1000s), consumables (£200 per chip) and maintenance (up to £40,000 annually).
Kinetic data	Easy to extract kinetic data such as a binding curve.	Easy to extract kinetic data such as a binding curve.

According to Table 1.2, WGM, a subset of optical sensors, offers numerous of advantages over other optical sensors. Quantitative information about target molecules and their interactions can be obtained in real-time with high sensitivity and selectivity. In addition, modifications of the WGM technique give it many applications as a simple, ultrasensitive and label-free sensor. Selected applications of WGM are highlighted below, in Figure 1.1. WGM sensors can be applied to a wide variety of analytes that include biomolecules and their interactions as well as virions [28, 29], protein [30-34] and DNA [35, 36]. The approach can also be extended to, for example, a single molecule of the above-mentioned analytes such as a single molecule of nucleic acids [24]. Other than for the analysis of biomolecules, a WGM sensor can be used in cell-based assays. Although experiments with prototypes have demonstrated the great potential of the WGM technique, there is still plenty of room for improvement. More detail about WGM based sensing and its application can be found in section 1.3.

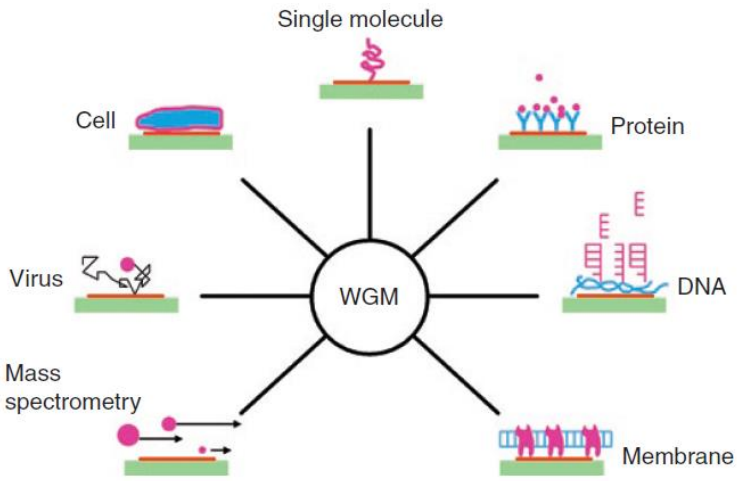


Figure 1.1 Highlighted applications of the WGM technique. Reprinted with permission from [25].

1.2 Theories of optical WGM

1.2.1 Gallery of whispers

At the whispering gallery in St Paul's Cathedral in London, a sound from a whisperer is perceptible more than thirty meters away within the gallery. More importantly, the whisper can be heard by the listener clearly at any point. This occurrence was well elucidated in Rayleigh's textbook, "The Theory of Sound", published in 1878. At that time, the whispering gallery effect was considered a useful tool only for detecting imperfection in curvatures [37-39]. In 1938, A. E. Bate reported experiments carried out in the whispering gallery, finding that whispers composed of high frequencies and also of low frequencies projected similarly [39].

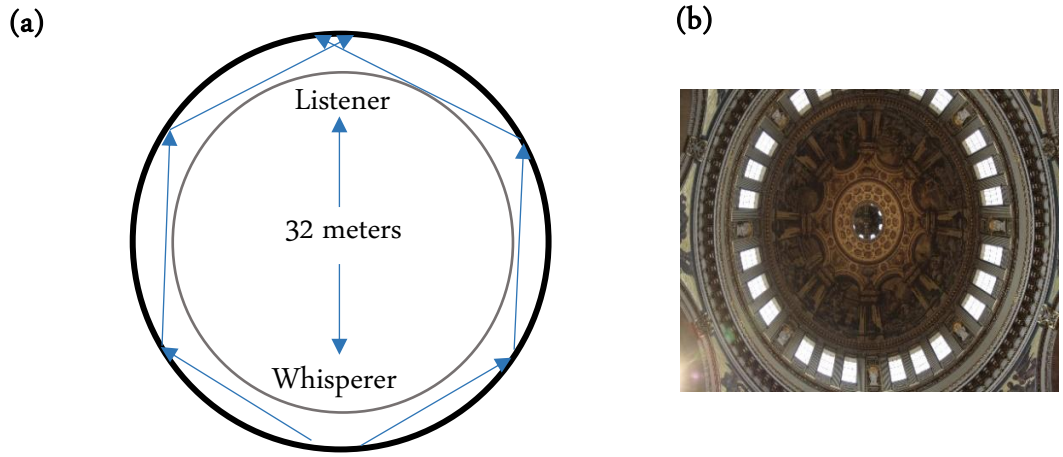


Figure 1.2 (a) The phenomenon of the refocusing effect as the sound propagates inside a rounded dome. Adapted from [40, 41] and (b) the actual picture of the whispering gallery at St Paul's cathedral in London.

1.2.2 From the whispering gallery to a chemical and a biological sensor

For many decades after Rayleigh's theory was published there were no applications of the whispering gallery in research fields such as chemistry until the laser was discovered. In fact, not only sound but also light can act as whispering-gallery waves and can be confined inside a circular dielectric material. Utilising the whispering gallery phenomenon of St Paul's Cathedral, by miniaturising the size of the circular dome into a small micron size, using light rays from a laser source and a photodiode detector, various kinds of WGM sensors can be integrated in both chemical and biological research fields. WGM sensors derive their extraordinary sensitivity from a high quality-factor (Q-factor) to detect the shift in the wavelength of signals upon binding of an analyte to the resonator surface, with the ability to detect even a single molecule [24, 25].

1.2.3 Resonant mode and total internal reflection effect

To understand the principle behind WGM sensors, it is necessary to understand resonant modes and total internal reflection (TIR). A resonance in cavities (or resonators) such as an acoustic or an optical resonance is normally dependent on the size, shape and material of the supporting structure. As shown in Figure 1.2 part (a), the TIR effect can be represented by a sphere supporting the whispering gallery phenomenon. This effect explains how light is trapped near the surface of a resonator and circumnavigates a zigzag optical pathway around the equatorial plane. It should be noted that this phenomenon occurs when a ray of light strikes the surface of the resonator (in WGM case, glass in air or water) in phase condition, as this light will circulate along the sphere with a radius of R and refractive index of n_s. The angle of light incidence is denoted as θ_1. TIR occurs in WGM resonators only when $\theta_1 > \theta_c$ where θ_c is the critical angle. In WGM, the fabrication of a spherical resonator is focused on achieving perfect sphere in order to ensure all angles of incidence are the same so that the ray can be optimally trapped. The trapped ray propagates a distance $\sim 2\pi R$ in one round trip [1, 42].

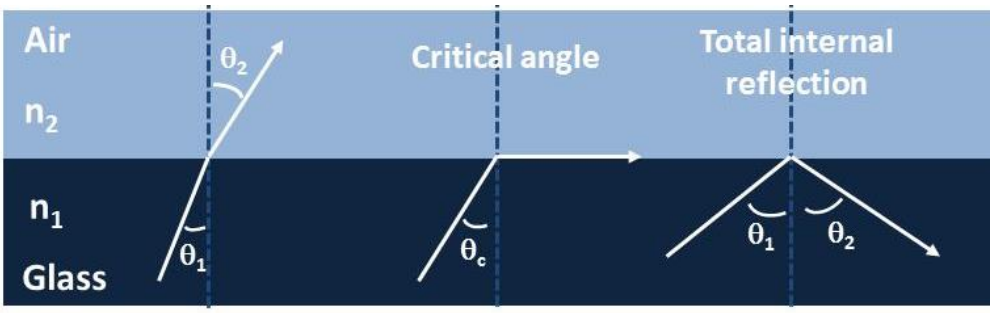


Figure 1.3 Simple illustration explaining the general idea behind the TIR effect which occurs at the boundary of glass and air (this can also be applied to glass and water). Adapted from [43].

Essentially, TIR of light occurs at the boundary of glass in air or water (in our case the resonator is made of glass), which will depend on the size of the angle of incidence, θ_1, compared with the critical angle, θ_c (the largest angle of the incidence at which maximum refraction occurs), Figure 1.3. Normally, if a light ray travels from glass into air, the incident angle is enlarged enough, with the transmitted angle in air approaching 90 degrees ($\sin \theta_1 = 1$). At this point no light is transmitted into air but instead propagates at the surface boundary. According to Snell's law, the critical angle, θ_c, can be defined as follows:

$$n_{in} \sin \theta_c = n_{out} \sin \theta_1 \quad (1.1)$$

$$\theta_c = \arcsin\left(\frac{n_{out}}{n_{in}}\right) \quad (1.2)$$

If $\theta_1 < \theta_c$ the ray will be split. Part of it will reflect off the boundary while some will bend as it passes through. In contrast, if $\theta_1 > \theta_c$ the ray completely reflects from the boundary. No light passes through, which is "total internal reflection" or "TIR" [44].

Multiple, repeated TIR in a perfectly circular dielectric WGM resonator can be seen in Figure 1.4. There, the angle of incidence will always be greater than the critical angle and thus the light will always undergo TIR. In a WGM resonator, there are many different losses which can be explained by the quality-factor (Q-factor) in Equations 1.3 [45].

$$Q = \frac{2\pi n}{\lambda_r \alpha} \tag{1.3}$$

$$\alpha = \alpha_{material} + \alpha_{radiative} + \alpha_{surface\ scatering} + \alpha_{coupling} \tag{1.4}$$

Here, α can be defined as the total optical loss coefficient, with the most significant distinct components given by material, radiative, surface scattering and coupling losses, as described in Equation 1.4. More detail about the Q-factor can be found in section 1.2.8.

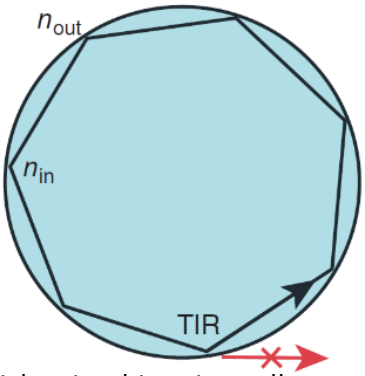


Figure 1.4 Schematic of a dielectric whispering gallery mode resonator. Reprinted with permission from [45].

1.2.4 The operating principles of WGM

Generally, the function of WGM sensors is to track changes in the WGM transmission spectra, affected by changes in the composition of the resonator's surrounding medium. The WGM technique enables quantitative information even at the single molecule level. The interaction between the molecule of interest and the surface of the resonator can be explained using different theories, as discussed below.

1.2.4.1 Perturbation theory (in phase/out of phase theory)

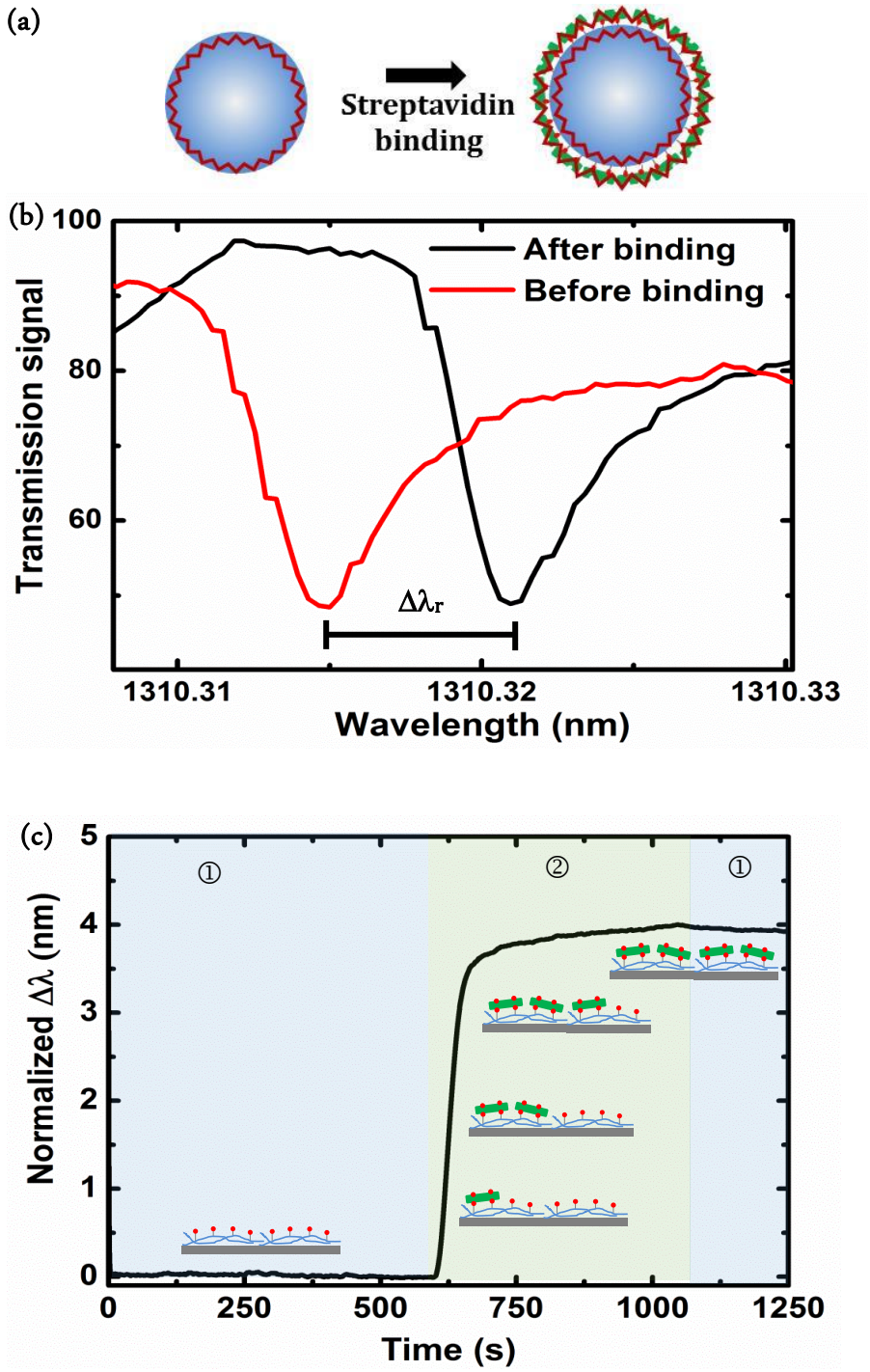
An optical WGM technique is based on a light wave from a tunable laser which is strongly confined and circumnavigates the surface of a dielectric microresonator, returning back upon itself in phase, Figure 1.5 part (a). Resonance from a whispering-wave will occur when the microresonator (such as a microsphere, microring or microtoroid) is made resonant

by coupling to a light guide (for example, a tapered waveguide or a prism) via the evanescent field. As the laser wavelength is tuned through the resonance wavelength (λ_r), power is extracted from the light guide. As a result, a dip, or a negative peak, occurs. For example, a dip in the light transmission was detected by a photodiode detector from the light coupled to the 3-aminopropyl triethoxysilane (APTES)-functionalised microsphere resonator in Figure 1.5 part (b) from the G-quadruplex experiment, Chapter 4. The surface of the resonator needs to be functionalised in order to make it specific only to the molecule of interest. When the analyte binds to the functionalised microresonator, it increases the light path length of the resonance. In order to maintain the microsphere resonator in phase the resonator needs energy to compensate for the lost energy; as a result, the resonance wavelength shifts. Therefore, binding of the analyte is identified from a resonance wavelength shift ($\Delta\lambda_r$) and this $\Delta\lambda_r$ depends on the amount of the analyte. The greater the number of analyte molecules bound the more the resonance shift increases. A plateau is reached when all the receptors are occupied as shown in Figure 1.5 part (c).

A resonance phenomenon in a spherical cavity is able to confine light on a circular path length due to the TIR effect as was mentioned section 1.2.3. The resonance is caused by coupling the waveguide with a resonator through the evanescent field which allows photons to be confined. The photon can travel around 300 m in vacuum conditions [46]. After one round trip the light returns to the same point with the same phase. This happens many times, as shown in Figures 1.4 and 1.5 part (a). The whispering gallery mode phenomenon occurs when the light completes one round trip along the equator of the sphere and begins to overlap with its own path. This phenomenon can be explained by Equation 1.5, where N is an integer, λ is the wavelength of light and R is the radius of a given sphere; $N\lambda$ is therefore an integer number of wavelengths fitting the circumference of the sphere [19].

$$N\lambda = 2\pi R \tag{1.5}$$

The multiple roundtrips of the photon can amplify the signal intensity. However, the number of roundtrips can be limited by the loss of photons via absorption or scattering. Thanks to the advantages of using silica glass spheres, these losses are minimal [47] as the glass sphere is an excellent light container, thereby enabling high sensitivity and possibly even single-molecule detection.



① 10 mM KCl in 10 mM Tris buffer ② 25 μg/ml streptavidin in ①

Figure 1.5 (a) Light circumnavigates a silica microsphere by the TIR effect. The binding of the molecule of interest (in this case streptavidin) increases the path length and disturbs the resonance of the laser. It was recorded as an induced shift of the resonant wavelength ($\Delta\lambda_r$). (b) and (c) show examples of normalized $\Delta\lambda$ and binding curves, both before and during the binding of streptavidin on a biotinylated surface, from the G-quadruplex work; for further detail see Chapter 4.

To summarise, when a sphere couples with a waveguide it leads to a resonance in phase, and when a molecular layer of small thickness adsorbs or binds on the sphere the resonance is shifted out of phase. The adsorption of a molecular layer causes the wave to circumnavigate a larger circumference, increasing the optical path length. In order to maintain the resonance (back to being in phase again), the wavelength needs to increase to compensate the size change [19, 30, 46, 48-50]. This perturbation theory underlies the use of WGM as a valuable tool for the analysis of biomolecular interactions where the analyte binds as a thin layer on the resonator surface. The thickness of such a layer can be precisely calculated from a wavelength shift, such as the thickness of bovine serum albumin (BSA) and streptavidin [19]. Furthermore, this perturbation theory can also explain why WGM can detect single viruses and nanoparticles [51]. In Chapter 4, the induced wavelength shift from the binding of streptavidin is explained by this principle.

1.2.4.2 Refractive index contrast between the medium and the resonator surface

Another explanation of WGM can be elucidated by the refractive index. When the refractive index of the surrounding medium changes, shifts in resonance frequency occur. The greater the refractive index contrast between the resonator and the surrounding medium (Δn) the less the radiative loss, and the higher and the stronger the confinement of light. The wavelength shift induced by a change in refractive index for a resonator which is larger than the optical wavelength can be calculated from Equation 1.6 [52, 53].

$$\lambda_r = \frac{2\pi R n_s}{m} \tag{1.6}$$

Here, λ_r is the resonant wavelength (or spectral position), R is the radius of the resonator, n_s is the effective refractive index of the sphere experienced by WGM and m is an integer that describes the WGM angular momentum. The change in radius and refractive index leads to the red shift in the WGM system which is called "reactive WGM sensing" as shown in Equation 1.7, where $\Delta\lambda_r$ is the resonant wavelength shift, and where (ΔR) and Δn are the increases in the radius and refractive index from a resonance shift in WGM, respectively [25].

$$\frac{\Delta\lambda_r}{\lambda_r} = \frac{\Delta R}{R} + \frac{\Delta n}{n} \tag{1.7}$$

In practice, for a WGM biosensor where dielectric properties of the sphere and the bound protein layer are similar, the difference of the dielectric constants of the sphere and the adsorbate are negligible. Thus the thickness (ΔR) can be precisely calculated. This reasonable assumption can be applied to most proteins with a refractive index of ca. 1.5 and the sphere

with a refractive index from ca. 1.44 (silica) to 1.55 (polystyrene). With only the radius increased, thus the thickness of the adsorption layer can be calculated according to Equation 1.8 [19, 25, 52].

$$\Delta R = \frac{\Delta\lambda_r R}{\lambda_r} \tag{1.8}$$

1.2.4.3 Molecular polarisability

Evanescent coupling to the WGM resonator can be achieved by positioning a tapered optical waveguide close to the resonator surface. The transmitted power can be monitored as the frequency of the incident laser. Figure 1.5 part (b) shows a Lorentzian resonance dip which can be tracked after the resonator couples with the waveguide. The depth of the given transmission dip is based on the coupling efficiency. Quantification of the wavelength shift based on the polarisability begins when the electromagnetic wave circumnavigating the sphere induces the polarisation of a bound molecule. The energy required to polarise the bound molecule at the evanescent field is measured as a resonant wavelength shift [19],

$$\frac{\Delta\lambda_r}{\lambda_r} = \frac{\alpha_{ex}\sigma}{\epsilon_0(n_s^2 - n_m^2)R} \tag{1.9}$$

where n_s and n_m are refractive indices of the sphere and exterior medium, respectively, $\Delta\lambda_r$ is the resonance shift, λ_r is the nominal wavelength of the laser, α_{ex} is the excess polarisability, σ is the average surface density, and R is the radius of a sphere [19, 25].

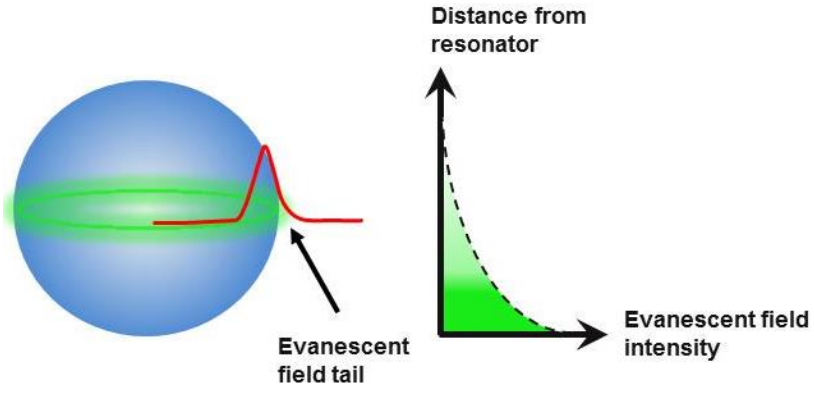


Figure 1.6 The optical resonance with an evanescent field extending from the surface to the surrounding medium. This evanescent field triggers the polarisation of bound molecules leading to a resonant wavelength shift. Adapted from [42].

According to Figure 1.6, the evanescent field from a resonator surface decays with distance from the resonator. The field decays as an exponential with a decay constant d in the following equation.

$$d = \frac{\lambda}{2\pi(n_s^2 \sin^2 \theta - n_m^2)^{1/2}} \tag{1.10}$$

Here, λ is the wavelength, n_s is the refractive index of the resonator, n_m is the refractive index of the surroundings, and θ is the angle at which total internal reflection takes place at the internal surface of the resonator [55, 56].

It is well known that an optical resonator can trap light and that such light travels inside the cavity multiple times. The cavity size needs to be decreased in order to amplify the light intensity and enhance the light confinement. In practice to achieve these tasks, technical challenges for microresonator fabrication must be overcome. The resonance in WGM is described in Equation 1.11, where n_s is the resonator refractive index, R is the resonator radius, m is an integer.

$$2\pi n_s R = m \lambda_r \tag{1.11}$$

The light field is confined within the resonator. The evanescent tail from the coupling of the light and the WGM resonator spreads out into the surrounding medium with an exponential decay length of around a few hundred nanometres [57] as shown in Figure 1.5.

In this project's work on the Pb(II) sensor, the resonance wavelength shift is explained based on the theory above (more detail can be found in Chapter 3 or in reference [20]). It is important to note that there may be more than one theory that could explain the resonant wavelength shift, as seen in Equation 1.9. There is a strong correlation between refractive index and polarisability. This means that the wavelength shift from the binding depends on both the fraction of the energy found (evanescent field) at the position of the bound molecule and the excess polarisability of the molecule [55]. A single mechanism alone is not sufficient to explain the induced resonance shift.

1.2.5 WGM microresonators

Since numerous sensors have exploited the WGM technique, there has been much research published on many geometries of resonators for potentially monitoring changes in the resonant frequency, for instance microspheres [48-50, 52, 58-64], microrings or microdisks [18, 62, 65-81], microtoroids [82-88], microbottles [89-93] and microcylinders [94-101], as shown in Figure 1.7 [25].

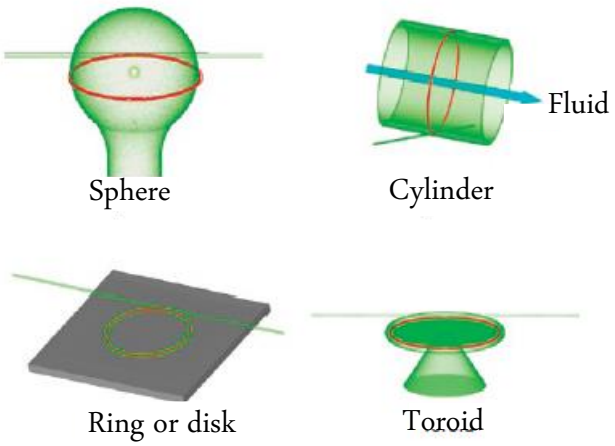


Figure 1.7 WGM resonator geometries. Reprinted with permission from [25].

The latest geometry of resonator used in a WGM sensor is a microgoblet in which multiplex detection can be achieved [17, 102, 103]. Microspheres were used throughout this project, as it is the most simple resonator to fabricate and can support high Q-factors [1].

1.2.6 Microresonator surface modification

As was mentioned in the previous section, many geometries of WGM have been proposed. In this work, a silica spherical resonator was adopted, so only the surface modification of glass will be discussed here. Surface modification of the microresonator is a crucial step as it controls the selectivity and can enhance the sensitivity of the sensor. The advantage of using a silica resonator is not only in its low cost but also many surface functionalisation protocols of glass have already been published and can be directly applied to the resonators. For example, one of the most popular surface functionalisation processes is silanisation. In WGM work, many types of silane have been used to modify the surface of the resonator. For example, 3-aminopropyl trimethoxysilane (APTMS) [104] or 3-aminopropyl triethoxysilane (APTES) have been used to biotinylate the silica surface through N-hydroxysuccinimide-biotin. APTMS was also used to attach gold nanoparticles onto the surface [20]. Other kinds of silane such as (tridecafluoro-1,1,2,2-tetrahydrooctyl)-1-

dimethylchlorosilane (13F) and silane-polyethylene glycol (SiPEG) were also used to modify the surface for protein adsorption [105].

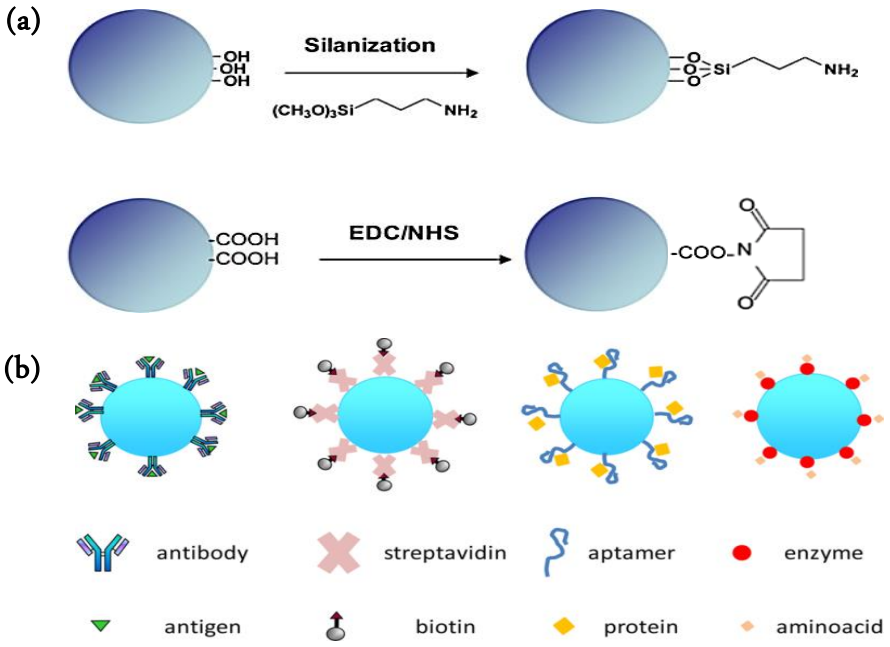


Figure 1.8 (a) Functionalisation of a WGM sensor using a silane agent, primary amine groups and carboxyl groups (COOH) activated with 1-ethyl-3-(3dimethylaminopropyl)-carbodiimide (EDC)/N-Hydroxysuccinimide (NHS) chemistry. (b) A sketch of several biosensors based on a functionalised WGM resonator, interfaced with the biological recognition element. Reprinted with permission from [42].

1.2.7 Light coupling into a microresonator

In order to fully understand the basic principles and practical applications of resonators, light coupling should also be discussed. Various methods of evanescent coupling of light to the WGM sphere resonator can be used, such as a prism, a wave-guide, or angle-polished fibre as shown in Figure 1.9 [1]. Among these, the fibre taper coupled sphere is the simplest method. There are several benefits from the use of a fibre tapered waveguide: it is easy to fabricate, the material is cheap, it is simple to focus, align, inject the input beam and collect the output beam [63, 64]. Most importantly, the coupling efficiency can reach above 99% under appropriate conditions using fibre taper coupling to high-Q silica microspheres [106].

However, the downside of this technique is that the tapered region is easy to break and can easily deteriorate. The integrated waveguide coupler is more robust but it is more difficult to achieve an efficient coupling, as is also the case with prism-to-sphere coupling [1]. Finally, the angle polished fibre technique is limited by the high refractive index of the fibre.

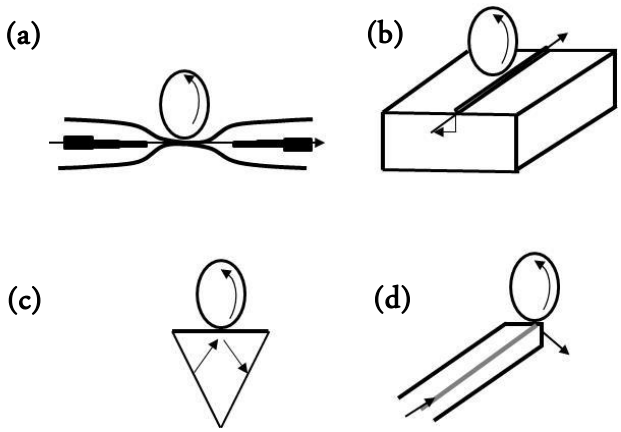


Figure 1.9 Schemes of evanescent wave couplers used to inject light into a microsphere: (a) tapered optical fibre (b) integrated waveguide (c) prism and (d) angle-polished fibre. Reprinted with permission from [1].

1.2.8 Cavity Q-factor

The detection limit and the sensitivity in WGM sensing are dependent on the Q-factor of the resonator. The higher the Q-factor, the smaller the resonant shifts. Q-factor in WGM sensor has is high so the sensor offers promising advantages in many applications. The resonance Q-factor can be defined as shown in Equation 1.12. The Q-factor is mathematically described as the ratio of the wavelength where the resonance occurs (λ_r) to the spectral linewidth of the resonant wavelength ($\delta\lambda$) which is the full width at half-maximum of the attenuation peak as described in Equation 1.12 [107]. Herein, $\delta\lambda$ is estimated using Origin software and a non-linear Lorentz equation (more detail can be found in Chapter 2).

$$Q = \frac{\lambda_r}{\delta\lambda} \tag{1.12}$$

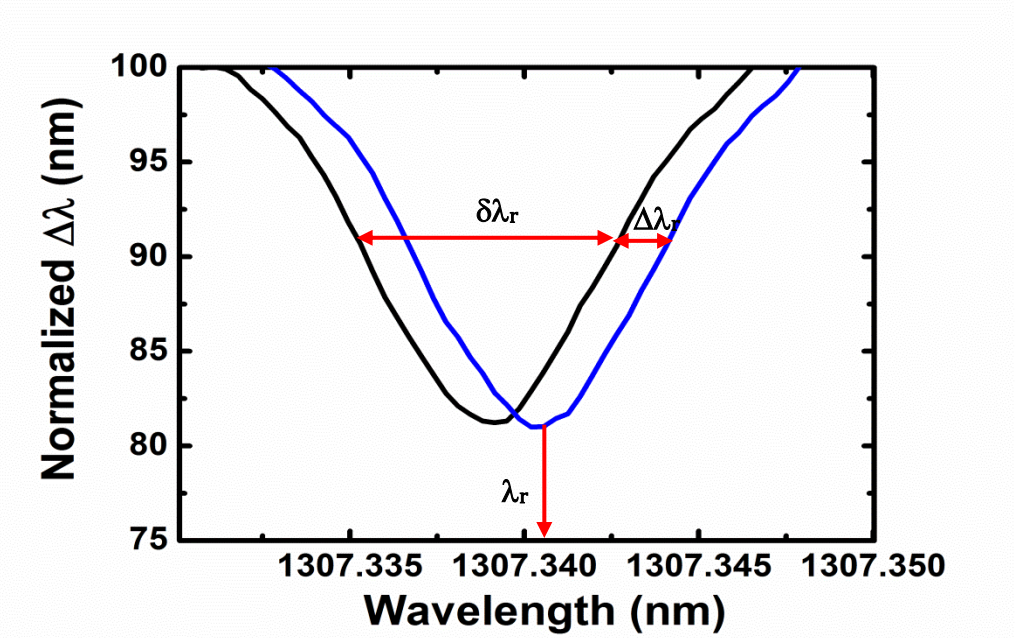


Figure 1.10 An example of wavelength shift explaining terms used in the WGM experiments.

Fundamentally, there are four terms which can be considered to affect the Q-factor. The terms are Q_{mat}, Q_{rad}, $Q_{s.s}$ and Q_{count} which can be described as intrinsic material absorption, radiation loss, surface scattering losses, and coupling loses, respectively. The mathematics of the Q factor equation can be defined as in Equation 1.13 [1].

$$Q_0^{-1} = Q_{mat}^{-1} + Q_{rad}^{-1} + Q_{s.s}^{-1} + Q_{count}^{-1} \tag{1.13}$$

Q_{mat} is related to absorption and Rayleigh scattering from the material of the resonator which can be estimated by Equation 1.14.

$$Q_{mat} \cong \frac{4.3 \times 10^3}{\alpha} \frac{2\pi N}{\lambda} \tag{1.14}$$

Where α is an attenuation which is 0.17 dB/km for silica glass spheres. λ is the nominated wavelength of the laser. Thus, $Q_{mat} \cong 10^{11}$ [1].

Q_{rad} indicates radiation loss from the curvature of the resonator. Q_{rad} decreases exponentially with increasing size of the resonator. When the ratio of the diameter and the wavelength is ≥ 15 then $Q_{rad} > 10^{11}$ and the diffraction loss is negligible [1].

$Q_{s.s}$ is referred to as surface scattering losses due to the inhomogeneous nature of the resonator surface which can be estimated from Equation 1.15 [49],

$$Q_{s.s} = \frac{\lambda^2 D}{2\pi^2 \sigma^2 B} \quad (1.15)$$

where σ and B are the roughness and the length of inhomogeneity respectively. $Q_{s.s}$ is expected to be less than 10^{10} when the diameter of the resonator is greater than 100 μm [108]. Finally, Q_{count} denotes the losses by surface adsorption of contaminants in water, which cannot be easily calculated mathematically [108].

1.3 WGM based sensing and applications

1.3.1 Chemical WGM based sensing

1.3.1.1 Heavy metal detection

Previous studies have reported on an optical sensor for Hg(II) detection by employing a silica microsphere ring resonator that was functionalised with 2-mercaptobenzothiazole (2-MBT) in order to make the surface selective only to Hg(II). The detection limit was approximately 50 ppb (w/w) [62].

1.3.1.2 Gas Sensing

More recently, attention has focused on the use of WGM resonators as gas sensors, utilising a variety of different techniques. One such method was the use of a modified resonator adsorbing the targeted gas. For example, a water vapour sensor based on a silica nano-coated microresonator has recently been reported [109] in addition to a porous ZnO coated sphere for ethanol vapour detection [110]. Other gases have also been investigated, including isopropanol [16], ammonia [111], ethanol [112], hexane vapour [113], acetone vapour [114], methane, methyl chloride and ethane [115].

1.3.2 Biological WGM based sensing

WGM biosensors are becoming increasingly popular because of their high sensitivity and label-free capability. As a result, many important applications incorporate them. A large and growing body of literature has investigated WGM techniques to detect, recognise and study biological molecules and their interactions, including DNA [17, 96, 97], protein [27, 92, 93, 95], single virus particles [18, 91] and biomarkers [32, 98]. This type of information is very useful for discovery of a small molecule which has the potential to be a drug.

1.3.2.1 Single viruses

It is desirable to be able to detect single viruses, so more recently attention has focused on single molecule detection. A well-known paper in the WGM biosensor field was published (currently holding more than 450 citations) by F. Vollmer and S. Arnold [25]. The work demonstrated biosensing, in particular showing that by reducing the size of the resonator to 45 μm, one virion of HIV could easily be sensed. In 2011, influenza single viruses and single particle of polystyrene (PS) nanoparticles were detected as reported by L. He *et al.* Virus- or particle-binding events were tracked by a small wavelength shift at the pm level [51]. In the following two years, single particles of MS2 virus were detected using a silica microsphere with a radius of around 45 μm by V. R. Dantham and co-workers [29]. In summary, WGM is a highly practical technique for integrating into sensors in order to detect single viruses, thus offering important applications for medical research.

1.3.2.2 Protein adsorption

Many applications of WGM are focused on proteins and/or their interactions; particularly label-free detection. In 2002, the binding of streptavidin to biotinylated BSA was demonstrated using a ~300 μm spheroidal shaped resonator [30]. The adsorption of BSA was demonstrated by M. A. Santiago-Cordoba and co-workers [92] using WGM integrated with a metallic nanoparticle-based assay. The resonance frequency shifts of adsorption were in good agreement with the theoretical model [116]. As BSA is one of the most widely studied proteins, V. R. Dantham *et al.* [32] successfully demonstrated the detection of single thyroglobulin (TG) and BSA proteins using their hybrid microcavity platform. Through immobilisation of DNA-aptamer sequences in 2012, thrombin or vascular endothelial growth factor (VEGF) protein in blood samples could be detected, as reported by L. Pasquardini and co-workers [33]. Recent work on protein sensing using WGM was published in 2015 by Y-L Sun *et al.* [34], where protein-based 3D WGM microlasers were demonstrated for the first time. All the results and publications mentioned here provide the proof-of-principle for WGM biosensors in protein detection applications. Furthermore, by choosing the right bio-recognition surface functionalisation, proteins can be detected in a label-free manner.

1.3.2.3 DNA studies

Much of the current literature on WGM biosensors focuses on DNA research. The transient interaction kinetics of a 22-mer oligonucleotide of 7 kDa was studied by M. D. Basske *et al.* in 2014 [24]. A single-nucleic-acid molecule can be detected from a small shift (~2.5 fm) within the plasmon-enhanced WGM cavity of gold nanorods. Several thousand orders of sensitivity can be gained from plasmon-enhanced WGM biosensors, which aids characterisation of matched and mismatched strand kinetic interactions. Mutated DNA oligonucleotides were characterised, as reported by A. Taeb and co-workers in 2013 [35], using a planar dielectric waveguide with a disc resonator WGM biosensor. Based on this method, the sensor is scaled down, with low-cost and simple fabrication. Y. Wu and co-workers [36] demonstrated a label-free nucleic acid WGM sensor by integrating a DNA strand displacement circuit in 2013. A 22-mer oligonucleotide at 80 pM or 32 fM was detected, setting a new record for nucleic acid sensitivity, which is a 25-fold improvement over previous records. Furthermore, five cycles of two dissimilar nucleic acid sequences were repeated, indicating the sensor reusability. Considering all of the evidence, WGM is a highly recommended technique for DNA detection.

1.3.2.4 Detection of biomarkers

Biomarkers are one of the most interesting targets in clinical research. H. A. Huckabay and co-workers [53] presented research combining sensitive fluorescence imaging coupled with a WGM resonator to develop a label-free and multiplexed sensor for two markers of ovarian cancer. By immobilising antibodies specific for CA-125 and TNF-α, the detection limits achieved for the markers were more than three-fold lower than ELISA kits. Two years later, the same author extended the advantages by simplifying the approach using excitation light coupled into a dove prism. The improved phase matching allows enhancements in the signal-to-noise ratio. Their standard blocking protocols reduced non-specific interactions satisfactorily before quantification of CA-125 in serum samples. Finally, fluorescence imaging of over 120 microsphere resonators indicated the potential for large-scale multiplexed detection [23].

1.3.3 Other sensing

1.3.3.1 Temperature sensing

One of the simplest and straightforward experiments for temperature detection by WGM was demonstrated in 2008 by M. Qiulin and co-workers [27]. Temperature changes were measured by optical resonance shifts using silica beads. The air in the cell was heated and the temperature changes were detected as a function of resonance wavelength shift, with a range from room temperature to about 10 K higher. Two years later, the group used the same

platform but instead of heating, the experiment was cooled down to below 110 K and the temperature raised gradually [117]. In 2011, L. L. Martin [58] demonstrated that a WGM sensor can be used to track a minor change in temperature by using microspheres of Nd(III) doped barium titanium silicate glass in conjunction with the fluorescence intensity ratio (FIR) technique. An average red-shift of 10 pm/K from temperatures varying from 300 K to 950 K was detected successfully. WGM sensing can be therefore be integrated not only into chemical or biological sensors but also into temperature sensors, demonstrating the versatility of the WGM technique.

1.3.3.2 Refractive index sensing

Refractive index sensing was demonstrated in ethanol solution using a planar quartz microring resonator (which served both as a fluidic channel and as a ring resonator) by I. M. White and co-workers [65]. The sensitivity achieved was 16.1 nm/RIU with the detection limit around 5×10^{-7} RIU. The waveguide enabling light coupling was aligned perpendicular to the resonator. In 2015, a three-component mixture of salt cations including Na^+, Li^+, and K^+ was separated and detected by the integrated capillary electrophoresis (CE) with phase sensitive WGM (PS-WGM) sensing. The PS-WGM detection monitored wavelength shifts due to changes in the surrounding refractive index in real-time. The detection limits can be enhanced almost 300-fold by using this approach [118].

1.3.3.3 Electric and magnetic field sensing

One of the many potentials of WGM is the ability to detect materials undergoing deformation under the effect of an external electric field. One experiment investigated this property by observing the wavelength shifts of polymeric spheres made of PDMS [119]. Additionally, magnetorheological polydimethylsiloxane (MR-PDMS) spheres as micro-optical resonators have also been used as a magnetic field sensor. The applied field induces a mechanical deformation, causing shifts in the resonance wavelengths. The microspheres are made of PDMS with embedded magnetically polarisable particles. An experiment was carried out to demonstrate the magnetic field-induced WGM shifts in an MR-PDMS microsphere. The results indicate that MR-PDMS microspheres can be used as high Q-factor tunable optical cavities with potential applications in sensing [120].

1.4 Project aims and objectives

The development of sensors has received enormous attention in the chemical, biological and other fields as mentioned earlier. The aim of this research project has therefore been to develop the WGM technique in order to solve some of the key problems in sensor development. The aims of the project are different depending on each experiment, as follows.

1.4.1 Chapter 3: Pb(II) sensor experiment

This research project investigated the development of a WGM-based chemical sensor for quantification of trace amounts of Pb(II) in water using a fused silica microsphere. The major objective of this study was to improve the detection limit of the WGM technique using the plasmonic enhancement of gold nanoparticles (AuNPs). The study, therefore, set out to assess and improve the selectivity of the WGM Pb(II) sensor using glutathione (GSH) as a chelator. The novelty of this work is attaching GSH-AuNPs on the surface of the resonator to detect Pb(II) at low concentrations.

1.4.2 Chapter 4: G-quadruplex experiment

The aim of this experiment was to develop a WGM assay for interrogating G-quadruplex structure/function, such as discriminating between folded and unfolded states of the G-quadruplex region of the c-myc promoter, an oncogene associated with a wide number of cancers. Another objective was to measure the binding of complementary sequences to folded and unfolded sequences, and to study the kinetics binding and duplex–ligand binding.

1.4.3 Chapter 5: thrombin experiment

This experiment aimed to develop an ultrasensitive sensor for thrombin (TB) detection by integrating WGM with thrombin–fibrinogen (FB) interaction to develop a sensor for TB detection and study the kinetics of the interaction between TB and FB.

1.4.4 Chapter 6: Conclusion

This chapter aims to summarise, conclude and discuss the work that has been undertaken. A critical examination of the limitations and challenges of the work, as well as the insights it has given into the studied molecules, will be presented. This chapter will also discuss the significance of the findings and recommendations for future work.

1.5 References

1. Chiasera, A., Dumeige, Y., Feron, P., Ferrari, M., Jestin, Y., Nunzi C. G., Pelli, S., Soria, S and Righini, G. C., *Spherical whispering-gallery-mode microresonators.* Laser & Photonics Reviews, 2010. 4(3): p. 457-482.
2. Fan, X., White, I. M., Shopova, S. I., Zhu, H., Suter, J. D. and Sun, Y., *Sensitive optical biosensors for unlabeled targets: A review.* Analytica Chimica Acta, 2008. 620(1–2): p. 8-26.
3. Baaske, M. and Vollmer, F., Optical Resonator Biosensors*:* Molecular Diagnostic and Nanoparticle Detection on an Integrated Platform*.* ChemPhysChem, 2012. 13(2): p. 427-436.
4. Panich, S., Wilson, K. and Edel, J. B., *Trace heavy metal analysis using whispering gallery mode sensing.* Chemical and Biological Microsystems Society. The 17th International conference on miniaturized systems for chemistry and life sciences (MicroTAS 2013), 2013. 27-31 October. Freiburg, Germany.
5. Foreman, M. R., Swaim, J. D. and Vollmer, F., *Whispering gallery mode sensors.* Advances in Optics and Photonics, 2015. 7(2): p. 168-240.
6. Vollmer, F. and Roy, S., Optical Resonator Based Biomolecular Sensors and Logic Devices. Journal of the Indian Institute of Science, 2012. 92(2): p. 233-251.
7. McGrath, M. and Scanaill, C. N., *Sensor Technologies: Healthcare, Wellness and Environmental Applications*. 2013: Apress Publishing. p 332.
8. Hulanicki, A., Geab, S., Ingman, F., *Chemical sensors definitions and classification.* Pure and Applied Chemistry, 1991. 63: p. 1247-1250.
9. Thevenot, D. R., Toth, K., Durst, R. A. and Wilson, G. S., *Electrochemical biosensors: recommended definitions and classification*1. Biosensors and Bioelectronics, 2001. 16(1–2): p. 121-131.
10. Potyrailo, A. R., Hobbs, E. S. and Hieftje, M. G., *Optical waveguide sensors in analytical chemistry: today's instrumentation, applications and trends for future development.* Fresenius' Journal of Analytical Chemistry. 362(4): p. 349-373.
11. Leung, A., Shankar, P. M. and Mutharasan, R., *A review of fiber-optic biosensors.* Sensors and Actuators B: Chemical, 2007. 125(2): p. 688-703.
12. Wu, Y. and F. Vollmer, *Cavity-Enhanced spectroscopy and Sensing*. Springer Series in Optical Science. 2014: Springer. 179: p323-349.
13. McDonagh, C., Burke, C. S. and MacCraith, B. D., *Optical Chemical Sensors.* Chemical Reviews, 2008. 108(2): p. 400-422.
14. Ahmed, F. E., Wiley, J. E., Weidner, D. A., Bonnerup, C. and Mota, H., *Surface Plasmon Resonance (SPR) Spectrometry as a Tool to Analyze Nucleic Acid–Protein*

Interactions in Crude Cellular Extracts. Cancer Genomics-Proteomics, 2010. 7(6): p. 303-309.

15. Dahlin, A. B., Size Matters*:* Problems and Advantages Associated with Highly Miniaturized Sensors*.* Sensors (Basel, Switzerland), 2012. 12(3): p. 3018-3036.
16. Ksendzov, A., M. L. Homer, and Manfreda, A. M., *Integrated optics ring-resonator chemical sensor with polymer transduction layer.* Electronics Letters, 2004. 40(1): p. 63-65.
17. Bog, U., Brinkmann, F., Kalt, H., Koos, C., Mappes, T., Hirtz, M., Fuchs, H. and Kober, S., Large-Scale Parallel Surface Functionalization of Goblet-type Whispering Gallery Mode Microcavity Arrays for Biosensing Applications*.* Small, 2014. 10(19): p. 3863-3868.
18. Redding, B., Creazzo, T., Marchena, E., Shi, S. and Prather, D. W., *Coupling Si nanocrystal microdisk emission to whispering-gallery modes in a concentric SiO_2 ring.* Optics Letter., 2009. 34(9): p. 1384-1386.
19. Vollmer, F., *Taking detection to the limit.* Research, 2005. 20: p. 239-244.
20. Panich, S., Wilson, K. A., Nuttall, P., Wood, C. K., Albrecht, T. and Edel, J. B., Label-Free Pb(II) Whispering Gallery Mode Sensing Using Self-Assembled Glutathione-Modified Gold Nanoparticles on an Optical Microcavity*.* Analytical Chemistry, 2014. 86(13): p. 6299-6306.
21. Shopova, S. I., Rajmangal, R., Holler, S. and Arnold, S., *Plasmonic enhancement of a whispering-gallery-mode biosensor for single nanoparticle detection.* Applied Physics Letters, 2011. 98(24): p. 243104.
22. Zhu, J., Ozdemir, S. K., Xiao, Y. F., Li, He, L., Chen, D. R. and Zhu, L. Y., *On-chip single nanoparticle detection and sizing by mode splitting in an ultrahigh-Q microresonator.* Nature Photonic, 2010. 4(1): p. 46-49.
23. Huckabay, H. A., Wildgen, S. M. and Dunn, R. C., *Label-free detection of ovarian cancer biomarkers using whispering gallery mode imaging.* Biosensors and Bioelectronics, 2013. 45(0): p. 223-229.
24. Baaske, M. D., Foreman, M. R. and Vollmer, F., *Single-molecule nucleic acid interactions monitored on a label-free microcavity biosensor platform.* Nature Nanotechnology, 2014. 9(11): p. 933-939.
25. Vollmer, F. and S. Arnold, Whispering-gallery-mode biosensing*:* label-free detection down to single molecules*.* Nature Methods, 2008. 5(7): p. 591-596.
26. Avino, S., Krause, A., Zullo, R., Giorgini, A., Malara, P., Natale, P. D., Loock, H. P. and Gagliardi, G., *Direct Sensing in Liquids Using Whispering-Gallery-Mode Droplet Resonators.* Advanced Optical Materials, 2014. 2(12): p. 1155-1159.

27. Qiulin, M., R. Tobias, and G. Zhixiong, *Temperature sensitivity of silica micro-resonators.* Journal of Physics D: Applied Physics, 2008. 41(24): p. 245111.
28. Fan, X., White, I. M., Shopova, S. I., Zhu, H., Suter, J. D. and Sun, Y. *Sensitive optical biosensors for unlabeled targets: a review.* Analytica Chimica Acta, 2008. 620(1-2): p. 8-26.
29. Dantham, V. R., Holler, S., Kolchenko, V., Wan, Z. and Arnold, S. *Taking whispering gallery-mode single virus detection and sizing to the limit.* Applied Physics Letters, 2012. 101(4): p. 43704.
30. Vollmer, F., Braun, D., Libchaber, A., Khoshsima, M., Teraoka, I. and Arnold, S. *Protein detection by optical shift of a resonant microcavity.* Applied Physics Letters, 2002. 80(21): p. 4057-4059.
31. Soteropulos, C. E., Zurick, K. M., Bernards, M. T. and Hunt, H. K. *Tailoring the Protein Adsorption Properties of Whispering Gallery Mode Optical Biosensors.* Langmuir, 2012. 28(44): p. 15743-15750.
32. Dantham, V. R., Holler, S., Barbre, C., Keng, D., Kolchenko, V. and Arnold, S., *Label-Free Detection of Single Protein Using a Nanoplasmonic-Photonic Hybrid Microcavity.* Nano Letters, 2013. 13(7): p. 3347-3351.
33. Pasquardini, L., Berneschi, S., Barucci, A., Cosi, F., Dallapiccola, R., Insinna, M., Lunelli, L., Conti, G. N., Pederzolli, C., Salvadori, S. and Soria, S., *Whispering gallery mode aptasensors for detection of blood proteins.* Journal of Biophotonics, 2013. 6(2): p. 178-187.
34. Sun, Y. L., Hou, Z. S., Sun, S. M., Zheng, B. Y., Ku, J. F., Dong, W. F., Chen, Q. D. and Sun, H. B., *Protein-Based Three-Dimensional Whispering-Gallery-Mode Micro-Lasers with Stimulus-Responsiveness.* Scientific Reports, 2015. 5: p. 12852.
35. Taeb, A., Basha, M. A., Gigoyan, S., Marsden, M. and Safieddin, S. N., *Label-free DNA sensing using millimeter-wave silicon WGM resonator.* Optics Express, 2013. 21(17): p. 19467/1-19467/6.
36. Wu, Y., Zhang, D. Y., Yin, P. and Vollmer, F., Ultraspecific and Highly Sensitive Nucleic Acid Detection by Integrating a DNA Catalytic Network with a Label-Free Microcavity. Small, 2014. 10(10): p. 2067-2076.
37. Matsko, A. B., Savchenkov, A. A., Strekalov, D., Ilchenko, V. S. and Maleki, L., *Review of applications of whispering-gallery mode resonators in photonics and nonlinear optics.* InterPlanetary Network Progress Report, 2005. 42: p. 162.
38. St Paul's Cathedral., *Climb the Dome*. 2016 [cited 2016 30/01/2016]; Available from: https://www.stpauls.co.uk/history-collections/history/explore-the-cathedral/climb-the-dome.

39. Bate, A. E., *Note on the whispering gallery of St Paul's Cathedral, London.* Proceedings of the Physical Society, 1938. 50(2): p. 293.
40. Fotiadi, A. A. and Megret, P., *Surface-emitting fibre lasers: Perfect ring-like beam.* Nature Photonic, 2012. 6(4): p. 217-219.
41. Sound Tourism; A travel guide to sonic wonder., *Whispering Gallery, St Paul's Cathedral*. 2016; [cited 2016 30/01/2016] Available from: http://www.sonicwondersorg/whispering-galleries/#filelinks.
42. Soria, S., Berneschi, S., Brenci, M., Cosi, F., Nunzi C. G., Pelli, S. and Righini, G. C., *Optical Microspherical Resonators for Biomedical Sensing.* Sensors, 2011. 11(1): p. 785.
43. Josell, *total internal reflection*, in *UploadWizard*, Optical reflection: critical angle and total internal reflection., Editor. 2012: wikimedia.
44. Zhmakin, A. I., *Enhancement of light extraction from light emitting diodes.* Physics Reports, 2011. 498(4–5): p. 189-241.
45. Carpintero, G., Garcia, M. E., Hartnagel, H. and Preu, S. R., *Selected Emerging THz Technologies*, in *Semiconductor TeraHertz Technology: Devices and Systems at Room Temperature Operation*. 2015, Wiley-IEEE Press. p. 1-408.
46. Arnold, S., Noto, M. and Volmer F., *Ultra sensitive detection perturbations by biomolecules.* B. Di Bartolo and O Forte, Frontiers of optical spectroscopy, Drodrecht, The Netherland: Kluwer Academic Publisher, 2005: p. 337-357.
47. Payne, D. N. and Gambling, W. A., *New silica-base low loss optical fiber.* Electronic Letter, 1974. 10(15): p. 289-290.
48. Arnold, S., Khoshsima, M., Teraoka, I., Holler, S. and Vollmer, F., *Shift of whispering-gallery modes in microspheres by protein adsorption.* Optics Letters, 2003. 28(4): p. 272-274.
49. Gorodetsky, M. L., Savchenkov, A. A. and Ilchenko, V. S., *Ultimate Q of optical microsphere resonators.* Optics Letters, 1996. 21(7): p. 453-455.
50. Teraoka, I., Arnold, S. and Vollmer, F., Perturbation approach to resonance shifts of whispering-gallery modes in a dielectric microsphere as a probe of a surrounding medium. Optical Society of America, 2003. 20: p. 1937-1946.
51. He, L., Sahin K. O., Jiangang, Z., Woosung, K. and Yang, L., *Detecting single viruses and nanoparticles using whispering gallery microlasers.* Nature Nanotechnology., 2011. 6: p. 428-432.
52. Himmelhaus, M., Krishnamoorthyl, S., and Francosis, A., Optical sensors based on whispering gallery modes in fluorescent Microbeads*:* response to specific interactions*.* Sensors, 2010. (10): p. 6257-6274.

53. Huckabay, H. A. and Dunn, R. C., *Whispering gallery mode imaging for the multiplexed detection of biomarkers.* Sensors and Actuators B: Chemical, 2011. 160(1): p. 1262-1267.

54. Suter, J. D. and Fan, X., *Overview of the optofluidic ring resonator: a versatile platform for label-free biological and chemical sensing.* Conference of the IEEE Engineering in Medicine and Biology Society, 2009. p. 1042-10444.

55. Boleininger, A., Lake, T., Hami, S. and Vallance, C.,Whispering Gallery Modes in Standard Optical Fibres for Fibre Profiling Measurements and Sensing of Unlabelled Chemical Species. Sensors, 2010. 10(3): p. 1765.

56. Ahmad, M. and Hench, L. L., Effect of taper geometries and launch angle on evanescent wave penetration depth in optical fibers. Biosensors and Bioelectronics, 2005. 20(7): p. 1312-1319.

57. He, L., Ozdemir, S. K. and Yang, L., *Whispering gallery microcavity lasers.* Laser & Photonics Reviews, 2013. 7(1): p. 60-82.

58. Martin, L. L., Rodriguez P. C., Gonzalez H. P. and Martin, I. R.,*Whispering gallery modes in a glass microsphere as a function of temperature.* Optics Express, 2011. 19: p. 25792-25798.

59. Beier, H. T., Cote, G. L. and Meissner, K. E., *Whispering gallery mode biosensors consisting of quantum dot-embedded microspheres.* Annals of Biomedical Engineering, 2009. 37: p. 1974-1983.

60. Panitchob, Y., Senthil M. G., Zervas, M. N., Horak, P., Berneschi, S., Pelli, S., Nunzi C. G., and Wilkinson J. S., *Whispering gallery mode spectra of channel waveguide coupled microspheres.* Optics Express, 2008. 16: p. 11066-11076.

61. Zhu, H., Suter, J. D., White I. M. and Fan, X., *Aptamer Based Microsphere Biosensor for Thrombin Detection.* Sensors, 2006. 6(8): p. 785-795.

62. Hanumegowda, N. M., White, I. M. and Fan, X., *Aqueous mercuric ion detection with microsphere optical ring resonator sensors.* Sensors and Actuators B: Chemical, 2006. 120(1): p. 207-212.

63. Peng, X., Song, F., Jiang, S., Peyghambarian, N., Gonokami, M. K. and Xu, L., *Fiber-taper-coupled L-band Er^{3+}-doped tellurite glass microsphere laser.* Applied Physics Letters, 2003. 82(10): p. 1497-1499.

64. Cai, M., Painter, O. and K. J. Vahala, Observation of Critical Coupling in a Fiber Taper to a Silica-Microsphere Whispering-Gallery Mode System. Physical Review Letters, 2000. 85(1): p. 74-77.

65. White, I. M., Zhu, H., Suter, J. D., Hanumegowda, N. M., Oveys, H., Zourob, M., Fan, X., *Refractometric Sensors for Lab-on-a-Chip Based on Optical Ring Resonators.* Sensors Journal, IEEE, 2007. 7(1): p. 28-35.

66. Han, J., Effects of metallic nanoparticles on whispering gallery modes in silicon-on-insulator ring resonators. Sae Mulli, 2014. 64(2): p. 194-199.
67. Arbabi, E., Kamali, S. M., Arnold, S. and Goddard, L. L., *Hybrid whispering gallery mode/plasmonic chain ring resonators for biosensing.* Applied Physics Letters, 2014. 105(23): p. 231107/1-231107/4.
68. Cho, H. K. and Han, J., Numerical study of opto-fluidic ring resonators for biosensor applications. Sensors, 2012. 12: p. 14144-14157.
69. Scholten, K., Fan, X. and Zellers, E. T., *Microfabricated optofluidic ring resonator structures.* Applied Physics Letters, 2011. 99(14): p. 141108/1-141108/3.
70. Lin, N., Jiang, L., Wang, S., Xiao, H., Lu, Y. and Tsai, H., *Ultrasensitive thermal sensors based on whispering gallery modes in a polymer core optical ring resonator.* Applied Optic, 2011. 50(33): p. 6254-6260.
71. Chu, Y., Mintairov, A. M., He, Y. J., Merz, L., Kalugnyy, N. A., Lantratov, V. M. and Mintairov, S.A., *Lasing of whispering-gallery modes in GaInP waveguide micro-discs and rings with InP quantum dots.* Physica status solidi (c), 2011. 8(2): p. 325-327.
72. Zhu, H., Suter, J. D. and X. Fan, *Label-free optical ring resonator bio/chemical sensors.* Chemical Sensors and Biosensors., 2010. 8(Optical Guided-Wave Chemical and Biosensors II): p. 259-279.
73. Sun, Y., Suter, J. D. and Fan, X., *Optofluidic ring resonator dye lasers.* Proceedings of SPIE, 2010. 7606 (Silicon Photonics V): p. 76060X/1-76060X/9.
74. Sun, Y., Jing, L., Daniel J. H, Mason, G. F., Thompson, A. K., Shiou, J. J. and Fan, X., *Rapid tandem-column micro-gas chromatography based on optofluidic ring resonators with multi-point on-column detection.* Analyst, 2010. 135(1): p. 165-171.
75. Zhu, H., Dale, P. S. and Fan, X. *Optofluidic ring resonator sensor for sensitive label-free detection of breast cancer antigen CA*15-3 *in human serum.* Proceedings of SPIE, 2009. 7322(Photonic Microdevices/Microstructures for Sensing): p. 732204/1-732204/7.
76. Sun, Y., Liu, J., Mason, G. F., Thompson, A., Ja, S. J. and Fan, X., *Development of optofluidic ring resonator based chemical vapor sensing platform.* Proc. SPIE, 2009. 7322 (Photonic Microdevices/Microstructures for Sensing): p. 73220E/1-73220E/8.
77. Sherstnev, V. V., Grebenshchikova, E. A., Monakhov, A. M., Astakhova, A. P., Il'inskaya, N. D., Boissier, G., Teissier, R., Baranov, A. N. and Yakovlev Y. P., *A semiconductor whispering-gallery-mode laser with ring cavity operating at room temperature.* Technical Physics Letters., 2009. 35(8): p. 749-752.
78. Sakhnenko, N. K., Nerukh, A. G., Benson, T. M., and Sewell, P., *Whispering gallery mode transformation in a switched micro-cavity with concentric ring geometry.* Optical Quantum Electron., 2009. 40(11-12): p. 813-820.

79. Yang, G., I. M. White, and X. Fan, *An opto-fluidic ring resonator biosensor for the detection of organophosphorus pesticides.* Sensor Actuators B., 2008. 133(1): p. 105-112.

80. Xing, M., Zheng, W., Zhang, Y., Ren, G., Du, X., Wang, K., and Chen, L., *The whispering gallery mode in photonic crystal ring cavity.* Processing of SPIE, 2008. (Sixth International Conference on Thin Film Physics and Applications, 2008): p. 698438/1-698438/4.

81. Sun, Y., Shopova, S. I., Mason, G. F., and Fan, X., *Rapid chemical vapor sensing and micro gas chromatography detection using optofluidic ring resonators.* Materials Research Society Symposium Proceedings., 2008. p. 1133E**.**

82. Toren, P., Ozgur, E. and Bayindir, M., *Real-Time and Selective Detection of Single Nucleotide DNA Mutations Using Surface Engineered Microtoroids.* Analytical Chemistry., 2015. 87(21): p. 10920-10926.

83. Ozgur, E., Toren, P., Aktas, O., Huseyinoglu. E. and Bayindir, M., *Label-Free Biosensing with High Selectivity in Complex Media using Microtoroidal Optical Resonators.* Scientific Reports., 2015. 5: p. 13173.

84. Zheng, C., Jiang, X., Hua, S., Chang, L., Li, G., Fan, H. and Xiao, M., *Controllable optical analog to electromagnetically induced transparency in coupled high-Q microtoroid cavities.* Optical. Express, 2012. 20(16): p. 18319-18325.

85. Jager, J. B., Calvo, V., Delamadeleine, E., Hadji, E., Noe, P., Ricart, T., Bucci, D. and Morand, A., *High-Q silica microcavities on a chip: From microtoroid to microsphere.* Applied Physics Letters., 2011. 99(18): p. 181123/1-181123/3.

86. Hunt, H. K., Soteropulos, C. and Armani, A. M., *Bioconjugation strategies for microtoroidal optical resonators.* Sensors, 2010. 10: p. 9317-9336.

87. Orucevic, F., Guattari, F., Hare, J., Seguin,V. L., Verbert, J., Hadji, E., and Gerard, J. M., *Neodymium photoluminescence in Whispering Gallery Modes of toroidal microcavities.* Journal de Physique IV, 2006. 135(COLOQ 9): p. 245-246.

88. Kalkman, J., Tchebotareva, A., Polman, A., Kippenberg, T. J., Min, B. and Vahala, K. J., *Fabrication and characterization of erbium-doped toroidal microcavity lasers.* Journal of Applied Physics., 2006. 99(8): p. 083103/1-083103/9.

89. Nasir, M. N. M., Ding, M., Murugan., G. S. and Zervas, M. N., *High-Q plasmonic bottle microresonator.* Processding of SPIE, 2014. 8960 (Laser Resonators, Microresonators, and Beam Control XVI): p. 89600M/1-89600M/8.

90. Todorov, F., Ctyroky, J., Michal, J., Chomat, M., Matejec, V., Kubecek, V., Martan, T., and Berkova, D., *Bottle microresonators fabricated by shaping optical fibers with a beam of a CO_2 laser.* Sensor Letter., 2011. 9(6): p. 2279-2282.

91. Murugan, G. S., Wilkinson, J. S., Zervas, M. N., Jiang, S., Digonnet, M. J. F., Glesener, J. W. and Dries, J. C., *Novel fiber bottle microresonator add-drop filters.* Proceeding of SPIE, 2010. 7598 (Optical Components and Materials VII): p. 75980K/1-75980K/9.

92. Bianucci, P., Wang, X., Veinot, J. G. and Meldrum, A., *Silicon nanocrystals on bottle resonators: mode structure, loss mechanisms and emission dynamics.* Optics Express, 2010. 18(8): p. 8466-8481.

93. Zervas, M. N., Murugan, G. S. and Wilkinson, J. S, International Conference on *Transparent Optical Networks (ICTON) 2008.* 22-26 June. Athens, Greece. p.1-4

94. Terranova, B., Bellingham, A. A., Herbert, S. and Fontecchio, A. K.,Cylindrical channel plasmon resonance for single-molecule sensing. Proceeding of SPIE, 2014. 8994 (Photonic and Phononic Properties of Engineered Nanostructures IV): p. 899413/1-899413/8.

95. Peter, J., Saleem, R., Sebastian, A., Radhakkrishnan, P., Nampoori, V. P. N. Girijavallabhan, C. P. and Kailasnath, M. *Pumping scheme dependent multimode laser emission from free-standing cylindrical microcavity.* Optics Communication., 2014. 320: p. 125-128.

96. Yang, J. J., Huang, M., Dai, X. Z., Huang, M. Y., and Liang, Y. *A., A spoof surface WGM sensor based on a textured PEC cylinder.* A letter journal exploring the frontiers physics, 2013. 103(4): p. 44001-44005.

97. Yang, J. J., Huang, M., Ding, H. W., Mao, F. C., *Surface WGM sensor based on a cylindrical dielectric waveguide.* Laser Physical Letter., 2013. 10(1): p. 15901-15906.

98. Nagai, Y., Fujimura, R. and Kajikawa, K., *Core-resonance cylindrical whispering gallery mode laser of dye-doped nematic liquid crystal.* Journal of the Optical Society of America B, 2013. 30(8): p. 2233-2239.

99. Mostafazadeh, A. and M. Sarisaman, *Spectral singularities and whispering gallery modes of a cylindrical gain medium.* Physical Review A: Atomic, Molecular and Optical Physics, 2013. 87(6-B): p. 063834/1-063834/9.

100. Kang, X. L., Zhang, X. B., Li, Y. P. and Liu, J. F., *Suppression of high-radial-order whispering-gallery modes and directional emission of anisotropic cylindrical microcavity.* Journal of the Optical Society of America B, 2012. 29(8): p. 1942-1946.

101. Wang, D. L., Jiang, N., Jiang, L. Q., Zhang Z. L. and Pu, X. Y., *The precise assignment of whispering gallery modes for lasing spectra emitting from cylindrical micro-cavities.* Guangpuxue Yu Guangpu Fenxi, 2008. 28(12): p. 2749-2753.

102. Flatae, A. M., Burresi, M., Zeng, H., Nocentini, S., Wiegele, S., Parmeggiani, C., Kalt, H. and Wiersma, D., *Optically controlled elastic microcavities.* Light: Science and Application., 2015. 4(4): p. 282.

103. Beck, T., Schloer, S., Grossmann, T., Mappes, T. and Kalt, H., *Flexible coupling of high-Q goblet resonators for formation of tunable photonic molecules.* Optical Express, 2012. 20(20): p. 22012-22017.

104. Soteropulos, C. E., Hunt, H.K. and Armani, A. M., *Determination of binding kinetics using whispering gallery mode microcavities.* Applied Physics Letters, 2011. 99(10): p. 103703.

105. Wilson, K. A., Finch, C. A., Anderson, P., Vollmer, F. and Hickman, J., Whispering gallery mode biosensor quantification of fibronectin adsorption kinetics onto alkylsilane monolayers and interpretation of resultant cellular response. Biomaterials, 2012. 33: p. 225-236.

106. Spillane, S. M., Kippenberg, T. J., Painter, O. J. and Vahala, K. J., *Ideality in a fiber-taper-coupled microresonator system for application to cavity quantum electrodynamics.* Physical Review Letters, 2003. 91(4): p. 43902.

107. Luchansky, M. S. and Bailey, R. C., *High-Q Optical Sensors for Chemical and Biological Analysis.* Analytical Chemistry, 2011. 84(2): p. 793-821.

108. Gorodetsky, M. L., Savchenkov, A. A. and Ilchenko, V. S., *On the ultimate Q of optical microsphere resonators.* Proceeding of SPIE - the international society for optics and photonics, 1996. 2799 (Atomic and Quantum Optics: High-Precision Measurements): p. 389-391.

109. Ma, Q., Huang, L., Guo, Z. and Rossmann, T., *Spectral shift response of optical whispering-gallery modes due to water vapor adsorption and desorption.* Measurement Science and Technology, 2010. 21(11): p. 115206.

110. Yebo, N. A., Lommens, P., Hens, Z. and Baets, R., An integrated optic ethanol vapor sensor based on a silicon-on-insulator microring resonator coated with a porous ZnO film. Optics Express, 2010. 18(11): p. 11859-11866.

111. Passaro, V., Dell'Olio, F. and Leonardis, F. D., *Ammonia Optical Sensing by Microring Resonators.* Sensors, 2007. 7(11): p. 2741.

112. Liu, J., Sun, Y. and Fan, X., *Highly versatile fiber-based optical Fabry-Perot gas sensor.* Optics Express, 2009. 17(4): p. 2731-2738.

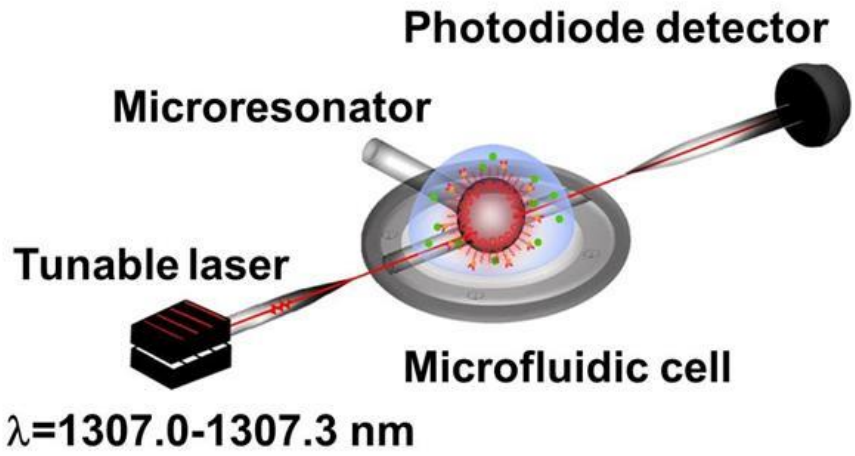
113. Sun, S., Shopova, I., Mason, G. F. and Fan, X., *Rapid chemical-vapor sensing using optofluidic ring resonators.* Optics Letters, 2008. 33(8): p. 788-790.

114. Ta, V. D., Chen, R. D., Nguyen, M. and Sun, H. D., *Application of self-assembled hemispherical microlasers as gas sensors.* Applied Physics Letters, 2013. 102(3): p. 31107.

115. Farca, G., Shopova, S. I. and Rosenberger, A. T., *Cavity-enhanced laser absorption spectroscopy using microresonator whispering-gallery modes.* Optics Express, 2007. 15(25): p. 17443-17448.

116. Miguel, A. Cordoba, S., Boriskina, S. V., Vollmer, F. and Demirel, M. D., *Nanoparticle-based protein detection by optical shift of a resonant microcavity.* Applied Physics Letters, 2011. 99(7): p. 73701.
117. Qiulin, M., Tobias, R. and Zhixiong, G., *Whispering-gallery mode silica microsensors for cryogenic to room temperature measurement.* Measurement Science and Technology, 2010. 21(2): p. 25310.
118. Kim, D. C. and Dunn, R. C., Integrating Whispering Gallery Mode Refractive Index Sensing with Capillary Electrophoresis Separations Using Phase Sensitive Detection. Analytical Chemistry, 2016. 88(2): p. 1426-1433.
119. Ioppolo, T., Stubblefield, J. and Otugen, M. V., *Electric field-induced deformation of polydimethylsiloxane polymers.* Journal of Applied Physics, 2012. 112(4): p. 044906.
120. Ioppolo, T. and Otugen, M. V., *Magnetorheological polydimethylsiloxane micro-optical resonator.* Optics Letters, 2010. 35(12): p. 2037-2039.

Chapter 2 | Instrumentation and Methodology



Whispering gallery mode (WGM) sensing has recently gained an enormous level of interest due to the levels of sensitivity that can be achieved alongside the low-cost and footprint. The simplest form of a WGM setup consists of a glass microsphere coupled with a tapered waveguide made of a single mode optical fibre. By incorporating appropriate surface modification strategies, such a platform is able to detect minute changes in the local concentration.

In this chapter, the operational platform and procedures will be discussed including equipment, and experimental protocols for fabricating various components such as microresonators, tapered waveguides, and fluidic cells. Operational requirements and strategies for performing data analysis will also be discussed. This chapter forms the basis of all experiments performed in the subsequent chapters albeit in each case with slight modifications (e.g. Pb(II) sensing–Chapter 3, G-quadruplex kinetics and dynamics–Chapter 4, and Thrombin sensing–Chapter 5).

2.1 WGM experiment set-up

The WGM set-up consists of four main components, namely a microresonator, a wave guide, a light source (tunable laser) and a photodiode detector. Assembling a benchtop WGM setup allowed the optical sensor to detect minute changes in the surrounding medium that matched the experimental needs. The surface of the resonator will be modified in order to track only a specific analyte in each work. The simple diagram demonstrating the WGM set-up is shown in Figure 2.1. The system consists of a tapered waveguide coupled to the WGM sphere resonator, laser controller, temperature controller, laser source and the photodiode detector. Each component details are discussed in the following section.

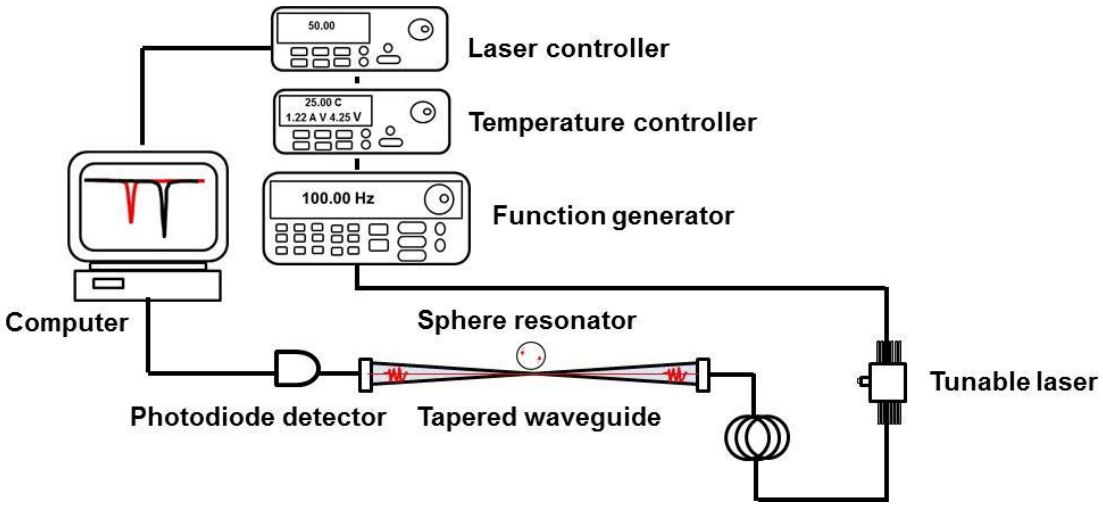


Figure 2.1 WGM experimental configuration for the WGM system

2.1.1 Instrumentations and devices

The WGM sensor has many advantages over other techniques such as high sensitivity - as a result complicated sample preparation is not necessary, only filtration and/or dilution. However a few key steps are still required of the user, for example surface functionalization. Nevertheless, the setup of the WGM is quite straightforward. For our in-lab assembled setup experiment, the components used are listed below.

2.1.1.1. Devices

1. Function generator (model 4086, BK Precision) used to create constant, accurate output signals for arbitrary waveforms and for tuning the laser wavelength through a narrow range of wavelengths using a saw-tooth function generated from an 80 MHz arbitrary wave form generator.

Function generator parameters used in WGM setup
Wave forms: Saw tooth, (ramp)
Frequency: 100 Hz
Amplitude: 5 VPP

2. Thermoelectric temperature controller (model TED 200C, Thorlab) is for controlling the temperature of laser diodes and detectors, (not the fluidic or flow cell) stabilizing the wavelength of laser diodes, reducing noise of the detector and modulation of the wavelength by tuning the temperature.

3. Laser diode controller (model LDC201 C, Thorlab) is used with the temperature controller for the injection current or the optical output power and controlling the temperature simultaneously.

4. Butterfly laser diode mount (model LM 14S2, Thorlab) is for mounting 14 pin butterfly laser diodes. The mount is a universal template where the thermal electric coolers and thermistor sensors are integrated.

5. Light or laser source (model D2304G, Lucent) to provide a wavelength-tunable distributed feedback laser, DFB, at 1310 nm. An InGaAsP semiconductor laser excitation source provides a wavelength-tunable distributed feedback laser, with a maximum power output of 10 mW. The laser was mounted on a LM14S2 butterfly laser mount and driven using a laser diode controller and temperature controller to control the output wavelength.

6. Photodiode detector (model BNC 2110, National Instrument) to detect the output laser light. The photodetector was interfaced with a labview data acquisition card and the signal was analyzed using a custom written labview script that could track all the given resonance peaks as a function of time [1]. All data were then post processed using statistical software such as Origin 8.6.

7. Fusion splicer (model S123c, Fitel, Furukawa Electric) to connect the fibre optic cables which consisted of one from the laser source to the waveguide, and the other was from the waveguide to the photodiode detector. In the thrombin (TB) and G-quadruplex work, the

splicer was also used to fabricate the sphere resonator in order to control the precise size of the resonator (more detail about fabricating the resonator by using the splicer can be found in section 2.1.2).

8. Optical fibre cleaver (model S325 A, Furukawa Electric) is for cleaving the fibre in order to make the junction surface of the cable smooth before splicing.

9. Fibre Optic Strippers for stripping fibre optic coatings and cutting the cable before using the cleaver to smooth the cutting. There are two different strippers as the following.

FO 103-D-250 is for stripping 250 micron coating from 125 micron optical fibre.

FO103 T (three holes model) is for stripping 2-3 mm patch cord jackets, 900 micron tight buffer from 250 micron buffer coating and standard 250 micron buffer from 125 micron buffer coated optical fibre cables.

2.1.1.2 Consumable fibre cables

1. Guiding fibre optics to guide the laser through the waveguide to couple with the resonator then to the detector**.** The laser output from the laser source was guided and enclosed by a single mode optical fibre patch cable (F-SMF-28, Newport). The low attenuation F-SMF-28 single-mode fibre supports single-mode light propagation for a 1310 nm operating wavelength with 9.3±0.5 μm mode field core diameter, a 125±1 μm cladding diameter, a 250 μm acrylate coating, a 900 μm sheath, aramid yarn and a 2.5 mm polyvinyl chloride (PVC) outer jacket. The core is a glass rod that forms in the centre of the cladding, which is also glass. Additionally there are protective polymers [2].

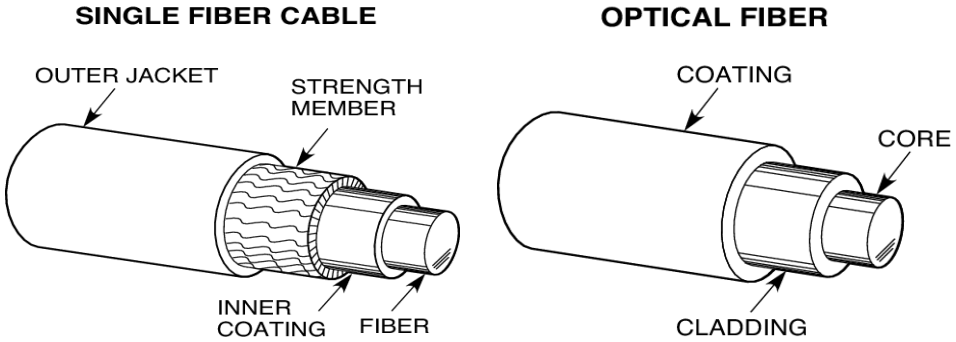


Figure 2.2 (a) The single mode fibre patch cord used to connect the waveguide with the laser source and the waveguide with the detector. This fibre patch cord is a 900 μm jacket surrounded by a layer of aramid yarn and with a 3 mm outer PVC cable jacket to afford additional environmental protection. Reproduced from [2]. (b) single mode fibre optic cable with a small core that permits only one ray of light to propagate along the fibre. The number

of light reflections created as the light passes through the core decreases, lowering attenuation and creating the ability for the signal to travel faster. Reproduced from [3].

A protective fibre jacket accompanied the laser from the laser source to the waveguide and from the waveguide to the detector. In our experiment, the fibre optic cables were rapidly and consistently spliced by an electric arc using a fusion splicer (S123c, Fitel).

2. Tapered waveguide to guide the laser light to the detector and it is the place at which the coupling occurs. The bare single mode fibre optic cable (F-SMF-28, Newport) stripped of its acrylate coating, was used to fabricate the tapered waveguide. Approximately 1 metre of a bare single mode cable was connected with a single mode optical fibre patch cable with a 1310 nm laser source at one end and with a photodiode detector at the other end.

3. Glass sphere WGM resonator to trap and couple light. This coupling relies on total internal reflection. The efficiency of the coupling can be controlled by the distance between the waveguide and the resonator.

4. Flow cell or fluidic cell to carry the solution.

2.1.1.3. Instruments

1. Confocal camera (model IX71, Olympus) to measure the diameter of the waveguide and resonator at which coupling occurs, Figure 2.3 part (a). The image was recorded and the diameter of the resonator was analyzed using Ueye software.

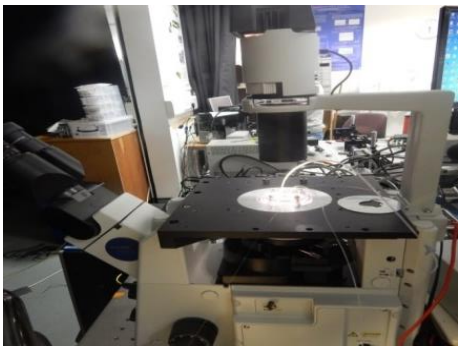
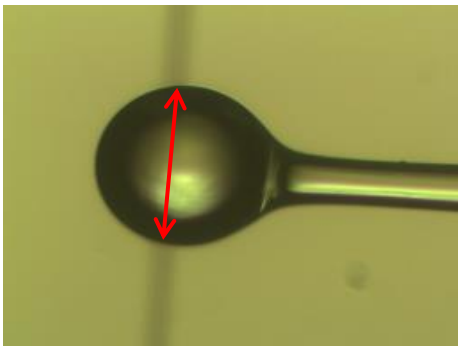
(a)  (b) 

Figure 2.3 (a) The Olympus microscope used for measuring the diameters (b) (red arrow) when the resonator couples to the waveguide.

2.1.2 Fabrication process

2.1.2.1 Glass spherical microresonator

As described in Chapter 1, section 1.2.5, there are several possible geometries of a WGM resonator such as sphere, toroid and cylindrical. In terms of material, glass is the most popular. WGM is sensitive but making this technique specific to only the molecule of interest is not straightforward. The crucial step in this technique is the functionalization of the surface so as to recognise only the analyte, and this is time consuming. If such a step can be simplified, the WGM sensor will be a perfect sensor not only in heavy metal analysis but also in many other fields. Consequently the resonator is the most important component in WGM sensors. In this work, two methods of fabricating glass sphere resonators were utilized.

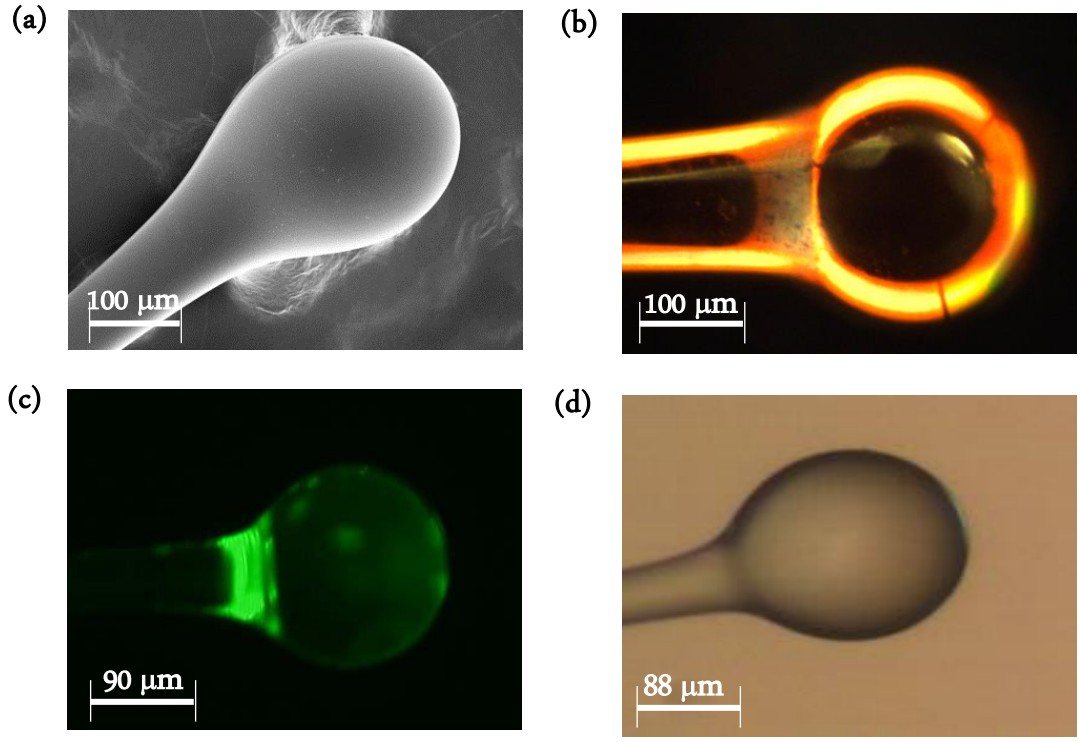


Figure 2.4 (a) and (b) Microresonator fabricated by hydrogen-oxygen torch and (c) and (d) by splicer photo by different techniques (a) SEM (b) dark field (c) fluorescence and (d) under the confocal microscope.

In Chapter 3, the Pb(II) sensor, the resonator was fabricated by inserting and rotating the tip of the bare fibre optic cable (from which the coating was removed) in the mixing flame of an oxygen and hydrogen torch. The generated diameter of such a resonator was found to be around 300±50 µm. The drawback of this method is that it is very difficult to control shape and size of the resonator. Therefore an alternative fabrication process was developed by using the splicer machine. Figure 2.5 illustrates fabrication of the small sphere resonator from a single

mode fibre optic cable. The microsphere resonator can easily be fabricated directly at the tip of a single mode fibre optic cable. In order to produce a small size of the resonator, the fibre was first cleaved (after removing the coating) then was tapered by heating and stretching the fibre until it breaks using the flame from butane torch. Next the tip of the fibre was inserted into one arm of the splicer and was aligned in the centre of the electrode. Multiple arc shots were then fired - as a result the tip melts and the spherical shape is induced by surface tension forces. The size of the sphere can be controlled by the number of arc shots. The greater the arc shot number the greater the size of the resonator.

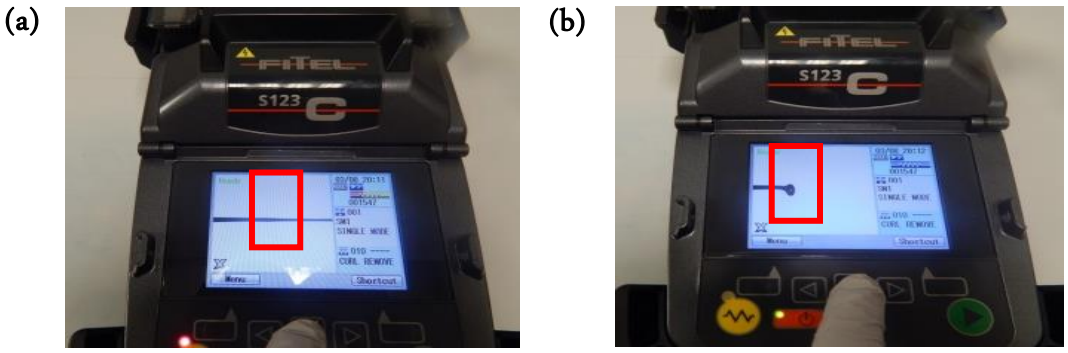


Figure 2.5 Fabricating the microresonator using the splicer machine (a) before and (b) after the arc shot.

2.1.2.2 Fibre tapered waveguides

The tapered waveguide is also an important component in the WGM set up technique as the light coupling will occur at this position. A good waveguide should be thin but strong enough to secure in the flow cell. The fabrication process starts by cutting around 1 metre of single mode fibre optic cable (F-SMF-28, Newport) and use the cleaver to smooth the cutting. ~1 cm cable coatings at the two ends were removed by cable strippers and the ends were cleaned with iso-propanol. At the middle of the cable the coating was also removed ~2.5 cm and cleaned with iso-propanol. This area will become a tapered waveguide.

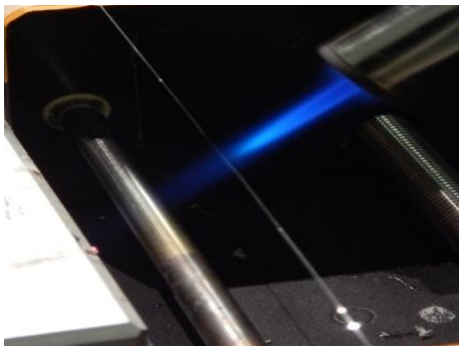
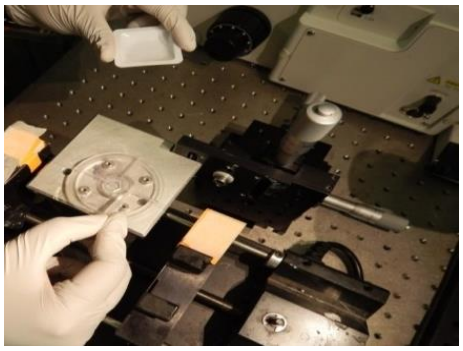
(a)  (b) 

Figure 2.6 (a) Softening the waveguide using a butane flame torch and (b) securing in the cell.

The cable was attached onto the syringe pump platform with sticky tape by aligning the middle of the wave guide at the middle of the syringe pump. The next process was pulling the waveguide by softening the cable with a butane torch whilst simultaneously pulling the fibre apart by turning on the syringe pump at 100 μL min^{-1}, Figure 2.6 part (a). In order to test the waveguide, a fresh bare microresonator was fabricated (which can be seen from the previous section), then was aligned to couple with the tapered region, Figure 2.8 part (c). When the characteristic resonance wavelengths occur, the waveguide was deemed ready for the experiment. An example of a resonance wavelength peak spectrum is shown in Figure 2.10 part (b). The tapered waveguide was inserted in the flow/fluidic cell using a translator (Thorlabs, UK) and then was secured in the cell using epoxy glue (Ecoflex 5, Bentley advanced Material, UK) as shown in Figure 2.6 part (b).

2.1.2.3. Fluidic cell designs and fabrication

The pattern of the fluidic/flow cell used throughout the experiments was published in [4]. Transparent material such as an acrylic sheet was used to fabricate the flow or fluidic cell using a Bridgeport (HARDINGE®) milling machine with mili power controller, Figure 2.7 part (a) and (b). The fluidic cell for carrying the resonator, the waveguide and sample in the Pb(II) sensor was fabricated using a 6 mm thick polycarbonate sheet, Figure 2.7 part (c). For the G-quadruplex work an acrylic sheet was used instead of a polycarbonate sheet.

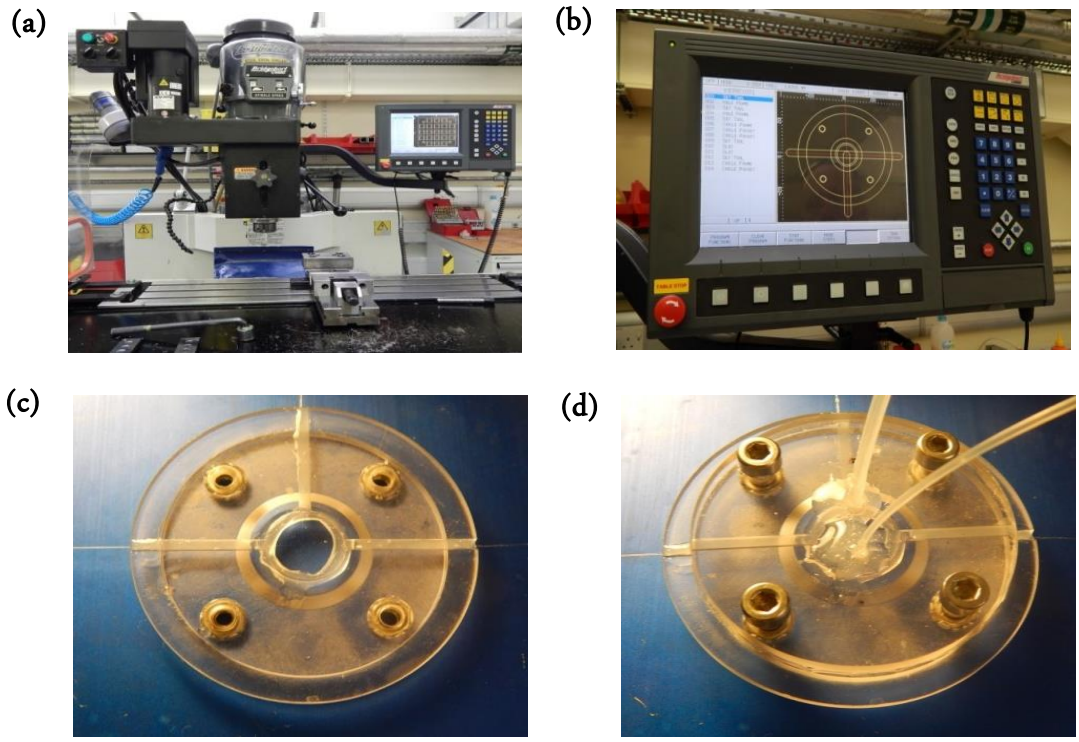


Figure 2.7 (a) The milling machine for fabricating the cell (b) the cell pattern was designed and inserted into the machine (c) the final cell for the Pb(II) sensor and (d) the cell was closed with the lid for G-quadruplex and thrombin (TB) experiments.

In the middle of the cell, a horizontal channel for mounting the waveguide was created with a 2 mm diameter and a vertical channel with 2 mm diameter was also produced for mounting the resonator. At the cross-section, there was a 350 µL rounded channel. In the Pb(II) sensor work, 500 µL of sample solution was introduced in order to generate a meniscus. The WGM signal was recorded in open system whereas in the G-quadruplex and thrombin (TB) work the fluidic cell was enclosed by the PDMS sheet and the cell lid in order to flow the solution continuously by using a syringe pump so that the WGM signal was recorded in closed system. Two tubes were inserted for introducing the solution through the inlet and washing it out through the outlet as shown in Figure 2.7 part (d).

2.1.3 Experimental set up for resonant wavelength shift detection

The WGM set-up consists of four main components as described previously, namely a microresonator, a waveguide, a light source and a detector, Figure 2.1. The waveguide is made of a single mode fibre optic cable. A tunable laser, which generates the laser light, is set up at one end of the waveguide. In order to detect the signal, the photodiode detector is attached at the other end. The sphere resonator, fabricated by melting the tip of the fibre optic cable, is aligned to couple with the waveguide.

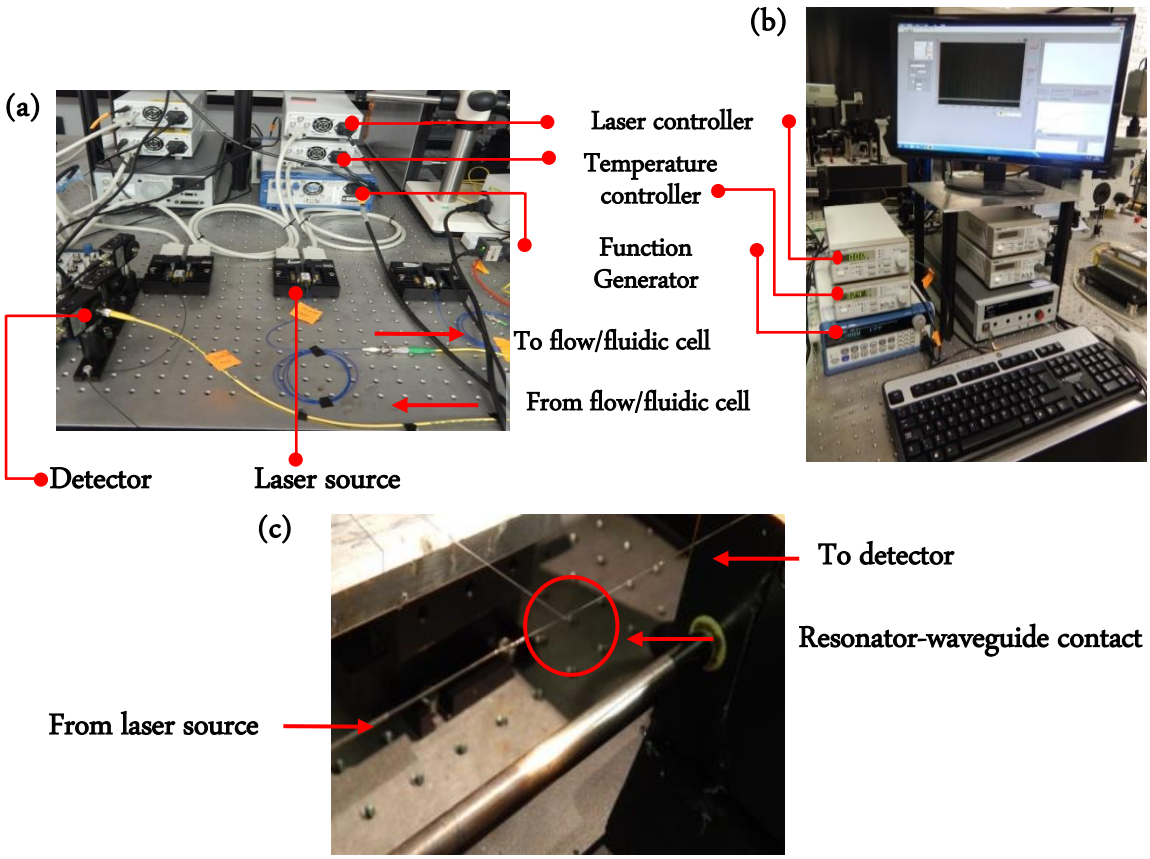


Figure 2.8 The WGM set-up (a) fibre optic connection (b) electronic equipment setting and (c) resonator-waveguide contact.

If the laser source is on, the laser light is confined inside the sphere and circumnavigates the surface due to the repeated total internal reflection (TIR) effect. The resonator is coupled with the waveguide and the resultant resonance wavelength shifts can be detected by the detector. The surface of the sphere is functionalized with the aim of protecting the microresonator from non-specific molecules binding onto the surface. The benchtop WGM set up is shown in Figure 2.8.

2.1.4 Parameters for resonant-shift recording

The WGM resonance shift signal was recorded using Labview software. The parameters used in this software are shown in the table below.

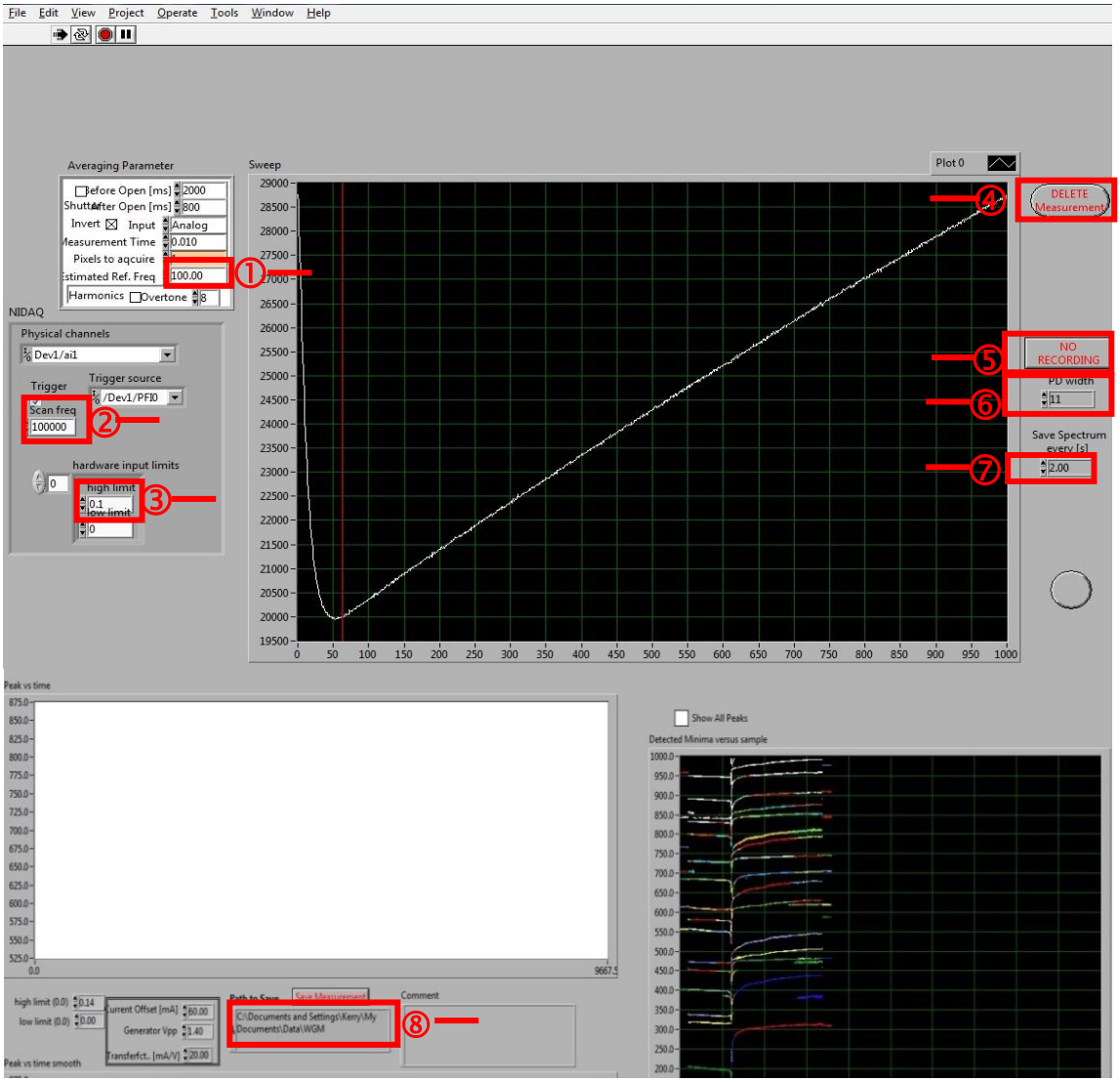


Figure 2.9 Screen capture of Labview software used to record the WGM signals

Table 2.1 Parameter for WGM recording

Parameters	
① Estimate reference frequency	Controlling the frequency in Hz which corresponded to the function generator device
② Scanning frequency	Controlling number of scanning. The higher the scanning frequency the more data points recorded
③ High limit	Controlling the width of the entrance window of the detector (0.1 to 5). The lower the number the less light goes through the detector
④ Delete bottom	Deleting unnecessary data
⑤ Record bottom	Recording the data
⑥ Width	minimum full width at half maximum (FWHM) value
⑦ Save spectrum every second	Time in second unit for interval recording data
⑧ File path	The name of a file or directory where the data is saved

2.2 Data analysis

2.2.1 Microsphere Q-factor calculation

The Q factor is mathematically described as the ratio of the wavelength where the resonance occurs (λ_r) to the spectral line width of the resonant wavelength, $\delta\lambda$, which is full width at half-maximum (FWHM) of the attenuation peak. Q is described in Equation 2.1 [5].

$$Q = \frac{\lambda_r}{\delta\lambda} \tag{2.1}$$

Practically, $\delta\lambda$ can be estimated from the transmission spectrum using Origin software and a non-linear Lorentz equation as shown in Equation 2.2.

$$y = y_0 + \frac{2A}{\pi}\frac{w}{4(x-x_c)^2+w^2} \tag{2.2}$$

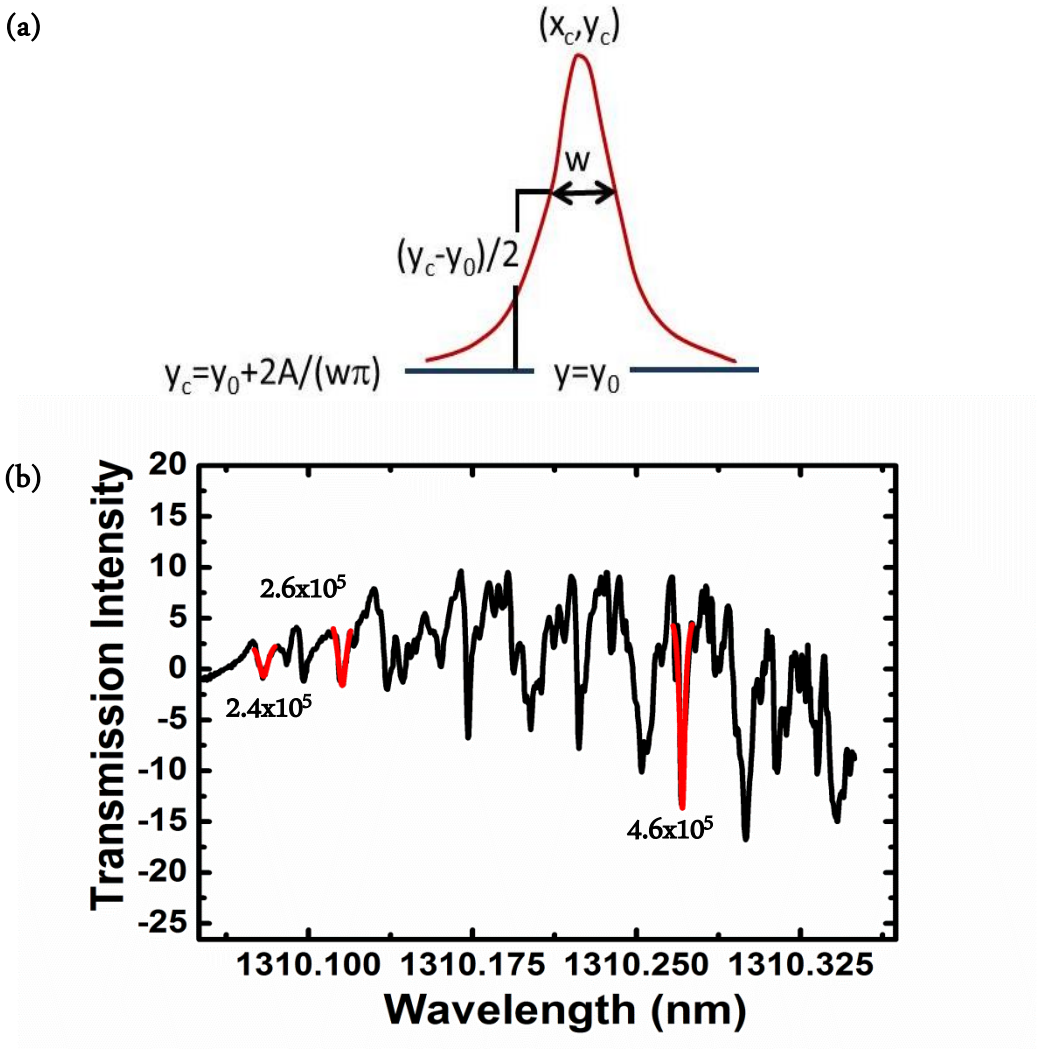
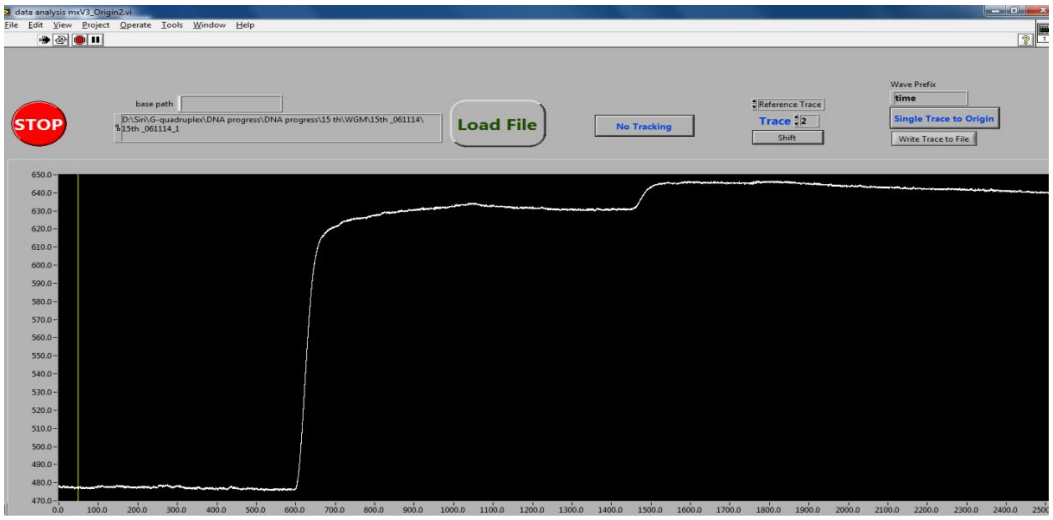


Figure 2.10 (a) Example curve of non-linear Lorentz equation for fitting δλ and (b) examples of Q-factor of APTES resonator at 10^5.

2.2.2 Programme and software for wavelength-shift analysis

The WGM signal can be recorded and collected using the Labview program. The recorded data was exported to Origin software for further analysis. A Labview M-series data acquisition card was used to connect with the photodiode detector then the data was analyzed using a virtual instrument (VI) written in Labview 7.0 (National Instruments, Austin, TX). The width at half maximum (FWHM) value was set to determine the position of the resonance peaks (see parameter ⑥ in Table 2.1) using a Bessel function. However, the data acquisition VI tracked all resonant peaks in the acquired spectrum using a peak fitting algorithm, so the position and the resonance wavelength shift of each resonance over time was saved for further analysis if required [1].

(a)



(b)

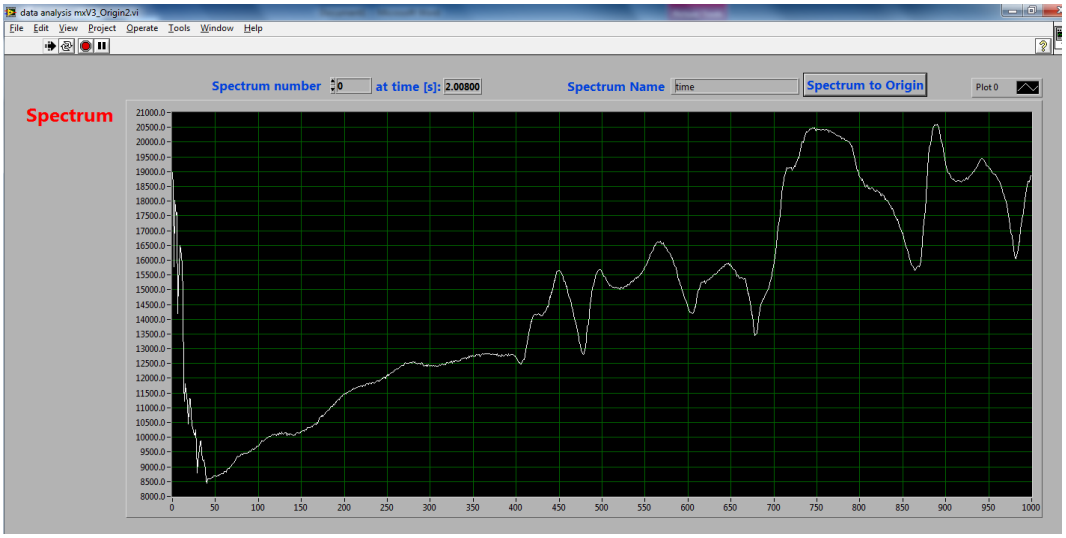


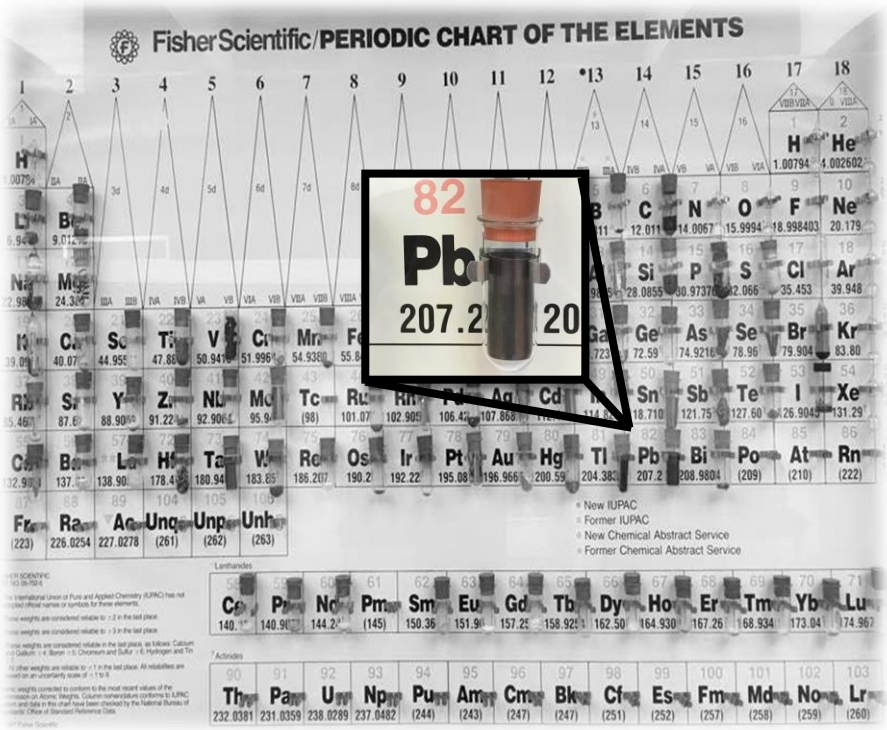
Figure 2.11 (a) Resonance wavelength shift and (b) transmission spectrum analysis

2.3 References

1. Wilson, K. A., Finch, C. A., Anderson, P., Vollmer, F. and Hickman, J., *Whispering gallery mode biosensor quantification of fibronectin adsorption kinetics onto alkylsilane monolayers and interpretation of resultant cellular response.* Biomaterials, 2012. 33: p. 225-236.
2. Corporation, Newport. *Singlemode Patch Cord, 1310/1550nm, F-SMF-28-C, 3m, ST/UPC Connectors* [cited 2016 12/01/2016]; Available from: http://search.newport.com.
3. Corporation, Newport. *Single Mode Optical Fiber, 1310/1550 nm, 0.13 NA* [cited 2016 12/01/2016]; Available from: http://search.newport.com.

4. Panich, S., Wilson, K. A., Nuttall, P., Wood, C. K., Albrecht, T. and Edel, J. B., *Label-Free Pb(II) Whispering Gallery Mode Sensing Using Self-Assembled Glutathione-Modified Gold Nanoparticles on an Optical Microcavity.* Analytical Chemistry, 2014. 86(13): p. 6299-6306.
5. Luchansky, M. S. and R. C. Bailey, *High-Q Optical Sensors for Chemical and Biological Analysis.* Analytical Chemistry, 2011. 84(2): p. 793-821.

Chapter 3 | Optical-Resonator-Based Chemical sensing: Heavy metal detection Pb(II) by optical microcavity



"Children in north-western Nigeria are no longer dying by the hundreds" said by Mary Jean Brown, chief of the lead poisoning prevention program at the Centres for Disease Control and Prevention. The health problems caused from acute lead poisoning had previously become a serious problem as at least 400 children were killed in Nigeria's Zamfara State by lead poisoning [1].

A key aspect of this chapter is to present and describe results from the work published in Analytical Chemistry "Label Free Pb(II) Whispering Gallery Mode Sensing Using Self-Assembled Glutathione modified Gold Nanoparticles on an Optical Microcavity" [2] in a systematic and detailed way.

This work was carried out to solve the problems associated with the detection of Pb(II) at extremely low concentrations (0.05 nM). Even though many advanced technique have been reported, only a few of them can be used to detect low concentrations of Pb(II) in real time by employing simple and fast methods. The introduction, experimental section and results and discussion are similar to that in the article [2] (modified and reprinted with permission. Copyright (2014) American Chemical Society), but an in-depth analysis of results and detailed discussions were attempted herein to demonstrate the novelty and applications of the presented work.

3.1 Introduction

The use of heavy metals such as lead (Pb), cadmium (Cd), mercury (Hg), arsenic (As) etc. for human activities have been known for thousands of years. Prolonged exposure to many of these metals is proved to cause several adverse health effects in humans and is an increasing concern especially in less developed countries resulting in significant mortality. Each metal has specific health effect at different dosage levels. As such, regulations emphasizing the exposure limits in food, natural sources or different environmental media have been prescribed by many international and national regulatory bodies, including the World Health Organization (WHO), Environmental Protection Agency (EPA) and the International Agency for Research on Cancer (IARC) in order to protect the global residents from heavy metal poisoning.

Among the various heavy metals, lead (Pb) is one of the most toxic, especially for children. Acute lead poisoning causes many symptoms including exhaustion, headaches, lung tumours and neurological disorders and behaviour or attention difficulties in children. Even though, lead is only weakly mutagenic, some evidence indicates that continuous exposure to Pb(II) could cause lung and stomach cancer [3]. Because of this, Pb(II) has been categorized as a possible carcinogen to humans by IARC [3]. In addition, EPA has set a safe threshold in drinking water to be 72.40 nM (15 ppb) while IARC has a lower threshold of 48.26 nM (10 ppb). On the other hand, recent data from clinical research demonstrated that there might be toxicological effects of lead at lower levels of considered acceptable exposure from IARC (10 ppb) in children. For example, the study conducted by Steenland *et al.* revealed that lead exposure can

cause intelligence decrements at a blood level below 9.65 nM (2 ppb) [4]. Therefore the Pb(II) levels in childrens blood should be reduced to lower levels than the limit established by the EPA or even the IARC [3, 5]. Taking into account about these very low concentration of Pb(II), it is obvious that detection technology of Pb(II) levels needs to be developed in order to control Pb(II) levels at such low concentrations.

A number of analytical techniques have already been reported to distinguish trace levels of Pb(II). Among them, atomic absorption spectrometry (AAS) [6-15] and inductively coupled plasma spectroscopy (ICP) are the most commonly employed techniques for Pb(II) detection [14]. Various contaminated samples including tap water and bottled water [16], paints [17], food samples [18], biological [19], and environmental samples [20] were investigated using these techniques with detection limits approaching up to 4.83 μM (1,000 ppb) [15]. However, one major drawback of these approaches is that the detection limits obtained are still higher than those set out by IARC. Because of this, sample pre-concentration cannot be avoided [13]. Many of these pre-concentration methods require long analysis times and complex instrumentation and hence are difficult to integrate for in-field measurements. Another problem with these techniques, both AAS and ICP, is that, they suffer memory effects and molecular or atomic interferences [14].

To address these limitations, various simple and sensitive assays have been reported recently employing both direct and indirect methods for Pb(II) detection. Among them, the most simple and promising technique involves the use of modified-gold nanoparticles (Au NPs) as probes with binding ligands such as DNA-modified enzymes [21], gallic acid [22], dithiocarbamate-modified 4'-aminobenzo-18-crown-6 [23] or catechin [24] that exhibit different optical and electronic properties in the presence Pb(II). Detection limits of such assays were shown to be very low and can be down to 1.45 nM (300 ppt); however, multifaceted labelling procedures and pricey DNA reagent cannot be avoided. A typical example of this technique is the method reported by Chai *et al.* [25] where a simple colorimetric aggregation-based assay using glutathione (GSH) capped Au NPs with detection limits down to 96.52 nM (20 ppb) was achieved. Later, Ali *et al.* [26] demonstrated a fluorescent probe for the indirect determination of Pb(II) concentration down to 19.30 nM (4 ppb) by using GSH-capped CdSe and CdTe quantum dots. Beqa *et al* [27] also employed the same chelator, GSH. They demonstrated that GSH modified with Au NPs can be used as an excellent probe to detect Pb(II) levels down to 0.48 nM (100 ppt). These works indicated that GSH is an excellent chelator for Pb(II). However, novel detection strategies are still required to improve analysis times, portability, sensitivity and enhance the selectivity of assays.

Herein we present a novel whispering gallery mode (WGM) sensing method for easy and sensitive detection of Pb(II). This new technique offers many advantages including real-time, sub-second detection time and label-free near single molecule sensitivity. The kinetic data can also be easily tracked and the sensor can be made using complementary metal–oxide–semiconductor CMOS processing methods, [28] used for in-field applications and is accessible to a non-professional manipulator. Review of the results from other techniques compared with our developed technique can be found in the Table 3.1.

Table 3.1 Comparison of the limit of detection of measuring Pb(II) from our work and previous studies. Modified and reprinted with permission from [2].

Reference	Methods	LOD
This work	WGM using GSH-Au NPs	0.05 nM
[27]	DLS with GSH-Au NPs	0.48 nM
[24]	Fluorescence detection using enzyme mimics of catechin-synthesized Au NPs	1.45 nM
[18]	Quenching of the fluorescence of CdTequantum dots	13.03 nM
[26]	Glutathione-capped quantum dots	38.61 nM
[21]	A colorimetric biosensor using DNAzyme-directed assembly of Au NP	96.52 nM
[29]	A thin-film microsensor based on chalcogenide glasses	96.52 nM
[25]	Colorimetric detection using glutathione functionalized Au NP	96.52 nM

3.2 Experimental methods

3.2.1 Chemical and Materials

All chemicals used in this experiment including gold(III) chloride hydrate ($HAuCl_4 \cdot 3H_2O$ Aldrich, U.K.), sodium citrate tribasic dehydrate ($HOC(COONa)(CH_2COONa)_2 \cdot 2H_2O$, Sigma-Aldrich, U.K.), (3-Aminopropyl) trimethoxysilane (APTMS, $H_2N(CH_2)_3Si(OCH_3)_3$ Sigma-Aldrich, U.K.) 1,000 ppm lead nitrate $Pb(NO_3)_2$ standard, Sigma-Aldrich, U.K.), reduced l-glutathione ($H_2NCH(CO_2H)CH_2CH_2CONHCH(CH_2SH)CONHCH_2CO_2H$, Sigma-Aldrich, U.K.) were analytical grade. All solutions used herein were prepared using Mill-Q water (resistivity ca. 18.2 MΩ cm at 25 °C).

3.2.2 Preparation and Characterization of the Au NPs

Gold nanoparticles (citrate stabilized, diameter ca. 16 nm) used in this experiment were synthesized in our laboratory according to a modification of the well-known Turkevich method [30]. Briefly, an aqueous solution of 8.86 mg of gold(III) chloride hydrate dissolved in 95 mL of deionized water was refluxed in a 250 mL round bottom flask connected with a condenser for 20 minutes at 150 °C and then 5 mL aqueous solution of 20 mg of sodium citrate tribasic dehydrate was added rapidly into the reaction solution. The mixture was then stirred continuously for at least 15 minutes and was then cooled to room temperature. The concentration of the Au NPs was determined by UV-Vis spectroscopy (Spectrometer, Thermo) using the molar extinction coefficients. The morphology and size of the particles was also determined by dynamic light scattering, (DLS, delsaTM) and scanning electron microscopy (SEM, Oxford).

3.2.3 Modification of the Au NP surface with GSH

In this work, GSH was used as a chelator for Pb(II). The preparation of Au NPs modified with GSH was synthesized according to the procedure previously published by Beqa *et al* [27] with a slight modification. The GSH-Au NP complex was synthesized in dark and N_2 atmosphere conditions with the aim of protecting the GSH complex from light and oxygen exposure. An aqueous solution of 0.59 nM gold nanoparticle (8 mL) was transferred to 100 mL 3-neck round bottom flask and was purged with N_2 gas for 3 minutes, after which, 1 mL of 0.59 μM reduced l-glutathione was added. The mixture was allowed to react for 2 hours at room temperature in dark conditions, with continuous stirring to ensure attachment of the GSH onto the surface of gold nanoparticles. A 0.01 M NaOH was then added to adjust the pH of the resulting mixture to 8.0. In the end, the solution was centrifuged at 10,000 rpm for 20 minutes with regard to remove unbound GSH molecules. The upper aqueous phase was aspirated off and the remaining complex was further washed with water three times. In order to confirm the successful functionalization of GSH on the Au NP surface, the spectrum of the complex between synthetic GSH-modified Au NPs and 4.83 μM (10 ppm) Pb(II) was recorded to check any red shift in order to prove success of the NP surface's modification.

3.2.4 Decoration of the GSH-Au NPs onto the modified silanized microresonator surface

The silanized, aminopropyltrimethoxysilane, APTMS, resonator was aligned to couple with the tapered waveguide by using a three-axis micromanipulator (PT3/M, Thorlabs). Several deep and sharp resonance peaks are expected to ensure good coupling. Next, the resonator and waveguide were inserted into a microfluidic cell in order to efficiently deliver Pb(II) solution. The modified Au NPs were delivered into the fluidic cell to decorate the surface of the microsphere. Resonance wavelength shift was recorded by selecting one resonance peak until a plateau was reached, indicating that the surface was saturated. Unbound NPs were removed by flushing the cell with deionized water at least five times.

3.2.5 Detection of Pb(II) by WGM resonance shift

The WGM set-up and WGM signal measurement protocol was already discussed in Chapter 2. Figure 3.1 displays the WGM platform for Pb(II) detection. In order to quantify Pb(II) ions, the fluidic cell was incorporated and was initially filled with 500 µL of DI water in order to generate a meniscus. The system was allowed to stabilize for at least 15 minutes (or until the baseline is stable). Varying concentrations of Pb(II) or other metal ions were then introduced by pipetting 50 µL of each solution into the meniscus. Resonance shifts were then tracked until the shifts reach a plateau. Between each concentration of heavy metal the solution in the fluidic cell was withdrawn and flushed with at least five volume equivalents of water.

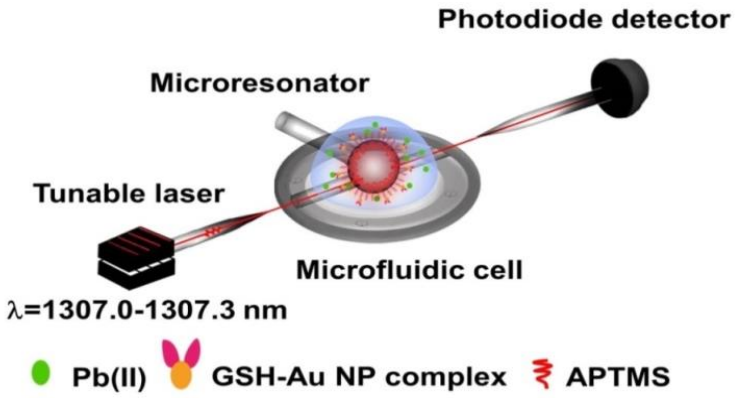


Figure 3.1 Schematic representation of a WGM platform for the detection of Pb(II). The light, generated by a tunable laser, circumnavigates the surface of a microresonator through a tapered waveguide made from an optical fibre. This light is strongly confined inside the microsphere by total internal reflection. Energy is extracted from the fibre, resulting in a negative peak detected by a photodetector. The surface of the resonator is functionalized with GSH to improve the specificity to Pb(II). When the metal ion binds to the modified resonator a spectra shift is observed which is used to quantify the concentration of the analyte. Modified and reprinted with permission from [2, 31].

3.3 Results and discussions

3.3.1 Characterization of Au NPs and GSH-modified Au NPs

3.3.1.1. Determination of Au NPs concentration from UV-Visible spectroscopy

Analysis of surface plasmon resonance adsorption band can provide information of size and concentration of the particles. The UV-Visible adsorption spectra recorded for the synthetic 16 nm Au NPs is shown in Figure 3.2.

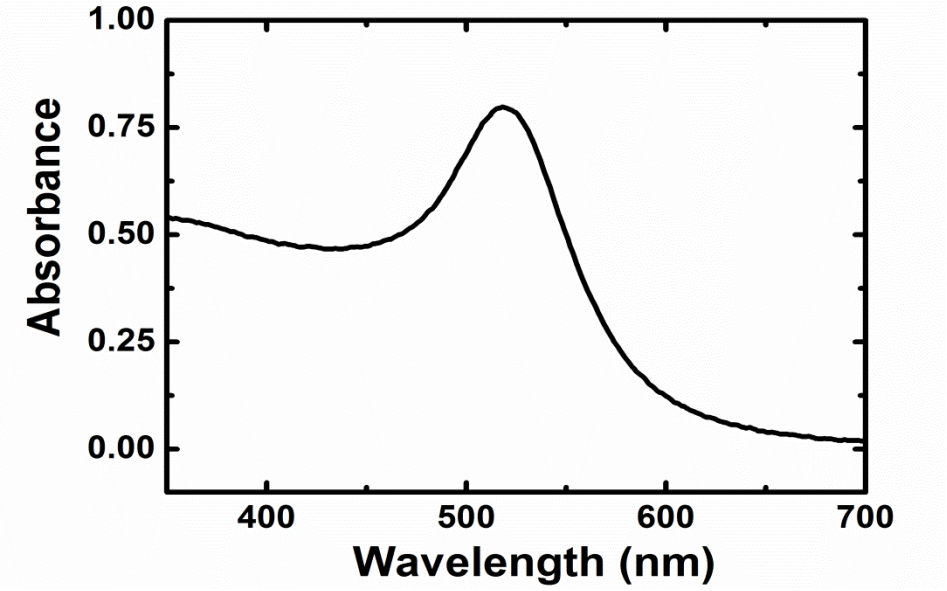


Figure 3.2 The surface plasmon resonance (SPR) absorption of Au NPs was clearly visible at maximum absorbance at 520 nm indicating successful NPs formation.

The surface plasmon resonance absorbance (A_{spr}) was clearly visible as a peak at 520 nm. According to Haiss *et al*'s work [32], the diameter of the Au NPs can be calculated using the ratio of A_{spr} and absorbance at 450 nm (A_{450}), A_{spr}/A_{450} (Note, A_{520}=0.863, A_{450}=0.50, A_{spr}/A_{450} = 1.72, d~20 nm). Au NPs diameter can be calculated and was found to be ~20 nm in this experiment.

However, in order to improve the precision of size determination other techniques were also used to confirm this information which will be discussed in next section. The molar concentrations of Au NPs were calculated using Equation 3.1 and 3.2 [33].

$$N = \frac{\pi \rho D^3}{6M} = 30.89602D^3 \quad (3.1)$$

N=average number of gold atoms per nanoparticle, ρ=density for FCC gold (19.3 g/cm^3), D=the average core diameter of the particle (nm), M=atomic weight of gold (197 g/mol)

$$C = \frac{N_{total}}{NVN_A} \quad (3.2)$$

C = Molar concentration of nanoparticles solution, N_{total} = equivalent to the initial amount of gold salt added to the reaction solution, V = volume of the reaction solution N_A = Avogadro's constant.

The concentration of Au NPs was found to be 0.60 nM using $\varepsilon = 8.42\times10^8$ and 0.59 nM by calculating from initial amount of gold salt.

3.3.1.2 Determination of Au NPs and GSH-Au NPs size distribution

In our experiment, a variety of methods were used to assess the size of Au NPs before and after modification. Using dynamic light scattering (DLS) technique the average diameter for Au NPs with and without GSH was determined to be 25.0±8.20 nm and 37.3±19.80 nm, respectively. Interestingly, values were slightly larger than that recorded by using both SEM and AFM (16±0.40 nm and 21±0.64 nm from SEM and 15.8±0.21 nm and 16.77±0.22 nm from AFM). A possible explanation for these differences may be the sample hydration. Since DLS measures the hydrodynamic diameter, it is possible that the particle size analysis from DLS could be larger than the "real" particle size recorded by SEM [34]. In SEM, the dehydrated diameter is measured. Another alternative possibility might be dimerization of the particle in solution.

3.3.1.3. Characterization of the GSH-Modified Au NPs

As was mentioned earlier in the introduction section, the major objective of this study was to develop the sensitivity at the same time as the selectivity of the Pb(II) sensor. Many current literature on this sensor pays particular attention to the Pb(II) probe. GSH has outstanding specificity when binding to Pb(II). In addition, GSH acts as a natural antioxidant [35] apart from its many vital biological roles, GSH is designed to protect cellular membranes from unwanted heavy metals via complex formation [36]. GSH is also a widely known chelator for Pb(II) because of its ability to distinguish Pb(II) from other heavy metal interferants [25, 27]. There are four functional groups of GSH molecule as shown in Figure 3.3, one amino ($-NH_2$), one sulfhydryl (-SH) and two carboxyl (-COOH) groups which can be used as a selective functional group for binding with Pb(II). In aqueous solution Pb(II) complexes with GSH via the thiol group [37]. The bonding between Au and –SH is very strong and therefore, in our case, the –SH group in GSH is occupied and cannot bind to Pb(II). Consequently, the binding is expected to occur via the two free $-COO^-$ groups which make the sensor more selective as –SH can bind with other heavy metals including Hg(II) and Cd(II) ions [27, 38].

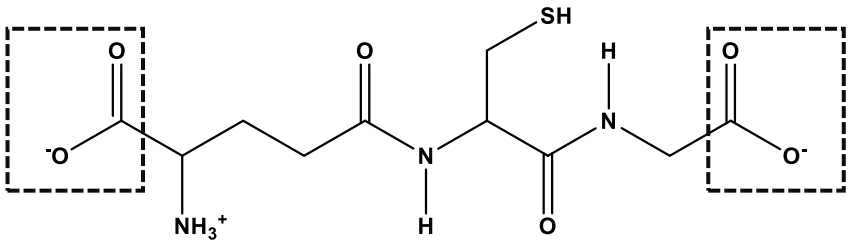


Figure 3.3 Chemical structure of reduced glutathione as a chelator in which -COO^- groups were used for chelating with Pb(II).

This Pb(II) selective chelator also was supported by the work by Kim *et al.* [39] which suggested that the Pb(II) binds with the two –COO^- units. Interestingly at pH 7, the carboxylic acids group in GSH-capped Au NP probe undergoes deprotonation to form –COO^- while the amine group gets protonated to –NH_3^+. Because of this reason, the probe is protected from binding with Zn(II) and Cd(II). Additionally, GSH also acts as a stabilizer for NPs [27].

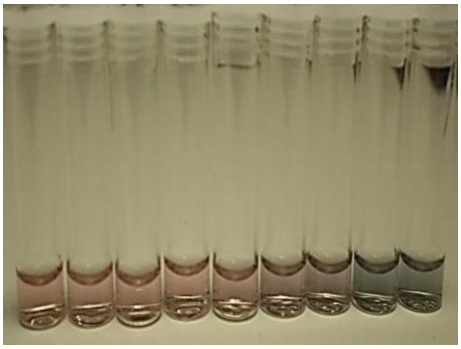


Figure 3.4 GSH-Au NP complex with 100 µL of water, 0.05, 4.83, 48.30, 96.60, 193.20, 241.50, 386.40 and 483.00 µM of Pb(II), respectively.

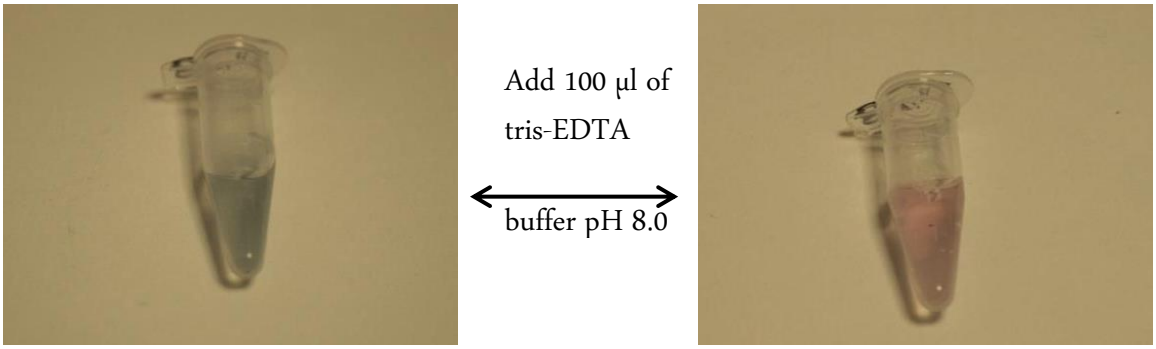


Figure 3.5 depicts the reaction between the Au NPs-GSH complex and Pb(II) before (left) and after (right) addition of 100 µL of tris-EDTA buffer pH 8.0.

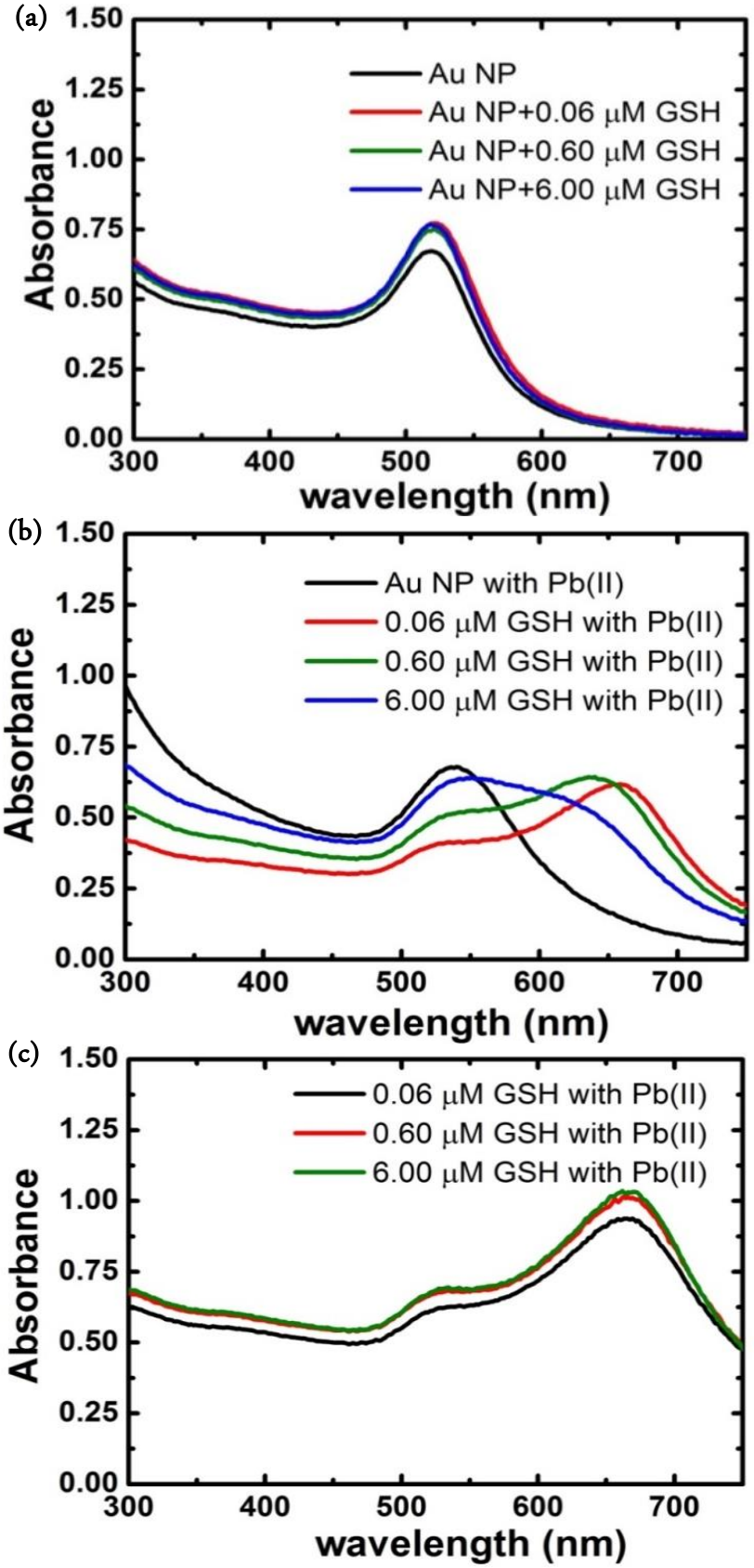


Figure 3.6 (a) The UV-Visible spectra of Au NP modified with various concentration of GSH and when Pb(II) binding in the solution (b) before and (c) after washing the excess GSH from the NPs complex with water. Modified and reprinted with permission from [2].

When Pb(II) binds onto the modified GSH-Au NPs the colour of the solution changes from red to blue or purple depending on the concentration of Pb(II) which can be seen using naked-eyes as shown in Figure 3.4. Unfortunately, this process can be observed at only high concentration of Pb(II) at least 193.2 μM (10 ppm) which is higher than the safety threshold. In addition, the complexation reaction between Au NP-GSH and Pb(II) is reversible. In Figure 3.5 the colour change can be observed by adding EDTA as a chelator for Pb(II).

As described in the previous section the Au NPs were modified with GSH complex prior to decoration onto the surface of the WGM resonator. A shift or broadening in the UV-visible spectrum does not occur during GSH bound to NPs as shown in Figure 3.6 part (a). This finding has important implications as it suggests that there is no aggregation of the GSH-Au NP complex. The ratio of NP (0.59 nM) and GSH (0.59 μM) used in the experiment was 8:1 and is in good agreement with that from the work published previously by Beqa *et al.* [27]. In fact, the NPs are stabilized by the GSH complex. The absorbance of the GSH-Au NP complex increased in a comparison with the absorbance of the unmodified Au NP in this study confirming the occurrence of surface coupling.

To estimate suitable GSH concentration, a serial dilution of GSH was examined at constant Au NP concentration of 0.59 nM, as shown in Figure 3.6 part (a). Aggregation and red shift of the plasmon resonance is observed during binding of 48.26 μM (10 ppm) Pb(II), which indicates the successful of functionalization of the Au NPs surface with GSH, Figure 3.6 part (b). The variation in spectra of different concentration of GSH can be attributed to the excess unbound GSH present in the solution. When the unbound GSH was removed from the solution, the spectra of all solutions were found to be the similar since the amount of GSH- Au NP complexes formed in each case is the same as shown in Figure 3.6 part (c).

From this observation, it is concluded that 0.06 μM GSH is sufficient to completely modify the Au NPs. Hence to ensure the successful functionalization, a GSH concentration of 0.60 μM was employed throughout the experiment. In fact, excess GSH can effects the analysis especially in the solution but since in WGM the unbound GSH can be easily washed away with water until the baseline is stable which indicated that there was no unbound GSH.

A very clear colour change (red shift) is observed with GSH-modified particles in solution whereas no colour change is observed with bare NPs in the presence of 48.26 μM (10 ppm) Pb(II), (Figure 3.7). This is a strong evidence of a promising colorimetric probe for detecting Pb(II). In fact, this colorimetric technique is simple and very compatible for developing into a

sensor. Despite this, colorimetric change is only observed for Pb(II) concentrations greater than 4.82 μM (1 ppm) which is not sensitive enough to track Pb(II) level at the safety level set by EPA or IARC, necessitating a pre-concentration step adding additional complexity into the sensor design. For a preliminary test, the complex of GSH-Au NPs complex was reacted with Pb(II) at the same concentration 38.64 μM of other heavy metal ions Hg(II), Cd(II) and divalent ions, which were Mg(II), Mn(II), Ca(II), Ni(II) Cr(II), Fe(II) and Figure 3.8. The colour of the solutions changed from red to blue when Pb(II) was added into the solution, whereas a change of the solution colour does not appear when other heavy metals were added. This strong evidence denoted that the approach had very high specificity toward Pb(II) compared to the other metals.

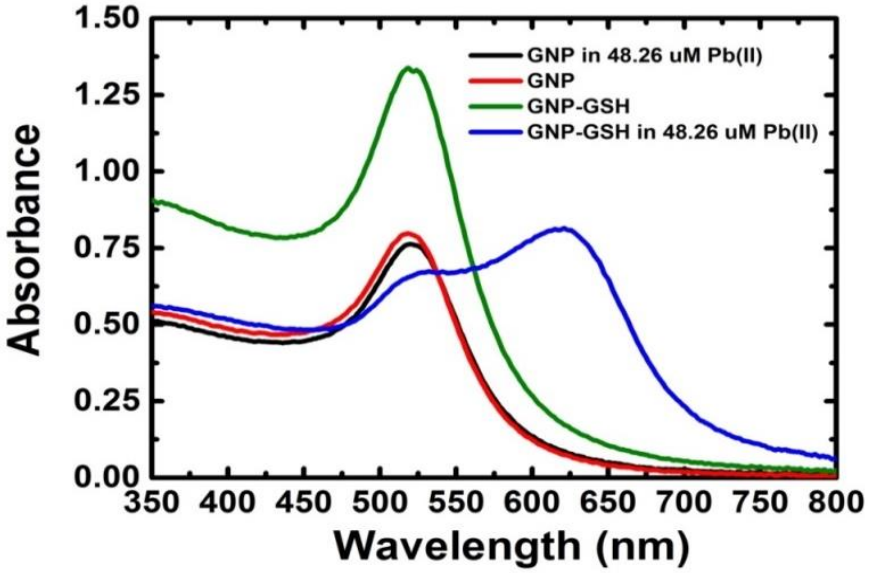


Figure 3.7 The UV-Visible spectra of Au NP and GSH-modified Au NP complex before and after addition of Pb(II) in solution. Modified and reprinted with permission from [2].

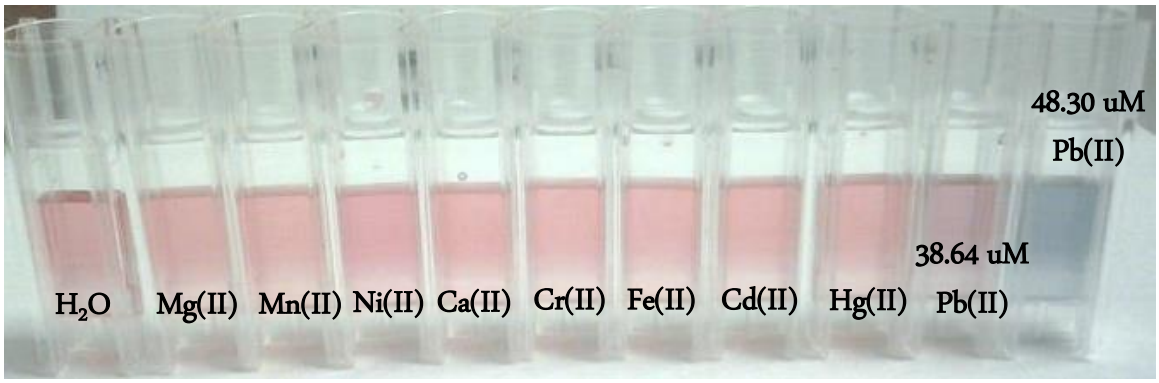


Figure 3.8 The visible images of GSH-Au NPs containing 38.64 μM (8 ppm) other metal ions compared with 38.64 μM (8 ppm) and 48.30 μM (10 ppm) of Pb(II) (metal ions were incubated with GSH-Au NPs for 30 minutes).

3.3.2 Attaching GSH modified Au NP complex on the resonator surface

The major objective of this study was to sensitize a resonator specifically for Pb(II). Therefore, to achieve this, the resonator was coated with GSH modified Au NPs. Before decorating with the modified Au NP complex, we attempted to attach GSH directly onto the resonator surface in order to avoid the surface roughness increase associated with the NP adsorption. Without NPs, Q-factors will be higher (more detail about Q factor will be discussed in the next section) and can improve the detection limits.

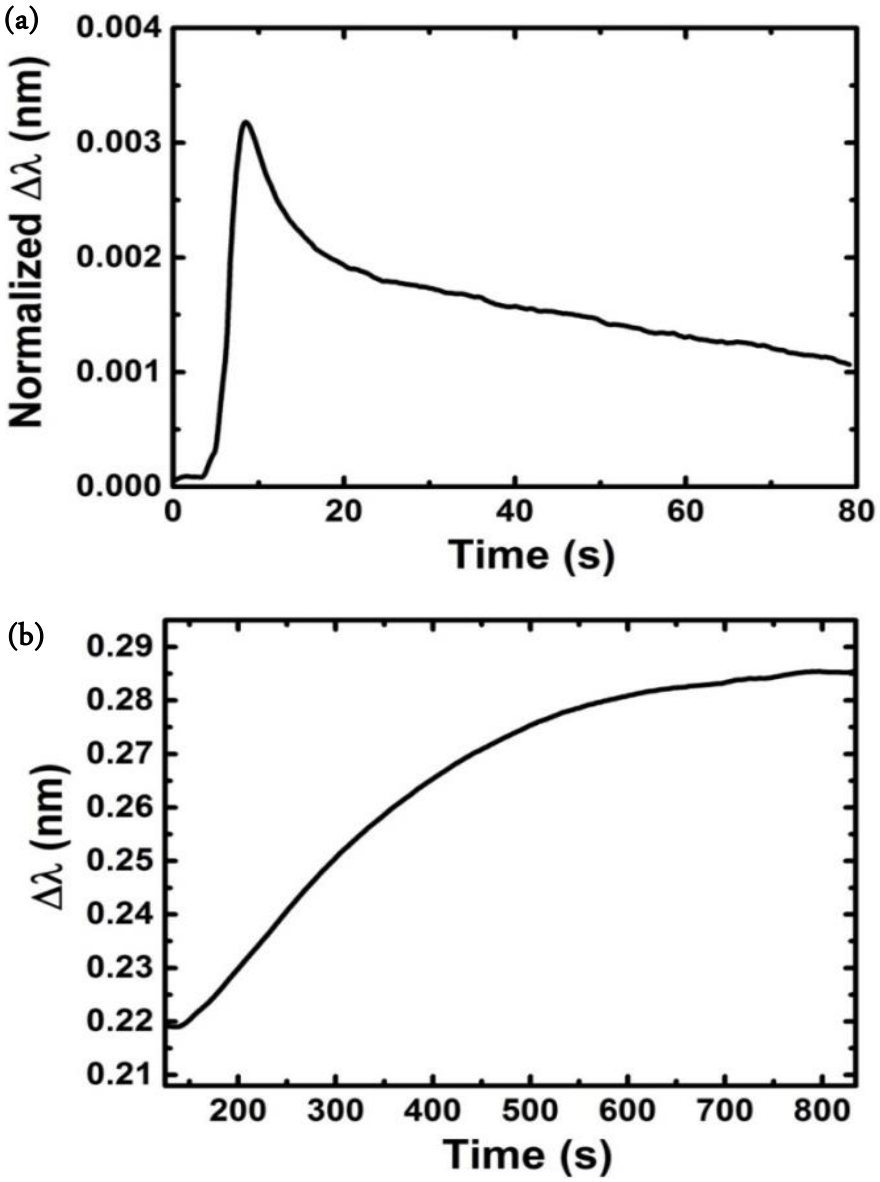


Figure 3.9 (a) Unsuccessful coating of GSH and (b) binding curve of successful attachment of GSH-modified Au NPs onto the APTMS-coated surface of the microresonator. Modified and reprinted with permission from [2].

One major drawback of this approach is the presence of unoccupied sulfhydryl (-SH) groups in the GSH [26] which can chelate to a large number of heavy metals, causing a decrease in specificity of the probe. Also the immobilization of GSH onto a glass or APTMS surface is not straightforward and requires a catalyst and high temperatures [40]. An example from attempting of adsorption of GSH adsorbed on APTMS surface is shown in Figure 3.9 part (a).

As was pointed out in the beginning of this section, attaching only GSH as a chelator without Au NPs could diminish the sensor selectivity and hence functionalization of the resonators with Au NPs mediated GSH is a simple and better solution. Figure 3.9 part (b) depicts the binding of GSH-Au NPs onto the surface resonator. Characterization of GSH-Au NPs onto the surface resonator will be described in section 3.3.4.

3.3.3 Quality or Q-factor

3.3.3.1. Q-factor from attaching 16 nm GSH-Au NP complex

Q-factor of a resonator can be defined as the ratio of the resonance frequency and the full width at half-maximum bandwidth of the resonance ($\delta\lambda$). As was mentioned in the previous chapter, the resonator used in this study was spherical shape as shown in Figure 3.10. Data from several sources have identified the high Q-factor supported by sphere resonator up to 10^8-10^{10} [41, 42]. Therefore, this sphere resonator can perform as a highly sensitive sensor.

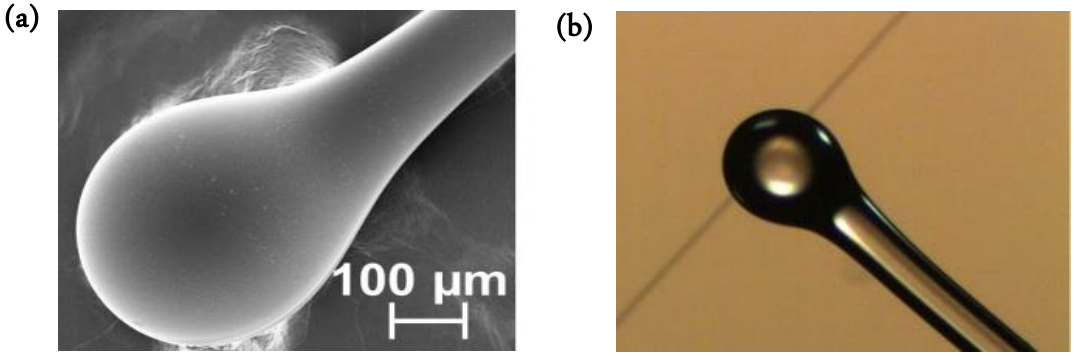


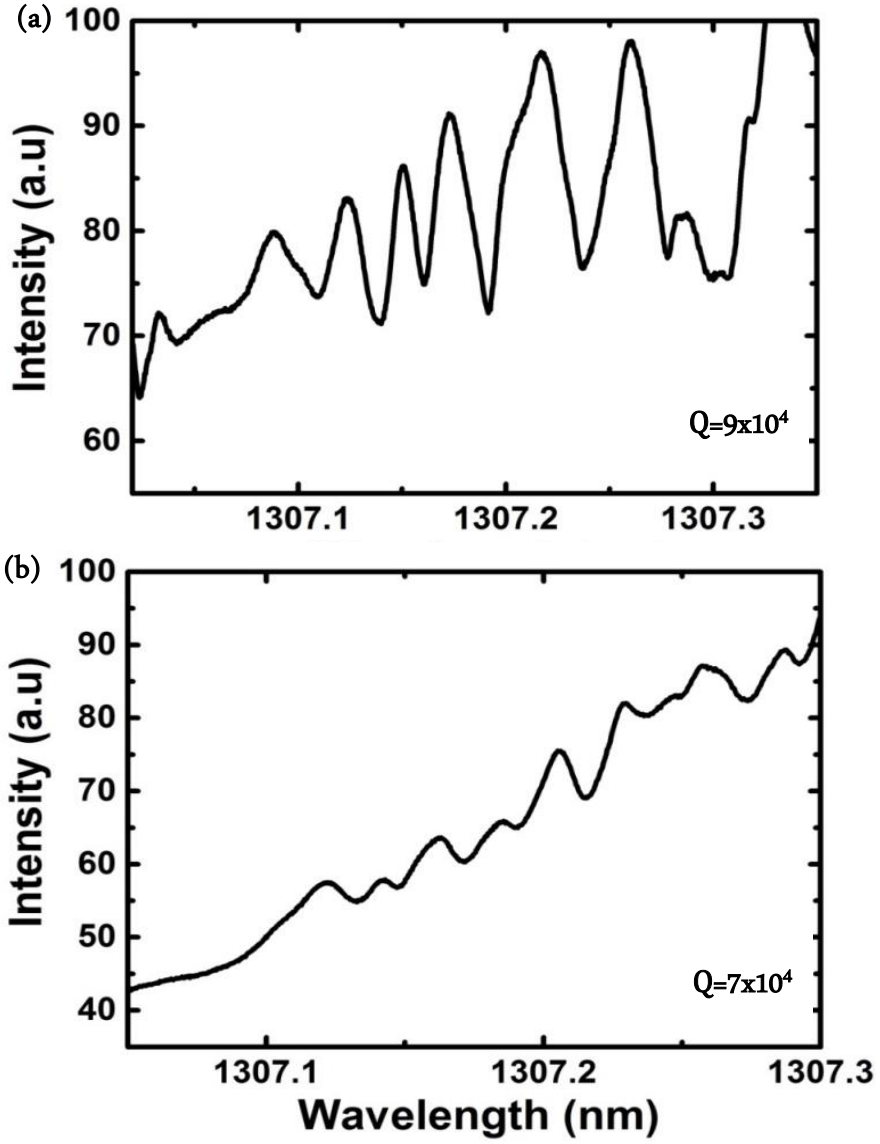
Figure 3.10 (a) The microresonator picture captured by SEM and (b) the microscopy image of the coupling between the microresonator and the tapered waveguide. Reprinted with permission from [2].

The Q-factor can be calculated using Equation (3.3) [41]. The line-width ($\delta\lambda_r$) can be determined from the full width at half-maximum (FWHM) estimation using origin 8.6 software.

$$Q = \lambda_r/\delta\lambda_r \tag{3.3}$$

The sensitivity of this WGM technique was demonstrated from a small $\Delta\lambda_r$ which indicates the binding of a few atoms of Pb(II). The Q-factor decreases from 6×10^6 to $4\times$

10^5 because NPs bind to the APTMS resonator surface, as shown in Figure 3.12. The reason for decreasing Q-factor could be due to the increasing of surface roughness from the Au NPs assembly on the resonator surface.



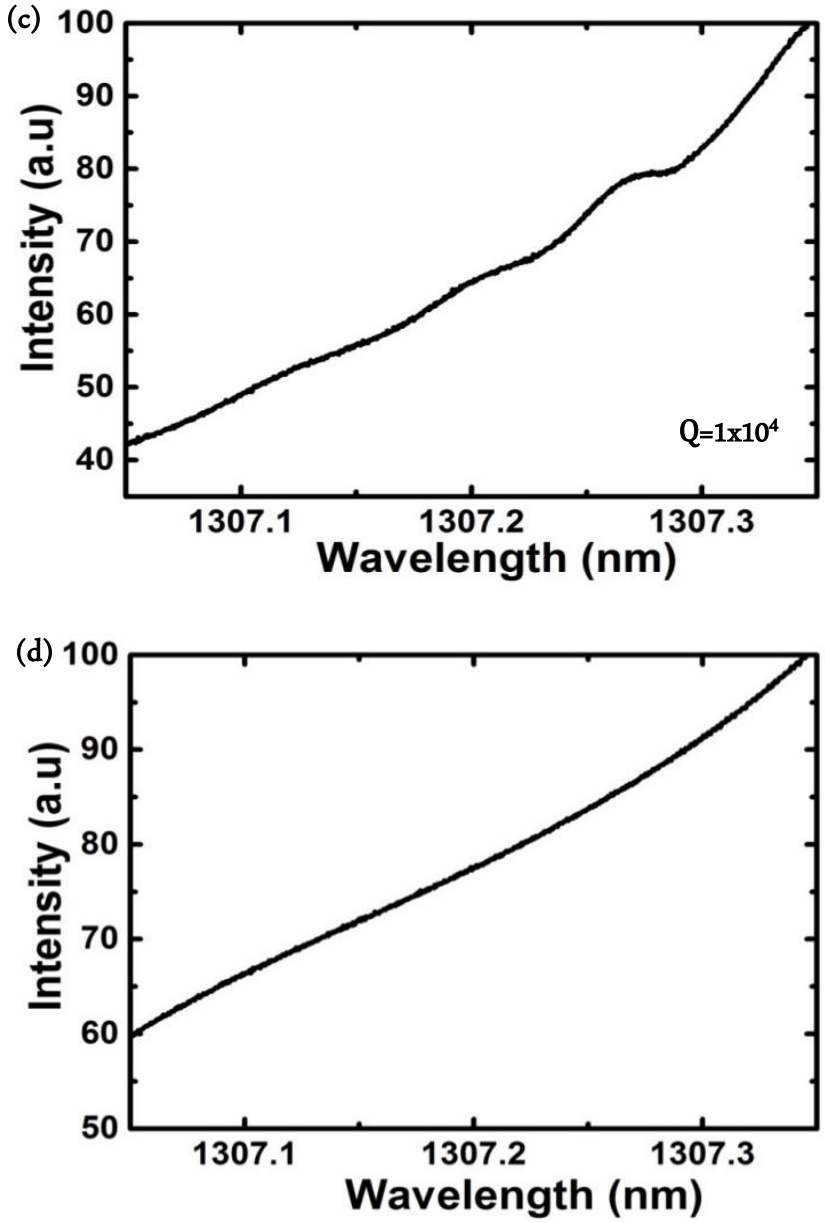


Figure 3.11 Comparison of the Q-factor of APTMS-coated surface with Au NPs at (a) 15 (b) 30 (c) 180 minutes and (d) 24 hours after which resonance dip cannot be tracked. Modified and reprinted with permission from [2].

A compromise between % Au NPs coverage and Q-factor are required to maximize Q-factor while there are still adequate particles on the surface to sense Pb(II) (more detail about Q-factor can be found in Chapter 1, section 1.2.8 and how to calculate Q-factor in Chapter 2, section, section 2.2.1).

In our case, $Q_{s.s}^{-1}$, scattering losses, is almost certainly the limiting component in decreasing the overall Q-factor due to surface inhomogeneity associated with the NP decoration. Actually, in our experiment GSH-Au NP complexes were left in the fluidic cell until the wavelength reached a plateau which took around 15 minutes. According to SEM and AFM data, Figure 3.15, ~40% NP coverage (16 nm in size) was achieved which still offered a sufficiently high Q-factor. Even upon NP binding the Q-factor decreased, in the section that follows, it will be debated that Au NPs can enhance the sensitivity of the sensor. Figure 3.11 demonstrates decrease in Q-factor upon binding for NPs for different times.

3.3.3.2. Pb(II) sensor with Au NPs plasmonic enhancement

Attachment of Au NPs on the resonator surface can lead to a decrease of Q-factor. In contrast to earlier findings, however, attaching plasmonic nanoparticles to the surface of a microsphere cavity can also enhance the sensor sensitivity by several orders of magnitude. Previous studies from Shopova *et al.* [43] demonstrated a physical mechanism enhancing the label-free sensitivity of a WGM sensor. Briefly, a bound nanoparticle is polarized by the evanescent field from orbiting of the laser light. This causes change in effective refractive index at the resonator surface. A shift in the resonance frequency is proportional to the particle's polarisability, number of particles and the local electric field. However, laser frequency noise is a classic problem in WGM and can limit the wavelength shift tracking. An alternative improvement can be achieved by increasing the frequency shift per particle that is attached onto the resonator's surface rather than changing laser source which is expensive. This can be achieved by increasing the electric field at the position of the particle.

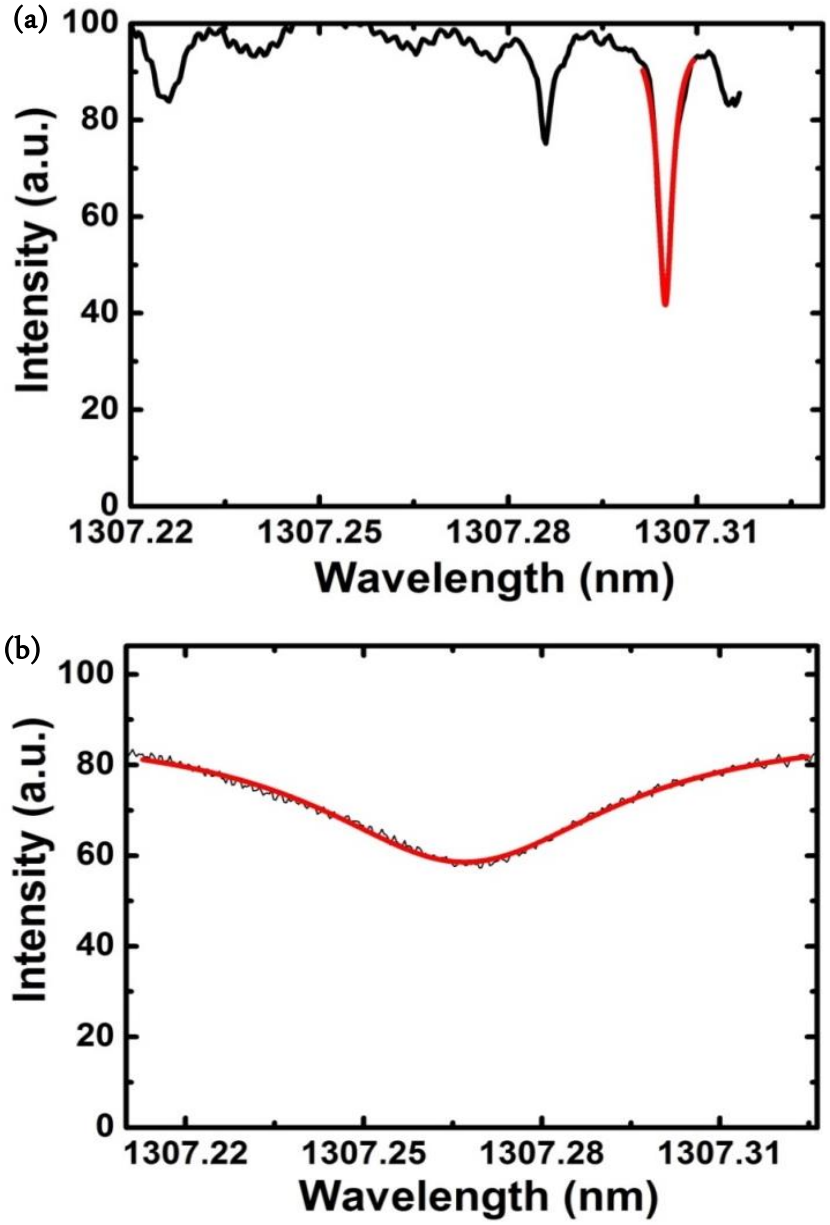


Figure 3.12 Comparison of the WGM signal for (a) APTMS-coated surface in water and (b) GSH-Au NP coated resonators. The signal was fitted using a Lorentzian function (red). The Q-factor can be calculated by dividing the resonance wavelength by the linewidth. The line-width ($\delta\lambda$) can be determined from the full width at half-maximum estimation using Origin 8.6. Modified and reprinted with permission from [2].

To put this result in perspective, plasmonic resonances from bound metallic nanoparticles can induce large field enhancements at or nearby to a cavity surface. This high electric field at bound particles can be called a "hot spot". When the analyte binds at this hot spot, an enhanced field increases the energy required to polarize the particle which is relative to the total energy in the resonator and ultimately leads to a larger frequency shift [43]. This is the reason why even though Q-factor decreases the sensor is still very sensitive to Pb(II).

3.3.4 Characterization of the functionalized resonator surface

To verify the successful functionalization of the resonator surface, UV-visible technique was first employed as it is the simplest technique. A glass cover slide coated with APTMS and the GSH-modified Au NP complex was used as the model to understand the spectral properties on the microresonator surface [30]. The spectra of GSH-Au NP complex on the microresonator surface with (red) and without (black) the presence of 48.26 nM (10 ppb) Pb(II) were plotted as shown in Figure 3.13. The maximum absorbance was observed at 526 nm indicating the successful assembly of the modified NPs onto the surface. No spectral shifts and changes in λ_{max} indicated that there was no aggregate of NPs when Pb(II) bound to the resonator. A possible explanation for this might be that the NPs were strongly attached and immobilize onto the cavity surface. This was confirmed by employing SEM and AFM imaging as shown Figure 3.15.

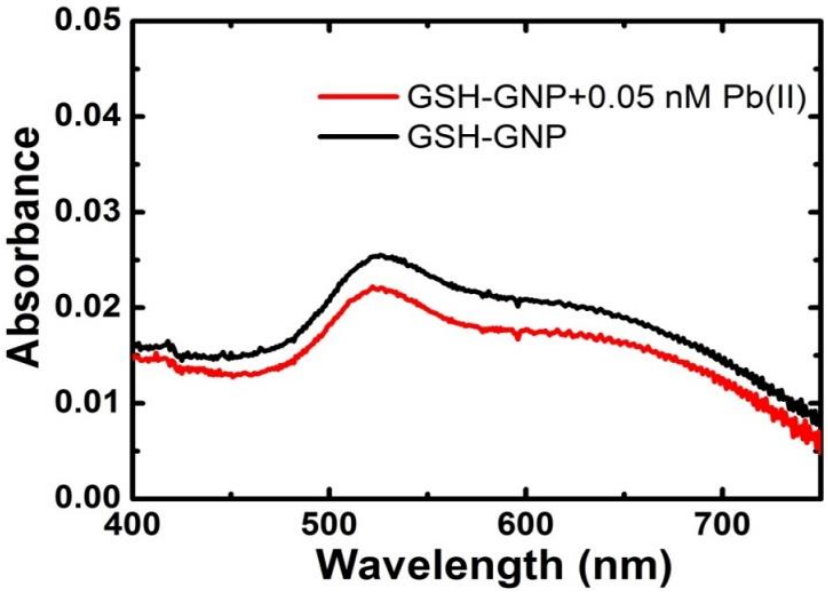


Figure 3.13 Example spectra of the GSH-Au NP complex deposited on an APTMS glass slide coated surface before and after binding with 48.26 nM of Pb(II). Modified and reprinted with permission from [2].

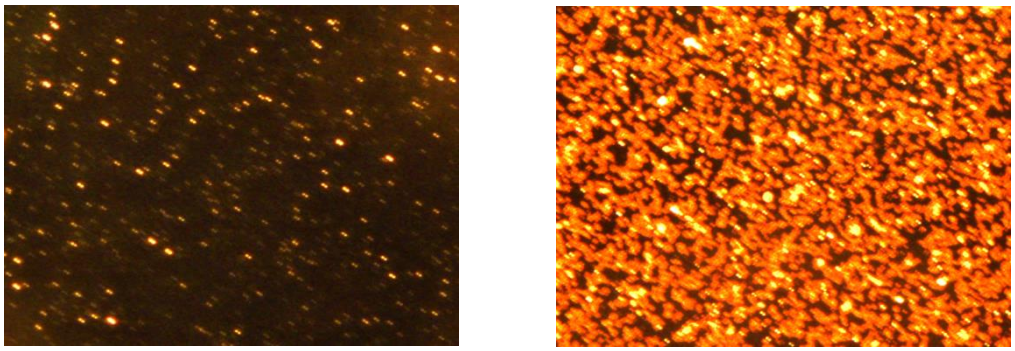


Figure 3.14 Dark field images of glass slide coated with APTMS before (a) and (b) after immobilized with GSH modified Au NPs complex as a model to confirm the success of functionalization of the glass surface.

Dark field images from glass slide coated with APTMS also confirm the success of Au NP modified GSH complex functionalization, Figure 3.14. Other techniques, such as electron backscatter diffraction scanning electron microscopy (EBSD-SEM, Oxford) and AFM (Agilent), were also performed to ensure the surface modification. A tapping mode AFM was used to overcome the problems related to the curvature of the sample and the NP dimensions. A super sharp cantilever with a non-coated n^{+}-silicon tip (Windsor Scientific, U.K.) was used at or near the cantilever's resonant frequency using a piezoelectric crystal. The piezo motion causes the

cantilever to oscillate with high amplitude to provide high resolution. APTMS-functionalized resonator surfaces with and without 15 minutes (the same time as used in WGM experiment) of exposure to the GSH-modified NPs were analyzed and are shown in Figure 3.15 part (a) and (b), respectively. WsxM program was used to manipulate all the results from AFM [44]. AFM result in Figure 3.15 shows the rms roughness of an APTMS-coated microresonator at 1.9 nm indicating the smoothness of the resonator surface. The roughness was increased in the case of the GSH-capped NPs from 4.2 to 5.8 for GSH-capped NPs with and without 48.26 nM (10 ppb) Pb(II), respectively. NPs attach to the APTMS resonator surface strongly and results are comparable to that of Liu *et al* [45]. Upon binding of Pb(II) at levels of 48.26 nM (10 ppb) or lower, minute or no agglomeration of the Au NP was observed as is shown in the AFM and SEM images in Figure 3.15 part (c).

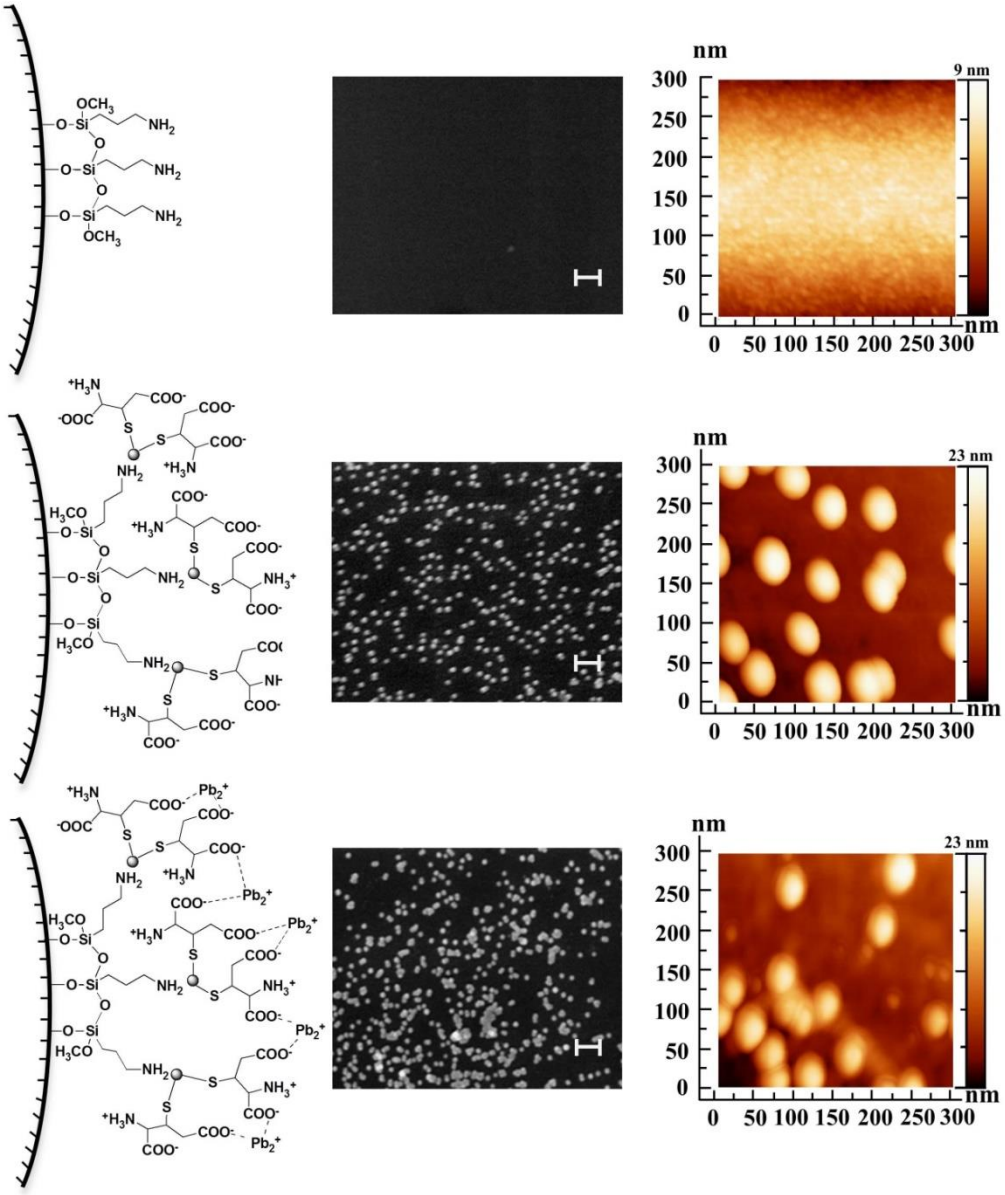


Figure 3.15 The chemical structure of the molecules used for surface functionalization (a) APTMS (b) APTMS coated with the GSH-Au NP complex and (c) GSH-Au NP's in the presence of Pb(II). Surface coverage was characterized using SEM (middle) and AFM (right). In these experiments, the resonators were soaked in a solution of GSH-Au NPs for 15 minutes followed by the addition of either 1 ppm (4.82 μM) and 10 ppb (48.26 nM) of Pb(II) respectively. The scale bars for SEM images are 200 nm. Reprinted with permission from [2].

The percentage coverages of GSH–Au NP coated with and without Pb(II) were 40% and 42% according to the result from AFM. At higher concentrations, minor aggregation was observed and was likely due to the rearrangement of the NPs on the resonator surface in the presence of Pb(II). Therefore, within the range of the WGM measurements, all shifts observed were likely due to the chelation of Pb(II), rather than induced aggregation of the modified Au NP complex. Furthermore, as Pb(II) has a high polarisability effect compared with other metals [46], this can enhance the wavelength shift. Beqa *et al*'s work [27] is one of the most intensive studies about GSH-mediated Au NP assembly. 12 GSH molecules bound per Au NP with a diameter of 10 nm was proposed by that work. Based on the same calculation, 30 molecules of GSH would bind per 16 nm NP. Assuming 1:1 binding between GSH ligand and Pb(II), as a result approximately 30 Pb(II) ions would bind per NP.

An unambiguous explanation of the binding chemistry between GSH-Au NPs and dimerization has been published by Stobiecka *et al* [47]. Several possible mechanisms were proposed for the assembly of n GSH-linked NPs where the number of Au NPs can be any number from 3 to 6. However, in our experiment the mechanism is likely to be dissimilar due to the NPs being immobilized on the surface of a resonator and no linking is expected according to AFM and SEM results.

3.3.5 WGM resonance shift measurements

Turning now to the experimental evidence on tracking Pb(II) with WGM sensor, Figure 3.16 displays the transmission spectrum from WGM sensor. Before coupling with the silanised, APTMS, resonator, the spectrum was shown to be saw tooth shape, which was selected from the function generator, Figure 3.16 part (a) and then several resonant wavelengths occurred after the waveguide coupled with the APTMS resonator, Figure 3.16 part (b). The best wavelength peak (sharpest and deepest) was selected as a representative for wavelength shift tracking; however, all resonant peaks were also recorded and can be analysed later.

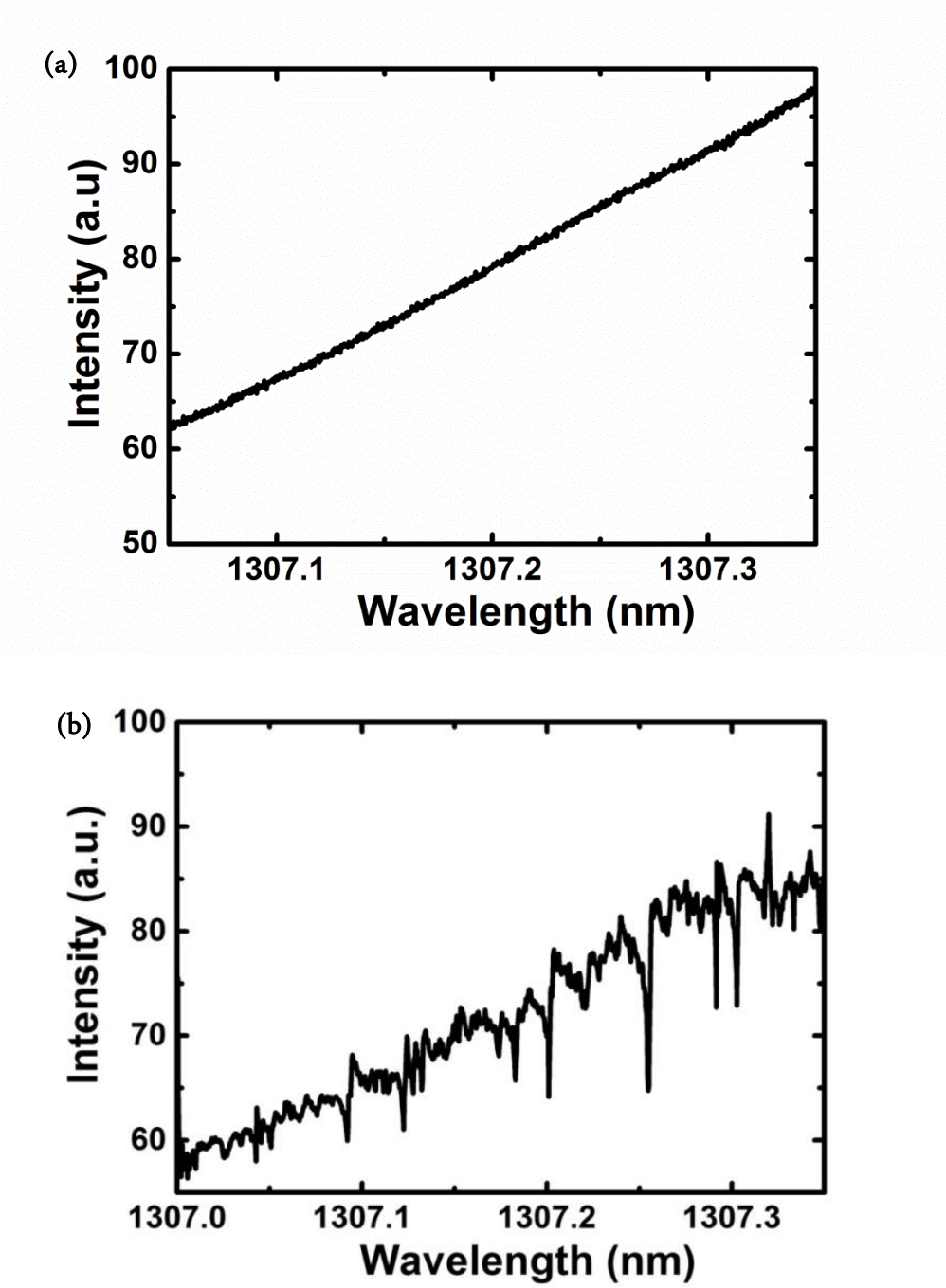


Figure 3.16 (a) Transmission spectrum before and (b) when coupled to a silanized microsphere resonator. Modified and reprinted with permission from [2].

3.3.6 Quantification of Pb(II) using WGM sensing

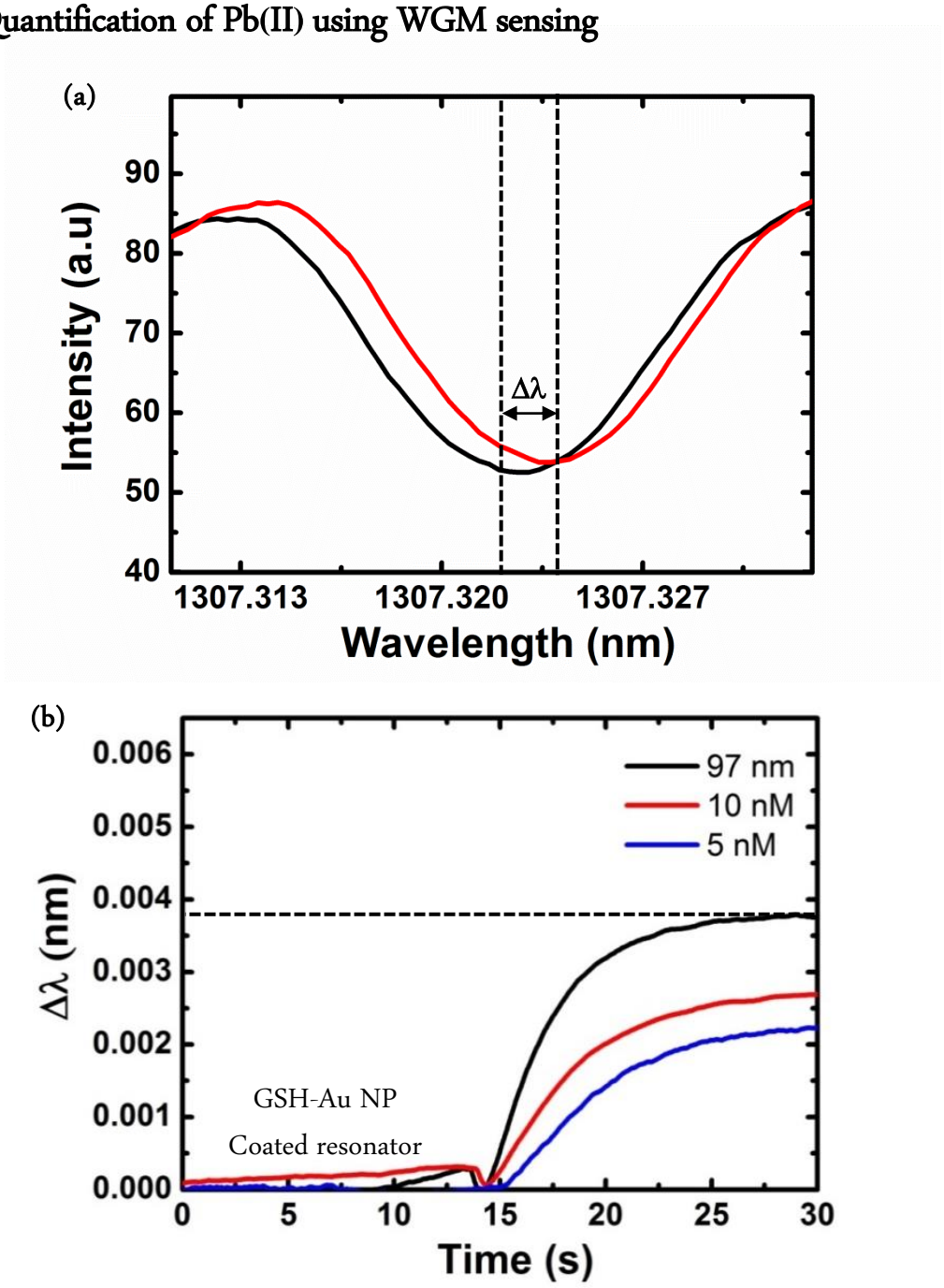


Figure 3.17 (a) Example wavelength shift due to the binding of Pb(II) at 2.40 nM. (b) time-dependent binding curves for 5, 10, and 97 nM Pb(II) (Modified and reprinted with permission from [2]).

After GSH-Au NP complexes bound with APTMS resonator (binding curve can be found in Figure 3.9 part (b) then Pb(II) can bind to the resonator surface via $-COO^-$ of the GSH complex which was immobilized on the surface of Au NP. The amount of Pb(II) is proportional to the wavelength shift. The more the wavelength shifts the higher the level of Pb(II) is. Based on this principle, the amount of Pb(II) can be easily quantified. Figure 3.18 part (a) demonstrates a nonlinear relationship in WGM signal at low concentration (less than 2.4 nM) and saturated at higher concentration upon addition of Pb(II). This trend was supported with Hanumegowda *et al.*'s work where Hg(II) was tracked by WGM sensor [48].

The reason behind this saturated trend was because all the receptors ($-COO^-$ groups) on the surface were occupied. The detection limit of the WGM sensor was found to be 0.05 nM (10 ppt), based on a threshold set at 3 times the standard deviation of the lowest concentration of Pb(II) as shown in Figure 3.20. Typical resonant shifts range between 1307.0 and 1307.3 nm can be monitored as a function of time as is shown in Figure 3.17 part (a). Therefore, a real-time binding curve was recorded at different concentration of Pb(II) Figure 3.17 part (b) which reveals not only the quantified data but also the rate constant of binding between GSH and Pb(II) at the same time. The normalized resonance shift was illustrated in Figure 3.18 parts (a) and (b) according to $(\Delta\lambda/\lambda)R$ where R is the radius of the resonator (μm), λ is the laser wavelength (1.307 μm), and $\Delta\lambda$ is the resonance shift before normalization. Interestingly, small changes in $\Delta\lambda$ indicate less than 10^{10} ions of Pb(II) bind to the resonator which highlights the sensitivity of this technique. This normalization was set out to compensate for differences between resonators with different radii. New calibration runs before every set is strongly recommended in order to take into account any potential effects associated with temperature fluctuations.

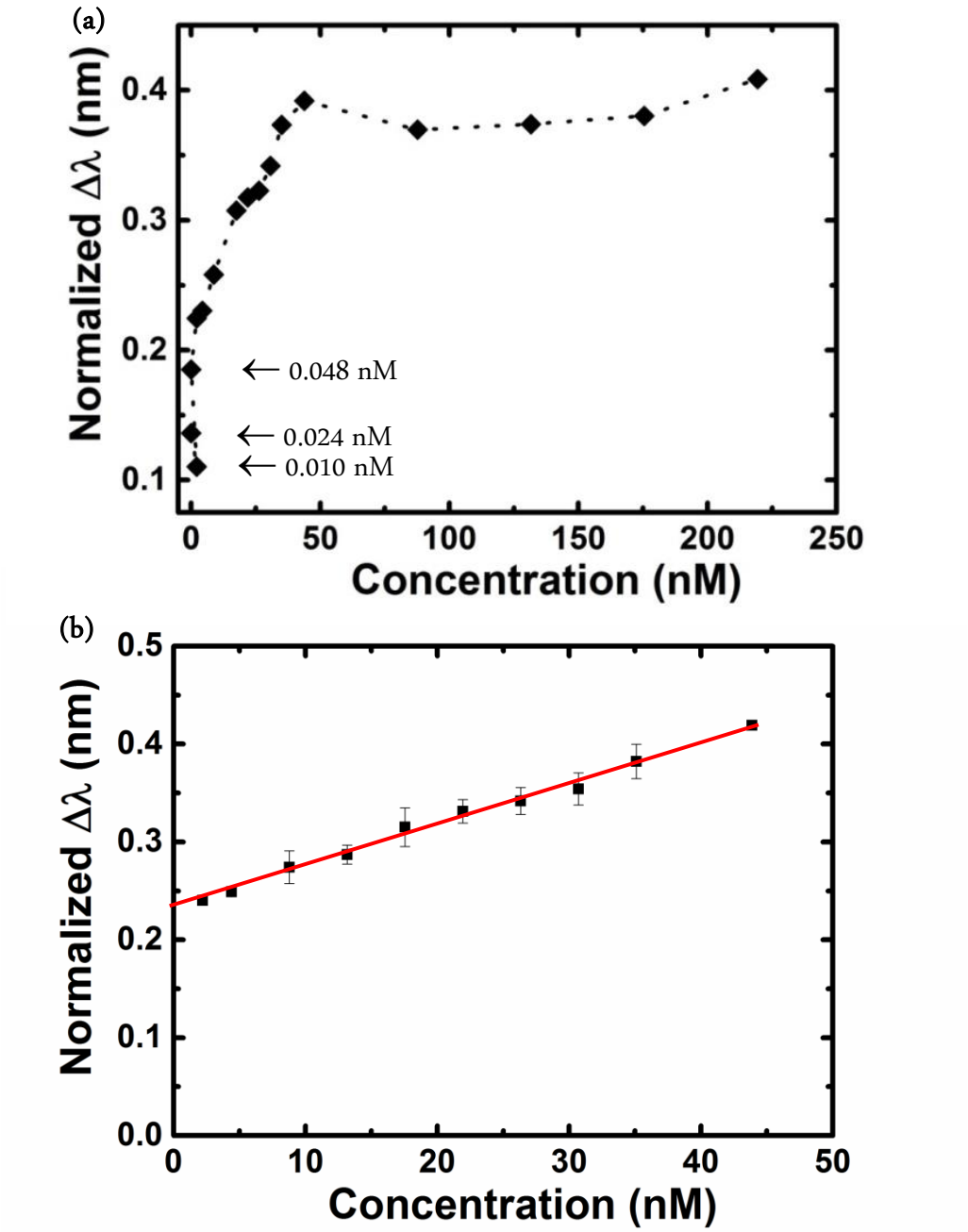


Figure 3.18 (a) Maximum normalized resonance wavelength shift is plotted as a function of Pb(II) concentration. (b) the dynamic range was determined to be between 2.40 and 48.26 nM with a detection limit of 0.05 nM. Modified and reprinted with permission from [2].

A linear range from our study was found to be between 2.40 and 48.26 nM with r^2 = 0.9973, Figure 3.18 part (b). WGM sensor also exhibits an excellent repeatability with only slight differences in standard deviations of the slope in the range of 0.004-0.019 from the calibration curve, according to the results from multiple repeat experiments.

Using our developed sensor, levels of Pb(II) were able to be sensed down to 0.05 nM (10 ppt). The result, as shown in Table 3.1, indicates that our sensor is able to track Pb(II) levels lower than the existing technique and also lower than a threshold set by IARC and EPA.

3.3.7 Kinetic study

WGM real-time binding curves can reveal not only the concentration of Pb(II) but also the rate of binding between GSH and Pb(II). This is one of many advantages of the WGM technique. The binding mechanism can be defined as follows in Equation 3.4.

$$mPb(II)+nC \underset{k_{-1}}{\overset{k_1}{\rightleftharpoons}} Pb_mC_n \tag{3.4}$$

k_1 and k_{-1} are the association and dissociation rate constants, respectively. The binding between Pb(II) and $-COO^-$ of GSH can be described by a mono exponential growth Equation or pseudo-first-order reaction as shown in Equation 3.5 [49, 50].

$$\Delta\lambda_t=\Delta\lambda_{max}(1-e^{-k_{obs}t}) \tag{3.5}$$

where $\Delta\lambda_t$ is the time-dependent resonance wavelength shift and $\Delta\lambda_{max}$ is the maximum resonance wavelength shift at the plateau.

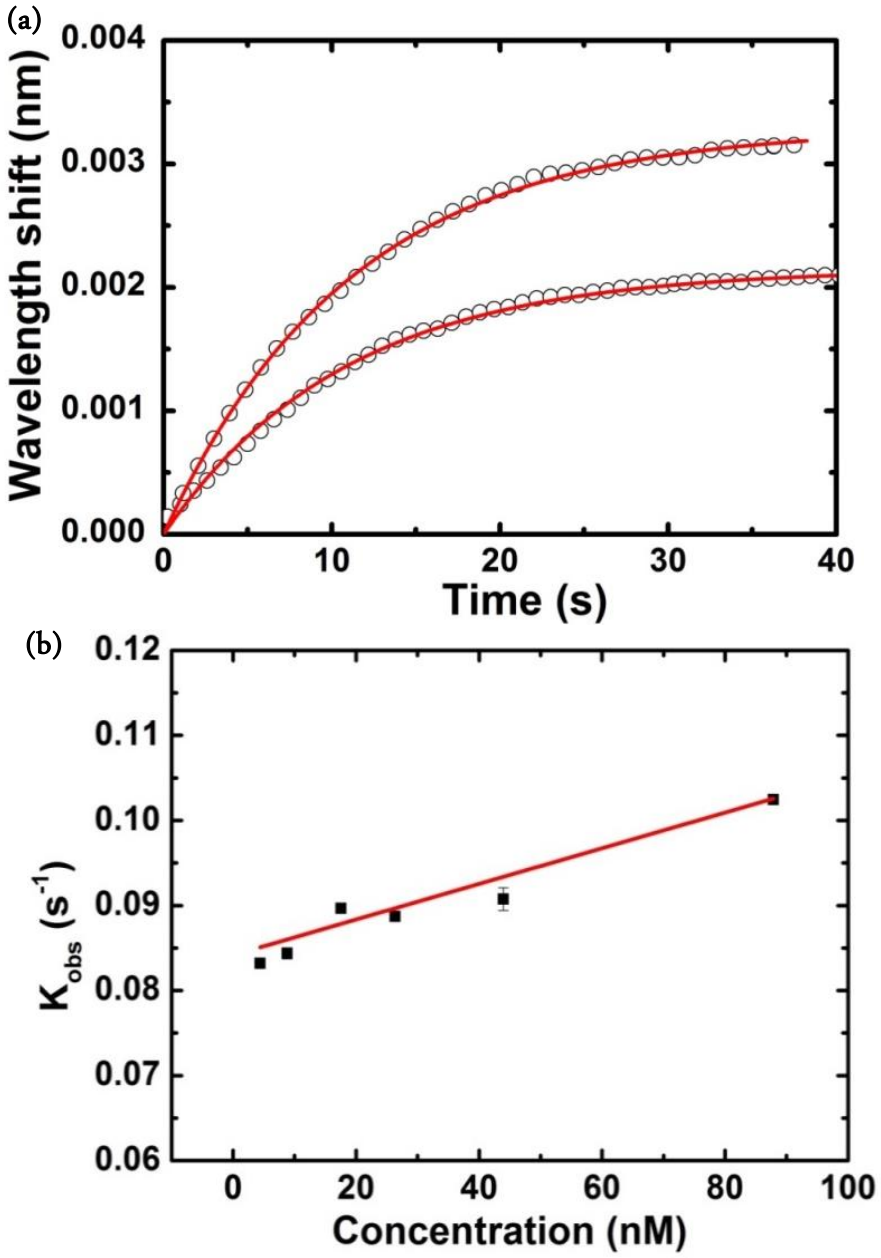


Figure 3.19 (a) Time dependent binding curves for 5 nM and 19 nM Pb(II). A non-linear least squares curve fitting using an exponential growth model is shown in red. (b) Observed rate constants as a function of Pb(II) concentration with a linear least squares fitting. The association rate constant (k_1) as calculated from the slope was determined to be 2.15×10^5 $M^{-1}s^{-1}$. Modified and reprinted with permission from [2].

The observed rate constant (k_{obs}) could then be estimated by fitting the curve using a non-linear least-square fitting. The association constant, k_1 was obtained from a linear relationship from Equation 3.6 plotted between k_{obs} as a function of Pb(II) concentration, Figure 3.19 part (b), whereby a slope equals to k_1 and y-intercept of k_{-1}.

$$k_{obs}=k_1[Pb(II)]+k_1 \quad (3.6)$$

The association rate constant was determined to be 2.15×10^5 $M^{-1}s^{-1}$. This finding is in good agreement with the value reported by Hatai *et al*'s work at 3.90×10^5 M^{-1} where Pb(II) bind to a similar synthetic ligand [49]. The result is also supported by the work which reported on Hg(II) binding to 2-mercaptopropyltrimethoxysilane [48]. Unfortunately, however, binding affinity of Pb(II) to GSH result has not previously been described up until now.

3.3.8 Noise and detection limit

The detection limit in this technique was calculated based on the value of three times the standard deviation of the level of lowest detectable signal as shown in Figure 3.20. Our current study found that the detection limits were well below the minimum recommended concentrations so no pre-concentration or other complex sample preparation is required. Consequently, samples can be collected directly from the field and assayed without any manipulation or if the concentration of Pb(II) is higher than the linear range the sample can be easily diluted with water. The baseline was also found to be highly stable. The histogram of the wavelength distribution from the baseline was shown in Figure 3.21.

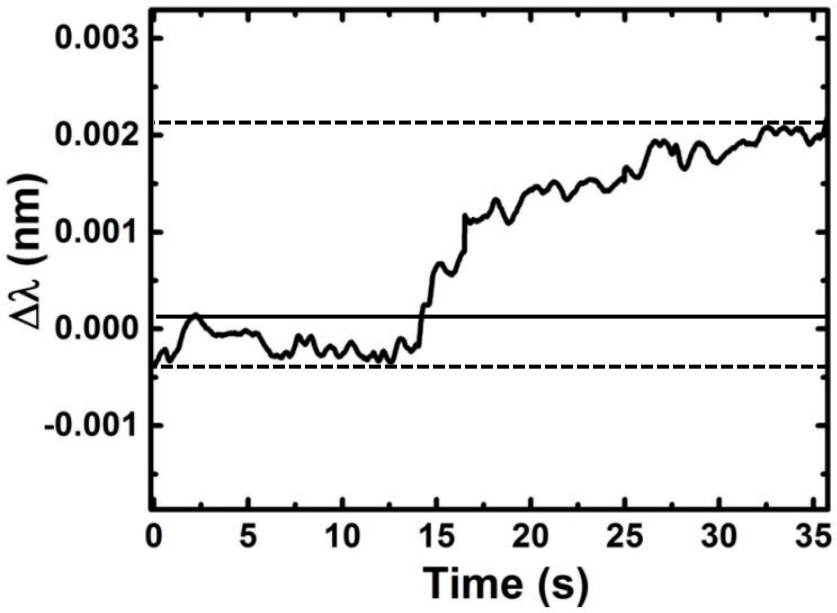


Figure 3.20 Signal to noise ratio from 0.05 nM Pb(II). It should be noted that above 48.26 μM a plateau is observed resulting from saturation of the binding sites on the surface of the resonator. Modified and reprinted with permission from [2].

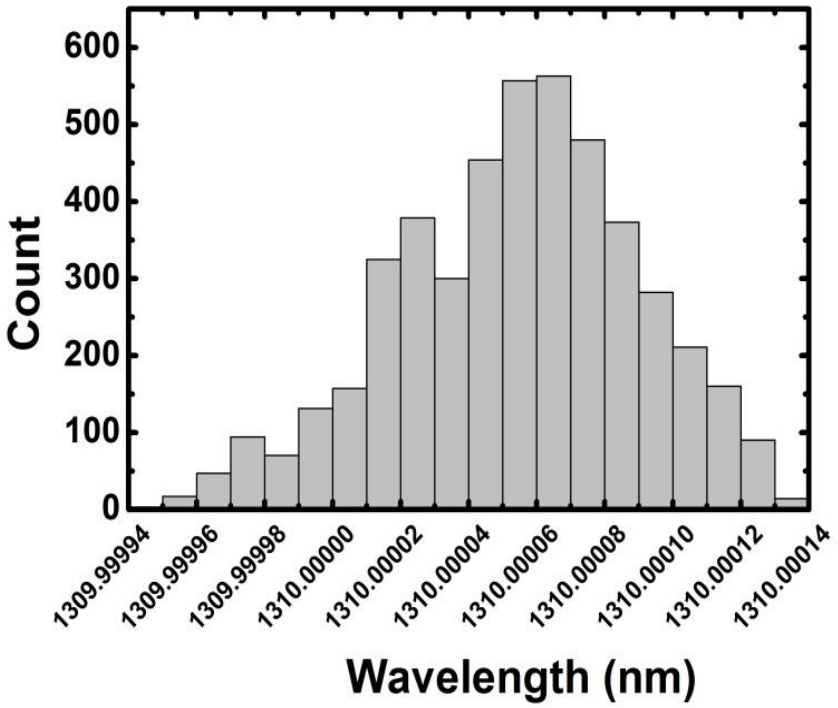


Figure 3.21 The stability of histogram of the wavelength distribution after a blank injection for 100s. Modified and reprinted with permission from [2].

3.3.9 Interference, sensitivity and selectivity study of the sensor

Various alkaline and heavy metals which are frequently present as contaminants in the environment were examined as interferants in order to assess the selectivity of the developed sensor. Many advantages from using the GSH-Au NPs as a colourimetric probe for Pb(II) was nicely described and published previously by Chai *et al* [25] and then Beqa *et al* modified the method with DLS detection [27].

For understanding this selectivity in more detail, we also investigated the change in absorbance spectra of GSH-Au NPs for the presence of various interference metals at 48.30 μM (10 ppm). The colour of the solution changes from red to blue indicating the formation of a complex between Pb(II) and GSH-AuNP. However, within a 24 hour observation period this colour change is found only in the presence of Pb(II), not in the presence of other metals, Figure 3.22 part (a). The reaction took at least five days to see differences in colour from the complexation of other heavy metals and the NPs, Figure 3.22 part (b). These results demonstrated that the GSH-Au NPs assay was selective to only Pb(II). An implication of this is the possibility that the kinetics between other heavy metals and the NPs are slower than Pb(II). The selectivity of WGM was also considered by comparing the resonance shifts upon the adding several heavy metals as shown in Figure 3.22. The wavelength shift was obviously found only when Pb(II) bound to the resonator, Figure 3.23 part (a). The signal from Pb(II) is higher than the signals from all interferents even though the concentration of Pb(II) is less than the other heavy metal by 10,000 and 1,000 times as shown in Figure 3.24. These findings suggest that the sensor is not only sensitive but also selective to Pb(II). One of the more significant findings to emerge from this study is that only Pb(II) showed an obvious wavelength shift and obvious binding curve while there were no noticeable binding curves for the other metal ions. Example of Hg(II) binding is shown in Figure 3.23 part (b).

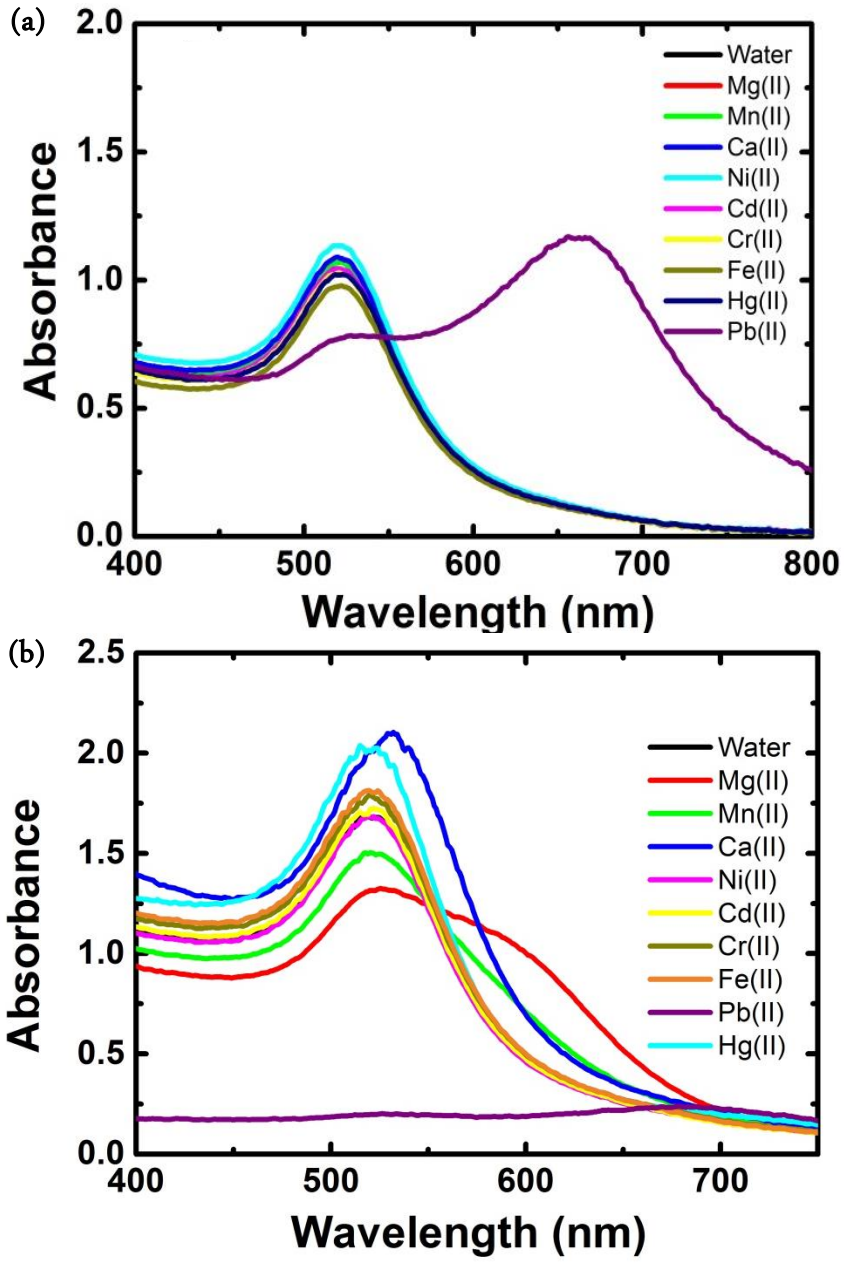


Figure 3.22 The UV-Visible spectra of GSH modified Au NP complex in the presence of different metals as interferants for (a) 1 day and (b) 5 days. All spectra were obtained at 48.26 μM of heavy metal. Modified and reprinted with permission from [2].

In the GSH-AuNP solution, a colour change and a red-to-blue wavelength shift can be easily observed due to aggregation of the Au NPs in the presence of high concentrations of Pb(II). There are two possible explanations for this bathochromic shift (red shift). Firstly, the specific binding of Pb(II) with the GSH-conjugated gold nanoparticles causes a refractive index

change. Secondly, the positive charge of Pb(II) brings the negative charge of Au NPs to be closer to each other resulting in the assembly of nanoparticles.

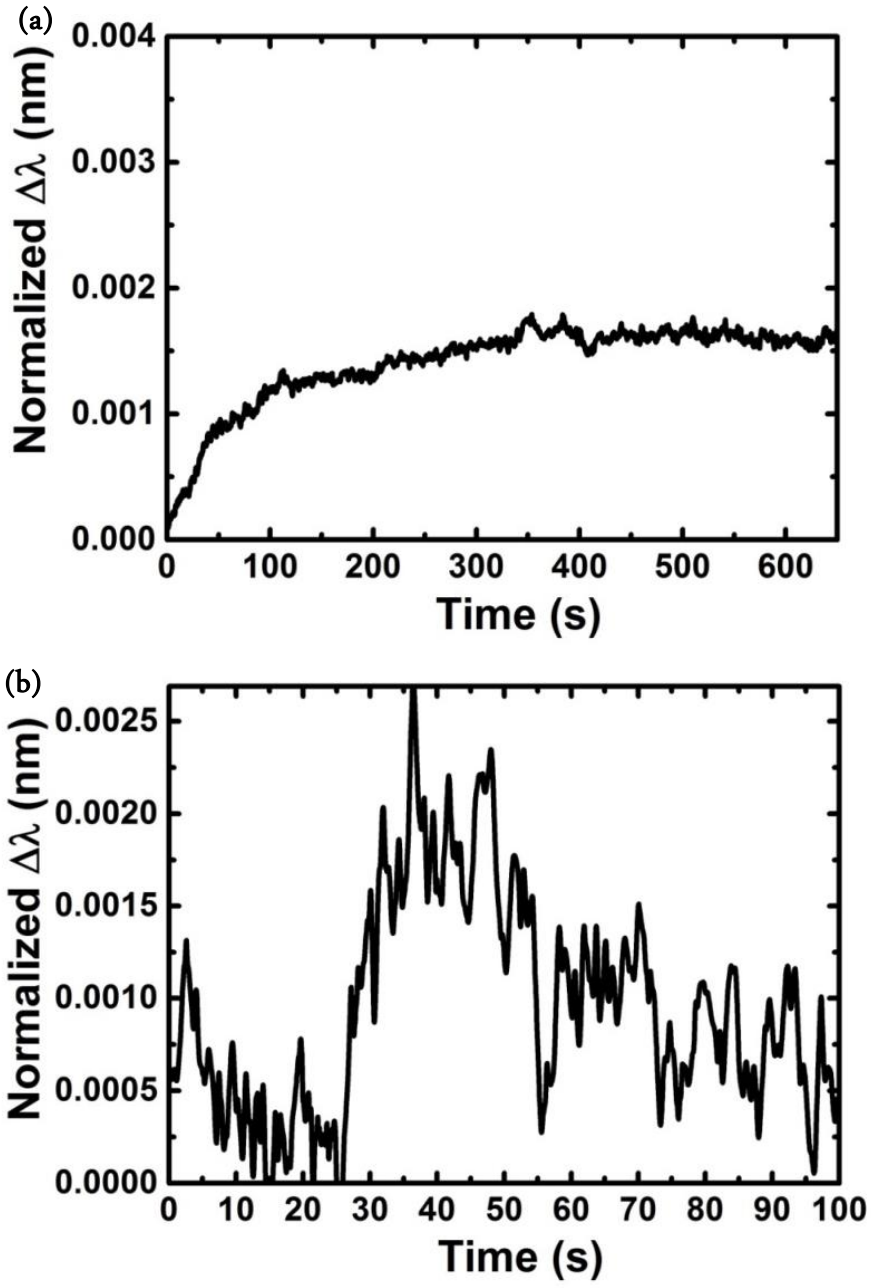


Figure 3.23 (a) The wavelength shift from 0.5 nM Pb(II) and (b) 48 nM Hg(II). Modified and reprinted with permission from [2].

In our WGM experiment, the second factor is not included and was proved by adding various concentrations of Pb(II) in the Au NPs solution. Only Pb(II) concentrations higher than 96.6 μM (20 ppm) displayed significant bathochromic shift of UV-Visible spectra. However, the

concentration of Pb(II) used in the WGM experiment was less than 4.83 nM (10 ppb) as a result the wavelength shifts should be only due to the complexation of Pb(II) with NPs and the aggregation of particles on the surface do not take place. This finding is in good agreement according to AFM and SEM results as was mentioned before.

Control experiments were performed on a bare APTMS-coated resonator at high concentration of Pb(II) ranging from 0.04 mM to 4.80 mM, Figure 3.25; however, there was no observable shift at concentration less than 0.04 mM. One possible explanation is that this is due to the electrostatic repulsion between the positive charge of the APTMS-terminated amine group and the positive charge of Pb(II). As a result Pb(II) cannot attach or bind onto the surface of the resonator. This can confirm that there are no artefact or non-specific binding between APTMS and Pb(II).

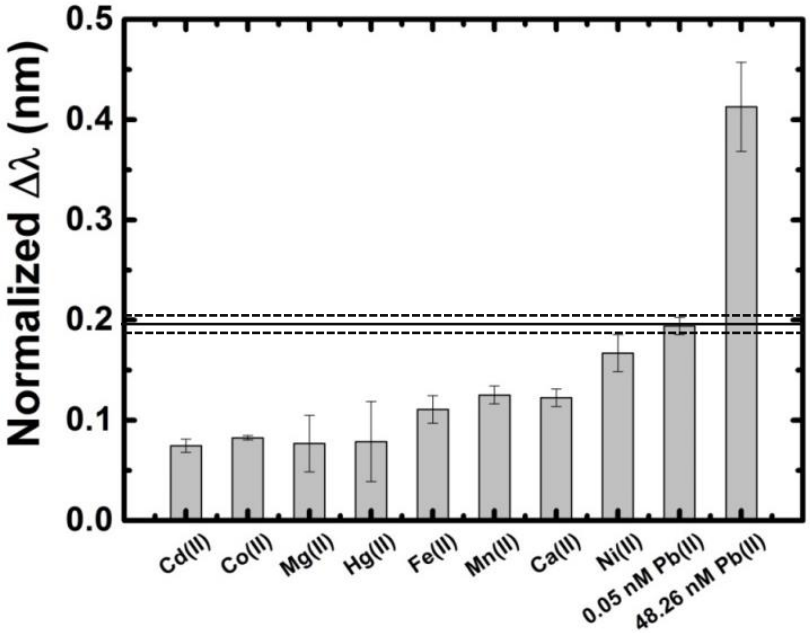


Figure 3.24 A comparison of maximum normalized resonance shift is shown for potential interferences at a concentration of 48.26 μM. For comparison, the signal from 0.05 and 48.26 nM Pb(II) is also shown. Modified and reprinted with permission from [2].

A normalized wavelength shift as a function of Pb(II) concentration was found to be linear, Figure 3.25 part (b); however, shifts could not be observed when the concentration of Pb(II) was less than 0.04 mM, so the limit of detection is worse than after functionalization with Au NPs. Although the linear relationship is excellent, in this mode the surface is non-specific to Pb(II) and nonspecific binding could easily be washed out using DI water.

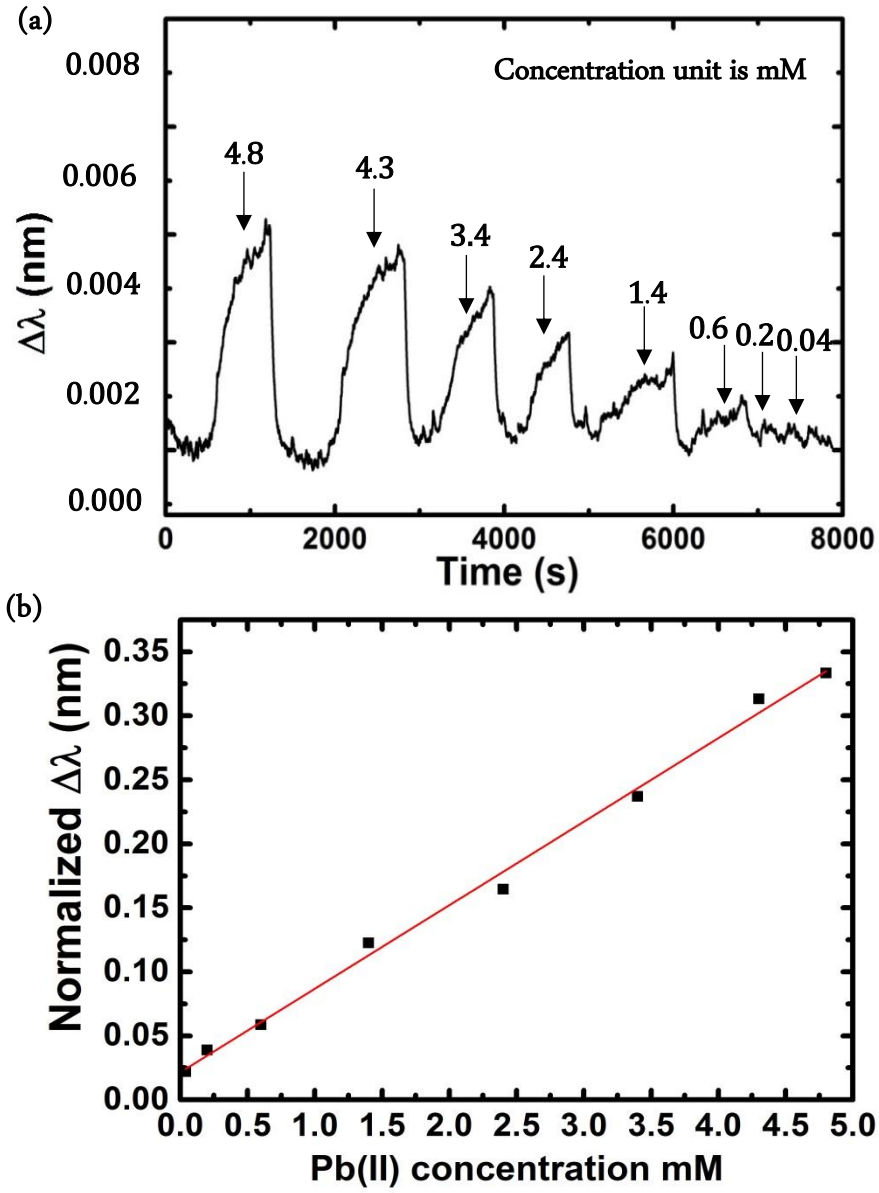


Figure 3.25 (a) Wavelength shifts due to the binding of Pb(II) from bare resonator. Shifts could not be observed when the concentration of Pb(II) was less than 0.04 mM. (b) normalized wavelength shift from a bare microresonator at concentrations of Pb(II) ranging from 0.04-4.8 mM. Modified and reprinted with permission from [2].

3.4 Conclusion

This study has demonstrated, for the first time, that a WGM sensor can be employed as a promising sensor in order to track a trace amount of Pb(II) with detection limit at 0.05 nM (10 ppt) which is considerably lower than the other detection limits reported previously. The most obvious finding emerging from this study is that the Pb(II) can be detected in real time with high sensitivity and selectivity against other commonly contaminating divalent ions including Fe(II), Hg(II), Mn(II), Cd(II), Mg(II), Ca(II), Co(II) and Ni(II). Furthermore, Pb(II) is detected speedily, accurately and highly selective. The reason behind the highly selective for the detection of Pb(II) ion is mainly due to several factors as follow (1) Pb(II) binds with carboxylate strongly was reported by Ik-Bum K. and co-workers [51]. (2) at pH lower than 9.0, only the carboxyl group of the glutamyl residue is available for the binding site so other ions with weak affinity to the carboxyl groups such as Ca(II), Ni(II), Zn(II) are not able to form the complex with GSH [52]. (3) NH_2 group is protonated to $-NH_3^+$ so as the binding ability of Fe(II), Zn(II), and Cd(II) are low [27]. (4) GSH links with Au NPs through –SH as a result the metals which can bind to –SH will not be an interference such as Cd(II) or Hg(II). (5) WGM is real time detection so the final explanation of the selectivity is because the aggregation rates of other ions which are comparatively slow compared to Pb(II) [25].

By integrating plasmonic nanoparticles to the surface of a microsphere, the sensor sensitivity can be enhanced by several orders of magnitude due to a change in an effective refractive index at the resonator surface. The detection limit of the sensor reaches a limit below the level set by IARC or WHO. As a result complicated sample preparation is not necessary, only dilution and filtration are required.

The sensor set-up is easy to operate and can be used by non-experienced researchers. The sensor does not incorporate any costly consumables. In addition, both quantitative information and kinetic information can be acquired in one signal in real time.

3.5 Outlook and future work

In this chapter we demonstrated sensitive detection of Pb(II) ions using a microsphere optical resonator coupled with glutathione-modified gold nanoparticles. The results demonstrate impressive sensitivity and specificity, with low baseline noise. The selective Pb(II) WGM sensor incorporating GSH-Au NPs reaches a detection limit below IARC levels. This suggests that the sensor could be used to detect Pb(II) easily without pre-concentration or complicated sample preparation. Moreover, the sensor has the potential to be developed as a portable device for in-field applications. However, thermal fluctuations are a major concern; these can affect noise associated with the reproducible coupling of light via a tapered fibre. Outside the laboratory, the temperature of the environment might be varied; as a result a temperature controller for the sensor may be required.

3.6 References

1. Gilkey, D. *Lead Poisoning Nightmare In Nigeria May Be Easing*. 2014 [cited 2015 31/01/2015]; Available from: http://www.npr.org/sections/health-shots/2014/04/21/303766353/lead-poisoning-nightmare-in-nigeria-may-be-easing.
2. Panich, S., Wilson, K. A., Nuttall, P., Wood, C. K., Albrecht, T. and Edel, J. B., Label-Free Pb(II) Whispering Gallery Mode Sensing Using Self-Assembled Glutathione-Modified Gold Nanoparticles on an Optical Microcavity. Analytical Chemistry, 2014. 86(13): p. 6299-6306.
3. Steenland, K. and Boffetta, P., *Lead and cancer in humans: Where are we now?* American Journal of Industrial Medicine, 2000. 38(3): p. 295-299.
4. Lanphear, B. P., R Hornung, R., Khoury, J., Yolton, K., Baghurst, P., Bellinger, D. C., Canfield, R. L., Dietrich, K. N., Bornschein, R., Greene, T., Rothenberg, S. J., Needleman, H. L., Schnaas, L., Wasserman, G., Graziano, J. and Roberts. R., *Low-Level Environmental Lead Exposure and Children's Intellectual Function: An International Pooled Analysis.* Environmental Health Perspectives, 2005. 113(7): p. 894-899.
5. Lidsky, T. I. and Schneider, J. S., Lead neurotoxicity in children: basic mechanisms and clinical correlates. Brain, 2003. 126(1): p. 5-19.
6. Shah, F., Soylak, M., Kazi, T. G., and Afridib, H. I., Preconcentration of lead from aqueous solution with activated carbon cloth prior to analysis by flame atomic absorption spectrometry: a multivariate study. Journal of Analytical Atomic absorption spectrometry, 2013. 28(4): p. 601-605.

7. Najafi, N. M., Eidizadeh, M., Seidi, S., Ghasemi, E. and Alizadeh, R., Developing electrodeposition techniques for preconcentration of ultra-traces of Ni, Cr and Pb prior to arc-atomic emission spectrometry determination. Microchemical Journal, 2009. 93(2): p. 159-163.
8. Dalman, O., Demirak, A. and Balc, A., Determination of heavy metals (Cd, Pb) and trace elements (Cu, Zn) in sediments and fish of the Southeastern Aegean Sea Turkey by atomic absorption spectrometry. Food Chemistry, 2006. 95(1): p. 157-162.
9. Bakircioglua, Y., Segadeb, S. R., Yourdc, E. R. and Tysonc, J. F., Evaluation of Pb-Spec® for flow-injection solid-phase extraction preconcentration for the determination of trace lead in water and wine by flame atomic absorption spectrometry. Analytica Chimica Acta, 2003. 485(1): p. 9-18.
10. Myohanena, T., Mantylahtib, V., Koivunenb, K. and Matilainenc, R., Simultaneous determination of As, Cd, Cr and Pb in aqua regia digests of soils and sediments using electrothermal atomic absorption spectrometry and fast furnace programs. Spectrochimica Acta Part B: Atomic Spectroscopy, 2002. 57(11): p. 1681-1688.
11. Zhao, Z., Zhang, P. and Li, F., *FAAS determination of Fe, Pb, Zn and Ni impurities in copper sulfate.* Guangpu Shiyanshi, 1995. 12(3): p. 56-60.
12. Gottelt, U., Henrion, G. and Stoyke, M., Simultaneous determination of the toxicologically relevant elements: lead, cadmium, and nickel with graphite furnace atomic absorption spectrometry. Nahrung, 1996. 40(2): p. 87-92.
13. Chen, Z. and He, H., Determination of trace copper, zinc, cadmium and lead in environmental water by extraction preconcentration FAAS. Guangdong Weiliang Yuansu Kexue, 1995. 2(4): p. 18-20.
14. Purdue, L. J., Enrione, R. E., Thompson, R. J. and Bonfield, B.A., *Determination of organic and total lead in the atmosphere by atomic absorption spectrometry.* Analytical Chemistry, 1973. 45(3): p. 527-530.
15. Zeeman, P. B. and Butler, L. R. P., *The Determination of Lead, Copper and Zinc In Wines by Atomic Absorption Spectroscopy.* Journal of Applied Spectroscopy, 1962. 16(4): p. 120-124.
16. Bakırdere, S., Yaroglu, T., Tırık, N., Demiroz, M., Fidan, A. K., Maruldalı,O. and Karaca, A., Determination of As, Cd, and Pb in tap water and bottled water samples by using optimized GFAAS system with Pd-Mg and Ni as matrix modifiers. Spectroscopy, 2013: (824817) p.1-7
17. Zhu, W. Y., Liu, X. T., Xue, Q. H. and Shan, B. T., *Simultaneous determination of Pb, Cr, Se and Co in paints by XRF spectrometry.* Fenxi Shiyanshi, 2009. 28(9): p. 95-98.

18. Wu, H., Liang, J. and Han, H., A novel method for the determination of Pb^{2+} based on the quenching of the fluorescence of CdTe quantum dots. Microchimica Acta, 2008. 161(1-2): p. 81-86.
19. Singh, K. P., Devender, S., Sapana, G., Sonia, V. and Ishwar, S., Tris[2,4,6-(2-hydroxy-4-sulpho-1-naphthylazo)]-s-triazine, trisodium salt as a spectrophotometric reagent for micro-determination of lead (II) in alloys, environmental and biological samples. Research Journal of Chemistry and Environment, 2013. 17(3): p. 53-58.
20. Yaman, M. and Erel, E., Combining preconcentration methods for the determination of lead and nickel in ambient air by FAAS. Atomic Spectroscopy, 2012. 33(6): p. 212-217.
21. Liu, J. and Lu, Y., *A Colorimetric Lead Biosensor Using DNAzyme-Directed Assembly of Gold Nanoparticles.* Journal of the American Chemical Society, 2003. 125: p. 6642-6643.
22. Huang, K. W., Yu, C. J. and Tseng, W. L., Sensitivity enhancement in the colorimetric detection of lead(II) ion using gallic acid-capped gold nanoparticles: Improving size distribution and minimizing interparticle repulsion. Biosensors and Bioelectronics, 2010. 25(5): p. 984-989.
23. Mehta, V., Solanki, J. and Kailasa, S., Selective visual detection of Pb(II) ion via gold nanoparticles coated with a dithiocarbamate-modified 4'-aminobenzo-18-crown-6. Microchimica Acta, 2014. 181(15-16): p. 1905-1915.
24. Wu, Y. S., Huang, F. F. and Lin, Y. W., Fluorescent Detection of Lead in Environmental Water and Urine Samples Using Enzyme Mimics of Catechin-Synthesized Au Nanoparticles. ACS Applied Materials & Interfaces, 2013. 5(4): p. 1503-1509.
25. Chai, F., Wang, C., Wang, T., Li, L. and Su, Z., *Colorimetric Detection of Pb^{2+} Using Glutathione Functionalized Gold Nanoparticles.* ACS Applied Materials & Interfaces, 2010. 2(5): p. 1466-1470.
26. Ali, E. M., Zheng, Y., Yu H. H. and Ying, J. Y., *Ultrasensitive Pb^{2+} Detection by Glutathione-Capped Quantum Dots.* Analytical Chemistry, 2007. 79(24): p. 9452-9458.
27. Beqa, L., Singh A. K., Khan, S. A., Senapati, D., Arumugam, S. R. and Ray, P. C., Gold nanoparticle-based simple colorimetric and ultrasensitive dynamic light scattering assay for the selective detection of Pb(II) from paints, plastics, and water samples. ACS Applied Materials & Interfaces, 2011. 3: p. 668-673.
28. Luchansky, M. S. and Bailey, R. C., *High-Q Optical Sensors for Chemical and Biological Analysis.* Analytical Chemistry, 2011. 84(2): p. 793-821.
29. Mourzinaa, Y., Schoningb, M. J., Schubertb, J., Zanderb, W., Legina, A. V., Vlasova, Y. G., Kordosb, P. and Luthb, H., *A new thin-film Pb microsensor based on chalcogenide glasses.* Sensors and Actuators B: Chemical, 2000. B71(1-2): p. 13-18.

30. Chaikin, Y., Kedem,O., Raz, J., Vaskevich, A. and Rubinstein, I., *Stabilization of Metal Nanoparticle Films on Glass Surfaces Using Ultrathin Silica Coating.* Analytical Chemistry, 2013. 85(21): p. 10022-10027.
31. Vollmer, F., Arnold, S. and Keng, D., *Single virus detection from the reactive shift of a whispering-gallery mode.* Proceedings of the National Academy of Sciences U.S.A., 2008. 105: p. 20701-20704.
32. Haiss, W., Thanh, N. T. K., Aveyard, J., and Fernig, D. G., *Determination of Size and Concentration of Gold Nanoparticles from UV−Vis Spectra.* Analytical Chemistry, 2007. 79(11): p. 4215-4221.
33. Liu, X., Atwater, M., Wang, J. and Huo, Q., *Extinction coefficient of gold nanoparticles with different sizes and different capping ligands.* Colloids and Surfaces B: Biointerfaces, 2007. 58(1): p. 3-7.
34. Bootz, A., Vogel, V., Schubert, D. and Kreuter, J., Comparison of scanning electron microscopy, dynamic light scattering and analytical ultracentrifugation for the sizing of poly(butyl cyanoacrylate) nanoparticles. European Journal of Pharmaceutics and Biopharmaceutics, 2004. 57(2): p. 369-375.
35. Sharma, B., Singh, S. and Siddiqi, N. J., *Biomedical Implications of Heavy Metals Induced Imbalances in Redox Systems.* Journal of Biomedicine and Biotechnology, 2014: p. 640754.
36. Sears, M. E., Chelation*:* Harnessing and Enhancing Heavy Metal Detoxification; A Review*.* The Scientific World Journal, 2013: p. 13.
37. Mah, V. and Jalilehvand, F., *Lead(II) Complex Formation with Glutathione.* Inorganic Chemistry, 2012. 51(11): p. 6285-6298.
38. Lagadic, I. L., Mitchell, M. K. and Payne, B. D., *Highly Effective Adsorption of Heavy Metal Ions by a Thiol-Functionalized Magnesium Phyllosilicate Clay.* Environmental Science & Technology, 2001. 35(5): p. 984-990.
39. Kim, I. B., Dunkhorst, A., Gilbert, J. and Bunz, U. H. F., *Sensing of Lead Ions by a Carboxylate-Substituted PPE: Multivalency Effects*. Macromolecules, 2005. 38(11): p. 4560-4562.
40. Allen, C. L., Chatwal, A. R. and Williams, J. M. J., *Direct amide formation from unactivated carboxylic acids and amines.* Chemical Communications, 2012. 48(5): p. 666-668.
41. Chiasera, A., Dumeige, Y., Feron, P., Ferrari, M., Jestin, Y., Nunzi C. G., Pelli, S., Soria, S. and Righini, G. C.,*Spherical whispering-gallery-mode microresonators.* Laser & Photonics Reviews, 2010. 4(3): p. 457-482.

42. He, L., Ozdemir, S. K. and Yang, L., *Whispering gallery microcavity lasers.* Laser & Photonics Reviews, 2013. 7(1): p. 60-82.
43. Shopova, S. I., Rajmangal, R., Holler, S. and Arnold, S., *Plasmonic enhancement of a whispering-gallery-mode biosensor for single nanoparticle detection.* Applied Physics Letters, 2011. 98(24): p. 243104.
44. Horcas, I. R. F., Gomez-Rodriguez, J. M., Colchero, J., Gomez-Herrero, J. and Baro, A. M., *A software for scanning probe microscopy and a tool for nanotechnology*. Review of Scientific Instruments, 2007. 78(1): p. 13705-13708.
45. Liua, F. K., Changb, Y. C., Koa, F. H., Chub, T. C. and Daia, B. T., *Rapid fabrication of high quality self-assembled nanometer gold particles by spin coating method.* Microelectronic Engineering, 2003. 67–68(0): p. 702-709.
46. Evans, B. J. and Peacor, D. R., Thermal expansion in $(La_{0.62}Pb_{0.38})MnO_3$*:* Possible evidence for a coupling between elastic and magnetic exchange forces. Journal of Solid State Chemistry, 1973. 7(1): p. 36-39.
47. Stobiecka, M., Coopersmith, K. and Hepel, M., Resonance elastic light scattering (RELS) spectroscopy of fast non-Langmuirian ligand-exchange in glutathione-induced gold nanoparticle assembly. Journal of Colloid and Interface Science, 2010. 350(1): p. 168-177.
48. Hanumegowda, N. M., White, I. M. and Fan, X., *Aqueous mercuric ion detection with microsphere optical ring resonator sensors.* Sensors and Actuators B: Chemical, 2006. 120(1): p. 207-212.
49. Hatai, J., Pal, S., Jose, G. P., Sengupta, T. and Bandyopadhyay, S., A single molecule multi analyte chemosensor differentiates among Zn^{2+}, Pb^{2+} and Hg^{2+}*:* modulation of selectivity by tuning of solvents. RSC Advances, 2012. 2(18): p. 7033-7036.
50. Goodrich, J. A. and Kugel, J. F., *Binding and Kinetics for Molecular Biologists*. 2007: Cold Spring Harbor Laboratory Press.
51. Ik-Bum, K., Anna, D., Gilbert, J. and Uwe H. F. B., *Sensing of Lead Ions by a Carboxylate-Substituted PPE: Multivalency Effects.* Macromolecules, 2005. 38(11): p. 4560-4562.
52. Rao, F., Jun, L. and Yanf. W., *Aggregation of glutathione-functionalized Au nanoparticles induced by Ni^{2+} ions*. Journal of Nanoparticle Research, 2012. p. 929-936.

Chapter 4 |Optical-Resonator-Based Biosensing: G-quadruplex (G4) structure and ligand study



London art trail: 'What's in your DNA?'

DNA sculpture displayed in front of the Royal Albert Hall, designed by Guy Potelli. Twenty one DNA sculptures appeared across London as part of Cancer Research UK's campaign with the aim of raising awareness and funds for a biomedical research centre [1]. The sculpture shows the DNA double helix discovered in 1953, which is one of the most significant discoveries in DNA research.

Many advantages are offered by utilising the WGM technique as a chemical sensor for Pb(II) detection, which have been already discussed in Chapter 3. In this chapter, other advantages will be illustrated to show that this is not only a chemical sensor but a biological sensor that can also be integrated and developed to solve the problems in DNA research such as lack of real time analysis, large amounts of DNA sample required and difficulties of tracking kinetic parameters. In this chapter, WGM was applied with a view to studying G-quadruplex (G4) function and their interaction with ligands. Moreover, some problems and challenges from the work will also be discussed. Some parts from this work were published in ACS sensors [2] and was re-printed with permission from ACS publications.

4.1 Introduction

4.1.1 Background and introduction to G-quadruplexes

DNA plays a vital role in drug development and drug discovery. There has been an enormous and rapid development of drug candidates that target specific DNA sequences in the past decade, especially in the pharmaceutical field [3, 4]. One of the most significant current studies aims to discover and design small molecules to bind with target nucleic acid structures and/or sequences of interest with both extraordinary affinity and specificity. Because of their potential as effective anticancer and antitumor chemotherapeutic agents, this type of small ligand might be a key to open a door for drug development in various diseases [5]. In general, methodologies are widely focused on targeting DNA, which normally forms in cells as a double helix [6, 7]. However, there have been a number of studies involving targeting alternative secondary structures to regulate specific biological processes. In fact, many structures can be adopted by nucleic acids, among them G-quadruplexes or G4, which are secondary structures formed from four guanines in a planar arrangement. These have received much attention due to their high prevalence in the human genome and have been recently found to form in living human cells i.e. c-myc, c-kit, k-ras [8-10]. Various severe conditions such as cancer, fragile X syndrome, Bloom syndrome and Werner syndrome have been connected to genomic defects that involve G-quadruplex forming sequences. Therefore, small molecules with an ability to bind and stabilize DNA, especially in its G-quadruplex form, thus possessing therapeutic potential, have been paid much consideration [2, 11-13].

4.1.2 Human Telomeric G-Quadruplexes

Telomeres are a region of repetitive nucleotide sequence at each end of a chromosome. A repetitive DNA sequence of d(TTAGGG) has been found to be present at the telomeres of human chromosomes [14]. Normally, telomeres are shortened because of cell replications. A ribonucleoprotein enzyme complex called telomerase preserves telomere length in 85% of cancer cells. In addition, the telomeric DNA is prevented from being extended because its 3' end can be sequestered by G-quadruplex. Equally importantly, telomeric DNAs can also fold into compact G-quadruplex structures [15] which is considered to have importance in the control of expression of certain genes involved in carcinogenesis i.e. c-myc, c-kit, k-ras, etc [16]. To sum up, the beneficial roles of G-quadruplexes include telomere capping and regulation of transcription; whereas the formation can also be harmful to some processes such as the progression of the replication fork (where the replication of DNA will actually take place) [17]. Figure 4.1 (a) shows that one possible role of G-quadruplexes in transcription is the inhibition of the transcription. Conversely, the transcription can also be enhanced by the formation of a stable G-quadruplex in the complementary strand part (b) or the protein binding part (c). Finally in part (d), transcription can be directly repressed via G-quadruplex binding with protein (green) or by binding with other proteins (blue).

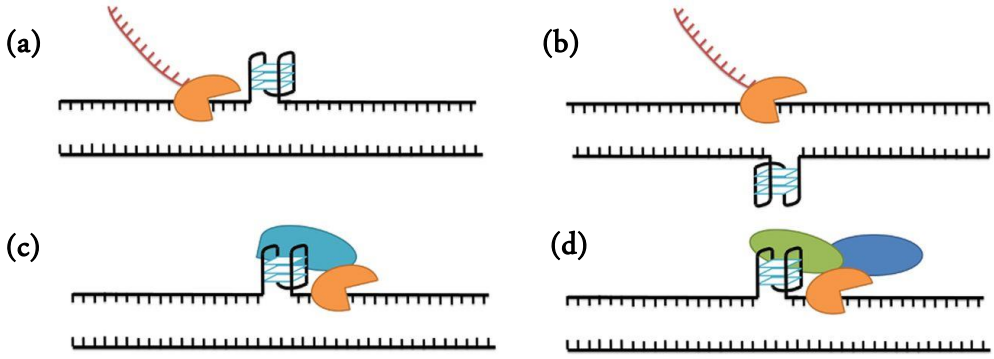


Figure 4.1 Transcription by RNA polymerase (orange). (a) blocking transcription (b) facilitating transcription (c) stimulating transcription (d) repressing transcription. The picture is reprinted with permission from [17].

4.1.3 Folding and topology of quadruplexes

The well-known anti-parallel double helical structure for DNA was proposed by Watson and Crick in 1953. The two antiparallel strands are held together by hydrogen bonds. In general, each nucleotide unit consists of three important building blocks-bases, sugars and phosphate groups. However, the bases are the key information component. Briefly, Adenine (A) interacts with Thymine (T) using two hydrogen bonds whereas Guanine (G) holds Cytosine (C) with three hydrogen bonds. For G-quadruplexes, four G repeats are required for the self-association

formation of a quadruplex. The π-π stacking of G-tetrads leads to the formation of four grooves with walls bounded by the sugar-phosphate backbone. The formation of G-rich sequence can have two forms: either intermolecular (tetramer or dimer) G4; or intramolecular G4. Based on strand orientation, the intramolecular G-quadruplex can be simply classified into three types which are parallel, antiparallel, and hybrid type [18] as shown in Figure 4.2.

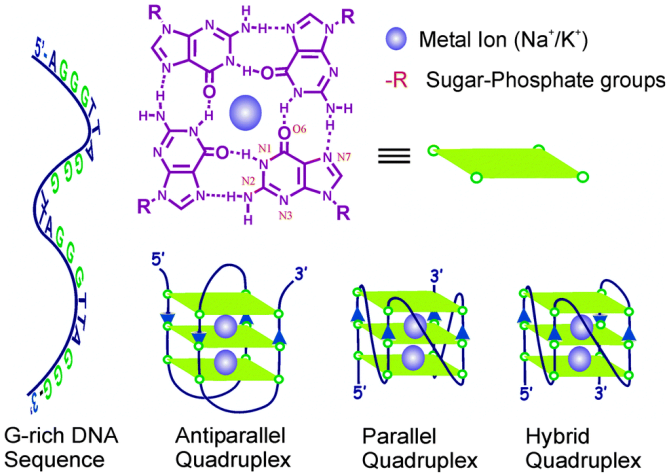


Figure 4.2 Structures of the G-quartet/tetrad and the various common folding topologies found in G-quadruplexes. The picture is reprinted with permission from [19]

In duplex DNA structures, base stacking, hydrogen bonding, hydration structure and electrostatic interaction are stabilizing factors. In contrast, for G-quadruplexes, the negatively charged cavities located between the G-tetrads need to be stabilized by the coordination of cations such as K^+ or Na^+. However, K^+ is more relevant as this mono cation is present in the cell at higher concentrations than Na^+. The stabilizing cations are required in order to coordinate with the electronegative O atom in the centre channel of G-tetrads. As a result, the formation of a G-quadruplex requires the coordination cations [20]. The coordination cation is commonly K^+ or Na^+. However, there are also other mono cations that can stabilize G-tetrads such as Rb^+, Cs^+ or NH_4^+ [21]. Not only monovalent but also divalent ions have been reported as G-quadruplex stabilizers such as Sr^{2+}, Ba^{2+} and Pb^{2+}. Conversely, it has been reported that both Ca^{2+} and Mg^{2+} cannot stabilize or promote the formation of G-quadruplexes [22-24].

4.1.4 Characterization of G-quadruplex structure

The first characterization of the G-tetrad structure was in a gel [25]. Up until now there have been many experimental methods used in the quadruplex characterization process. UV melting experiments are a rapid and simple method, with the DNA melting curve being monitored from a hyperchromic shift [22]. In terms of G-quadruplex topology, a parallel and an antiparallel orientation can be discriminated from different positive and negative peaks in Circular Dichroism, CD. A positive band at 260 nm is used to indicate the parallel form while a

negative band at 260 nm and a positive band at 295 nm are indicative of an antiparallel conformation [22].

4.1.5 Methods for investigating G-quadruplex DNA/ligand interaction

There are a large number of small molecule ligands that have a specificity for G-quadruplexes, with many of them causing telomere dysfunction and inhibiting telomerase activity in vitro [15]. It is well known that the formation of G-quadruplex structures has crucial consequences at the cellular level by (1) controlling the expression of carcinogenesis genes and (2) perturbation and inhibition of the telomere extension. Therefore, G-quadruplexes are a target for drug design by developing small molecules (ligands) to target this structure specifically, with the ability to interact only with quadruplex DNA, not duplex-DNA. In recent years, several basic experimental methods and new technological advances have been developed to monitor and/or characterise interactions between oligonucleotides and small molecules. There are various reviews that summarise methods for investigating G-quadruplex DNA/ligand interaction. For example in the book, "Quadruplex Nucleic Acids" by S. Neidle and S. Balasubramanian several methods were described [22]. Other excellent reviews were written by J. Jaumot and R. Gargallo [26] and P. Murat and co-workers [16]. As this work is focused on developing a novel method to investigate G-quadruplex DNA/ligand interactions, only some pre-existing techniques will be reviewed briefly.

4.1.5.1. UV-visible spectroscopy

Generally, ligands that have the ability to interact with G-quadruplexes have chromophores in their structures, so monitoring the interaction of such structures with G-quadruplexes can be easily conducted by observing the shifting from the maximum absorbance when the ligand is complexed with the DNA. In addition, experiments involving titration of DNA with the ligand are possible.

1. Absorbance measurement

UV-Visible spectroscopy is the simplest and most commonly employed method, and can provide information such as binding stoichiometry [27] and binding constants [28]. The method is rapid and non-destructive to the sample - however, these assays often require high amounts of DNA, high ligand concentrations, do not allow easy access to thermodynamic and kinetic parameters, and importantly, have low intensity signals.

2. Melting point measurement

An alternative strategy involves DNA melting techniques where DNA folding/unfolding is typically monitored by UV-visible spectroscopy. In this case, the stabilization or destabilization of the DNA by the ligand was observed from the thermal melting curve, comparing between the absence and presence of a ligand by increasing the melting temperature [29]. This strategy creates a melting profile which indicates the stabilization effect (i.e. in the presence of ligand showed greater stabilization effect) conferred by different ligand types such as platinum complexes [30, 31], ruthenium complexes [32, 33] and other compounds [34, 35]. A major limitation arises from the low intensity signal that leads to imprecise melting curves.

4.1.5.2. Circular Dichroism spectroscopy (CD)

Similar to UV-Visible spectroscopy, CD is a straightforward technique commonly used for characterization of G-quadruplex topology. It has been an essential technique for studying G-quadruplex-ligand interactions because DNA conformation changes due to factors such as temperature, concentration of cation, and pH can be monitored in a straightforward manner. The interaction between G-quadruplexes and ligands can also be extensively studied using the technique. Hence, when a non-chiral ligand binds to chiral DNA, such as a G-quadruplex, this induces a CD signal in the wavelength range of the absorption bands of the bound molecule [36]. CD is limited to providing qualitative data and kinetic data. Other limitations of CD are similar to those of UV-visible spectroscopy, such as requiring a high concentration and volume of DNA sample and ligand, as well as delivering only low signal intensity.

4.1.5.3. Fluorescence spectroscopy

Fluorescence spectroscopy has been found to be a very useful method over the last few years. The G-quadruplex-ligand interaction is studied by monitoring the decrease in fluorescence induced by displacement of ligand. For example, single molecule fluorescence resonance energy transfer (FRET) experiments have been developed to study ligand interactions. The assay can be carried out by labelling DNA with fluorescent dyes (for example, at the 5' with fluorescein (FAM) as the donor and at the 3' with tetramethyl-6-carboxyrhodamine (TAM) as the acceptor). The fluorescence of the donor is quenched when the donor and acceptor are in close proximity. The intensity of emission from the acceptor can increase. In contrast, only the fluorescence of the donor is enhanced as separation increases. Less intense fluorescence is obtained from the acceptor.[16, 26]. The melting curve can be easily determined due to large differences between the fluorescence properties of folded and unfolded forms. The relative strength of interaction can be utilised from the shift in T_m. However, the stabilization value induced by the ligand on the

G-quadruplex structure depends on the nature of the fluorescent tags, the incubation buffer, and a chemically modified fluorescent base in the DNA sequence of interest is expensive [26].

4.1.5.4. Surface Plasma Resonance (SPR)

SPR has been particularly useful for monitoring real time binding of small molecules to DNA molecules immobilized onto gold surfaces. Upon binding of a ligand of interest to the surface-immobilised DNA, a shift in plasmon resonance is produced that can be used to obtain real-time kinetic information. With these benefits it is not surprising that many applications using SPR to study G-quadruplex-ligand interaction have been published [37-43]. However, the complexity of the setup and the functionalization process, which is limited to only gold standard microchips, makes this technique expensive [40].

There are many similarities between SPR and WGM. Both of the techniques are optical sensors that are based on a resonance shift. C. E. Soteropulos and H. K. Hunt [44] drew an excellent comparison between the two techniques. The commercial Biacore system is a very popular SPR platform into which various surface modification techniques have been integrated. This leads to reduced or non-existent surface fouling and can be used with a variety of complex samples. While commercial biosensor SPR platforms are well-understood, WGM optical resonators are still novel. WGM possesses similar advantages compared to SPR but the functionalization of the spherical resonator is simpler, cheaper and faster. Protocols for surface functionalization of a glass surface, which are well established, can be easily applied in a standardized fashion.

There is a real need to develop a novel sensing strategy that is reliable, fast, and sensitive, and can be used for real-time DNA-ligand screening to extract binding affinities and kinetic information such as equilibrium or rate constants. Herein, we propose the use of WGM sensing where laser light is circumnavigated by total internal reflection in a silica sphere. Changes in optical path length occur in response to binding events and can be monitored in real time. Briefly, upon binding of small molecules to a DNA target immobilised at the surface of the resonator, the optical path length increases and perturbs the sphere out of resonance. Adjusting the sphere back into resonance requires compensation by increasing the wavelength of the laser. This shift offers valuable information on kinetic data.

As was mentioned earlier, there are many similarities between WGM and SPR although versatile functionalization, ease of multiplexing and significantly lower cost makes WGM sensing particularly attractive. Additionally, most commonly used SPR sensor chips used for testing DNA binding ligands are coated with streptavidin immobilised in carboxy-methylated dextran, a matrix often responsible for non-specific interactions with small molecules. Herein, to overcome this

limitation, the surface of the resonator was modified with a biotinylated silane that is stable under a large range of salt concentrations and pH [45]. Modification of the WGM resonator was then achieved by streptavidin grafting followed by immobilization of biotinylated DNA. With such a platform it was possible to differentiate between duplex and G-quadruplex DNA and to extract relevant binding kinetics.

4.1.6 Binding modes of ligand to G-quadruplex

G-quadruplexes have emerged as a new class of potential molecular targets for drug discovery, such as anticancer drugs. Elucidation of the interaction or binding mode between small molecules or ligands and G-quadruplexes is a crucial step for predicting and understanding the binding affinity of ligands [46]. Three predominant binding modes have been found in G-quadruplex-ligand binding. In principle, the specific degrees of ligand binding occur through inner intercalation between G-quartets, stacking from the top or bottom surface of the G-quadruplex, groove binding, or an assortment of more than one of these binding modes. The general principles underlying binding interactions of most ligands to G-quadruplexes are usually as follows.

4.1.6.1 Mode of interaction

Loop binding

A loop is an important in G-quadruplex conformation as it enables recognition during G-quadruplex targeting by drugs. The loop binding is one of the normal binding modes of ligand, acting through electrostatic interaction between the side chains of the ligand and the ionic centre of the aromatic core of the G-quadruplex. Cationic substituents also improve the binding affinities with the anionic phosphate backbone of the DNA. One key example is the planar G-tetrad 5,10,15,20-tetra (N-methyl-4-pyridyl) porphyrin (TMPyP) [47].

G-quartet through π-π interactions

Small organic molecules which consist of a large π-planar aromatic surface can interact via strong π-π stacking interactions (non-covalent interactions between aromatic rings that contain π-bonds). Additionally, extended planar aromatic ligands can form both a rigid flat or twisted surface, with a size and shape similar to that of a G-quadruplex, which can simply stack onto the G-quartet [18]. The cationic centre of the aromatic core of the ligand usually interacts with the negative electrostatic centre of the G-quadruplex by electrostatic interaction, and the electron-deficient nature of the ligand would also strengthen its cation-π interaction with the G-quartet [18].

Groove binding

The stacking of G-quartets creates four grooves in the G-quadruplex structure. Groove binding is an unique structural feature of G-quadruplexes which allows small molecules to interact with the loops and grooves; in addition, a stronger binding can be formed by cationic substituents interacting with the anionic phosphate backbone [19]. Hydrogen bonding patterns are also generated by specific molecular shapes, offering recognition to the groove regions of G-quadruplex [18].

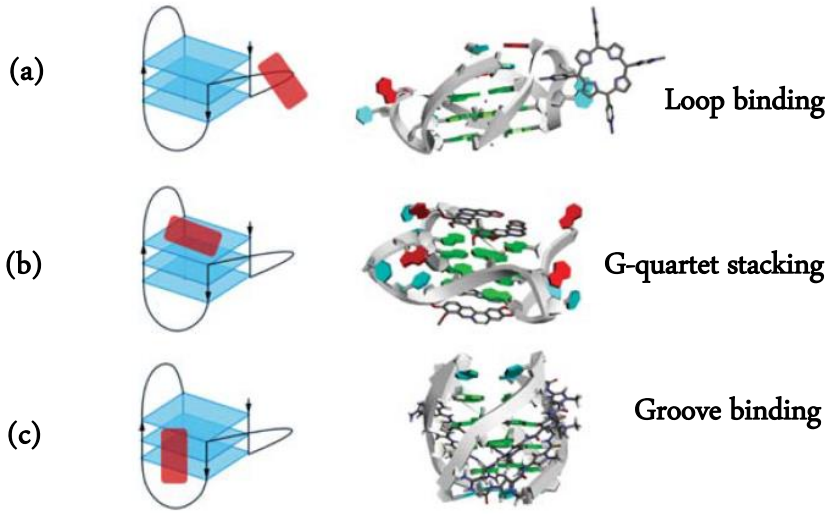


Figure 4.3 Example of basic binding modes of ligands to G-quadruplexes. The picture is reprinted with permission from [18].

4.1.6.2 Mechanistic discussion of five ligands used in this work

CV is a triphenylmethane dye which has already been used as a sensitive fluorescent probe for the discrimination of G-quadruplexes from duplex and single-stranded DNAs. This ligand can bind with high affinity with G-quadruplexes in the presence of K^+ [48, 49]. The propeller-like twisting phenyl rings in the CV molecule confers increased vibrational flexibility. Hence, stacking of the dye on the face of the G-quartet increases the rigidity of the dye structure. While CV stacks onto the two external G-quartets of the G-quadruplex, it is protected by end loops from the solvent [50]. Three phenyl rings of the dyes stack onto the two external G-quartets of the quadruplexes, and the overhanging positively charged dialkylamino substituents interact with the negatively charged phosphate backbone and loops [51].

CV and MG are both triphenylmethane dyes that can be used for quadruplex probes, primarily through π-stacking with the top G-tetrad [49, 50, 52]. MG structure is quite similar to that of CV, which has two dimethylamino substituents whereas MG has only one substituent. These dimethylamino substituents provide hydrogen-bonding and cation-dipole interactions with the negatively charged phosphate backbone and loops of G-quadruplexes. By considering this, it

can be understood why CV has a higher affinity of binding to G-quadruplex compared to MG. In addition, the binding affinity of MG to G-quadruplex and duplex DNA is very similar [47].

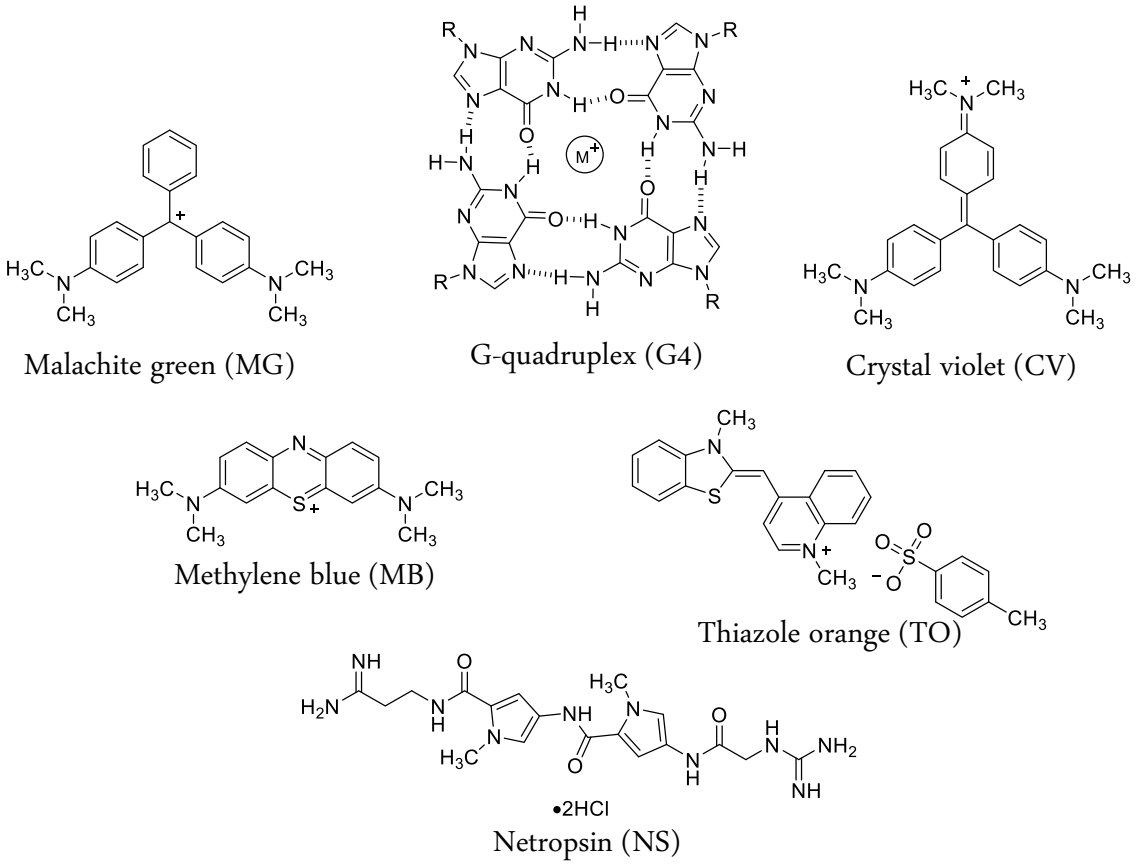


Figure 4.4 Structures of five selected ligands compared with G-quadruplex structure

MB is a cation dye with a fine planarity, and well-characterised photochemical properties. It has been used in a variety of photochemical applications including photodynamic therapy [53, 54]. Additionally, the interaction between MB and DNA has previously been widely investigated. MB binds with single-stranded DNA through a weak electrostatic bond while it interacts with double-stranded DNA via intercalation with the preferential G–C base pairs site due to more favourable π-stacking interactions. The interaction of a positively charged molecule with a large π-aromatic plane (MB) with nucleic acid can stabilize and encourage the formation of a G-quadruplex [54].

TO, a cyanine dye, was reported to bind very tightly to the double-, triple-, and quadruplex-stranded DNA, more than single stranded DNA, by Lubitz and co-workers [55]. TO prefers to stack on the G-quartet [56]. Examples of the binding between TO with G-quadruplex and duplex DNA are illustrated in Figure 4.5 and 4.6, respectively.

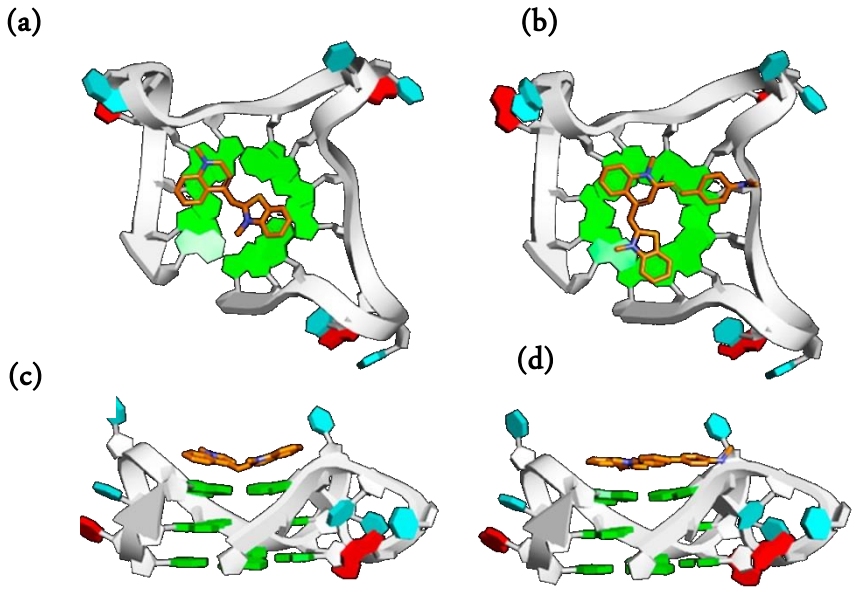


Figure 4.5 Top view (a), (b) and side view (c), (d) of the structure of Telo21 G-quadruplex in complex with TO, from computational simulation studies. The picture is reprinted with permission from [56].

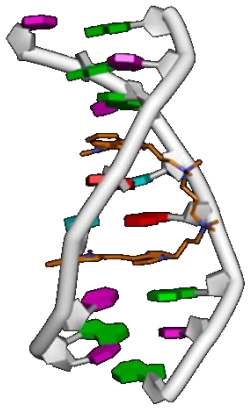


Figure 4.6 Duplex DNA in complex with homodimeric TO dye from NMR spectroscopy studies, which shows that the TO chromophore is stacking in the binding site; agreeing with computational simulation of molecular docking studies. The picture is reprinted with permission from [56].

NS is a typical double stranded DNA minor groove binder [57]. NS is also commonly used as a cell-permeable probe binding selectively to AT-rich duplex DNA with lower affinities for G-quadruplex DNA [58]. In addition, this ligand has low selectivity for G-quadruplexes over duplexes [57, 59].

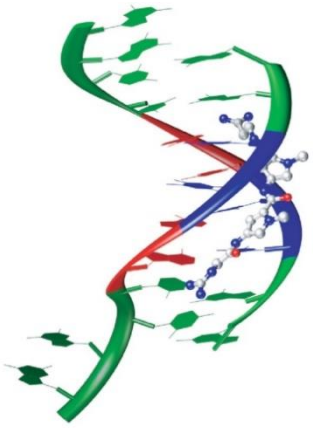


Figure 4.7 Structural information suggests a bimolecular ligand-DNA association. Crystal structure of the NS-DNA complex; nitrogen=blue, oxygen=red, carbon=grey; DNA=(5′-GGCCAATTGG-3′). The picture is reprinted with permission from [60].

4.2 Experimental methods

4.2.1 Chemical and Materials

All chemicals used in this experiment were analytical grade which were; 3-aminopropyltriethoxysilane, APTES ($C_9H_{23}NO_3Si$, Sigma-Aldrich, U.K.), biotin 3-sulfo-N-hydroxysuccinimide ester sodium salt, biotin-NHS ($C_{14}H_{18}N_3NaO_8S_2$, Sigma-Aldrich, U.K.), 99.8% anhydrous ethanol, (CH_3CH_2OH, Sigma-Aldrich, U.K.), Streptavidin from *Streptomyces avidinii* essentially salt-free lyophilized powder, (Sigma-Aldrich, U.K.), Trizma® hydrochloride buffer solution BioUltra, for molecular biology, pH 7.4. (Sigma-Aldrich, U.K.), potassium chloride (KCl, VWR, U.K.), lithium chloride (LiCl, VWR, U.K.), Biotin 3-sulfo-N-hydroxysuccinimide ester sodium salt, $C_{14}H_{18}N_3NaO_8S_2$ (Sigma-Aldrich, U.K.), biotin c-myc, TGAGGGTGGGTAGGGTGGGTAA (Sigma-Aldrich, U.K.), mutated biotin c-myc, TGAGTGTGTGTAGTGTGTGTAA (Sigma-Aldrich, U.K.), c-myc complementary strand TTACCCACCCTACCCACCCTCA (Sigma-Aldrich, U.K.). All nucleotides were used without further purification and were dissolved in autoclaved water and stored in the freezer at -20°C before use.

4.2.2 Circular dichroism (CD) experiment

CD experiments were run on a spectrophotometer (J-715, Jasco) using a quartz cell of 1 mm path length. The CD spectra of DNA oligonucleotides were recorded by taking the average of three scans made at 0.1 nm intervals from 200 to 350 nm at 25°C with a scan speed of 50 nm min^{-1}. The concentrations of all DNA samples were 10 μM.

4.2.3 Attenuated total reflection spectroscopy (ATR) experiment

ATR spectra were recorded using an FT-IR spectrometer (UATR Two, PerkinElmer). First, an open beam background spectrum was collected. For the collection of resonator sample spectra, 10 resonators were placed on the ATR crystal then pressed into the pressure arm over the crystal/sample to collect the spectrum.

4.2.4 Fluorescence experiment

A confocal microscope (DP71, Olympus) was employed to analyse the fluorescence on the functionalized microspheres. Microspheres carrying different DNA structures (all the resonators were from WGM experiment) were examined with a 20× magnification objective, using a Hg lamp. The resonators were dipped in 10 μM TO for 1 hour, then the image was recorded and the fluorescence signal was further analysed with analySIS docu software.

4.2.5 Fabrication and functionalization of the microsphere resonator

4.2.5.1. Preparation of amine-terminated, APTES, surfaces and biotinylation of APTES surfaces

All microresonators were fabricated from single mode optical fibres (F-SMF-28, Newport) by placing the tip in one arm of a splicer machine, which produces a sufficient electric arc to melt the glass. By precisely controlling the arc shot, a spheroidal shaped tip was then formed due to the surface tension of the molten glass. It is this tip that was used as the microresonator and was determined to be 200±10 μm in diameter. The microresonator surface was then cleaned with oxygen plasma and functionalized using an amino-silane called (3-aminopropyl) triethoxysilane or APTES in order to increase the covalent coupling between the glass resonator surface and biotin. Briefly, the microresonator was immersed in a 2% v/v solution of APTES in ethanol for 1 hour. In the following step, the silanized resonator was washed in fresh ethanol in order to wash off unbound silane and then dried in an oven to evaporate the solvent for 30 minutes. The resonator was subsequently immersed in 1.6 mg mL^{-1} sulfo-N-hydroxysuccinimide biotin ester sodium salt dissolved in 10 mM Tris·HCl buffer pH 7.4 in the presence of 100 mM KCl for 1 hour, and finally the biotinylated resonator was rinsed with the same buffer and dried with a stream of N_2.

4.2.5.2. Preparation of oligonucleotides

To better understand the oligonucleotides used in this work, the DNA can be classified into 6 distinct types: c-myc, mutated c-myc, duplex, mutated duplex, G-quadruplex and mutated G-quadruplex.

Explanation of the DNA used in this work

i) 'c-myc' is a 22-mer single strand G-rich DNA with a sequence of TGAGGGTGGGTAGGGTGGGTAA. In this thesis, when c-myc is mentioned, it refers to the aforementioned DNA sequence in the absence of K^+.

ii) 'Mutated c-myc' is a 22-mer single strand DNA which cannot fold into a G-quadruplex. The sequence of this DNA is TGAGTGTGTGTAGTGTGTGTAA. It is annealed in the same way as in c-myc (i). We expect that there is no four strand population from this oligonucleotide.

iii) 'Duplex' is a 22-mer double strand of c-myc DNA, with the TTACCCACCCTACCC ACCCTCA complementary strand.

iv) 'Mutated duplex' is a 22-mer DNA of mutated c-myc (ii) with the TTACCCACCCTACCCACCCTCA strand. Thus there are two strands in the mixture which are not complementary and we expected that there is no double strand population from these oligonucleotides.

v) 'G-quadruplex' is a 22-mer four stranded c-myc DNA structure prepared by folding in K^+ solution. In this thesis when G-quadruplex is mentioned, it means four strands of c-myc in the presence of K^+ although in varying concentrations which depend on the propose of each experiment.

vi) 'Mutated G-quadruplex' is 22-mer of mutated c-myc prepared with the same process as in G-quadruplex (v). In this thesis when mutated G-quadruplex is mentioned, it means mutated of c-myc in the absence or in the presence of K^+ but varying concentrations which depend on the propose of each experiment. We expect that there is no four strand population from this oligonucleotide.

Please note that all the definitions above apply in this work only.

1. Preparation of G-quadruplex and mutated G-quadruplex

The c-myc or mutated c-myc DNA sequences, TGAGGGTGGGTAGGGTGGGTAA and TGAGTGTGTGTAGTGTGTGTAA, from 5′ to 3′, labelled with biotin at 5′, were diluted in 10 mM Tris•HCl buffer pH 7.4 in the presence of 100 mM KCl. The DNA was heated at 95 °C for 5 minutes then slowly cooled down to room temperature overnight.

2. Preparation of duplex and mutated duplex

The c-myc or mutated c-myc DNA was diluted in 10 mM Tris buffer then the sequence (TTACCCACCCTACCCACCCTCA) DNA was added. The mixture was heated at 95°C for 5 minutes then slowly cooled down to room temperature overnight.

3. Preparation of ligands

Five ligands including Crystal violet (CV), Methylene blue (MB), Thiazole orange (TO), Malachite green (MG) and Netropsin (NS) were directly dissolved in the same buffer as used in the preparation of oligonucleotides.

4.2.6. WGM assay for interrogating G4 structure/function

A diagram of the WGM setup is shown in Figure 4.8. A nominated wavelength of 1310 nm from a DFB laser was employed and coupled to the spherical resonator via the tapered waveguide made of a single mode fibre with a diameter ~2 μm. By doing so, the laser light circumnavigates the sphere and is confined to the sphere's surface. The detected output resonance wavelength from the waveguide will shift to a longer wavelength (known as red shift) as the modification thickness and/or density increases or refractive index changes. It is this effect which can be used to easily quantify binding and kinetics in real-time (more detail about the WGM principle can be found in Chapter 1, Introduction). For example, streptavidin bound to the biotinylated-silane resonator surface will result in the optical path length being increased and the refractive index at the surface being changed, resulting in loss of resonance. This mechanism is similar for DNA and ligand binding. Gradually as the number of available binding receptors becoming occupied increases, the resonance shift will increase and reach a plateau when all the receptors are engaged.

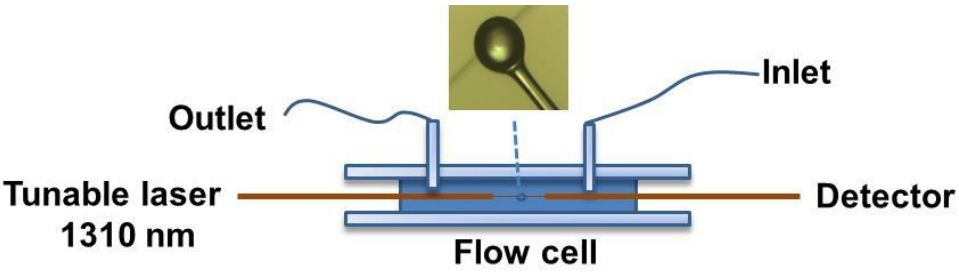


Figure 4.8 A schematic representation of a flow cell for a typical WGM platform to monitor the interactions between a G-quadruplex and ligands on the resonator's surface. The picture is reprinted with permission from [2].

4.2.7. WGM assay for ligands' interaction with G4 structure

A binding interaction between a ligand and DNA analysed with WGM begins with the immobilization of G-quadruplex (which was pre-folded and well-characterized by CD spectroscopy to confirm the correct structure) on the resonator surface by continuous flow into the WGM platform, as described in the previous section. The following step was binding of the ligand of interest by flowing the ligand over the DNA surface. The interaction of the ligand and G-quadruplex was then monitored by WGM as a change of the wavelength shift of the resonator over time of a serial dilution. Ligand samples were injected into the running buffer. Typically, sample injections were performed at a high flow rate of 100 μL min^{-1} in order to reduce any mass transport effects that may be present if a low flow rate is used. Each injection was performed once the baseline was stable. From this, the association or dissociation rate constant (k_d or k_{off}) and equilibrium (K_D) constants can be derived which will be described in the next section.

4.3 Results and Discussions

4.3.1 Characterization of G-quadruplex structure in solution

In this study, a well-characterized c-myc G-quadruplex was chosen as a candidate for the G-quadruplex and ligand interaction study [61]. Fundamentally, c-myc presents several different structures, which are; single strands (ss), double strand (ds) and four strands or G-quadruplex.

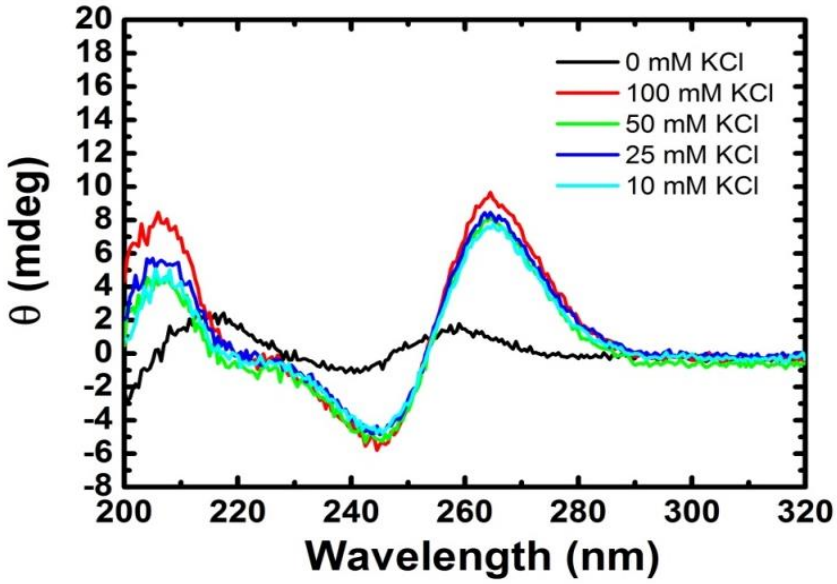


Figure 4.9 CD spectra of 10 μM pre-folded c-myc at different concentration of KCl

Before immobilising DNA on the resonator surface, c-myc was pre-folded and hybridized into G-quadruplex and duplex forms, then each was simply checked to ensure correct structure formation using CD spectroscopy, which is the most convenient and rapid technique to assess G-quadruplex structure. Subsequently, the study was set up to observe the folding and hybridization of c-myc on the surface of the resonator and to monitor the whole process, i.e. folding, unfolding, hybridization, breaking four strands into double strands and interaction with small molecules or ligands in real time. Unfortunately, the results from folding and hybridizing c-myc on the surface were not entirely promising and will be discussed in section 4.3.10-4.3.11. One key limitation lies in the fact that in order to fold or hybridize DNA there are two factors that need to be considered (1) high temperature (90-95°C at the critical temperature called the melting temperature, Tm) to denature and separate the strand and (2) time required for annealing the DNA which normally requires slow cooling over 1 night. There is, therefore, a definite need for an optimised pre-folding or hybridization process before immobilizing verified pre-folded (G-quadruplex) and hybridized (duplex) c-myc on the resonator, in order to study the interaction between ligands and various different forms of c-myc DNA.

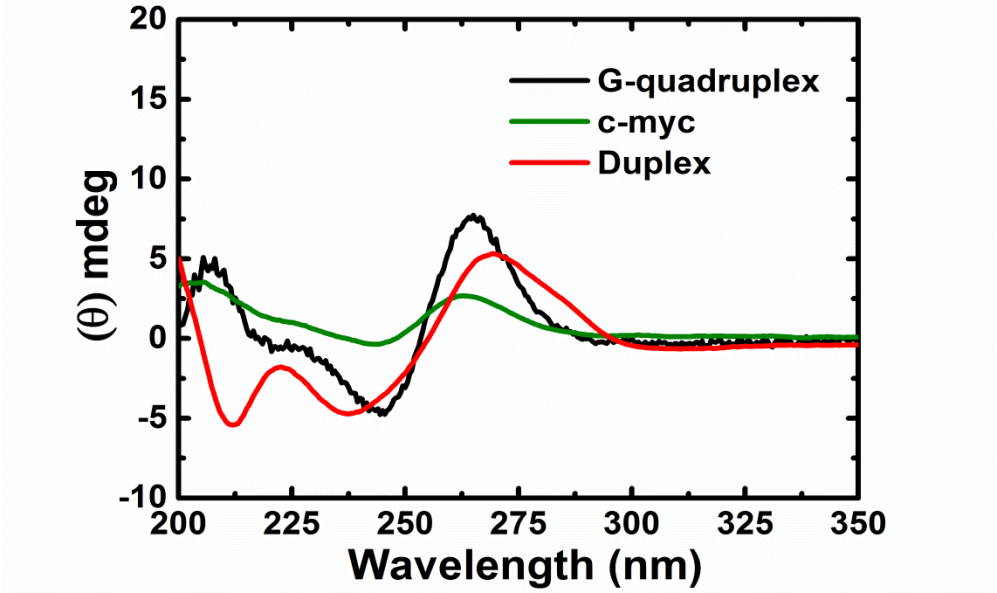


Figure 4.10 CD spectra represent different forms of c-myc including single strands (ss), double strand (ds) and four strand or G-quadruplex at 10 mM Tris buffer pH 7.4 (G-quadruplex sample was pre-folded in 10 mM Tris buffer pH 7.4 in the presence of 100 mM KCl).

It is well known that K^+ is required to preserve G-quadruplex structure. Herein, to investigate which concentration of K^+ is optimal for c-myc DNA (labelled with biotin) in order to fold into G-quadruplex structure, different concentrations of KCl were utilised to pre-fold c-myc, ranging from 0-100 mM. There were no significant differences between CD spectra at different concentrations ranging from 10 to 100 mM KCl, whereas at 0 mM KCl no CD peaks were present, indicating no G-quadruplex structures were observed in the absence of KCl, Figure

4.9. This finding might indicate that only 10 mM KCl or less is required to fold c-myc into the G-quadruplex form in the solution. As shown in the CD spectra in Figure 4.9, the parallel folded topology of c-myc was confirmed by a positive absorbance at 265 nm and a negative minimum at 245 nm, which is in good agreement with values from the literature [22, 36]. No negative absorbance was observed from single strand c-myc, whereas two negative peaks were observed at 212 and 240 nm and one positive peak at 270 nm for duplex topology, Figure 4.10. K^+ was selected to stabilize the G-quadruplex structure in this experiment because it is more effective than other alkali metal ions [23]. Moreover, the conformational polymorphism of c-myc can be controlled as it will form an anti-parallel conformation at low K^+ and a parallel topology at high concentrations of K^+ [62]. This finding agrees very well with the result from our CD spectra, Figure 4.9, therefore we can conclude that the topology of pre-folded c-myc in this experiment was parallel. The concentration of KCl at 100 mM was chosen for the G-quadruplex-ligand interaction to ensure that the G-quadruplex structure was formed and was stabilized on the surface of the resonator.

In terms of this G-quadruplex-ligand interaction study, it is important to take into account that a possible bias might be inherent from the presence of some nucleotide populations that cannot fold into G-quadruplexes. On this point, the CD results, see Figure 4.9, were not very useful, as they cannot be used to determine which KCl concentration is optimal for the experiment. Normally, different concentration of KCl used for G-quadruplex studies range from 10-100 mM [48, 61, 63, 64]. So considering this literature and our data, the highest concentration of KCl at 100 mM was used herein to fold and stabilize c-myc to G-tetrad topology to ensure that all or almost all c-myc folds into G-quadruplexes.

4.3.2 Immobilization of DNAs onto the resonator surface and discrimination between folded and unfolded states of the G4 region of the c-myc promoter

As mentioned in the introduction of this chapter, there are many similarities between WGM and SPR although functionalization of the WGM glass sphere resonator is superior and simpler. For example, in SPR, dextran is often used to immobilize the DNA [37]. This leads to the non-specific interaction problem of small molecules with dextran. Often to reduce this, a non-specific binding reducer (NSB) or a high concentration of salt is added to reduce the interaction [65]. However, such a high concentrations can destroy the surface [66]. We decided to use silane-biotin surface functionalization for initial glass functionalization then streptavidin-biotin interaction to immobilize DNAs on the resonator surface. For this immobilization to take place, the oligonucleotides were modified with biotin in order to have linkage to streptavidin which was immobilized on the silane-biotinylated resonator surface. This system was selected because biotin is stable, very small and rarely interferes with the function of labelled DNA. Silane-

biotinylated functionalization was chosen as the reactive group on the glass resonator surface because it is tolerant of extreme conditions. The schematic diagram of surface functionalization is depicted in Figure 4.11. The terminal amino group (-NH_2) of the APTES functionalized surface reacts with the ester linkage in sulfo-NHS-biotin thus leading to the formation of a stable amide bond and a biotinylated surface [67].

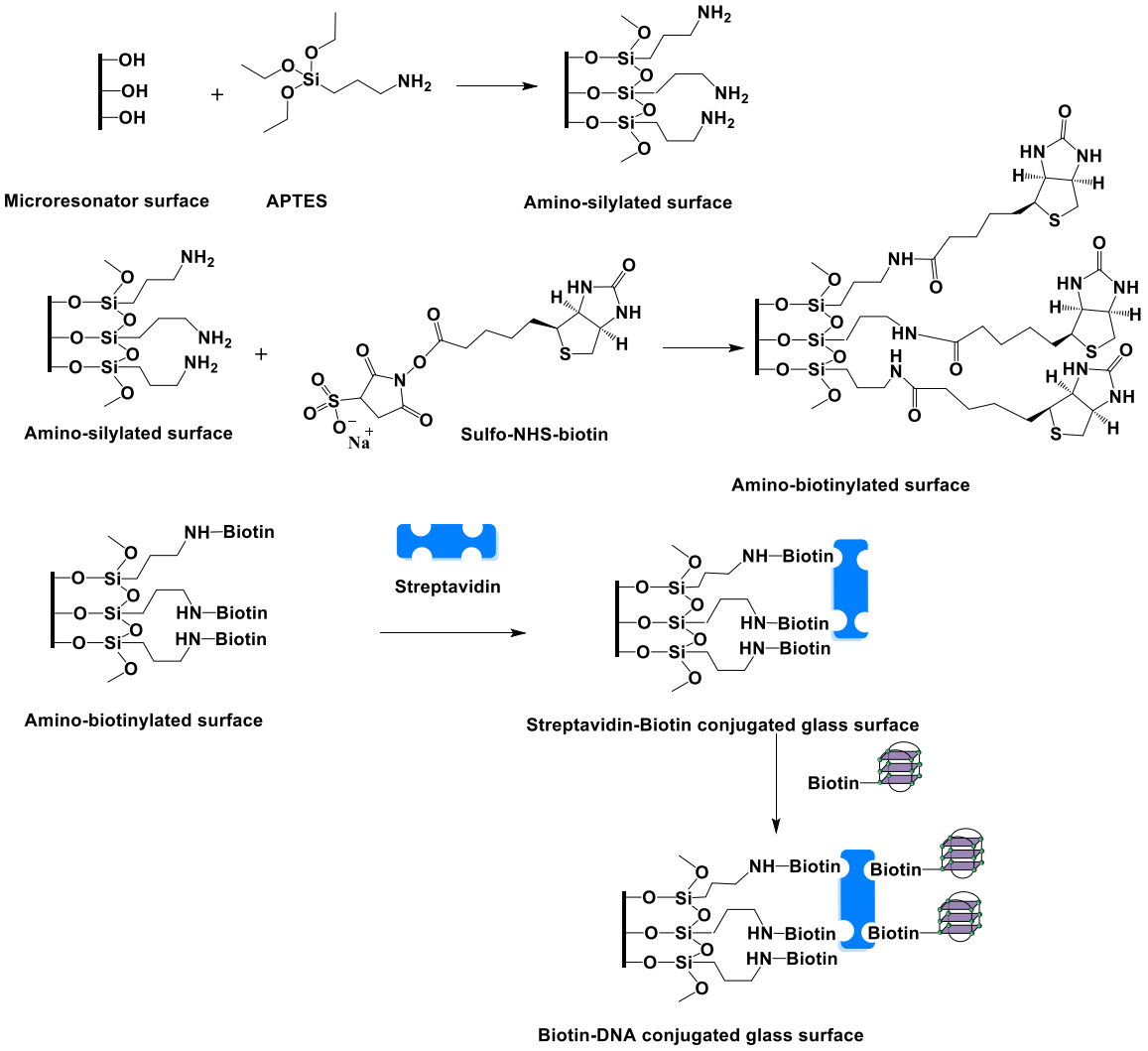
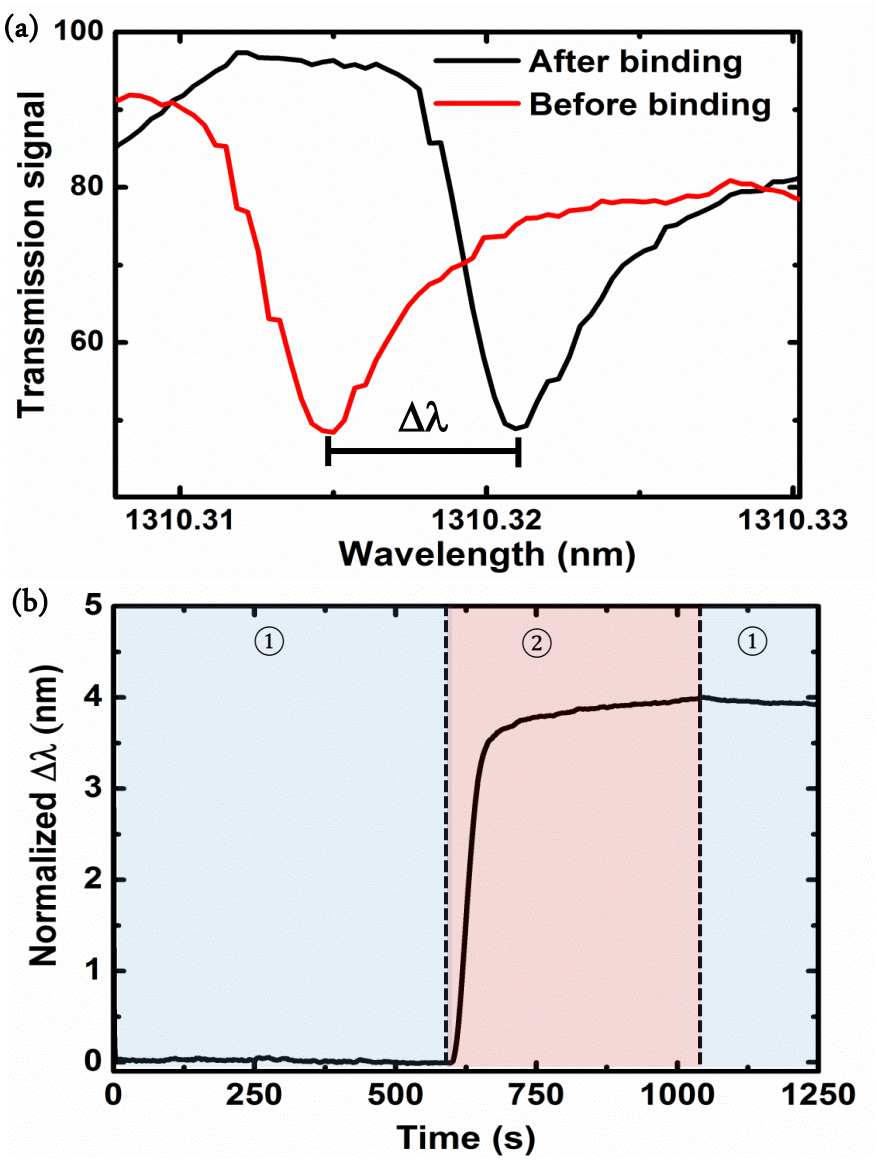


Figure 4.11 Schematic diagram depicts biotin-DNA immobilization onto a streptavidin [68] layer bound to a biotinylated-silane microresonator surface. The picture is reprinted with permission from [2].

Herein, streptavidin served as a binder to link biotin-DNAs and the biotinylated-silane resonator surface. Streptavidin was chosen based on a number of considerations. First, streptavidin itself is a tetramer which has a net negative surface charge at the assay pH and very low affinity for DNA. Second, the biotin-streptavidin interaction is specific, fast and has very robust attachment chemistry [69, 70]. The diameter of streptavidin in solution was found to be 4.5 nm × 4.5 nm × 5.0 nm [71], and the binding of streptavidin molecules can be either single or

double layer. However, for the binding of streptavidin to a biotinylated surface, where only one side of the structure (see the model of streptavidin in Figure 4.11) was modified with biotin, the height of streptavidin was found to be ~3.8 nm, as reported by Li et al. using AFM [69]. This height agrees very well with the normalized Δλ of streptavidin observed by WGM (which is equal to the thicknesses of streptavidin) at ~3.5 nm. The real time binding curve of streptavidin can be found in Figure 4.12 part (b). As mentioned in section 1.2.4.2 the thickness of the adsorption layer can be precisely calculated according to equation 1.8. However, it should be taken into consideration that part of this shift could be attributed to bound ion such as K^+.

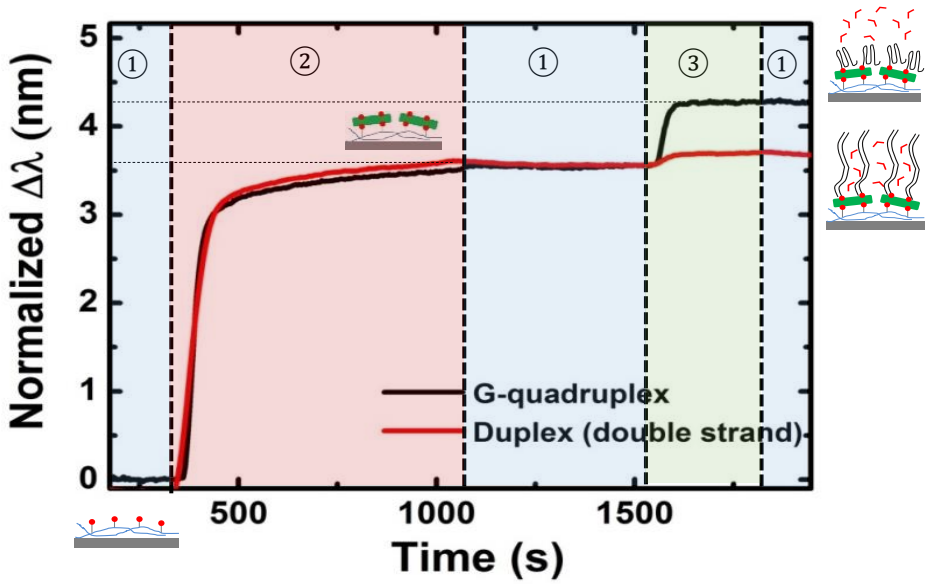


① 100 mM KCl in 10 mm Tris buffer ② 25 ug/ml Streptavidin in ①

Figure 4.12 (a) Binding of streptavidin causes an induced shift of a resonant mode (Δλ) (b) real time WGM binding curve from streptavidin.

The interaction between biotin and streptavidin is the strongest known non-covalent bond, so even when the surface was flushed with buffer streptavidin cannot wash off from the surface (at 1000s-1250s), Figure 4.12 part (b). The evidence from this study therefore suggests that streptavidin is attached on the surface. Moreover, once the biotin-streptavidin bond was formed, it is known to be unaffected by extreme conditions such as pH, temperature, solvents and other denaturing agents [72, 73]. This strong interaction was also utilised when DNA labelled with biotin was attached on the streptavidin surface.

In terms of attaching DNA, c-myc nucleotides can form a stable four tetrad structure in the presence of K^+. Representative WGM binding curves for the immobilization of four-stranded (G-quadruplex) and double-stranded (duplex) biotinylated DNAs onto the streptavidin-coated resonators are shown in Figure 4.13. After the initial streptavidin curve and wash, the biotinylated DNAs were introduced to the surface, whereupon a real time binding curve was recorded.



① 100 mM KCl in 10 mm Tris buffer ② 25 ug/ml Streptavidin in ①
③ 1 μM G-quadruplex or duplex in ①

Figure 4.13 The WGM binding curve of 1 μM of pre-folded c-myc (G-quadruplex) and duplex of c-myc DNA; the WGM sensor is likely more sensitive to G-quadruplex than the duplex because of its compact structure which can interact with the evanescent field closer to the surface where the intensity is higher. The picture is reprinted with permission from [2].

Pre-folded c-myc or G-quadruplex thickness was found to be ~0.72 nm. The finding of this diameter was supported by previous research from G.N. Parkinson and co-workers in 2002 [74]. The team conducted experiments using x-ray crystallography techniques to determine G-quadruplex size in the 22-mer intramolecular region, which was found to be ~0.63 nm. In this WGM experiment, a G-quadruplex structure was found to induce a large resonance shift (0.72

nm) around five times greater than the double helix form (0.14 nm). A likely explanation is that the compact structure of G-quadruplex interacts more with the evanescent field close to the surface when compared to double-stranded DNA (more detail about the evanescent field can be seen in Chapter 1, Figure 1.6). Using this strategy, WGM can discriminate between the different structures of duplex and G-quadruplex of c-myc, a feature which will be discussed further in section 4.3.9.

4.3.3 Characterization of functionalized and immobilized DNAs on the resonator surface

A good understanding of working with the surface chemistry of biological assays is essential to control the quality and properties of the assay surfaces. In order to verify and support the data from WGM experiments, the resonator needs to be well characterized. Herein, various techniques were performed to characterize the resonator surface after the functionalization step.

4.3.3.1. Attenuated total reflection (ATR) characterization for APTES resonator

Attenuated total reflection-infrared spectroscopy (ATR-IR) is a highly sensitive technique that yields direct information about the chemical bonds formed on a surface. A representative ATR-IR spectrum from a bare resonator illustrates bands peaking near 1040 $cm^{-1}$and 1140 cm^{-1}, Figure 4.14. These bands correspond to a combination of Si-O-Si vibrational modes including those of bonds formed between crosslinking between silane molecules at the surface [17]. A spectrum of an APTES coated resonator would typically have bands in the region of 2800–2990 cm^{-1} (centered at 2930 cm^{-1}) and ~1500–1700 cm^{-1} (centered near 1580 cm^{-1}), which are assigned to CH_2 stretching and NH_2 bending, respectively [17,18]. More details about interpreting spectra compared with references can be seen in Table 4.1. This study has shown that the APTES functionalization process was successful on the surface of the resonator.

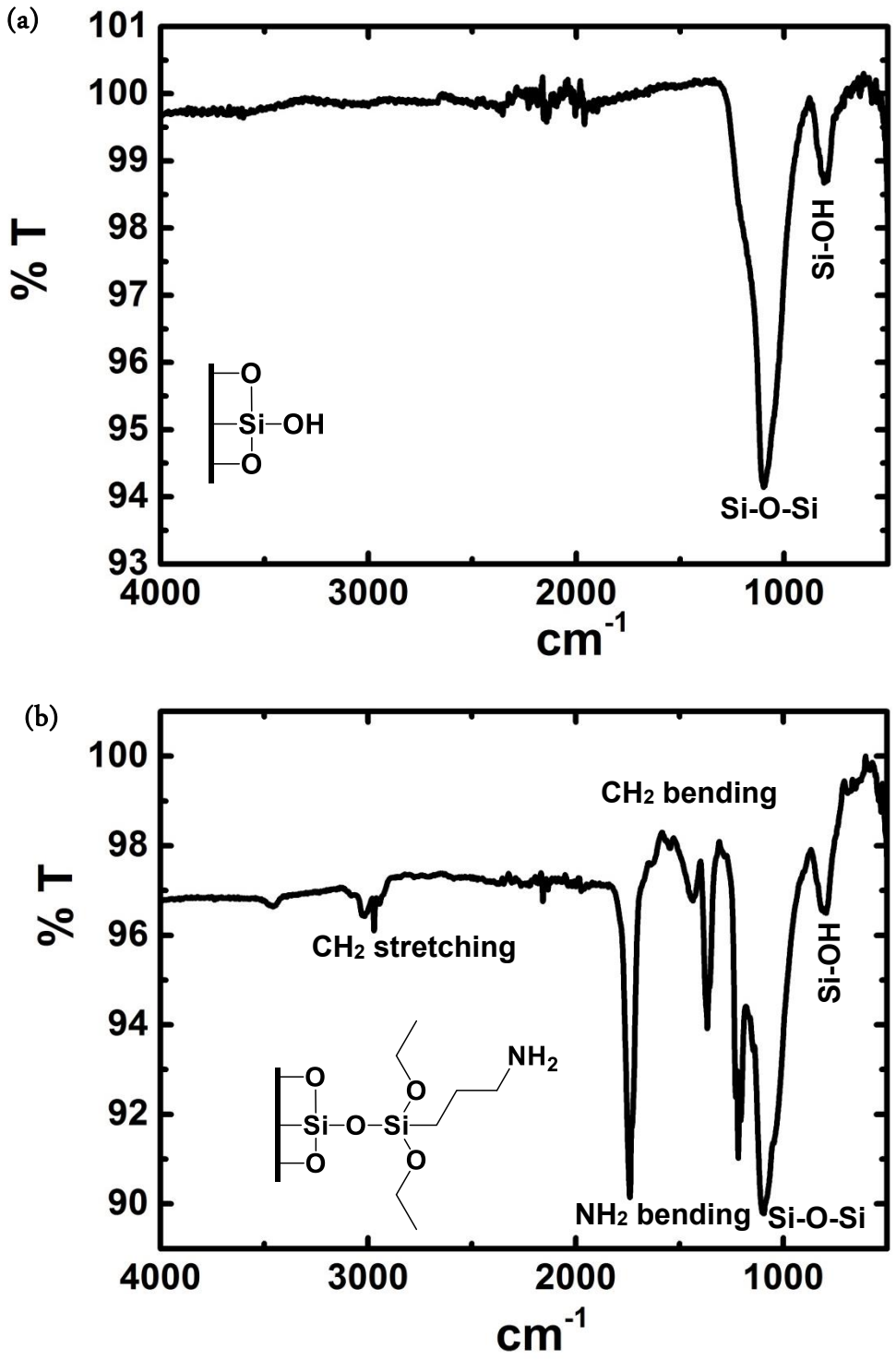


Figure 4.14 ATR-IR characterization of (a) glass and (b) APTES surface of the microresonator. The picture is reprinted with permission from [2].

Table. 4.1 Summaries of frequencies found in APTES resonators compared with references

Group	Frequency (cm^{-1})	References
Si-O-Si vibrational	1023-1116	1040-1140 [75], 1000-1130[76]
CH_2 stretching	2898-3000 Center peak at 2955	2800-2990 Center peak at 2955 [75]
NH_2 bending	1741	1500-1700 [75]
Si-OH	800	810-950 [76]

4.3.3.2. Atomic Force Microscopy (AFM)

AFM is one of the most powerful techniques for surface study. In chapter 3, the technique was used to characterize the resonator surface, Figure 3.15. Functionalization and characterization of a silicon wafer surface coated with 3-aminopropyltriethoxysilane (APTES) and afterwards biotinylated for the selective immobilization of streptavidin was described nicely using AFM by E. H. Williams and co-workers in 2012 [67]. AFM was also used to characterize the surface of the sphere microresonator in several WGM studies [77-79]. Herein, the surface of the resonator was analysed by AFM in tapping mode with a super sharp tip.

The APTES-biotinylated resonator surface was revealed to be very smooth and uniform with the RMS roughness at 0.51 nm and height at 2.14 nm, whereas the RMS roughness was increased to 2.99 nm with height at 9.52 nm when the APTES-biotinylated resonator was exposed to streptavidin. However, because of resonator morphology and small size (less than 300 μm) of sample, caution must be applied, as the findings might not be transferable to reproducible results.

All we can conclude from the AFM results was that in our experiments the silane on the surface of the APTES-biotinylated resonator was quite uniform and streptavidin attached on the surface, as the RMS roughness was increased when the APTES-biotinylated resonator was exposed to streptavidin. The height from this resonator was unexpected and higher than the usual streptavidin dimension. We postulate it might be related to the aggregation of streptavidin on the surface as the surface was dried with N_2 gas before the AFM experiment. The solution for this might be conducting the AFM experiment in solution, which is possible but time consuming. However, according to combined results from AFM and WGM we can confirm the successful attachment of streptavidin on the surface.

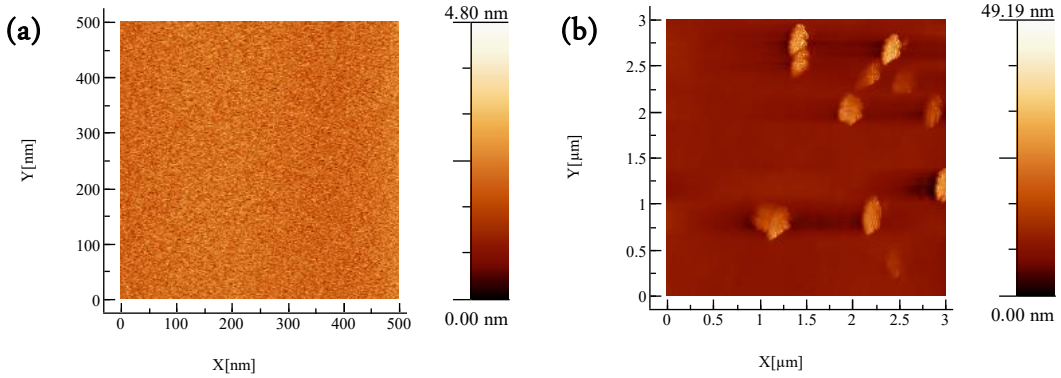


Figure 4.15 AFM images of (a) biotinlyted-APTES resonator (b) biotinlyted-APTES resonator coated with streptavidin.

4.3.3.3. Fluorescence characterization of DNAs attaching on the resonator surface

Fluorescence experiments are one of the most commonly used techniques to characterize the surface of microsphere resonators. A rhodamine-labeled protein on a microsphere resonator was characterized and described nicely in the work published by L. Pasquardini et al. [79]. In order to verify whether the pre-folded c-myc or pre-folded duplex were still stable and kept their pre-folded form on the surface, the resonators from the WGM experiment (after attaching the DNAs) were immersed in Thiazole orange (TO) solution; the dye can produce strong fluorescence only when bound to double strand (ds) or four strand DNA [55].

According to the result, Figure 4.16, it can be concluded that c-myc that was pre-folded into a G-quadruplex structure can bind onto the surface of the microresonator and was stabilized excellently. The highest fluorescent intensity was observed in pre-folded c-myc that was in the G-quadruplex structure, followed by the duplex. The mutated pre-folded G-quadruplex and duplex c-myc did not give high fluorescence intensity compared with non-mutated double and G-quadruplex forms.

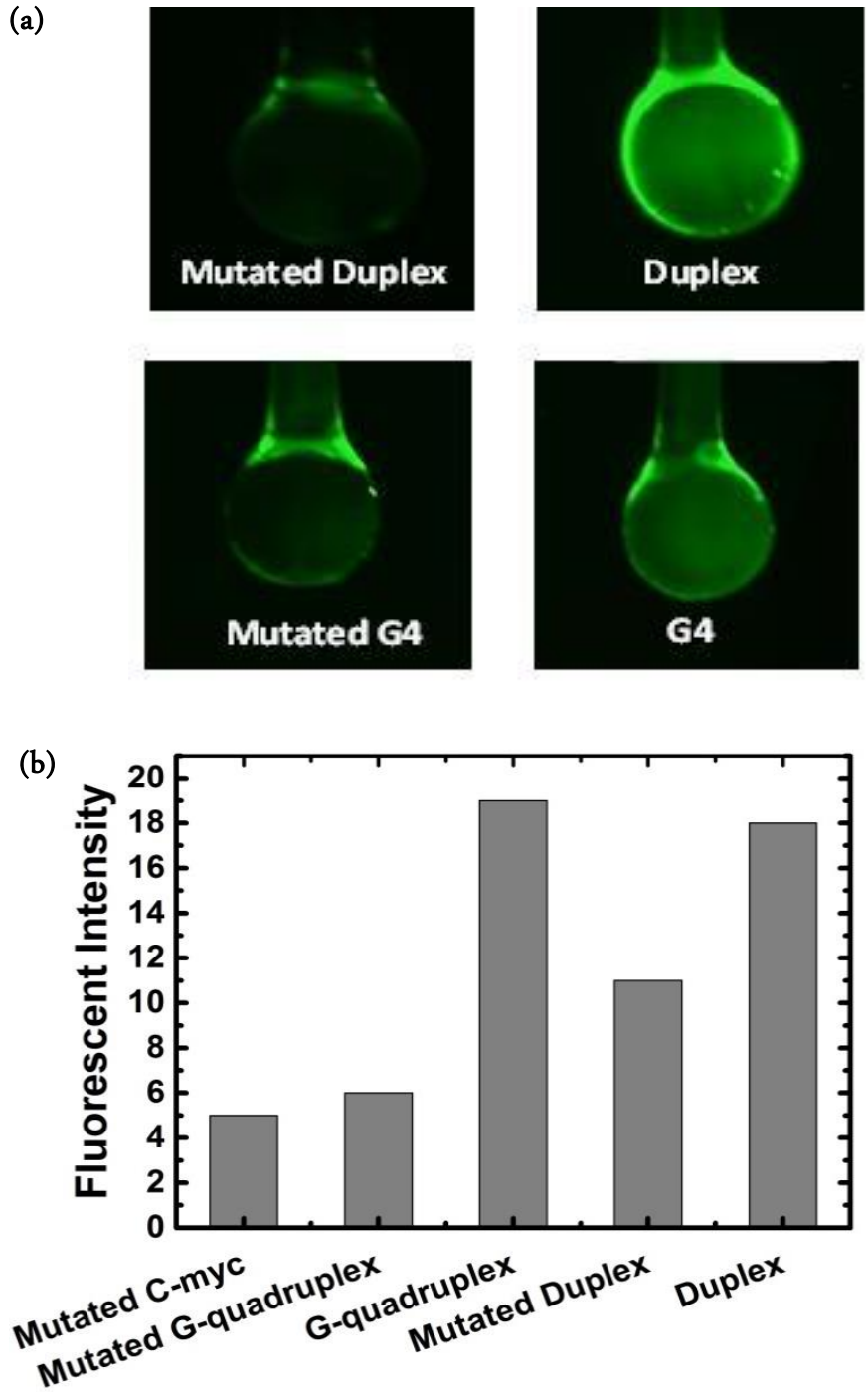
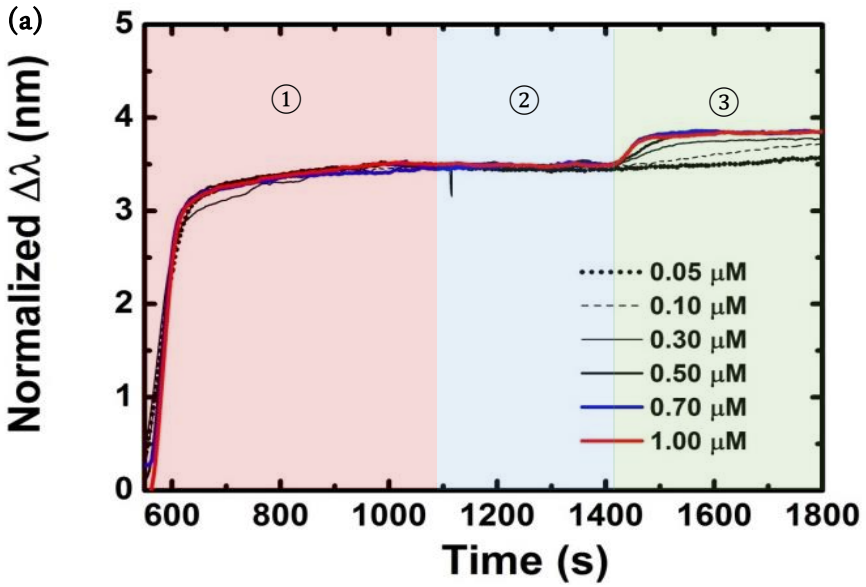


Figure 4.16 (a) Fluorescent image of a microsphere coated with different forms of c-myc after exposure to TO. Fluorescent intensity from a microsphere indicates the success of DNA attachment (b) fluorescent intensities values from each DNA form on the resonator. The picture is reprinted with permission from [2].

4.3.4. Kinetics of G-quadruplex binding from the WGM signal

Herein, the DNA concentrations were optimized to ensure the saturation of the G-quadruplex DNA on the surface i.e. all available streptavidin binding sites were occupied. Apart from the information about saturation, kinetic data of biotin-DNA and streptavidin can also be extracted. For the interaction of biotin-streptavidin, the association rate constant, k_a, was found to be 2.42×10^8 $M^{-1}s^{-1}$, which was in good agreement with the values reported in the literature for this interaction [80]. Figure 4.17 part (a) reveals that the normalized Δλ from each concentration of the DNA gradually increased and reached the plateau at different values. The higher the concentration the greater the normalized Δλ plateau that was produced until the surface became saturated; at that point there was no difference in normalized Δλ whether at 0.70 μM or 1.00 μM. The similar normalized Δλ values from these two concentrations suggest that the surface was already saturated at 0.70 μM. However, to ensure that all the receptors were engaged the concentration of 1.00 μM was subsequently used for the whole experiment.



① 25 μg/ml Streptavidin in 100 mM KCl in 10 mm Tris buffer

② 100 mM KCl in 10 mm Tris buffer

③ G-quadruplex in ②

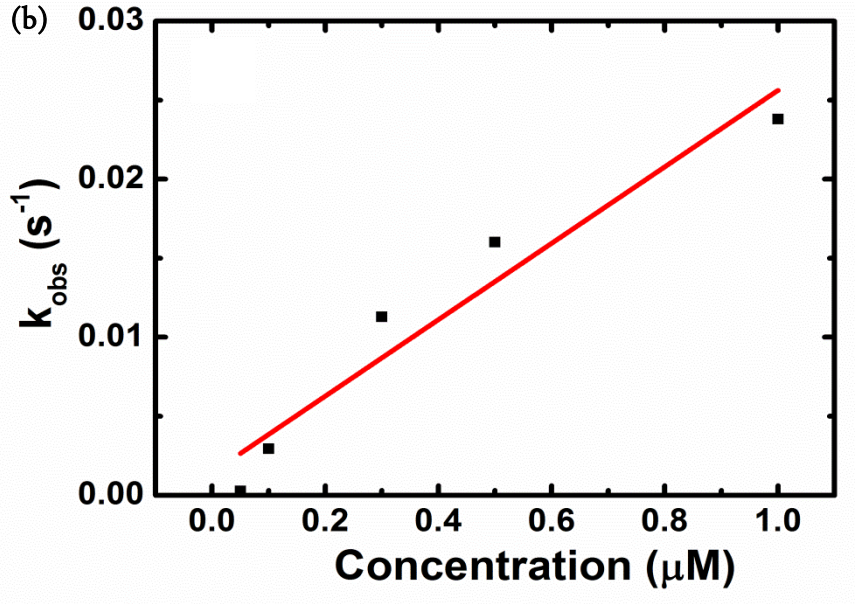


Figure 4.17 (a) WGM binding curve of the pre-folded G-quadruplex at different concentrations (b) k_a was found to be 2.42×10^8 $M^{-1}s^{-1}$ from linear regression. The picture is reprinted with permission from [2].

4.3.5 Mass transported limitation (MTL)

Turning now to the experimental evidence on the binding of ligands to G-quadruplexes on the WGM sphere surface sensor which can be described as in (4.1).

$$L_{bulk} \underset{\leftarrow k_m}{\overset{k_{m\rightarrow}}{}} L_{surface} + G4 \underset{\leftarrow k_d}{\overset{k_{a\rightarrow}}{}} G4L \tag{4.1}$$

There are two steps included in the G-quadruplex–ligand interaction as shown in Figure 4.18. First, the ligand is transported out of the bulk solution towards the surface of the resonator sensor, which is coated with G-quadruplex DNA.

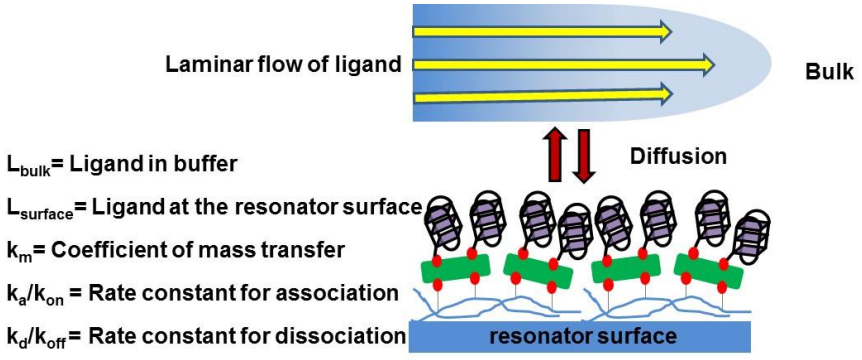


Figure 4.18 Schematic depiction of the two steps in the G-quadruplex–ligand interaction.

Second, the ligand in the laminar flow interacts with the G-quadruplex, inducing the resonance shift. The first step is also known as mass transfer and is carried out by convection and diffusion. The mass transfer depends on the flow cell dimension, the diffusion coefficient of the ligand and the flow rate of the bulk solution [81].

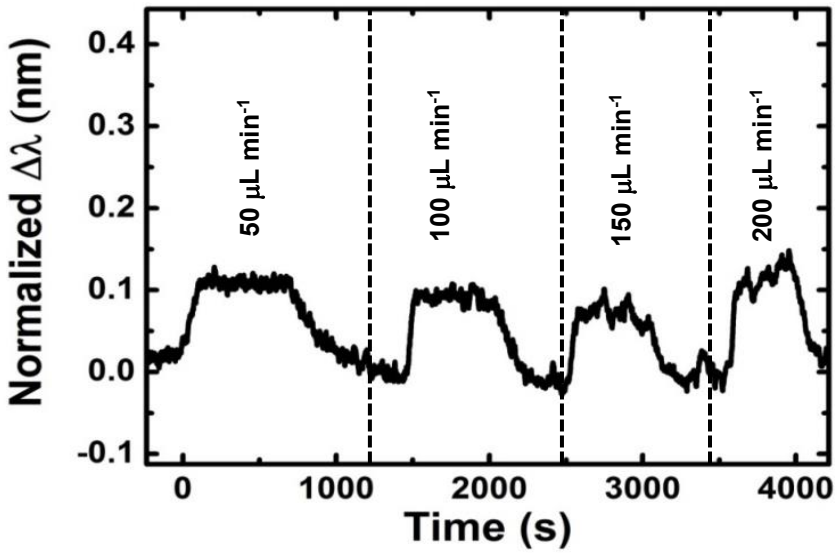


Figure 4.19 Kinetic analysis of the mass transfer limited interaction from the different flow rates when 1.5 μM Crystal violet (CV) interacts with G-quadruplex and k_{obs} were found at 1.04, 2.53, 1.67 and 1.79×10^{2} s^{-1}, respectively. The flow rate at 100 μL min^{-1} was chosen as the selected flow rate. The picture is reprinted with permission from [2].

To determine whether the reaction is mass-transport-limited or not, a fixed ligand concentration at different flow rates was monitored, Figure 4.19. If the binding curves are different, then the reaction is mass transport-limited. In this experiment, to ensure the rates are not perturbed by mass transport limitations, high flow rates at 100 μL min^{-1} were used to minimize the diffusion distance. The normalized Δλ, as seen in Figure 4.19, are independent from the flow rate so the interaction is not limited by mass transport.

4.3.6 Interpreting kinetic parameters of ligand binding to G-quadruplex or duplex DNA

The bimolecular interaction of ligand and G-quadruplex can be described as shown in Figure. 4.20, where G4 is G-quadruplex, L is ligand and G4L is a complex from the interaction between G-quadruplex and ligand.

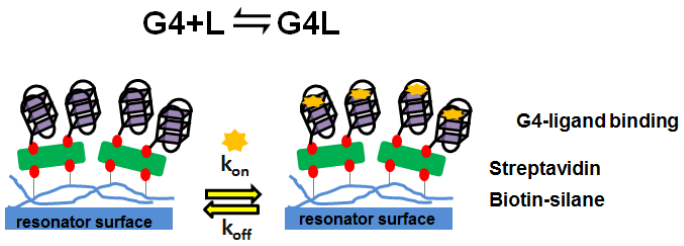


Figure 4.20 A schematic description of an interaction of ligand and G-quadruplex taking place on the WGM resonator surface. The picture is reprinted with permission from [2].

An equilibrium constant, designated by an upper case K, (where a lower case k refers to rate constant) is the ratio of the equilibrium concentrations of reaction products to reactants. Herein, for the bimolecular of ligand and G-quadruplex interaction, the equilibrium dissociation constant (K_d) or an equilibrium association constant (K_a), can be defined as shown below:

$$K_d = \frac{[G4][L]}{[G4L]} \tag{4.2}$$

$$K_a = \frac{[G4L]}{[G4][L]} \tag{4.3}$$

When the rates of the forward and backward reaction become equal, the reversible reactions reach equilibrium. At some point, there would be no longer any change in the concentrations of [G4], [L] or [G4L]. Consider the overall rate at which [G4L] changes for the reaction G4+L ⇋ G4L.

$$d[G4L]/dt = k_{on}[G4][L] - k_{off}[G4L] \tag{4.4}$$

If the reaction is initiated by mixing free G4 and free L, then the association rate ($k_{on}[G4][L]$) would dominate the reaction and the dissociation rate ($-k_{off}[G4L]$) would be negligible as there would be a very small amount of G4L complex. As more complexes form, however, the association rate (k_a or k_{on}) would begin to decrease and the dissociation rate (k_d or k_{off}) would increase because the concentrations of [G4] and [L] would decrease and that of [G4L] would increase. At some point the rates of the opposing reactions would become equal and there would no longer be any change in the concentrations of [G4L], [G4], and [L].

$$d[G4L]/dt = -d[G4]/dt = - d[L]/dt = k_{on}[G4][\ L] - k_{off}[G4L] = 0 \tag{4.5}$$

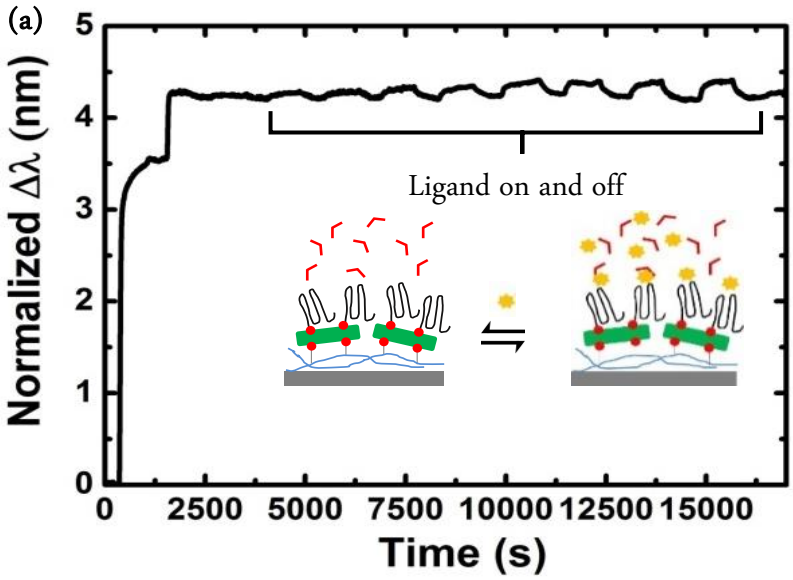
In this condition, the equilibrium concentrations of reactants and products will have a constant ratio which is equal to the ratio of the reverse and forward rate constant. In this case, K_D is called the equilibrium dissociation constant and can be defined as:

$$K_d = \frac{[G4][L]}{[G4L]} = \frac{k_{off}}{k_{on}} \tag{4.4}$$

The study of ligand interaction with G-quadruplex DNA has been paid enormous attention. Many ligands have been developed to specifically and selectively target these structures. This has led to the development of potential therapeutic agents, especially for anticancer agent [13]. A good way to monitor the interactions of ligands with G-quadruplexes is kinetic study. Kinetic fingerprints of target-drug binding can give a lot of useful information for drug discovery. Normally binding kinetics studies focus on two important parameters; the rate constants of ligand association (k_{on}) and ligand dissociation (k_{off}). The equilibrium dissociation constant of the ligand (K_d) can be established from the ratio of the dissociation to the association rate constant (k_{off}/ k_{on}) as shown in equation 4.4. All of these three parameters are intrinsic to the target-drug interaction question [82]. Equilibrium measurement of receptor-ligand binding is familiar to most biochemists. A simple one-step binding is described in Figure. 4.20.

4.3.6.1. Dissociation equilibrium constant (K_d)

Figure 4.21 part (a) shows the WGM response-binding events of different concentrations of Crystal Violet (CV) ligand from low to higher concentrations. When the wavelength shift reached a plateau, the ligand was replaced by a continuous flow of buffer before a higher ligand concentration was injected.



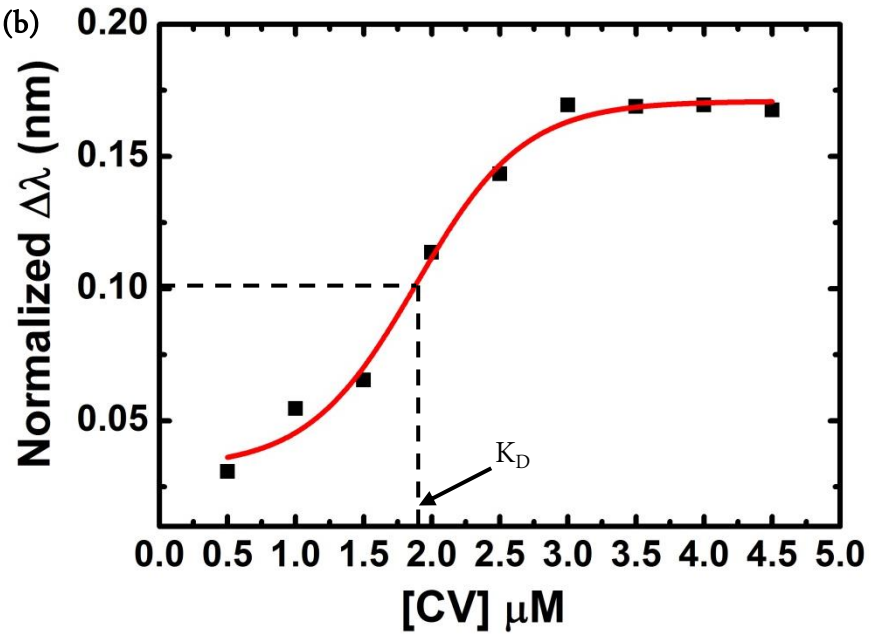


Figure 4.21 (a) Real time WGM binding curve and (b) sigmoidal binding curve illustrating K_D of CV. The picture is reprinted with permission from [2].

A binding curve illustrating K_D, which is equal to the ligand concentration at which the half maximal response is reached (a.k.a., EC_{50}), is fitted using Origin software where curves were fitted by the DoseResp model while sigmoidal curves were fitted by the Boltzman model Figure 4.21 part (b). The detail of both fitting models will be illustrated in next paragraph.

(1) Boltzmann model

Equation

$$y = \frac{A_1 - A_2}{1 + e^{(x - x_0)/dx}} + A_2$$

Meanings: A_1 = initial value, A_2 = final value, x_0 = centre, dx = time constant

The concentration at half response (K_D): $EC_{50}=\exp(x_0)$

Example of Boltzman model parameters from CV-G-quadruplex binding

Reduced Chi-Sqr		$4.0497E^{-5}$
Adj. R-Square		0.98722
	Value	Standard Error
A1	0.0321	0.01
A2	0.1709	0.00
x_0	**1.88**	0.08
dx	0.39	0.07

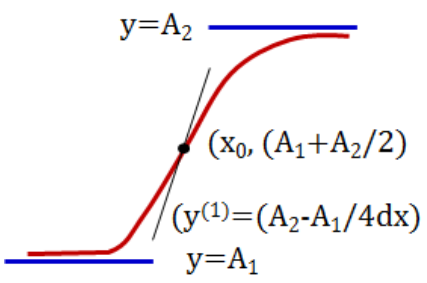


Figure 4.22 Example of Boltzman model parameters (left) and example of graph and parameter labelling (right). K_D value is highlighted in bold.

(2) DoseResp model

Equation

$$y=A_1+\frac{A_2-A_1}{1+10^{(\log x0-x0)p}}$$

Meanings: A_1 = bottom asymptote, A_2 = top asymptote, LOGx0 = centre, p = hill slope

LOGx0 = -5.0 (vary), p = 1.0 (vary)

The concentration at half maximal response (K_D): EC_{50}=10^LOGx0

Example of DoseResp model parameters from NS-G-quadruplex binding

Model	DoseResp	
Reduced Chi-Sqr	8.8723E-4	
Adj. R-Square	0.9588	
	Value	Standard Error
A_1	0.0079	0
A_2	0.3764	0
LOGx0	1.71	0.5
p 2.11	0.40	
span	0.3685	0
EC50	**51.40**	5.54

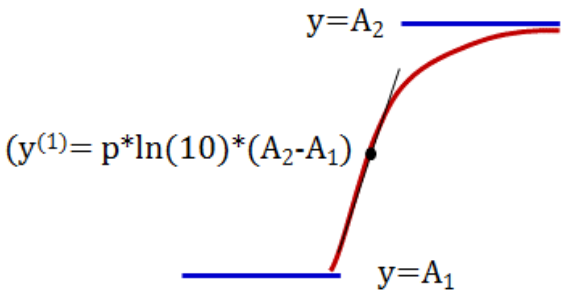


Figure 4.23 Example of DoseResp model parameters (left) and example of graph and parameter labelling (right). K_D value is highlighted in bold.

All WGM data were also re-fitted using a different software called Matlab. Each ligand K_D was calculated twice from independent data parameters (observed peak height, and observed binding slopes). The former was obtained with an automated 'findpeaks' function and plotted to a Dose Response Curve, where the K_D value is given by the EC_{50} value, i.e. the concentration of ligand that gives a response value of 50% of the maximum. The latter was obtained by fitting a two-term polynomial to the association curves to give initial binding slope (a.k.a. the observed rate constant, k_{obs}), and plotted against a linear fit to give gradient (k_{on}) and intercept (k_{off}). Equilibrium constants ($K_D = k_{off}/k_{on}$) were then calculated for each ligand. The two different methods provided K_D values in mostly good agreement (and the K_D was further validated in additional fluorescence experiments). All new K_D values and more detail about the fitting can be found in [2].

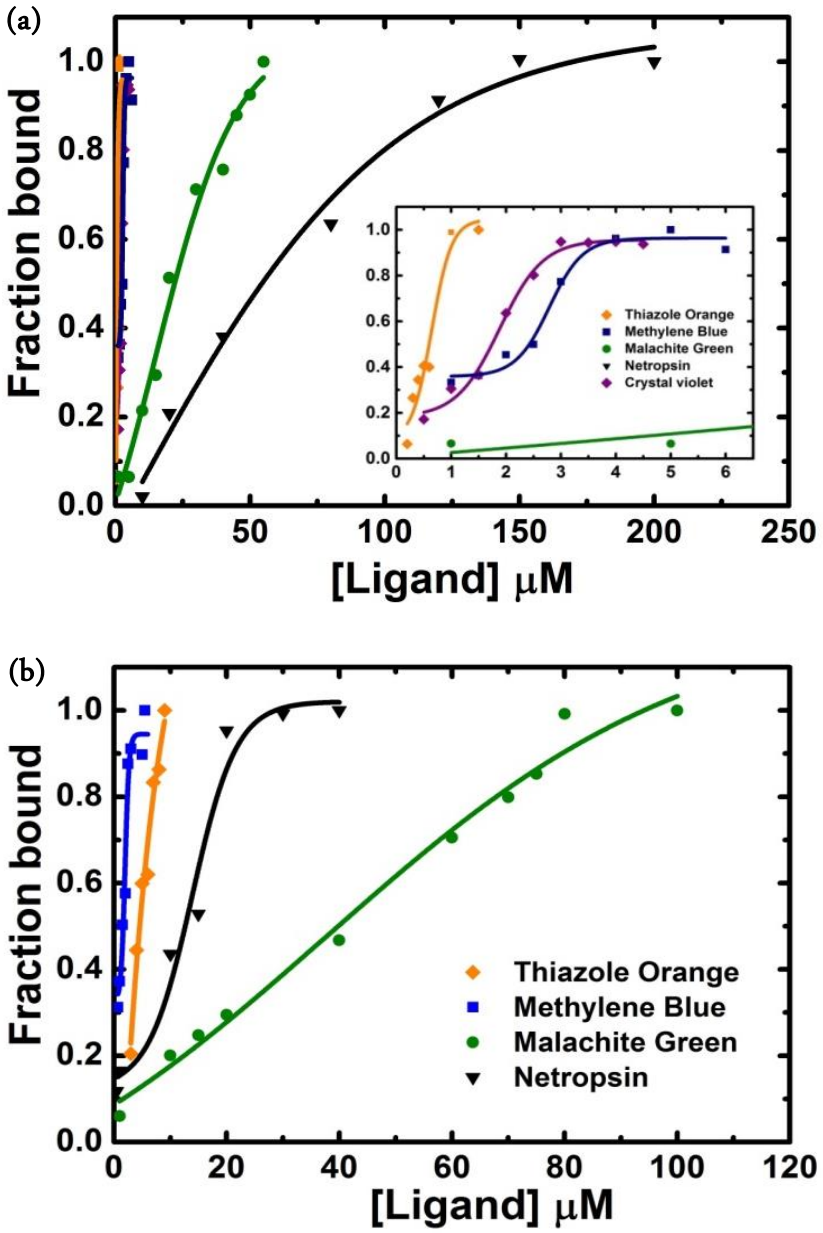


Figure 4.24 Fraction bound of different ligands with (a) G-quadruplex and (b) duplex in order to estimate K_D.

By comparing the affinity of the ligand to G-quadruplex and duplex c-myc, five selected ligands were studied as shown in Figure 4.4. The results in Figure 4.24 part (a) show bimolecular binding curves of five selected ligands with G-quadruplex and (b) duplex. It is obvious that NS can bind to duplex better than G-quadruplex whereas TO can bind both G-quadruplex and duplex equally well. More details about the binding affinities of the five ligands will be discussed in section 4.3.7.

4.3.6.2 Association and dissociation rate constants (k_{on} and k_{off})

If either k_{off} or k_{on} are slow on the time scale of the experiment, the concentration of G4L over time appears to follow a pseudo-first–order process described by the observed pseudo-first-order rate constant k_{obs}.

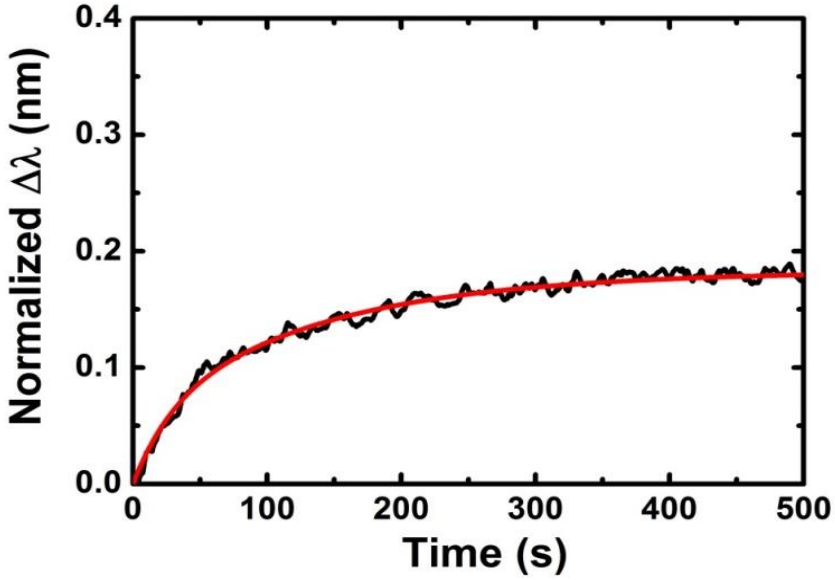
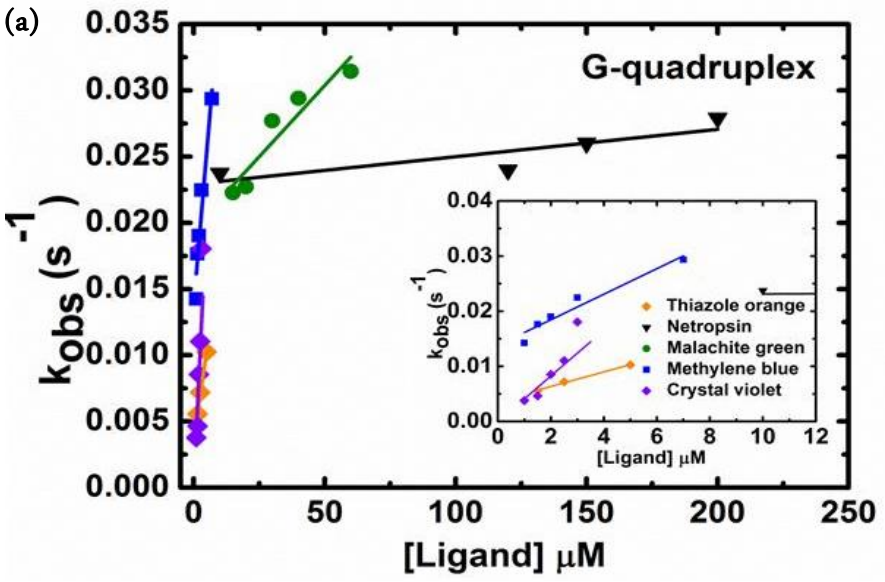


Figure 4.25 Example of curve fitting from 4 μM CV interacting with G-quadruplex by using a pseudo-first-order equation.

A plot of k_{obs} as a function of ligand concentration is linear with a slope equal to k_{on}, see Figure 4.26. The binding between DNA and the selected ligand can be described by a mono-exponential growth equation or pseudo-first-order reaction as shown in Equation 3.5



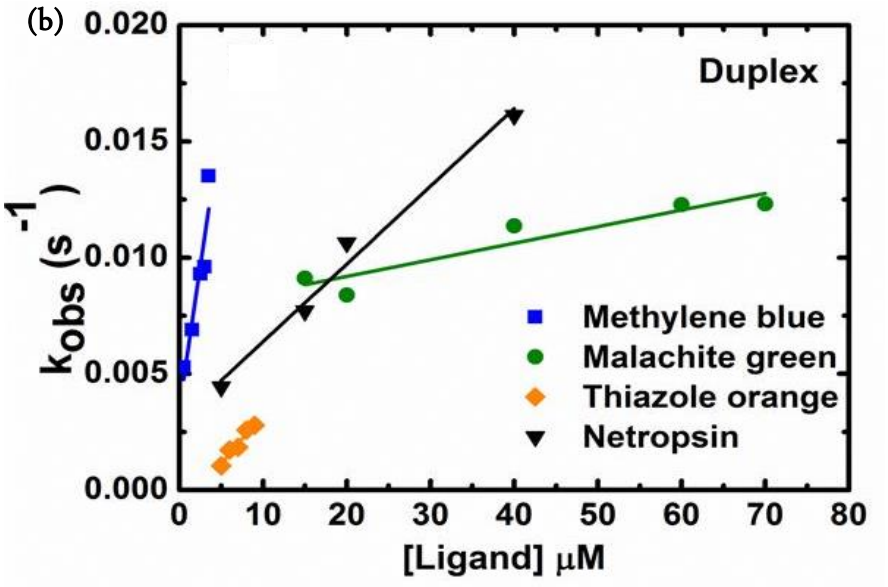


Figure 4.26 Plots of k_{obs} as a function of ligand concentration with WGM functionalized with either G-quadruplex (a) or (b) duplex DNA.

4.3.7 Binding affinities for selected five ligands

Herein, five ligands which are known to bind preferentially to different forms of DNA were selected and examined including CV, MB, TO, MG and NS. The reason behind choosing these five ligands is that this is the first time that WGM has been developed as a sensor for G-quadruplex-ligand binding so it was necessary to use ligands which had their ligand affinity already published so we could verify our system from these results.

A summary of binding affinities for the five ligands tested is given in Table 4.2 and shows good agreement with values published in the literature, for those that are available (shown in parentheses). Experimentally, as expected, TO and MG both bind to G4-DNA with a moderate specificity, MB binds to both duplex and quadruplex DNA with comparable affinities and NS preferentially binds to duplex DNA. CV was shown to bind quadruplex DNA with high specificity, with no binding to duplex DNA being detectable at ligand concentrations up to 12 μM, which is in agreement with the work of Kong *et al.* [51].

The data in Table 4.2 reveals the binding affinity of five ligands. The smaller the K_D the higher the ligand's affinity to DNA. The order of ligand affinity to G-quadruplexes according to K_D values from smaller to larger was TO>CV>MB>MG>NS. On the other hand, the order of ligand affinity to duplexes according to K_D value was MB>TO>NS>MG. Additionally k_{on} can be used to estimate the order of ligand affinities. The trend of k_{on} of the ligands to G-quadruplexes was CV>MB>TO>MG>NS and for duplexes was MB>NS>TO>MG. Taken together, we can conclude that the affinities of ligand to duplex was MB>TO>NS>MG, in which both K_D and k_{on} agreed with each other. However, the order of TO to G-quadruplex and duplex were alternated.

Table 4.2. The comparison of K_D, k_{on} and k_{off} between G4 and duplex obtained by the WGM sensors. The table is reprinted with permission from [2].

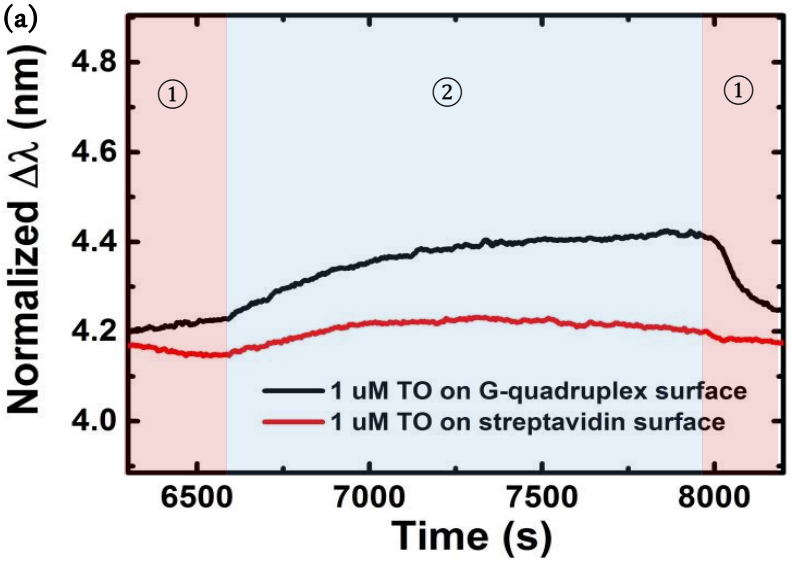
	G-quadruplex			Duplex		
	K_d (μM)	k_{on} ($\times 10^6$ M^{-1} s^{-1})	k_{off} (s^{-1})	K_d (μM)	k_{on} ($\times 10^6 M^{-1}$ s^{-1})	k_{off} (s^{-1})
Crystal violet	1.90	0.00698	1.32×10^{-2}	*	*	*
Methylene blue	2.80 (4.00) [54]	0.00586	1.64×10^{-2}	1.97	0.00162	3.19×10^{-3}
Thiazole orange	0.62 (0.30-3.00) [47]	0.00132	8.11×10^{-4}	2.87 (0.30-3.00) [47]	0.00043	1.23×10^{-3}
Malachite green	19.08 (2-35) [47]	0.00019	3.62×10^{-3}	51.44 (>50) [47]	0.00006	3.08×10^{-3}
Netropsin	51.39	0.00002	1.02×10^{-3}	7.54	0.00033	2.48×10^{-3}

* Cannot be estimated because at high ligand concentration (>12 μM), the transmission spectrum was disappeared because of no resonance wavelength peak occurs from high polarizability of CV; the values in brackets are extracted from the literature.

4.3.8 Control and competition experiment

4.3.8.1. Control experiment

In terms of validating the signal, this control experiment is a crucial part of the investigation and was set up to ensure that there is no false positive interfering with the signal. Herein, the resonator was functionalized with the same process as used for studying G-quadruplex-ligand interaction (biotinylated-APTES and then streptavidin); except there was no DNA on the surface, in order to perceive the artefact signal from ligand binding. TO was selected as a candidate ligand.



① 100 mM KCl in 10 mM Tris buffer ② 1 μM TO in ①

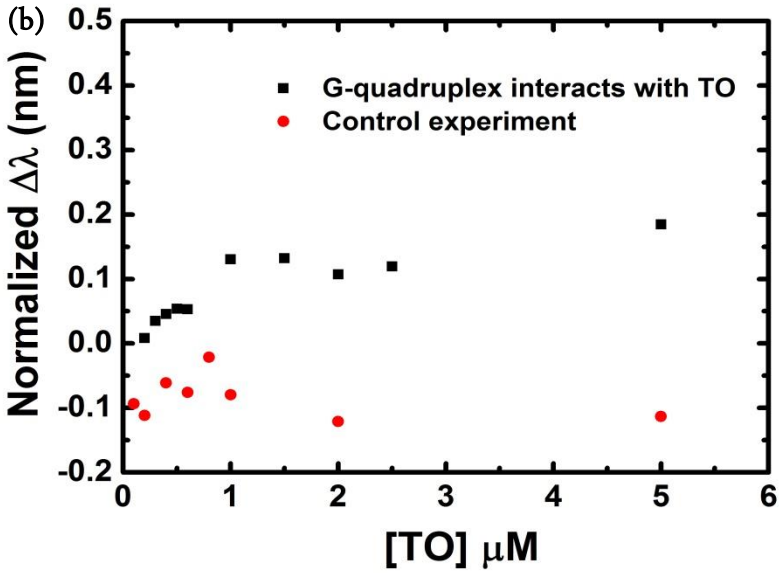


Figure 4.27 (a) Binding curve of TO to resonators with and without G-quadruplex (b) normalized wavelength shifts illustrate differences in the signal from ligand binding with and without G-quadruplex (control experiment). The picture is reprinted with permission from [2].

The result in Figure 4.27 part (a) provides a binding curve from the TO ligand comparing between with and without G-quadruplex on the surface. There was a large normalized Δλ from G-quadruplex surface binding with TO whereas normalized Δλ was negligible when G-quadruplex was absent on the surface. Figure 4.27 part (b) compares the result obtained from the control experiment and the binding of TO with G-quadruplex at different concentrations. From the data in Figure 4.27, it is apparent that the signal is from ligand binding.

4.3.8.2. A duplex-quadruplex competition experiment

A competition experiment is a useful tool for the study of the binding selectivity of ligands to different DNA structures. Instead of looking at only the interaction of ligand with the DNA on the surface of resonator, herein duplex-quadruplex competition was also studied. The experiments are an efficient and relevant way of assessing the ability of small molecules to discriminate between quadruplex and duplex DNA.

1. Competition of the ligand that has an ability to bind only G-quadruplex

Herein, CV was chosen as a representative ligand as CV has one of the highest specific binding affinities to G-quadruplexes according to our findings, Table 4.2. In addition, the work reported by D. M. Kong also supported the finding that CV can discriminate G-quadruplex from duplex [51]. In order to compare the binding affinity of CV to G-quadruplex or duplex, the "reference" competitor used in this experiment was Calf Thymus (CT) DNA. Here, binding of CV to G-quadruplex DNA was carried out in the absence and in the presence of Calf Thymus (CT) DNA as a competitor (CV and CV*, respectively).

In order to compare the signal from the competition, the concentration of ligands was fixed (5 μM for CV). The signal from CV was monitored in 10 mM Tris·HCl in the presence of 100 mM KCl, then the buffer was switched to 10 mM Tris·HCl in the presence of 100 mM KCl plus 10 μg mL^{-1} of the random sequence of duplex, CT. CV* (the same concentration as CV) were dissolved in the same buffer which contained CT duplex to maintain the surrounding medium composition. There is no significantly different mean signal (n=3) between CV and CV*.

The results, Figure 4.28, show that the WGM binding curve of CV to G-quadruplex attached on the surface was not affected when competitor DNA was present in the surrounding medium at high concentration, thus confirming highly specific binding of CV to G-quadruplex DNA.

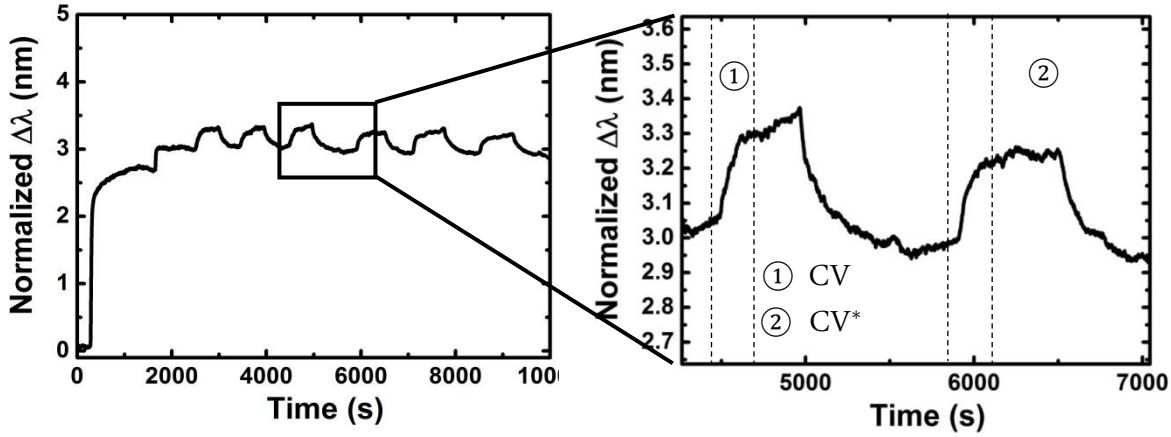


Figure 4.28 Competition experiment for ligand binding. CV can bind specifically to G-quadruplex. The picture is reprinted with permission from [2].

2. Competition of the ligand that has an ability to bind both G-quadruplex and duplex

On the other hand, MB can bind both G-quadruplex and duplex so in this experiment MB was selected as a candidate ligand. MB binding to the G-quadruplex-functionalized WGM resonator was completely inhibited in the presence of competitor CT-DNA and no wavelength shift could be detected Figure 4.29. This result can be explained by the fact that MB, previously shown to bind with comparable affinities to both duplex and quadruplex DNA, would no longer be available to interact with immobilized G-quadruplex DNA when already complexed with a large excess of CT duplex DNA in solution. Taken together, these results suggest that our established WGM platform is suitable for studying the ability of ligands to discriminate between G-quadruplex and duplex.

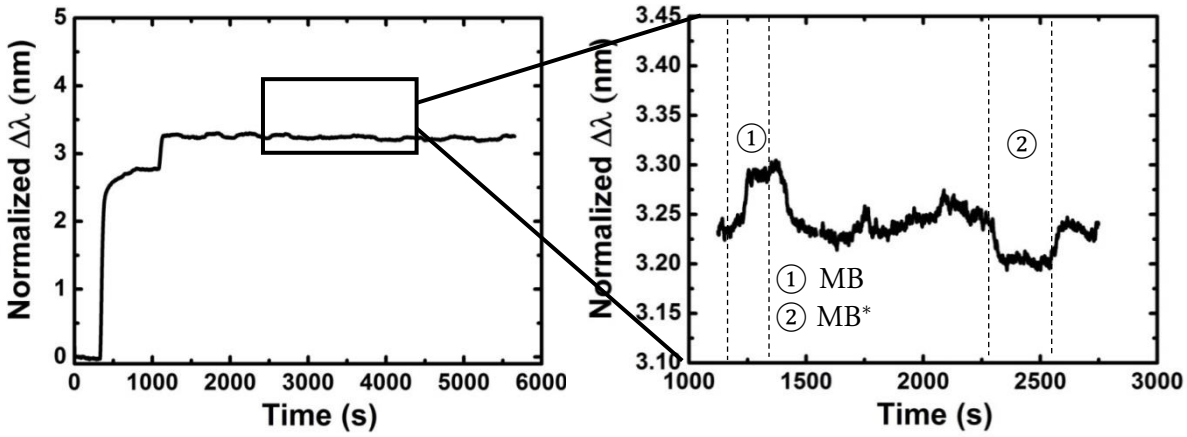


Figure 4.29 Competition experiment between G-quadruplex (on the surface of the resonator) and duplex in the surrounding medium; with MB, which can bind both G-quadruplex and duplex. The picture is reprinted with permission from [2].

4.3.9 Discriminate different forms of c-myc by WGM

As described in section 4.3.2, different forms of c-myc and mutated c-myc including single strand, ss (c-myc, mutated c-myc), double strand, ds (duplex, mutated duplex which is actually not a duplex) and pre-folded c-myc (G-quadruplex) or four strand, were continuously flowed in the WGM system and was monitored to obtain real time binding curves. The normalized Δλ results obtained from the real time binding curve of different forms of DNAs can be compared and shown in Figure 4.30. The normalized Δλ of pre-folded c-myc or G-quadruplex was higher than duplex which was already mentioned in section 4.3.2. Overall, these results indicate that different strand numbers (i.e. single or double) of c-myc provided individual profiles of normalized Δλ. Additionally, we attempted to fold c-myc in 10 mM Tris buffer in the presence of 10 mM KCl without annealing, the evidence from normalized Δλ of c-myc in KCl for 2 nights

indicates that G-quadruplex can possibly form but further experiments are required to confirm this.

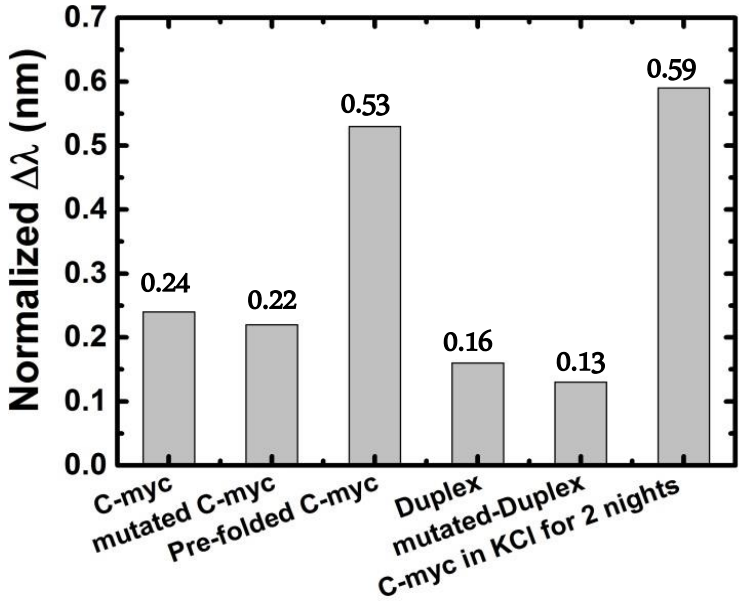


Figure 4.30 Normalized Δλ from different structures of c-myc in 10 mM Tris buffer pH 7.4 containing 10 mM KCl from real time binding curve WGM.

4.3.10 Attempting to fold and unfold G-quadruplex on the resonator surface

The key advantage of WGM over most other techniques is that the interaction can be monitored in real time, hence the idea of this study was to observe each single step in real time starting from attaching single-stranded c-myc, then trying to fold this single strand into a G-quadruplex form. Figure 4.31 illustrates the folding and unfolding of c-myc. WGM was used to discriminate between folded and unfolded states of G-quadruplex region of the c-myc promoter, with the used buffer being changed from 10 mM Tris to 10 mM Tris in the presence of 10 mM KCl in order to fold c-myc to its G-quadruplex form. We expected that this folding and unfolding could be performed cyclically on the surface of the resonator, as shown in Figure 4.31. However, a problem was that after increasing the KCl concentration, it could not be ascertained whether the accompanying signal change was due to the c-myc folding or the salt itself (WGM is sensitive to salt). In order to ascertain this, another experiment was designed.

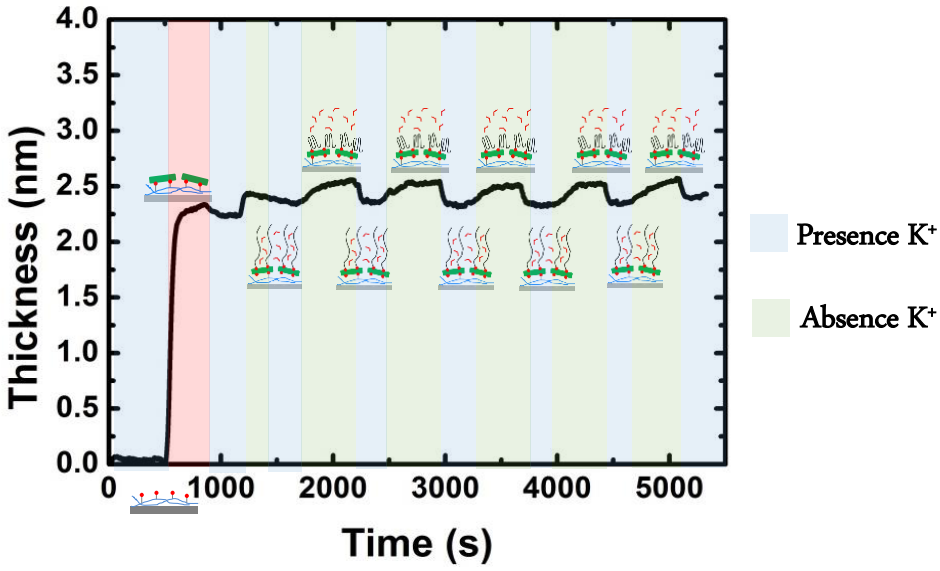


Figure 4.31 Folding and unfolding cycles of 2 μM c-myc on the surface using 10 mM Tris buffer pH 7.4 containing 10 mM KCl.

4.3.10.1. Compare with mutated c-myc

Upon binding of K^+, c-myc folds into a more compact conformation, the G-quadruplex. The final estimated layer thickness was found to be 0.53 nm (see Figure 4.30). When K^+ is flushed out the unfolded DNA should be formed. This can be conducted as a cycle. Only c-myc DNA can form a G-quadruplex upon binding of K^+, whereas mutated c-myc DNA cannot. Upon binding of K^+, the value of normalized $\Delta\lambda$ from non-mutated c-myc was found to be higher than mutated c-myc, Figure 4.30, which suggests that the signal might come from the compact structure of G-quadruplex, which interacts more with the evanescent field close to the surface, as previously mentioned in section 4.3.2. However, these results need to be interpreted with caution as to the normalized $\Delta\lambda$ which is related to the thickness. The thickness of c-myc before folding and after folding was found to be ~0.36 nm (the thickness of c-myc after folding supposes to be ~0.6 nm according to Figure 4.30) which is less than the dimension of the G-quadruplex which is ~0.6-0.7 nm [74]. The reason for this is not clear but it is possible that not every molecule of c-myc on the surface folded into G-quadruplex without annealing. This can be explained from the process of folding c-myc into a G-quadruplex. Briefly, in order to fold c-myc, the nucleotide needs to be heated to 95°C for 5 minutes and then annealed to room temperature slowly for 1 night. Based on this process, we can speculate that folding c-myc on the resonator was not complete without heating and even then the process of folding is very slow. Tracking c-myc folding into G-quadruplex by attaching c-myc on the resonator surface and binding with K^+ might be possible but we cannot currently fold all the c-myc into its G-quadruplex form. Therefore further investigation needs to be conducted.

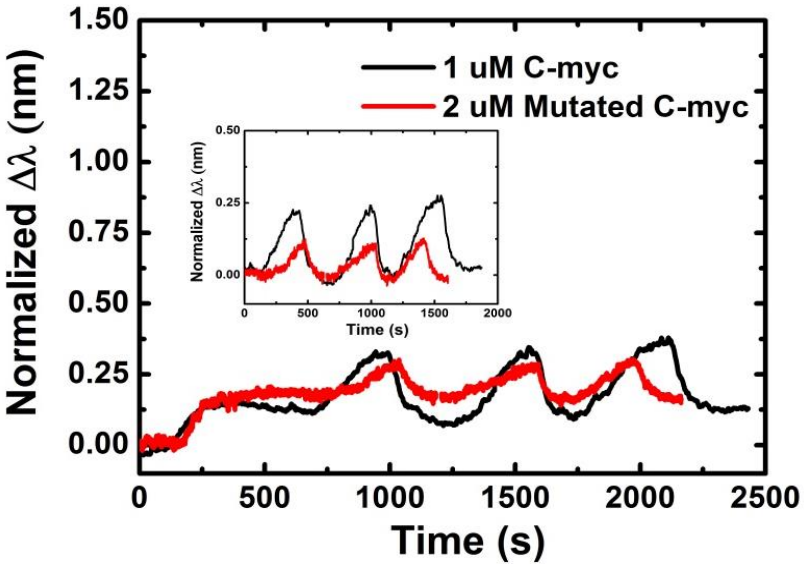


Figure 4.32 Unfolding and folding cycle comparing c-myc and mutated c-myc. The inset picture is the same data with the baseline subtracted.

4.3.10.2. Varying concentration of c-myc

Another experiment was also designed to verify whether it is possible to fold c-myc on the resonator surface to a G-quadruplex form. The normalized Δλ should increase after binding with K^+, and increase with surface concentration of c-myc. Figure 4.33 illustrates the folding and unfolding cycle with different concentrations of c-myc. The signals after flowing KCl were different at different concentrations of c-myc. However, these data must be interpreted with caution because WGM is sensitive to KCl. As a result the signal change might be due to two reasons; (i) KCl (ii) folded c-myc, as was mentioned before. The normalized Δλ is expected to increase with increasing concentrations of c-myc. In fact the normalized Δλ after binding with K^+ of 1.0 μM c-myc was higher than 0.1 μM c-myc. This indicates that some aspect of the signal is from folded c-myc. However, at 2.0 μM of c-myc the normalized Δλ after binding with K^+ was less than 1.0 and 0.1 μM. It is therefore likely that such a connection does not exist between c-myc concentration and the amount of G-quadruplex. Finally, the normalized Δλ was still less than 0.6 nm, which is key evidence against the formation of G-quadruplex.

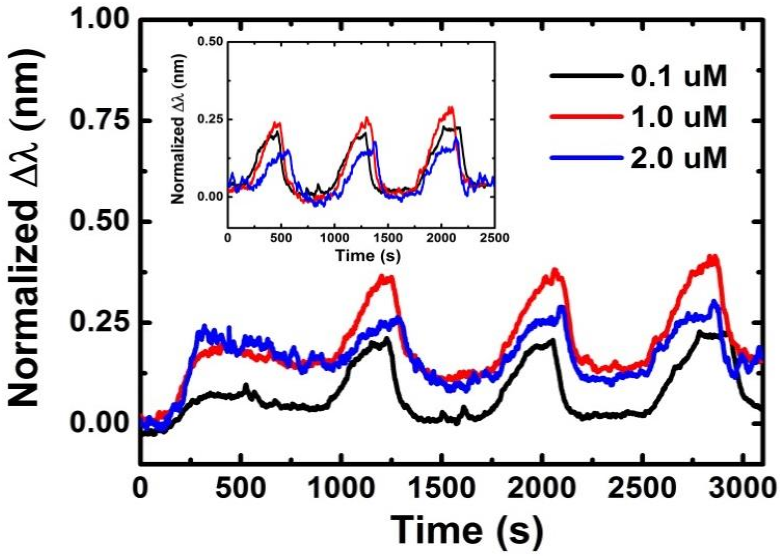


Figure 4.33 Unfolding and folding cycles from different concentration of c-myc; 0-500s shows the binding of different concentration of c-myc then the cycle started from 750s. The inset picture is the same data with the baseline subtracted.

4.3.10.3. Fluorescence experiment

We finally attempted to demonstrate the possibility of folding c-myc into its G-quadruplex form on the surface without annealing by submerging a c-myc resonator in 10 mM Tris buffer in the presence of 10 mM KCl in order to pre-fold the DNA for 2 nights. Then the resonator was tagged with TO to examine whether the G-quadruplex was formed. The fluorescence intensity from non-mutated c-myc in 10 mM Tris buffer in the presence of 10 mM KCl was higher than mutated-c-myc, which cannot fold into the G-quadruplex structure, Figure 4.34. This indicates the formation of some G quadruplex structures. However, using microscopy we cannot confirm that all of the c-myc DNA folded into G-quadruplexes or how many of them can fold, which can affect the kinetic fingerprint and layer thickness.

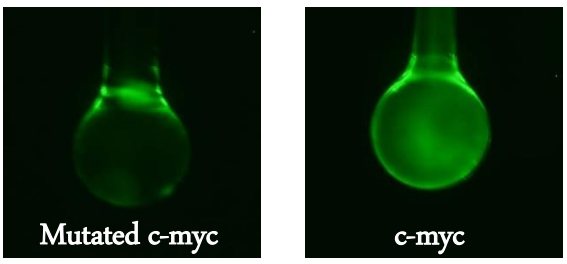


Figure 4.34 Functionalised fluorescent resonators after interaction with TO, which can bind specifically to double strand and G-quadruplex DNA. The picture is reprinted with permission from [2].

To sum up on the question of folding c-myc on the surface and monitoring folding in real time; the results of this study indicate that it is likely that some fraction of c-myc on the surface can be folded into the G-quadruplex form by KCl, but not 100 percent (the normalized Δλ was less than expected), and moreover, with a very slow kinetic of folding without annealing (or even with annealing, which requires at least one night). This makes it is very difficult to detect this folding process in real time. These results indicate this technique may not be applicable for studying the ligand interaction, so we decided to pre-fold c-myc into the G-quadruplex form or hybridize to duplex form before attaching on the surface for the ligand interaction work.

4.3.11 Hybridization of c-myc and pre-folded c-myc with complementary strand on the resonator surface

In section 4.3.9, we discriminated different forms of c-myc by WGM, and Figure 4.30 illustrates different normalized Δλ from different c-myc forms from single strand or pre-folded or hybridized c-myc. In order to hybridize single strands of c-myc to double stranded or duplex structures, the complementary strand was continuously flowed into the WGM platform at different concentrations from 6, 25 and 30 μM. The results from Figure 4.35 suggest that a link may exist between different forms of c-myc and normalized Δλ.

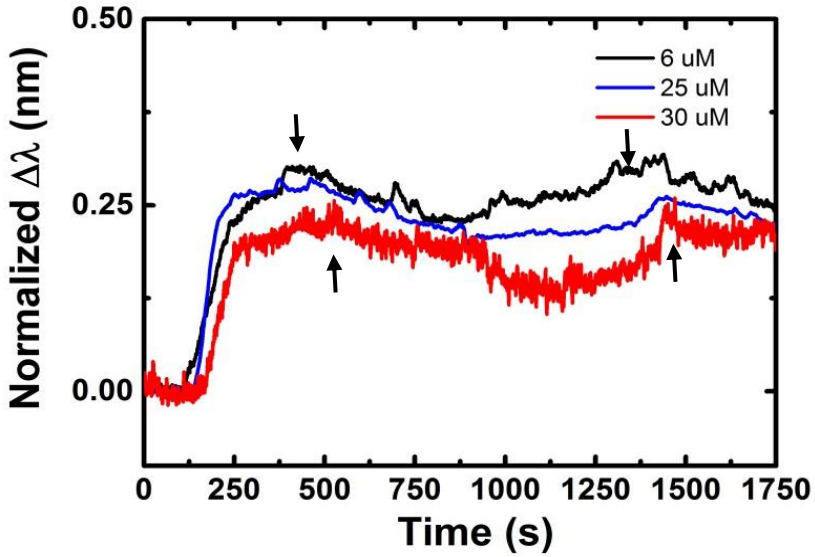


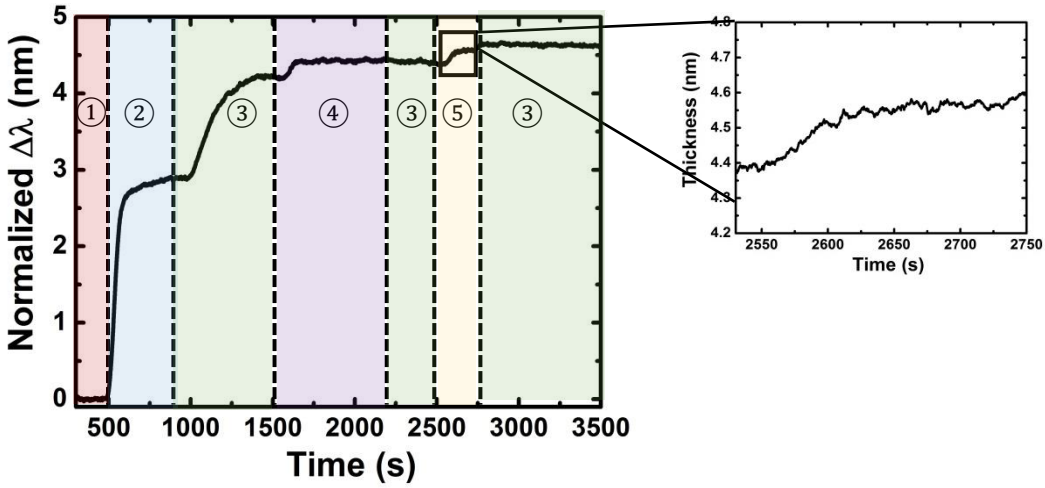
Figure 4.35 Hybridization of 1 μM c-myc (single strand) with its complementary strand at different concentrations. The arrows indicate when the complementary strand is introduced in the system and when the complementary strand is flushed out.

The normalized Δλ of G-quadruplex (~0.6 nm) or single stranded c-myc (~0.24 nm) were higher than the duplex (~0.16 nm). However, there was only a very minute difference in the normalized Δλ when the complementary strand was added to c-myc DNA at 6 μM. Indeed,

in other DNA work using WGM, binding with the complementary strand did not induce a large shift, as reported by W. Yuquang *et al.* [84].

Incidentally, the normalized Δλ from Figure 4.30 illustrates that the normalized Δλ from the duplex was found to be less than single stranded c-myc, so we therefore expected that if the duplex is formed on the surface, the normalized Δλ should decrease from 0.24 nm to 0.16 nm. When the concentration of complementary strands was increased more than 10 times that of the DNA concentration, the WGM signals decreased; this finding perfectly fits our hypothesis, and therefore it seems likely duplex can form on the surface. On the other hand, the induced shift of the resonant mode from c-myc to duplex was not large enough to be used for estimating the successful hybridization. This is an important issue for further experiments and further work is required to establish this.

The next strategy to evidence the hybridization of c-myc with its complementary strand is unfolding G-quadruplex into its duplex form in Li^+ instead of K^+. It is well known that G-quadruplex is not stable and can be unfolded in the presence of Li^+ [85].



① 10 mM KCl in 10 mM Tris buffer ② 25 μg/ml streptavidin dissolved in ①

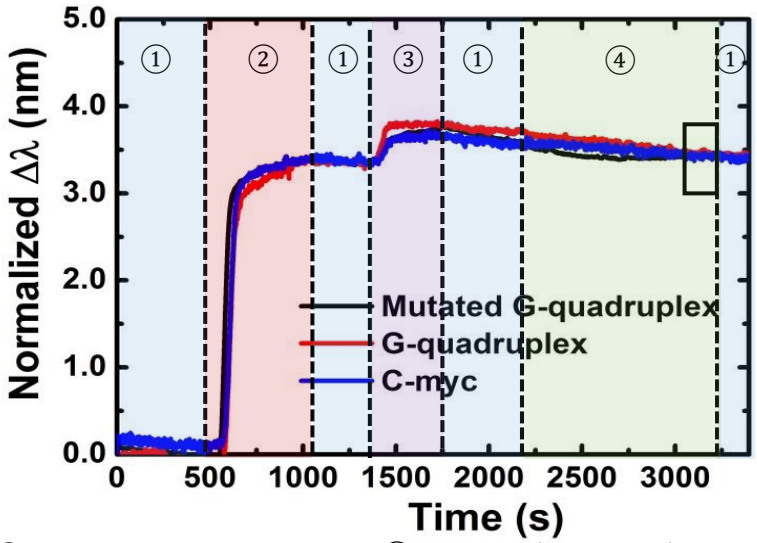
③ 100 mM LiCl in 10 mM Tris buffer ④ 1 μM G-quadruplex in ③

⑤ 2 μM complementary strand in ③

Figure 4.36 WGM binding curve from attempting to unfold G-quadruplex by Li^+ and hybridize to the duplex form using its complementary strand.

After stabilizing the system with 100 mM LiCl, the surface was then coated with G-quadruplex. The complementary strand was added to hybridize c-myc in order to form a duplex. The normalized Δλ from the binding of DNA with this complementary strand was found to be 0.17 nm, which correlated to the normalized Δλ of hybridized duplex at 0.16 nm (see Figure 4.30). The G-quadruplex was unfolded by replacing Li^+ with K^+ (see Figure 4.36). It was observed

that c-myc in G-quadruplex form, (red line), once unfolded by Li^+ cannot fold back into G-quadruplex according to the normalized Δλ which was less than the normalized Δλ of G-quadruplex form. This is strong evidence that although binding with 10 mM KCl in 10 mM Tris buffer cannot fully fold c-myc on the surface to its G-quadruplex structure, it is possible to unfold G-quadruplex on the surface according to the result in Figure 4.36 and 4.37. The normalized Δλ from unfolded G-quadruplex (red line at 3000s) decreases to the same value of single strand (black and blue). However, changing the salt composition in buffer (from Li^+ to K^+) makes the technique too complicated because WGM is also sensitive to salt. Consequently, to ensure that the normalized Δλ is from only the binding of the target molecules of interest it will be better to keep the buffer component consistent.



① 10 mM KCl in 10 mm Tris ② 25 μg/ml streptavidin
③ 1 μM DNA in ① ④ 10 mM LiCl in 10 mm Tris buffer

Figure 4.37 Unfolding G-quadruplex by replacing K^+ with Li^+.

To summarize, in section 4.3.10 and 4.3.11, folding and hybridization of c-myc on the surface was demonstrated. Unfortunately, these results were rather disappointing. These findings will doubtless be much scrutinized, but there are some conclusions.

(1) In terms of folding and hybridization of DNA, it is well known that the DNA needs to be annealed near its T_m before adding the complementary strand then cooling down very slowly to room temperature. This process makes using the WGM sensor to observe both processes in real time too difficult and complicated. Even though WGM is a powerful technique, this reaction on the surface is beyond the bounds of possibility.

(2) Switching the buffer component (from absence to presence of KCl or LiCl) is not convenient and too complicated for interpreting the resulting data.

4.4 Conclusion

This chapter demonstrated the use of WGM as a novel biosensor for tracking kinetic fingerprints from G-quadruplex-ligand interactions. Due to intense interest in the field, many techniques have been used to study this interaction before. Amongst them, SPR seems to be the best technique; so many publications have been published using it. WGM and SPR offer similar technical advantages such as real time analysis, and easy tracking of kinetic fingerprints. However, using a gold microchip in SPR is more complicated than functionalization of a glass sphere in WGM. As a result, WGM is one of the most promising alternative techniques for studying G-quadruplex-ligand interaction.

Returning to the hypothesis of this work, this project was undertaken to apply all the advantages of WGM sensing to solve a key problem in DNA research. We aimed to develop a novel biosensor for interrogating G-quadruplex function/structure and investigating G-quadruplex DNA/ligand interaction in real time. We can track the real time binding curves from DNA; however, folding c-myc into G-quadruplex on the surface was difficult. Hybridizing c-myc G-quadruplex or duplex is quite straightforward in solution, but according to our results hybridizing DNA on the surface could not induce changes in WGM signals.

Finally, the application of WGM sensors for real-time monitoring of small molecule binding to either duplex or quadruplex DNA was successful for the first time. Five known ligands were tested and showed DNA-binding profiles comparable to the data available in the literature, thus validating our technology. When compared to existing technologies we have demonstrated that WGM was highly sensitive, required minimal volumes of DNA and ligand and was suitable for real-time monitoring of DNA-ligand interactions. It also provides access to the same kinetic parameters as the gold standard SPR for only a fraction of the cost. The summary of the G-quadruplex experiments with varying degrees of success is shown in the diagram below.

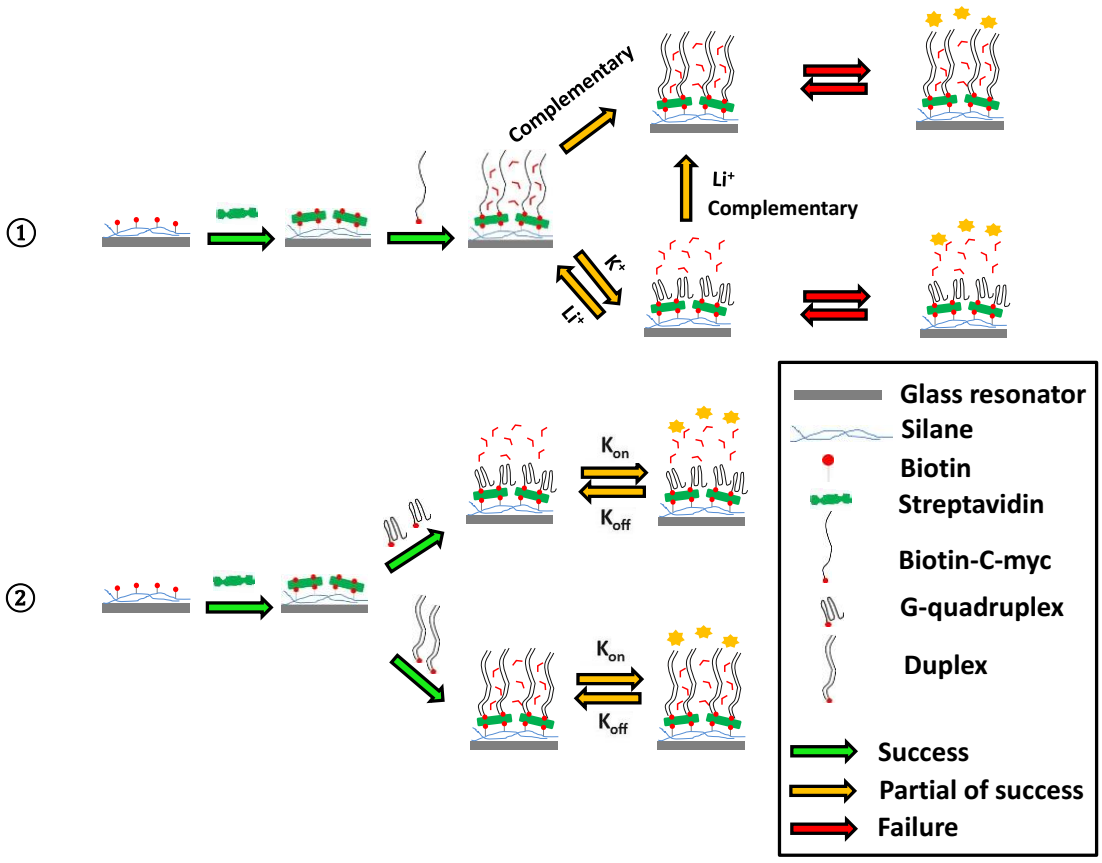


Figure 4.38 Summary and degree of success from the G-quadruplex WGM work. The c-myc binding is depicted in ①. The duplex and G-quadruplex binding are depicted in ②.

4.5 Outlook and Future work

The therapeutic potential of small molecules targeting G-quadruplexes has gained credibility since such structures have shown the ability to form in human cells and to be highly prevalent in the human genome, most notably at telomere ends and in oncogene promoters. So, it is clinically meaningful to study the binding between G-quadruplexes and ligands. Herein, we developed a novel strategy based on whispering gallery mode (WGM) sensing. WGM sensing offers numerous advantages including high sensitivity, real-time analysis, easy access to kinetic fingerprints and much lower cost than current gold standard technique of SPR chip. However, there are some issues which could be addressed in further work to improve performance in the future such as:

(1) The induced shift of the resonant mode from quadruplex (or duplex)–ligand binding was not large because of the diameter of 22 mers of c-myc. This signal can be amplified by using different surface functionalizations which increase the surface density of the quadruplex DNA.

(2) The WGM arrangement can be developed to have higher throughput and better multiplexing capabilities. However, metrics of the WGM measurement will be very sensitive to

the alignment of the tapered fibre optic next to the resonator. Small changes in the gap or position along the taper can affect metrics like the Q-factor, thus reducing the robustness of the approach for high throughput applications. In terms of developing WGM for portable analysis, another coupling method might be better than wave-guides, such as prisms.

(3) In terms of G-quadruplex-ligand interaction, the surface functionalization can be simplified by removing streptavidin from the system. Several alternative functionalization techniques can be applied such as click chemistry.

4.6 References

1. Cancer Research UK. *London art trail sculpture gallery - What's in your DNA?* [cited 2015 31/01/2015]; Available from: http://www.cancerresearchuk.org/support-us/donate/francis-crick-institute/DNA-trail/sculpture-gallery.
2. Panich, S., Sleiman., M. H., Steer, I., Ladame, S. and Edel, J. B., *Real-Time Monitoring of Ligand Binding to G-Quadruplex and Duplex DNA by Whispering Gallery Mode Sensing.* ACS Sensors, 2016.
3. Holt, P. A., Buscaglia, R., Trent, J. O., Chaires, J. B., *A discovery funnel for nucleic acid binding drug candidates.* Drug Development Research, 2011. 72(2): p. 178-186.
4. Chen, H., Chen, G., Du, F., Fu, G., Zhaob, Y. and Tang, Z., *DNA display for drug discovery.* RSC Advances, 2013. 3(37): p. 16251-16254.
5. Ali, A. and Bhattacharya, S., *DNA binders in clinical trials and chemotherapy.* Bioorganic & Medicinal Chemistry, 2014. 22(16): p. 4506-4521.
6. Baraldi, P. G., Bovero, A., Fruttarolo, F., Preti, D., Tabrizi, M. A., Pavani, M. G. and Romagnoli, R. *DNA minor groove binders as potential antitumor and antimicrobial agents.* Medicinal Research Reviews, 2004. 24(4): p. 475-528.
7. Han, H. and Hurley, L. H.,*G-quadruplex DNA: a potential target for anti-cancer drug design.* Trends in Pharmacological Sciences, 2000. 21(4): p. 136-142.
8. Biffi, G., Tannahill, D., McCafferty, J. and Balasubramanian, S., *Quantitative visualization of DNA G-quadruplex structures in human cells.* Nature Chemistry, 2013. 5(3): p. 182-186.
9. Lam, E. Y. N., Beraldi, D., Tannahill, D. and Balasubramanian, S. *G-quadruplex structures are stable and detectable in human genomic DNA.* Nature Communications, 2013. 4: p. 1796.
10. Rhodes, D. and Lipps, H. J. *G-quadruplexes and their regulatory roles in biology.* Nucleic Acids Research, 2015. 43(18): p. 8627-8637.
11. Ohnmacht, S. A. and Neidle, S., *Small-molecule quadruplex-targeted drug discovery.* Bioorganic & Medicinal Chemistry Letters, 2014. 24(12): p. 2602-2612.

12. Balasubramanian, S., Hurley, L. H. and Neidle, S., *Targeting G-quadruplexes in gene promoters: a novel anticancer strategy?* Nature reviews. Drug discovery, 2011. 10(4): p. 261-275.
13. Muller, S. and Rodriguez, R., *G-quadruplex interacting small molecules and drugs: from bench toward bedside.* Expert Review of Clinical Pharmacology, 2014. 7(5): p. 663-679.
14. Moyzis, R. K., Buckingham, J. M., Cram, L. S., Dani, M., Deaven, L. L., Jones, M. D., Meyne, J., Ratliff, R. L. and Wu. J. R., *A highly conserved repetitive DNA sequence, (TTAGGG)n, present at the telomeres of human chromosomes.* Proceedings of the National Academy of Sciences of the United States of America, 1988. 85(18): p. 6622-6626.
15. Moye, A. L., Porter, K. C., Cohen, S. B., Phan, T., Zyner, K. G., Sasaki, N., Lovrecz, G. O., Beck J. L. and Bryan T. M., Telomeric G-quadruplexes are a substrate and site of localization for human telomerase. Nature Communications, 2015. 6.(7643): p.1-12.
16. Murat, P., Singh, Y. and Defrancq, E., *Methods for investigating G-quadruplex DNA/ligand interactions.* Chemical Society Reviews, 2011. 40(11): p. 5293-5307.
17. Mendoza, O., Bourdoncle, A., Boule, J. B., Jr, R. M. B. and Mergny, J. L., *G-quadruplexes and helicases.* Nucleic Acids Research, 2016.
18. Yan, Y., Tan, J. H., Ou, T. and Gu., L., *DNA G-quadruplex binders: a patent review.* Expert Opinion on Therapeutic Patents, 2013. 23(11): p. 1495-1509.
19. Bhasikuttan, A. C. and Mohanty, J., *Targeting G-quadruplex structures with extrinsic fluorogenic dyes: promising fluorescence sensors.* Chemical Communications, 2015. 51(36): p. 7581-7597.
20. Neidle. S. and Balasubramanian, S. *The Role of Cations in Determining Quadruplex Structure and Stability*, in *Quadruplex Nucleic Acids*, Editors. 2006, The Royal Society of Chemistry. p. 100-130.
21. Shim, J. W., Tan, Q. and Gu, L. Q. *Single-molecule detection of folding and unfolding of the G-quadruplex aptamer in a nanopore nanocavity.* Nucleic Acids Research., 2009. 37(3): p. 972-982.
22. Neidle, S. and Balasubramanian, S., *Fundamentals of quadruplex Structures*, in *Quadruplex Nucleic Acids*, Editors. 2006, The Royal Society of Chemistry. p. 100-130.
23. Sen, D. and W. Gilbert, *A sodium-potassium switch in the formation of four-stranded G4-DNA.* Nature, 1990. 344(6265): p. 410-414.
24. Kotch, F. W., Fettinger, J. C. and. Davis, J. T., *A Lead-Filled G-Quadruplex: Insight into the G-Quartet's Selectivity for Pb^{2+} over K^{+}.* Organic Letters, 2000. 2(21): p. 3277-3280.
25. Gellert, M., Lipsett, M. N. and Davies, D. R., *Helix formation by guanylic acid.* Proceedings of the National Academy of Sciences of the United States of America, 1962. 48(12): p. 2013-2018.

26. Jaumot, J. and Gargallo, R., *Experimental methods for studying the interactions between G-quadruplex structures and ligands.* Current Pharmaceutical Design, 2012. 18(14): p. 1900-16.
27. Wei, C., Jia, G., Yuan, J., Feng, Z. and Li, C., *A Spectroscopic Study on the Interactions of Porphyrin with G-Quadruplex DNAs.* Biochemistry, 2006. 45(21): p. 6681-6691.
28. Galezowska, E., Masternaka, A., Rubisb, B., Czyrskic, A., Rybczyńskab, M., Hermannc,T. W. and Juskowiaka, B., *Spectroscopic study and G-quadruplex DNA binding affinity of two bioactive papaverine-derived ligands.* International Journal of Biological Macromolecules, 2007. 41(5): p. 558-563.
29. Agarwal, T., Roy, S., Chakraborty, T. K. and Maiti, S., *Selective Targeting of G-Quadruplex Using Furan-Based Cyclic Homooligopeptides: Effect on c-MYC Expression.* Biochemistry, 2010. 49(38): p. 8388-8397.
30. Wang, P., Leung, C. H., Ma, D. L., Yan, S. C. and Che, C. M., *Structure-Based Design of Platinum(II) Complexes as c-myc Oncogene Down-Regulators and Luminescent Probes for G-Quadruplex DNA.* Chemistry-A European Journal, 2010. 16(23): p. 6900-6911.
31. Ma, D. L., Che, C. M. and Yan, S. C., *Platinum(II) Complexes with Dipyridophenazine Ligands as Human Telomerase Inhibitors and Luminescent Probes for G-Quadruplex DNA.* Journal of the American Chemical Society, 2009. 131(5): p. 1835-1846.
32. Shi, S., Geng, X., Zhao, J., Yao, T., Wang, C., Yang, D., Zheng, L. and Ji, L., *Interaction of [Ru(bpy)2(dppz)]$^{2+}$ with human telomeric DNA: Preferential binding to G-quadruplexes over i-motif.* Biochimie, 2010. 92(4): p. 370-377.
33. Sun, J., An, Y., Zhang, L., Chen, H. Y., Han, Y., Wang, Y. J., Mao, Z. W. and Ji, L. N., *Studies on synthesis, characterization, and G-quadruplex binding of Ru(II) complexes containing two dppz ligands.* Journal of Inorganic Biochemistry, 2011. 105(2): p. 149-154.
34. Bhattacharya, S., Chaudhuri, P., Jain, A, K. and Paul, A., *Symmetrical Bisbenzimidazoles with Benzenediyl Spacer: The Role of the Shape of the Ligand on the Stabilization and Structural Alterations in Telomeric G-Quadruplex DNA and Telomerase Inhibition.* Bioconjugate Chemistry, 2010. 21(7): p. 1148-1159.
35. Barbieri, C. M., Srinivasan, A. R., Rzuczek, S. G., Rice, J. E., LaVoie, E. J. and Pilch, D. S., *Defining the mode, energetics and specificity with which a macrocyclic hexaoxazole binds to human telomeric G-quadruplex DNA.* Nucleic Acids Research, 2007. 35(10): p. 3272-3286.
36. Paramasivan, S., Rujan, I. and Bolton, P. H., *Circular dichroism of quadruplex DNAs: Applications to structure, cation effects and ligand binding.* Methods, 2007. 43(4): p. 324-331.

37. Read, M., Harrison, R. J., Romagnoli, B., Tanious, F. A., Gowan, S. H., Reszka, A. P., Wilson, W. D., Kelland, L. R. and Neidle, S., *Structure-based design of selective and potent G quadruplex-mediated telomerase inhibitors.* Proceedings of the National Academy of Sciences, 2001. 98(9): p. 4844-4849.

38. Redman, J. E., *Surface plasmon resonance for probing quadruplex folding and interactions with proteins and small molecules.* Methods, 2007. 43(4): p. 302-312.

39. Ren, L., Zhang, A., Huang, J., Wang, P., Weng, X., Zhang, L., Liang, F., Tan, Z. and Zhou, X., *Quaternary Ammonium Zinc Phthalocyanine: Inhibiting Telomerase by Stabilizing G quadruplexes and Inducing G-Quadruplex Structure Transition and Formation.* ChemBioChem, 2007. 8(7): p. 775-780.

40. Dash, J., Waller, Z. A., Pantos, G. D. and Balasubramanian, S., *Synthesis and Binding Studies of Novel Diethynyl-Pyridine Amides with Genomic Promoter DNA G-Quadruplexes.* Chemistry–A European Journal, 2011. 17(16): p. 4571-4581.

41. McLuckie, K. I. E., Waller, Z. A. E., Sanders, D. A., Alves, D., Rodriguez, R., Dash, J., McKenzie, G. J., Venkitaraman, A. R. and Balasubramanian, S., *G-Quadruplex-Binding Benzo[a]phenoxazines Down-Regulate c-KIT Expression in Human Gastric Carcinoma Cells.* Journal of the American Chemical Society, 2011. 133(8): p. 2658-2663.

42. Pillet, F., Romerae, C., Trevisiola, E., Bellond, S., Fichoug, M. P. T., Francoisa, J. M., Genevieve, P., Leberrea, V. A., *Surface plasmon resonance imaging (SPRi) as an alternative technique for rapid and quantitative screening of small molecules, useful in drug discovery.* Sensors and Actuators B: Chemical, 2011. 157(1): p. 304-309.

43. Von, H. A., Seifert, O., Menger, M., Schutze, T., Arora, A., Konthur, Z., Neubauer, P., Wagner, A. Weise, C. and Kurreck, J., *Identification and characterization of RNA guanine-quadruplex binding proteins.* Nucleic Acids Research, 2014. 42(10): p. 6630-6644.

44. Soteropulos, C. E. and Hunt, H. K., *Attaching biological probes to silica optical biosensors using silane coupling agents.* Journal of Visualized Experiments., 2012(63): p. E3866/1-E3866/7.

45. Chivers, C. E, Koner, A. L, Lowe, E. D. and Howarth M. *How the biotin–streptavidin interaction was made even stronger: investigation via crystallography and a chimaeric tetramer.* Biochemical Journal, 2011. 435(1): p. 55-63.

46. Hou, J. Q, Chen, S. B, Tan, J. H, Luo, H. B, Li, D, Gu, L. Q and Huang, Z. S. *New insights from molecular dynamic simulation studies of the multiple binding modes of a ligand with G-quadruplex DNA.* Journal of Computer-Aided Molecular Design, 2012. 26(12): p. 1355-1368.

47. Vummidi, B. R., Alzeer, J. and Luedtke, N. W., *Fluorescent Probes for G-Quadruplex Structures.* ChemBioChem, 2013. 14(5): p. 540-558.

48. Kong, D. M., Ma, Y. E., Wu, J. and Shen, H. X., *Discrimination of G-Quadruplexes from Duplex and Single-Stranded DNAs with Fluorescence and Energy-Transfer Fluorescence Spectra of Crystal Violet.* Chemistry–A European Journal, 2009. 15(4): p. 901-909.
49. He, H. Z., Chan, D. S. H., Leung, C. H. and Ma, D. L., *G-quadruplexes for luminescent sensing and logic gates.* Nucleic Acids Research, 2013.
50. Kong, D. M., Ma, Y. E., Guo, J. H., Yang, W. and Shen, H. X., *Fluorescent Sensor for Monitoring Structural Changes of G-Quadruplexes and Detection of Potassium Ion.* Analytical Chemistry, 2009. 81(7): p. 2678-2684.
51. Kong, D. M., Ma, Y. E., Wu, J. and Shen, H. X., *Discrimination of G-quadruplexes from duplex and single-stranded DNAs with fluorescence and energy-transfer fluorescence spectra of crystal violet.* Chemistry-A European Journal, 2009. 15(4): p. 901-909.
52. Kong, D. M., Guo, J. H., Yang, W., Ma, Y. E., Shen, H. X., *Crystal violet–G-quadruplex complexes as fluorescent sensors for homogeneous detection of potassium ion.* Biosensors and Bioelectronics, 2009. 25(1): p. 88-93.
53. Sun, H., Xiang, J., Zhang, Y., Xu, G., Xu, L., and Tang, Y., *Spectroscopic studies of the interaction between methylene blue and G-quadruplex.* Chinese Science Bulletin, 2006. 51(14): p. 1687-1692.
54. Zhang, F. T., Nie, J., Zhang, D. W., Chen, J. T., Zhou, Y. L. and Zhang, X. X., *Methylene Blue as a G-Quadruplex Binding Probe for Label-Free Homogeneous Electrochemical Biosensing.* Analytical Chemistry, 2014. 86(19): p. 9489-9495.
55. Lubitz, I., Zikich, D. and Kotlyar, A., *Specific High-Affinity Binding of Thiazole Orange to Triplex and G-Quadruplex DNA.* Biochemistry, 2010. 49(17): p. 3567-3574.
56. Lu, Y. J., Deng, Q., Hou, J. Q., Hu, D. P., Wang, Z. Y., Zhang, K., Luyt, L. G., Wong W. L. and Chow, C. F., *Molecular Engineering of Thiazole Orange Dye: Change of Fluorescent Signaling from Universal to Specific upon Binding with Nucleic Acids in Bioassay.* ACS Chemical Biology, 2016. 11(4): p. 1019-1029.
57. Boncina, M., Podlipnik, C., Piantanida, I., Eilmes, J., Teulade-Fichou, M. P. and Vesnaver, G., Lah, J., *Thermodynamic fingerprints of ligand binding to human telomeric G-quadruplexes.* Nucleic Acids Research, 2015. 43(21): p. 10376-10386.
58. Wartell, R. M., Larson, J. E. and. Wells, R. D, *Netropsin. A specific probe for A-T regions of duplex deoxyribonucleic acid.* The Journal of Biological Chemistry, 1974. 249(21): p. 6719-31.
59. Randazzo, A., Galeone, A., Esposito, V., Varra, M. and Mayol, L., *Interaction of distamycin A and netropsin with quadruplex and duplex structures: a comparative 1H-NMR study.* Nucleosides Nucleotides Nucleic Acids, 2002. 21(8-9): p. 535-545.
60. Lah, J., Drobnak, I., Dolinar, M. and Vesnaver, G., *What drives the binding of minor groove-directed ligands to DNA hairpins?* Nucleic Acids Research, 2008. 36(3): p. 897-904.

61. Adam. S. J., *Direct evidence for a G-quadruplex in a promoter region and its targeting with a small molecule to repress c-MYC transcription.* Proceedings of the National Academy of Sciences, 2002. 99(18): p. 11593-11598.

62. Rehm, C., Holder, I. T., Grob, A., Wojciechowski, F., Urban, M., Sinn, M., Dreschera, M. and Hartig, J. S., *A bacterial DNA quadruplex with exceptional K^+ selectivity and unique structural polymorphism.* Chemical Science, 2014. 5(7): p. 2809-2818.

63. Ranjan, N. and Arya, D. P., *Targeting C-myc G-Quadruplex: Dual Recognition by Aminosugar-Bisbenzimidazoles with Varying Linker Lengths.* Molecules, 2013.

64. Hou, X., Guo, W., Xia, F., Nie, F. Q., Dong, H., Tian, Y., Wen, L., Wang, L., Cao, L., Yang, Y, Xue, J., Song, Y., Wang, Y., Liu, D., and Jiang, L., *A Biomimetic Potassium Responsive Nanochannel: G-Quadruplex DNA Conformational Switching in a Synthetic Nanopore.* Journal of the American Chemical Society, 2009. 131(22): p. 7800-7805.

65. Drescher, D. G., Ramakrishnan, N. A. and Drescher, M. J., *Surface Plasmon Resonance (SPR) Analysis of Binding Interactions of Proteins in Inner-Ear Sensory Epithelia.* Methods in molecular biology, 2009. 493: p. 323-343.

66. Livney, Y. D., Ramon, O., Kesselman, E., Cogan, U., Mizrahi, S. and Cohen, Y., *Swelling of dextran gel and osmotic pressure of soluble dextran in the presence of salts.* Journal of Polymer Science Part B: Polymer Physics, 2001. 39(22): p. 2740-2750.

67. Williams, E. H., Davydov, A.V., Motayed, A., Sundaresanb, S. G., Bocchini, P., Richter, L. J., Stanb, G., Steffens, K., Zangmeister , R., Schreifels, J. A. and Raoc, M. V., *Immobilization of streptavidin on 4H–SiC for biosensor development.* Applied Surface Science, 2012. 258(16): p. 6056-6063.

68. Taglietti, A., Arciola, C. R., D'Agostino, A., Dacarro, G., Montanaro, L., Campoccia, D., Cucca, L, Vercellino, M., Poggi, A., Pallavicini, P., and Visai, L., *Antibiofilm activity of a monolayer of silver nanoparticles anchored to an amino-silanized glass surface.* Biomaterials, 2014. 35(6): p. 1779-1788.

69. Li, H., Park, S. H., Reif, J. H., LaBean, T. H. and Yan, H., *DNA-Templated Self-Assembly of Protein and Nanoparticle Linear Arrays.* Journal of the American Chemical Society, 2004. 126(2): p. 418-419.

70. Blainey, P. C., Luo, G., Kou, S. C., Mange, W. F., Verdine, G. L., Bagchi, B. and Xie, X. S., *Nonspecifically bound proteins spin while diffusing along DNA.* Nature Structural & Molecular Biology, 2009. 16(12): p. 1224-1229.

71. Zhang, M. and Li, G., *Modeling and Control for Micro/Nano Devices and Systems*. Modeling and simulation of silicon Nanowire-Base biosensor. 2013: Taylor & Francis. 175.

72. Marttila, A. T., Laitinen, O. H., Airenne, K. J., Kulik, T., Bayer, E. A., Wilchek, M. and Kulomaa, M. S., *Recombinant NeutraLite Avidin: a non-glycosylated, acidic mutant of*

chicken avidin that exhibits high affinity for biotin and low non-specific binding properties. FEBS Letters, 2000. 467(1): p. 31-36.

73. Green, N. M., *Avidin.The nature of the biotin-binding site.* Biochemical Journal, 1963. 89(3): p. 599-609.
74. Parkinson, G. N., Lee, M. P. H. and Neidle, S., *Crystal structure of parallel quadruplexes from human telomeric DNA.* Nature, 2002. 417(6891): p. 876-880.
75. Lapin, N. A. and Chabal, Y. J., *Infrared Characterization of Biotinylated Silicon Oxide Surfaces, Surface Stability, and Specific Attachment of Streptavidin.* The Journal of Physical Chemistry B, 2009. 113(25): p. 8776-8783.
76. Launer, P. J., *Infrared Analysis of Organosilicon Compounds: Spectra-Structure Correlations.* 1987.
77. Pluchon, D., Huby, N., Vie, V., Panizza, P. and Beche, B., *AFM Analysis on Polymer Optical Micro-Resonators: Investigation on Quality Factor Origin.* Optics and Photonics Journal, 2013. 3(4): p. 5.
78. Panich, S., Wilson, K. A., Nuttall, P., Wood, C. K., Albrecht, T. and Edel, J. B., *Label-Free Pb(II) Whispering Gallery Mode Sensing Using Self-Assembled Glutathione-Modified Gold Nanoparticles on an Optical Microcavity.* Analytical Chemistry, 2014. 86(13): p. 6299-6306.
79. Pasquardini, L., Berneschi, S., Barucci, A., Cosi, F., Dallapiccola, R., Lorenzo, I., Lunelli, M., Conti, G. N., Pederzolli, C., Salvadori, S. and Soria, S., *Whispering gallery mode aptasensors for detection of blood proteins.* Journal of Biophotonics, 2013. 6(2): p. 178-187.
80. Srisa-Art, M., Dyson, E. C., DeMello, A. J. and Edel, J. B., *Monitoring of Real-Time Streptavidin–Biotin Binding Kinetics Using Droplet Microfluidics.* Analytical Chemistry, 2008. 80(18): p. 7063-7067.
81. Oshannessy, D. J., Brigham, B. M., Soneson, K. K., Hensley, P. and Brooks, I., *Determination of Rate and Equilibrium Binding Constants for Macromolecular Interactions Using Surface Plasmon Resonance: Use of Nonlinear Least Squares Analysis Methods.* Analytical Biochemistry, 1993. 212(2): p. 457-468.
82. Nunez, S., J. Venhorst, and Kruse, C. G., *Target–drug interactions: first principles and their application to drug discovery.* Drug Discovery Today, 2012. 17(1-2): p. 10-22.
83. Soteropulos, C. E., Hunt, H. K. and Armani, A. M., *Determination of binding kinetics using whispering gallery mode microcavities.* Applied Physics Letters, 2011. 99(10): p. 103703/1-103703/3.
84. Wu, Y., Zhang, D. Y., Yin, P. and Vollmer, F., *Ultraspecific and Highly Sensitive Nucleic Acid Detection by Integrating a DNA Catalytic Network with a Label-Free Microcavity.* Small, 2014. 10(10): p. 2067-2076.

85. Shim, J. W., Tan, Q. and Gu, L. Q., *Single-molecule detection of folding and unfolding of the G-quadruplex aptamer in a nanopore nanocavity.* Nucleic Acids Research, 2009. 37(3): p. 972-982.

Chapter 5 | Thrombin (TB) detection by WGM



Stopping the bleeding

When our skin is cut, worn, or punctured, bleeding usually initiates. The bodies' priority is to stop the bleeding in as shorter time as possible, via clotting, in order to protect the wound from haemorrhage. The clotting of blood not only occurs when necessary, but also has the potential to cause harm, which can occur with internal blood clots. As a result, haemostasis (a human body's response when the body is injured resulting in the formation of a blood clot) and thrombosis (where haemostasis is excessively activated in the absence of bleeding or haemostasis in the wrong place) developmental research are cutting edge in the pharmaceutical and clinical area. The picture is reproduced from [1].

This chapter will summarise the challenges in the thrombin (TB)'s sensor experiments, which presented unexpected results. There were several interesting points to discuss from the experimental results although the results were negative, the outcome can indicate novel findings from unexpected scientific results. Herein, the motivation, experimental designs based on problem-solving, unexpected results from TB-based WGM sensors will be presented. A brief introduction about TB, fibrinogen (FB), blood clotting process and a short review of the research in the TB sensor will be provided, in order to understand the concept of this work.

5.1 Introduction to blood clotting

One of the essential processes in a human being body is a blood clot. The process stops the damage tissue from bleeding. A blood clotting disorder which results in slow or prolonged blood clotting after an injury can cause a serious problem. Abnormal blood clotting arising from a deficiency of TB is called "hemophilia". However, an excess of TB can also give rise to some diseases for example strokes or cardiovascular diseases when the clot occurs when not required. Even though blood clots are crucial for wound repair, if the clot is formed in an intravascular location this can prevent normal blood flow to tissues and can cause serious harm. An unusual blood clot called venous thromboembolism (VTE) is a condition where a blood clot forms in a veins, and includes conditions such as deep vein thrombosis (DVT), which happens in a leg vein or in a lung called pulmonary embolism (PE) [2, 3]. In the blood clotting process, there are important proteins involved for example TB and FB. The next section will give brief details about these crucial molecules.

5.1.1 TB and FB protein

TB, an endolytic serine protease, is an essential blood-clotting protein produced in the liver when the body is injured, in order to prevent a wound from bleeding. This protein selectively cleaves the soluble FB and turns the resulting product into insoluble fibrin (F), which triggers blood plasma to clot. The level of TB in blood at the high or even low concentration is related to coagulation irregularities within individuals [4]. There are two exosites (a secondary binding site which is located remote from the active site) in TB structure, exosite I and II as shown in Figure 5.1. The first exosite or exosite I, consists of Lys21, Arg62, Arg68, Arg70, Tyr71, Arg73, Lys106, and Lys107. This exosite is for the FB-binding and does not actively cleave FB, however is requisite for FB binding to the protein. Exosite II consists of Arg89, Arg98, Arg245, Lys248, and Lys252, is on the opposite side and is used for heparin binding which involves the recognition and cleavage of FB [5].

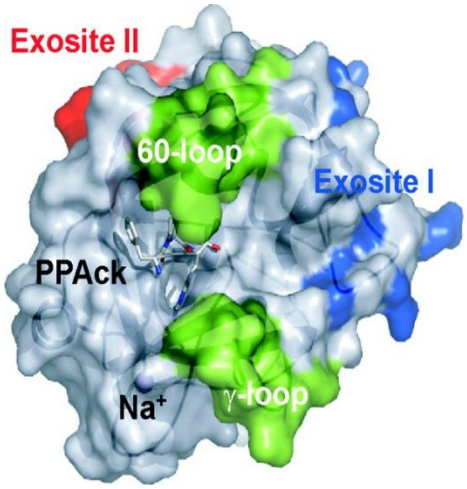


Figure 5.1 Thrombin topography. Reprinted with permission from [6].

FB or factor I, a soluble protein found in the blood plasma, synthesised by the liver, is rod-shaped with a molecular weight of 3.4×10^5 and plays an essential role in the formation of blood clots [7]. The structure of FB is shown in Figure 5.2. FB is converted by TB into fibrin (F) during blood coagulation. The clotting is initiated when platelets in the blood aggregate at the damage location [2]. FB is composed of a dimer of three non-identical pairs of polypeptide chains which are α, β and γ chains held together by disulfide bonds [8, 9].

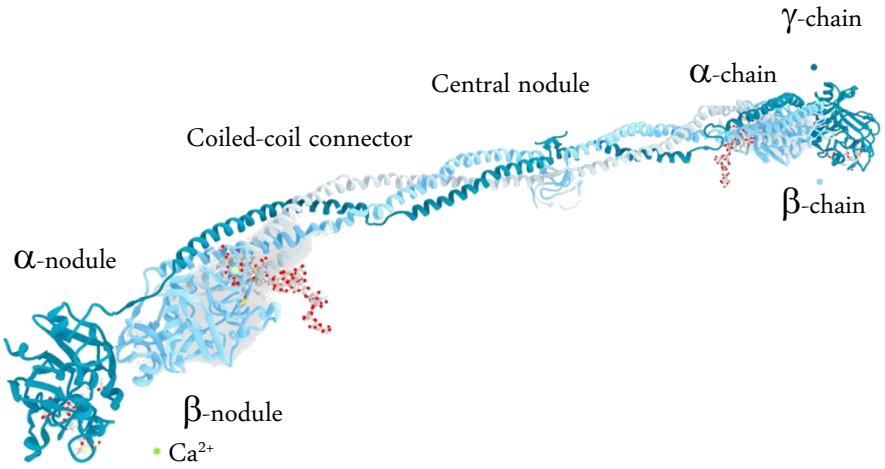


Figure 5.2 Schematic diagram of fibrinogen. Reprinted with permission from [9].

F within a blood clot, is a polymer which held together by a non-covalent bond or intermolecular interaction. Consequently, covalent crosslinks between adjacent units in the gel are introduced by a transglutaminase called 'factor XIII', which is activated by TB. F has two types of junctions. The first junction occurs when a double-stranded fibril connects with another fibril then a four-stranded fibril is formed called "bilateral" junction, Figure 5.3. The second type of branch junction called "equilateral" is formed by convergent interactions among three fibrin molecules. This junction leads to three double-stranded fibrils [2].

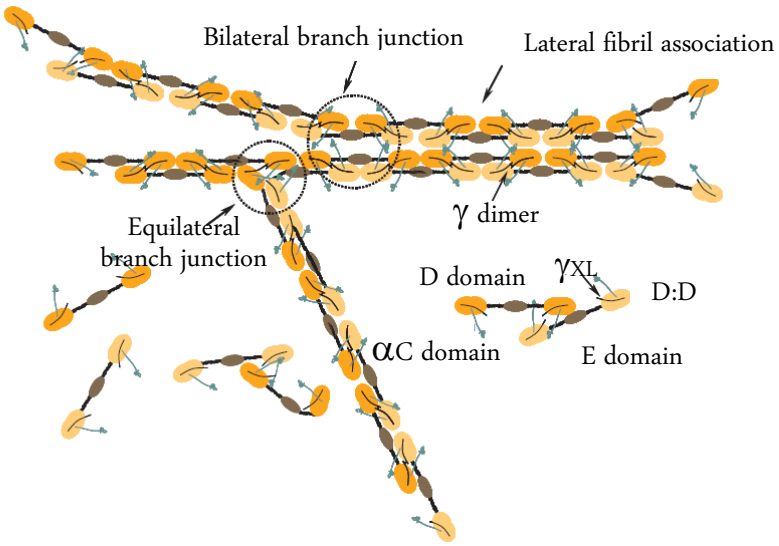


Figure 5.3 Schematic diagram of fibrin assembly, branching, lateral fibril association, and c-chain cross-linking. Reprinted with permission from [8].

5.1.2 Conversion of FB to F clot by TB

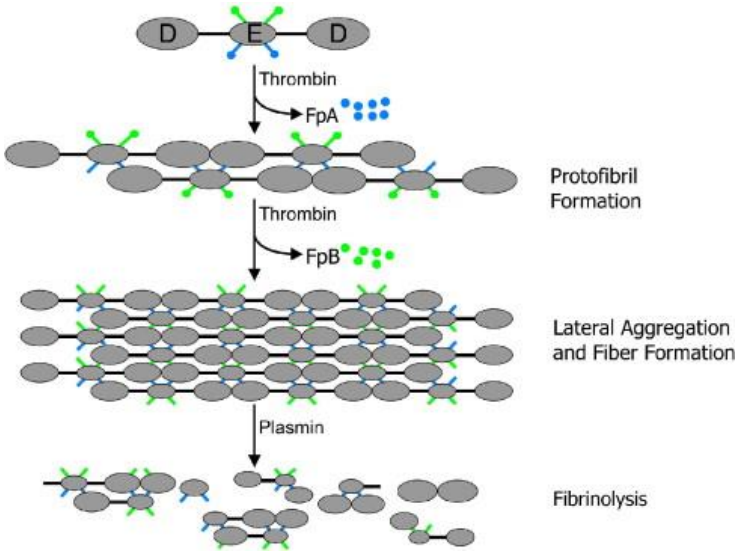


Figure 5.4 TB-mediated conversion of FB to F involves the sequential release of fibrinopeptide A, (FpA, blue) and fibrinopeptide B (FpB, green) from the central E nodule of FB. Reprinted with permission from [10].

The F production can be generated when there is enough T in a localised area, and is a result of FB release within the body. N-terminal peptide of the Aα- and Bβ-chain is released when TB binds to the central E nodule of F. Aα-chain is first cleaved by TB and then N-terminal 16 residue peptide (FpA) is removed and as a result a new N-terminal sequence called "A" site is exposed. It is this site which acts as a pocket and permits noncovalent bond with c chain of

the D nodule of another FB molecule. Later on, the removal of the N-terminal 14 residue peptide of the Bβ- chains (FpB) exposes the ''B'' site which interacts with an exposed ''b'' pocket in the Bβ-chain of the D nodule of another FB molecule [10].

5.2 Motivation and challenging in TB-based WGM sensor

Understanding the interaction between proteins in the human body plays an important role in the diagnosis of some diseases, as most of the functions of cells are controlled by these important molecules. Many proteins perform their functions independently, however, a few of them interact with others to control a biological activity. The protein-protein interactions assay are used to study the mutual behaviour of two or more types of proteins. Some diseases can be predicted before their final stages by using the interaction signals [11]. For example, blood clotting disorders can be monitored by studying the interaction between FB and T proteins. For a timely intervention, the faster the diagnosis the better the chance for the treatment. As mentioned from the previous section, TB is one of the essential proteins in the human body because its interaction with FB plays a key role in the process of blood coagulation. TB should not be generated in a normal conditions, but small amounts of TB are generated in the case of injury. Measuring levels of TB can be used to diagnose and assess many bleeding problems, in addition, monitoring of TB levels in the blood is an alternative way of predicting conditions including hemostasis or thrombosis [12-14]. Up until now, there have been a number of techniques used to detect TB at levels as low as nanomolar (nM) [15-20]. Unfortunately, few sensors can detect thrombin down to a picomolar (pM) level and cannot monitor the interaction between TB and FB in real time. WGM offers numerous advantaged over other optical technique as mentioned before in Chapter 1. By integrating WGM sensor with TB-FB interaction probe, we expected that the interaction between TB and FB should be recording in a few minutes and in real time. Not only providing quantitative information for TB, but kinetic data of real-time interactions could be tracked, in order to improve the sensor as a model for protein-protein interaction. Advantages from WGM-TB sensor over other sensors might be low cost, accuracy and fast analysis with a small amount of sample and without complicated sample preparation.

5.3 Reviews of TB-sensor

Up until now, there have been a number of techniques used to detect TB at levels lower than nanomolar (nM) [15-20]. Unfortunately, few sensors can detect TB down to picomolar (pM) levels, and more importantly cannot monitor the interaction between TB and FB in real time. Various techniques have already been integrated into TB sensors recently with a varying degree of success.

In 2002, Xiaokun, C. *et al* [18] published the TB sensor based on the interaction of anti-thrombin aptamer which has high affinity with TB. This interaction induced the change of the fluorescent polarization in the solution of the aptamer labelled with a fluorophore which was used as a useful tool for TB detection in human blood with a LOD at 0.09 IU mL^{-1}.

Zhengping, L., Yupei, L. and Wei, L. published a sensitive resonance light scattering (RLS) method for detection of TB in 2008. By incorporating of the RLS technique and oligonucleotides-functionalized Au NPs, TB was sensitively detected in the range of 6.0-32.5 nM with a LOD at 4.3 nM. Two oligonucleotide probes were designed in order to make the sensor specific to TB by immobilizing with an aptamer which has a high binding affinity to TB. The hybridization between oligonucleotide probes on the Au NP surface and aptamer triggered the Au NPs to aggregate and enhanced the RLS intensity. The specific interaction between the aptamer and TB will restrain the hybridization, and as a result the RLS intensity decreases [20].

In 2010, label-free highly sensitive and selective colorimetric detection of TB was achieved by using an Au NP-based assay presented by C. K. Chen and co-workers [21] in 2010 with highly selective and sensitive for TB protein. After adding TB to the modified-Au NP surface which was modified with FB protein, the electrostatic and hydrophobic interaction between TB and the complex induced the formation of the insoluble fibrin. As a result, FB-Au NP complex aggregated so the absorbance at 532 nm of the supernatants from the solution decreased upon increasing TB. The approach offered a LOD for TB in pM which is lower than using other aptamer-based detection methods at that time.

One year later, a TB-binding aptamer coupled with nanoparticles through sandwich DNA hybridization was presented as a sensitive and selective probe for DNA detection by J. W. Jian and the teams [22]. Even though the aim of the method was not to detect TB, but this piece of information is useful in confirming that TB can induce aggregation of FB-functionalized Au NPs.

Xu, H. and co-worker [23] developed a label-free and highly sensitive impedimetric aptasensor for the determination of TB which was based on electropolymerized film. The histidine labelled TB aptamer was functionalized onto the electrode via coordination of the histidine groups on the NTA-Cu^{2+} complex. A linear quantification of TB was obtained in the range 4.7×10^{-12}-5.0×10^{-10} mol L^{-1}.

WGM-sensors based on silica microspheres, have been demonstrated in 2013 by Pasquardini, L. and co-workers [24] as a tool for detection of TB. In this work, the DNA-aptamer sequence immobilization on WGM was used to recognize specifically TB or VEGF protein with

a high Q-factor. Two DNA-aptamers, 15-mer and 29-mer of TBA were studied in order to make the resonator surface to specific only towards TB.

5.4 Experimental methods

5.4.1 Chemicals and Materials

All chemicals used in this experiment including, gold (III) chloride hydrate ($^{*}HAuCl_4{\cdot}3H_2O$ Aldrich, U.K.), sodium citrate tribasic dehydrate ($HOC(COONa)(CH_2COONa)_2{\cdot}2H_2O$, Sigma-Aldrich, U.K.), 3-mercaptopropyl-trimethoxy-silane, MPTMS ($HS(CH_2)_3Si(OCH_3)_3$, Sigma-Aldrich, U.K.), N-hydroxysuccinimidobiotin ($C_{14}H_{19}N_3O_5S$, Sigma-Aldrich, U.K.), thrombin from bovine plasma lyophilized powder, (Sigma-Aldrich, U.K.), Fibrinogen from human plasma, (Sigma-Aldrich, U.K.), phosphate buffered saline tablet (PBS, Sigma-Aldrich, U.K.), were analytical grade. All solutions used herein were prepared using Milli-Q water (resistivity ca. 18.2 MΩ cm at 25 °C) and Amicon Ultra-4 Centrifugal Filter Units 10 K- (Merck-Millipore, U.K.).

5.4.2 Fabrication and functionalization of the microresonator and WGM resonance shift measurements for TB-sensor

All bare microresonators were made of single-mode optical fibres (F-SMF-28, Newport) and fabricated by using the same protocol as described in section 2.1.2.1, Chapter 2. In method: 1, APTMS resonators were prepared as described in [25]. In method 3, the microresonator surface was cleaned with oxygen plasma and functionalized using MPTMS in order to increase the adhesion between the glass resonator surface and FB. Briefly, the microresonator was immersed in a 0.25% v/v solution of MPTMS in toluene at 60 °C for 10 minutes. In the following step, the silanized resonator was washed in fresh toluene in order to wash off unbound silane and then dried in an oven to evaporate the solvent for 30 minutes. WGM set-up for TB-sensor was similar as the set-up used for G-quadruplex experiments in Chapter 4 as shown in the diagram, Figure 4.1, Chapter 4.

5.4.3 Quantification of TB using TB-based WGM sensing

Herein, the aim of the project was to develop TB-based WGM by integrating the WGM technique coupled with TB-FB interaction. The WGM sensors based on TB-FB interaction by using different ideas were demonstrated as shown in the next section.

5.4.3.1 Method 1: FB-Au NPs and TB

A microresonator surface was coated with the FB modified Au NP solution. The complex was synthesised by allowing 1 mL of 0.5 nM of 16 nm Au NPs (the synthesis of 16 nm Au NPs was mentioned in section 3.2.2, Chapter 3) to react with 1 mL 400 nM of FB in 0.2×biological buffer (25 mM Tris-HCl, 150 mM NaCl, 5 mM KCl, 1 mM $MgCl_2$, 1 mM $CaCl_2$ pH 7.4) for 1 hour. Based on the complex surface properties, a negatively charged FB-Au NPs can be easily adhered onto the microresonator surface by modifying the surface with a positively charge using silane solution (3-aminopropyltrimethoxysilane, APTMS) [25]. When TB is present the resonance wavelength shifted to a longer wavelength, this signal indicates the interaction between the TB and FB could be monitored in real time.

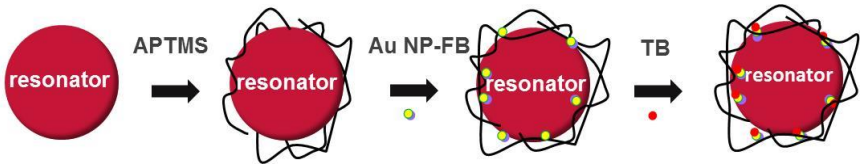


Figure 5.5 The concept for TB-WGM sensor based on FB-Au NPs and TB interaction

5.4.3.2 Method 2: Biotin-FB and TB

In this method, the TB-WGM sensor was based on biotin-FB and TB interaction. Herein, after the surface of the resonator was cleaned by using the plasma cleaner or the piranha solution, it was immersed in the 1 mg mL^{-1} of the dextran-biotin solution then was aligned in the fluidic cell. 0.05 mg mL^{-1} of streptavidin was incorporated in order to immobilize biotin-FB complex with the surface. The resonator surface was now ready to use for attaching the TB complex.

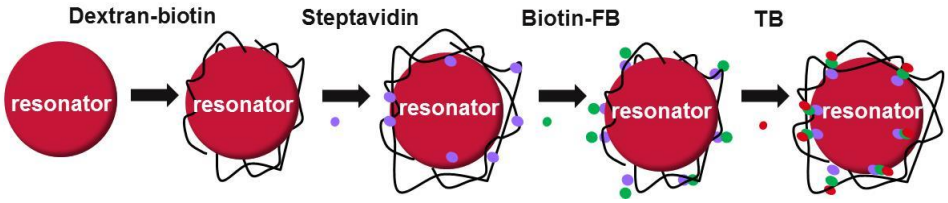


Figure 5.6 The idea for TB-WGM sensor based on biotin-FB and TB

The biotin-FB complex was produced from 0.30 mg mL^{-1} of FB in 0.2× biological buffer as a stock solution then 500 µL of a stock solution of FB was diluted with PBS buffer to 3 mL (0.15 µM). Next, 0.40 mg of biotin (0.40 mM) was mixed with 3 ml of 0.15 µM FB. Unbound biotin was removed by using amicon ultra-4 centrifugal filter units 10 K (Merck-Millipore, UK). The biotin-FB complex was washed with PBS buffer 3 times. The filtered solution spectrum was recorded to confirm that the excess and unbound biotin was completely removed as shown in Figure 5.12. The final step was flowing TB solution and recording the wavelength shift signal.

5.4.3.3 Method 3: MPTMS-FB and TB

In the final attempt at the TB experiment, the idea was simplified as much as possible by modifying the surface with silane solution (3-mercaptopropyl-trimethoxy-silane, MPTMS) then immobilized with 1 mg $mL^{-1}$of FB according to the covalent interaction between the silane surface and FB protein thus the surface was ready for studying the interaction between TB and FB.

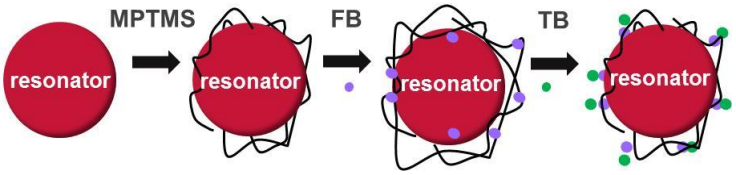


Figure 5.7 The idea for TB-WGM sensor based on MPTMS-FB and TB

5.5 Results and Discussions

5.5.1 Method 1: FB-Au NPs and TB

A successful label-free technique for TB detection at pM levels has been presented recently by C. K. Chen [21] using gold nanoparticles (Au NPs). These particles were conjugated with FB by binding FB protein onto a gold particle surface via an electrostatic interaction. When TB is present in the FB modified Au NP solution, this FB is cleaved and the insoluble polymer fibrin will be generated. This fibrin can induce Au NPs to aggregate and degree of the aggregation depends on the amount of TB. The greater the amount of TB the greater the aggregation. This process can be monitored with several imaging techniques such as scanning electron microscopy (SEM) or atomic force microscopy (AFM) and UV-Visible spectroscopy. The attained signals from all three mentioned techniques were not carried out in a real time read out, and so to provide a real-time signal other detection techniques are required. Figure 5.8 shows the basic concept for FB-Au NPs and TB method in order to detect the interaction signal between TB and FB in real time by WGM sensor, a microresonator surface is coated with the FB modified Au NP solution.

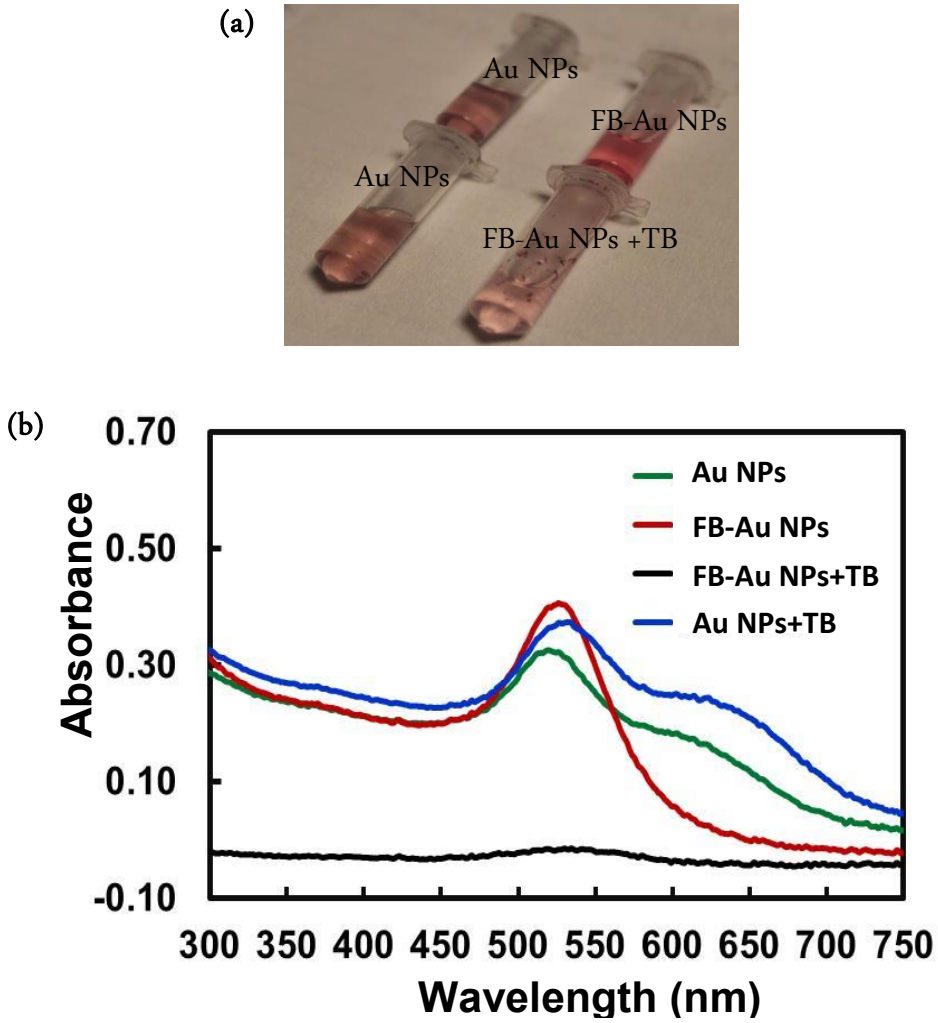


Figure 5.8 Preliminary results from the interaction between FB-AuNPs and TB that generated insoluble fibrin and induce the aggregation of the complex which can be observed by the naked eye (a) and (b) UV- visible spectrum.

In WGM experiment, Figure 5.9, the shift was from two reasons (i) aggregation of Au NPs complex (ii) the formation of the fibrin. These make the signals too complex to analyse. Moreover, washing of unbound FB in the flow cell cannot be confirmed.

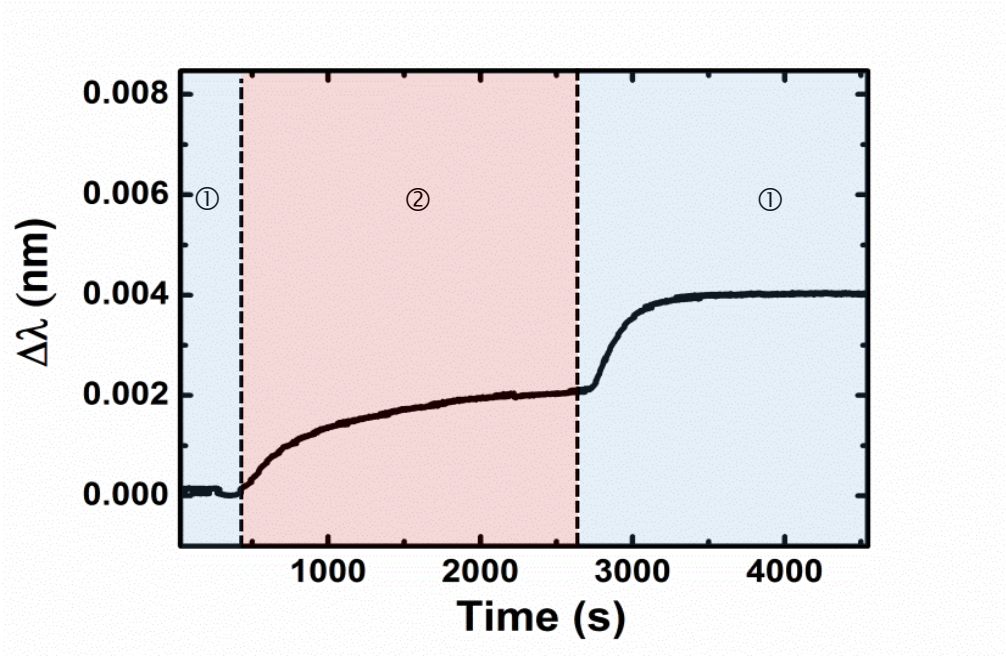


Figure 5.9 The resonance wavelength shift from Au NPs-FB complex

In summary, TB can react with FB generating insoluble fibrin. The fibrin can capture Au NPs and induce the particles to aggregate. This aggregation can be easily observed by naked eyes, or recording the decreasing of the spectrum at 520 nm as shown in Figure 5.8 part (a). The large resonance wavelength shift from 0.2× biological buffer was observed at 2750s at which might indicate the aggregation of Au NPs complex from the high concentration of salt in the buffer including NaCl, KCl, $MgCl_2$ and $CaCl_2$ as well as the formation of fibrin on the surface. Although this comprehensive insoluble fibrin production can be observed by naked eye, it does suffer from a number of flaws. Firstly, the major problem had arisen from unbound FB which cannot be effortlessly eliminated from FB-Au NPs complex. Secondly, the biological buffer consisted of a high concentration of salt that can induce Au NPs to aggregate so an observed wavelength shift was too complicated to analyse as it might be from the aggregation of Au NPs plus insoluble fibrin. In summary, the method 1 was unreliable and impractical.

5.5.2 Method 2: Biotin-FB and TB

The main limitations of the method 1 were an aggregation of Au NPs from the buffer and difficulties washing away unbound molecules. Therefore, in order to get rid of Au NPs, therefore in the method 2, dextran-biotin was introduced, Figure 5.10. In this method the problem from the method 1 was avoided including removing of Au NPs and washing unbound molecule unravelling.

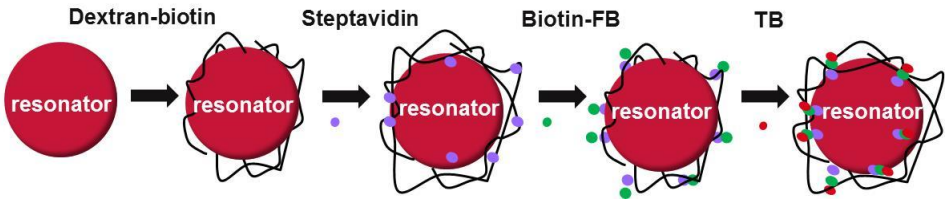


Figure 5.10 The idea for TB-WGM sensor based on biotin-FB and TB

In method 2, Au NPs were eliminated in order to avoid complicated analysis of the signal. The problem of unbound molecules of biotin was solved by using a centrifugal filtering. The strong interaction of biotin and streptavidin reinforced the surface to selectively bind to only biotin-FB complex. We expected that the excess biotin-FB complex can be washed out from the surface easily by observing the resonant wavelength shift. Moreover, washing of the excess biotin from biotin-FB complex can be confirmed by using the centrifugal filter. Figure 5.11 confirmed that there was no excess free biotin in the biotin-FB complex.

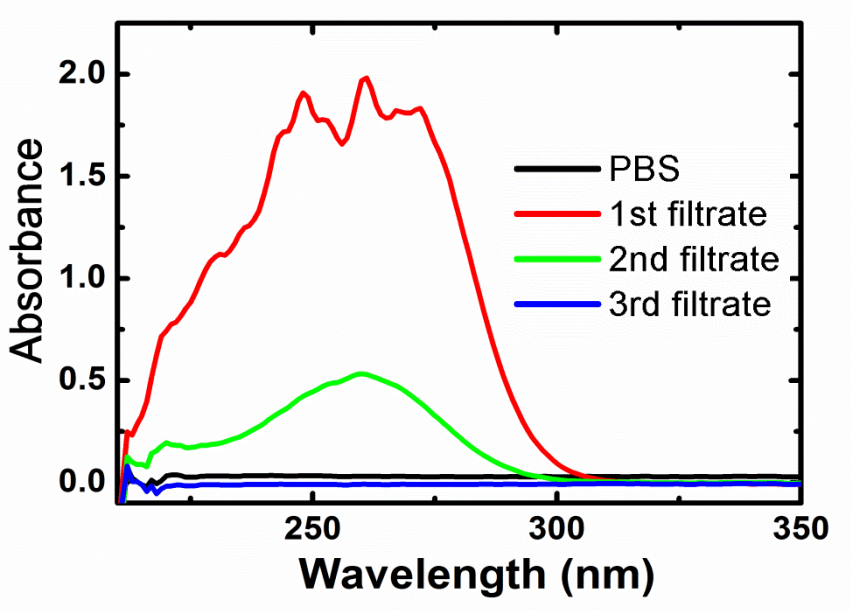
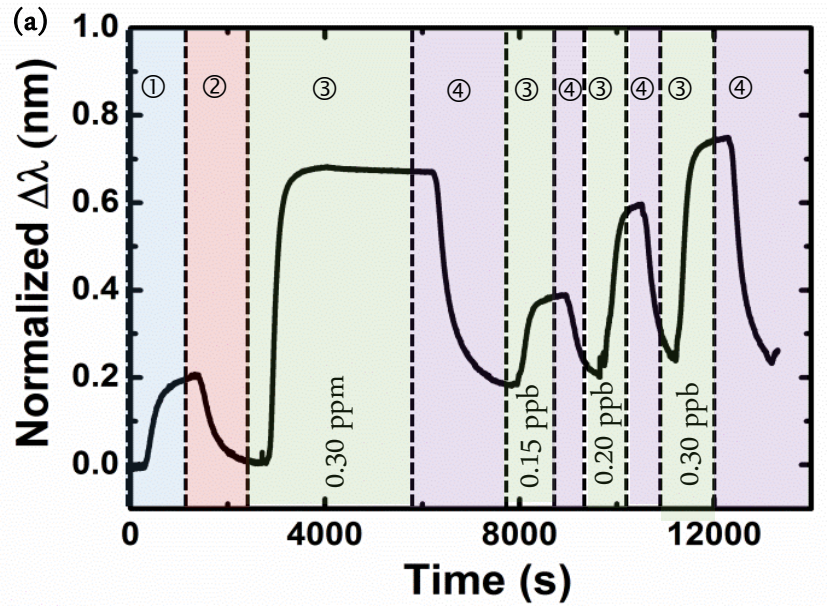


Figure 5.11 Confirmation of washing unbound biotin from biotin-FB complex.



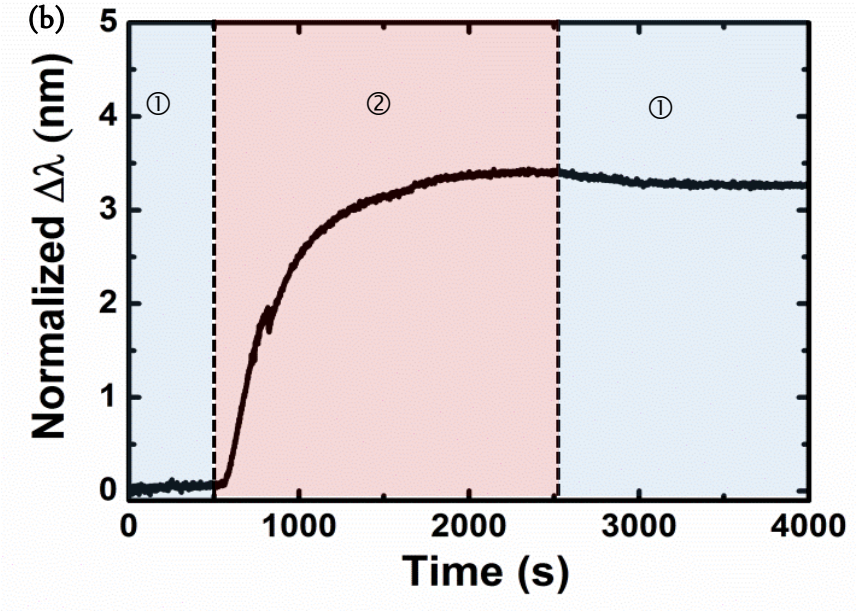


Figure 5.12 (a) Preliminary result of WGM signal from method 2 Biotin-FB and TB (b) TB signal from the sensor without the biotin-FB complex.

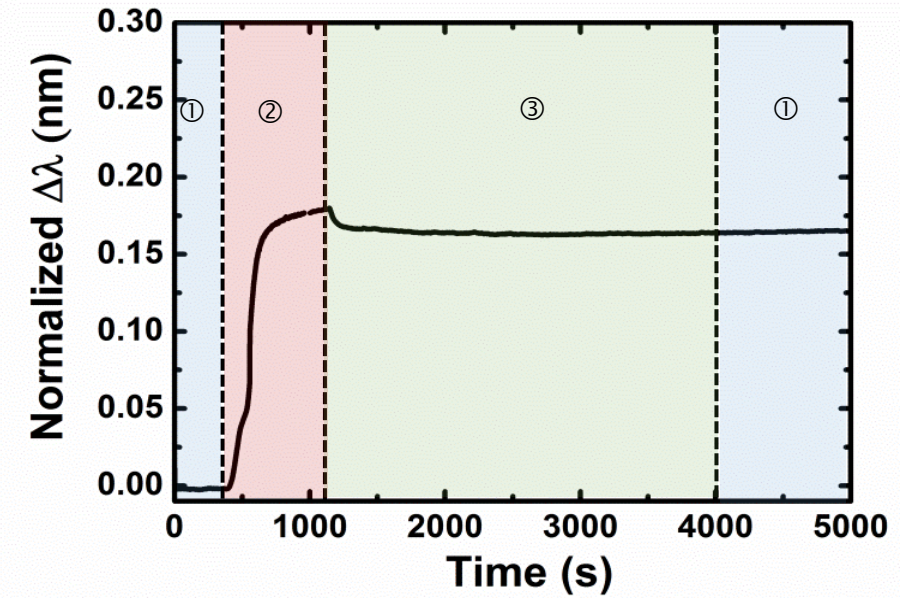
From Figure 5.12, the signal from TB binding was repeated several times. However, the result was not reproducible with a different signal value observed for the same concentration of TB, with even no signal seen on occasion. These irreproducibility may arise for many reasons.

Firstly, it was known that dextran itself inhibited TB activity [26]. If the streptavidin functionalization step does not completely cover the surface, dextran will inhibit TB activity. Method 2 was not selective to only TB as the control experiment Figure 5.12 part (b) showed

that even without FB a large TB wavelength shift signal can be observed from TB. As a result, this method proved ineffective.

5.5.3 Method 3: MPTMS-FB and TB

According to the problems arising from method 1 and method 2, the disadvantages of the new TB-WGM approach can be broken down into three stages; removing unbound or excess molecules (labelling step), complex signals resulting from a range of experimental factors, such as high concentration of salt, unselective surface of the resonator, multi-step functionalization, and low signal from TB. In the final attempt in TB experiment, the idea was simplified by modifying the surface with silane solution (3-mercaptopropyl-trimethoxy-silane, MPTMS) then immobilized with FB according to the covalent linkage between the silane surface and FB protein thus it is possible to study the interaction between TB and FB. Contrary to expectations, this study was unable to find a significant WGM signal difference from TB between 100 up to 150 ppb, Figure 5.13, even Ca^{2+} was added to enhance the aggregation of fibrin [27]. Figure 5.14 shows that insoluble fibrin was generated and lead to dead volume and blockage the flow cell. This may be the reason behind the inability to detect a wavelength shift, and may be the major difficulty in monitoring the TB and FB reaction. A non-uniform layer of the fibrin was generated as the surface was coated with FB, as a result, FB was cleavaged so the surface of the resonator was damaged. In addition, the generated fibrin remained on the surface provided a non-reproducible structure which affected WGM signal. Moreover, the generated fibrin was insoluble and caused the dead volume in the flow cell. To sum up, the TB-FB interaction on the microresonator surface is not compatible with WGM sensor.



① 50 mM Ca^{2+} in PBS ② 2 mg mL^{-1} FB in 50 mM Ca^{2+}
③ 100-150 ppb TB in 50 mM Ca^{2+} in PBS

Figure 5.13 WGM signal from method 3 MPTMS-FB and TB.

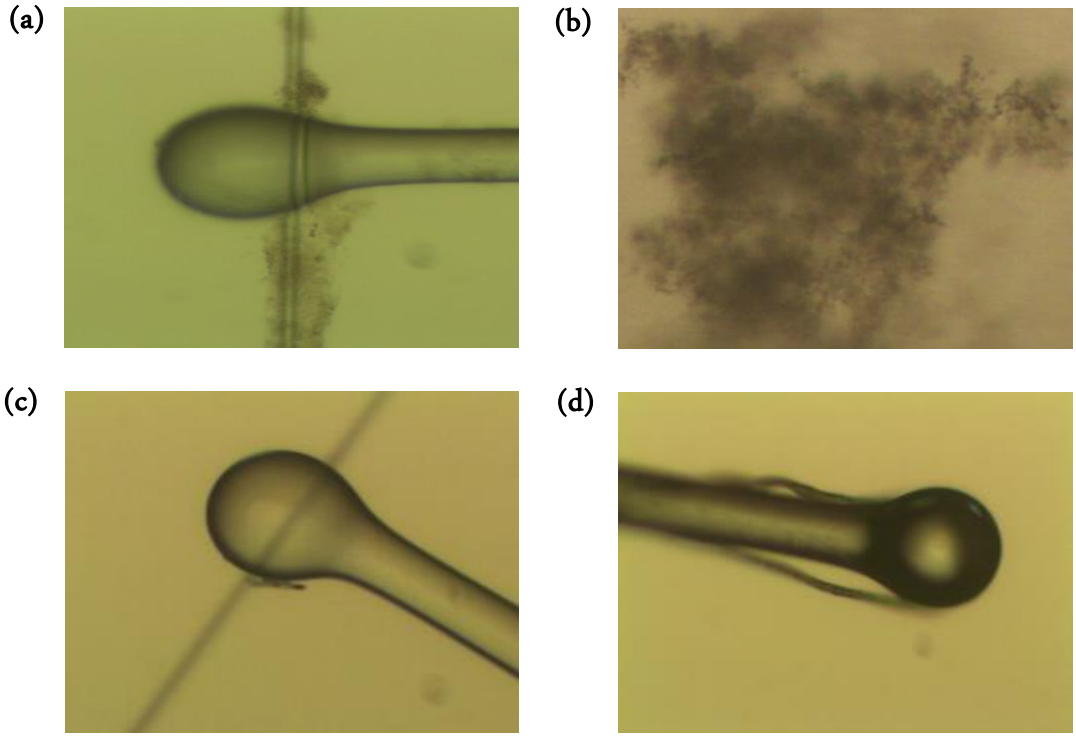


Figure 5.14 Insoluble fibrin generated at the surface of the resonator and in the flow cell in order to see the uncontrolled and non-uniformed the fibrin at a different point in the flow cell (a) and (b) and in the same condition (c) and (d) from a repeated experiment.

5.5.4 Conclusion from TB-based WGM sensor

The reasons behind the unsuccessful of thrombin WGM sensor can be explained as follows. Not only can fibrin induce the assembly of Au NPs, but there are also many other factors, such as salt concentrations that can affect the signal. The generated fibrin is non-uniform and uncontrollable so it can affect the solution and block the flow cell. The interaction between TB and FB, for TB recognition, is not compatible with WGM sensor.

The detection of TB down to pM levels is not simple, especially in blood samples which contain various kinds of interferants. The TB-FB interaction WGM sensor seems not to be a promising tool for TB detection, in its current form, due to the requirement of real-time monitoring. However, a blood sample in a real human body is even more complicated than in an *ex vivo* study. In order to create a reliable TB sensor, therefore many further studies are still required especially, surface functionalization for TB recognition.

5.6 Possible future outlook

This study set out with the aim of assessing the possibility of TB-FB interaction in WGM sensor TB experiment, unfortunately, the finding was unexpected and suggests that TB-FB

interaction is not compatible with WGM so another interaction or bio-recognition elements should be investigated such as aptamer which can bind specific to TB for example thrombin binding aptamer (TBA) or HD22.

5.7 References

1. WiseGeek. *What is Thrombin?* [cited 2016 24/07/2016]; Available from: http://www.wisegeekhealth.com/what-is-thrombin.htm.
2. Doolittle, R. F., *Fibrinogen and Fibrin*, 2001. John Wiley & Sons, Ltd.
3. Anderson, F. A. and Spencer, F. A., *Risk Factors for Venous Thromboembolism.* Circulation, 2003. 107(23): p. I9-I16.
4. Niu, Y., Wang, P., Zhaoa, Y. and Fan, A., *Turn-on colorimetric sensor for ultrasensitive detection of thrombin using fibrinogen-gold nanoparticle conjugate.* Analyst, 2013. 138(5): p. 1475-1482.
5. Davie, E. W. and Kulman, J. D., *An Overview of the Structure and Function of Thrombin.* Semin Thromb Hemost, 2006. 32(S1): p. 3-15.
6. Adams, T. E. and Huntington, J. A., *Thrombin-Cofactor Interactions: Structural Insights Into Regulatory Mechanisms.* Arteriosclerosis, Thrombosis, and Vascular Biology, 2006. 26(8): p. 1738-1745.
7. Kita, R., Takahashi, A., Kaibara, M. and Kubota, K. *Formation of Fibrin Gel in Fibrinogen–Thrombin System: Static and Dynamic Light Scattering Study.* Biomacromolecules, 2002. 3(5): p. 1013-1020.
8. Mosesson, M. W., *Fibrinogen and fibrin structure and functions.* Journal of Thrombosis and Haemostasis, 2005. 3(8): p. 1894-1904.
9. SCIENCE, D. V. *Fibrinogen structure*. [cited 2016 25/07/2016]; Available from: http://3dciencia.com/blog/2012/02/fibrinogen-structure/.
10. Wolberg, A. S., *Thrombin generation and fibrin clot structure.* Blood Reviews, 2007. 21(3): p. 131-142.
11. Brand, N., *Protein-Protein Interactions: A Molecular Cloning Manual. By Erica A. Golemis and Peter D. Adams.* Proteomics, 2006. 6(22): p. 6119-6120.
12. Huntington, J. A., *How Na(+) Activates Thrombin – A Review of the Functional and Structural Data.* Biological chemistry, 2008. 389(8): p. 1025-1035.
13. Wies, C. H., *The History of Hemostasis.* The Yale Journal of Biology and Medicine, 1929. 2(2): p. 167-168.
14. Chatterjee, M. S., Denney, W. S., Jing, H. and Diamond, S. L. *Systems Biology of Coagulation Initiation: Kinetics of Thrombin Generation in Resting and Activated Human Blood.* PLoS Computational Biology, 2010. 6(9): p. e1000950.

15. Mohamed, G., Barsoum, B., Shafi, S. E., Hafez, F. A., , *Spectrophotometric determination of thrombin in pure samples and biological fluids using π-acceptors.* Afinidad, 2012. 69(559): p. 217-223.
16. Peng, Y., *Label-free aptasensor array for determination of thrombin.* Fenxi Ceshi Xuebao, 2014. 33(2): p. 217-221.
17. Qia, H., Shangguana, L., Lia, C., Lib, X., Gaoa, Q. and Zhanga, C., *Sensitive and antifouling impedimetric aptasensor for the determination of thrombin in undiluted serum sample.* Biosensors Bioelectronics., 2013. 39(1): p. 324-328.
18. Xiaokun, C., Shunqing, X., Zhiren, Z., Zhiwei, L. and Wenhong, L., *Fluorescence polarimetric method for the determination of thrombin based on its interaction with aptamer.* Fenxi Huaxue, 2002. 30(3): p. 352-354.
19. Ding, C., Ge, Y. and Lin, J. M., *Aptamer based electrochemical assay for the determination of thrombin by using the amplification of the nanoparticles.* Biosensors Bioelectronics, 2010. 25(6): p. 1290-1294.
20. Li, Z., Li, Y. and Li, W., *Sensitive determination of thrombin by a resonance light scattering technique with oligonucleotides-functionalized gold nanoparticles.* Chemical Journal on Internet, 2008. 10(4): 104020pe
21. Chen, C. K., Huang, C. C. and Chang, H. T., *Label-free colorimetric detection of picomolar thrombin in blood plasma using a gold nanoparticle-based assay.* Biosensors Bioelectronics, 2010. 25(8): p. 1922-1927.
22. Jian, J. W. and Huang, C. C., *Colorimetric detection of DNA by modulation of thrombin activity on gold nanoparticles.* Chemistry-A European Journal, 2011. 17(8): p. S2374/1-S2374/5.
23. Xu, H., Gorgy, K., Gondran, C., Le, G. A, Spinelli, N., Lopez, C., Defrancq, E. and Cosnier, S., *Label-free impedimetric thrombin sensor based on poly(pyrrole-nitrilotriacetic acid)-aptamer film.* Biosensors and Bioelectronics, 2013. 41: p. 90-95.
24. Pasquardini, L., Berneschi, S., Barucci, A., Cosi, F., Dallapiccola, R., Insinna, M., Lunelli, L., Conti, G. N., Pederzolli, C., Salvadori, S. and Soria. S., *Whispering gallery mode aptasensors for detection of blood proteins.* Journal of Biophotonics, 2013. 6(2): p. 178-187.
25. Panich, S., Wilson, K. and Edel, J. B., *Label-Free Pb(II) Whispering Gallery Mode Sensing Using Self-Assembled Glutathione-Modified Gold Nanoparticles on an Optical Microcavity.* Analytical Chemistry, 2014. 86(13): p. 6299-6306.
26. Suzuki, K. and Hashimoto, S., *Effect of dextran sulphates on thrombin activity.* Journal of Clinical Pathology, 1979. 32(5): p. 439-444.

27. Carr, M. E., Gabriel, D. A. and McDonagh, J., *Influence of Ca^{2+} on the structure of reptilase-derived and thrombin-derived fibrin gels.* Biochemical Journal, 1986. 239(3): p. 513-516.

Chapter 6 | Conclusions and Future Outlooks



This final chapter aims to summarize the work presented in the thesis, in addition to providing an outlook regarding future work in this area. An outline of each chapter is also presented, followed by key conclusions from each chapter. In addition, the chapter also includes a critical assessment of the strengths and weaknesses of the WGM methods developed throughout this thesis.

6.1 Conclusions

WGM has an unquestionable importance as a novel detection technique in applied sensor research fields. The work presented in this thesis focuses on developing a WGM-based sensor for both chemical and biological applications. As mentioned throughout, WGM offers many advantages over other optical detection techniques including low cost, fast and label-free detection. Whereby, this thesis covered WGM detection in three applications: Pb(II), G-quadruplex and thrombin (TB) sensors.

In Chapter 1, the motivation and inspiration for integrating WGM detection in sensors were presented. Progression from the basic principles, illustrated by the whispering gallery at St's Paul cathedral, to an advanced outlook in sensors was presented. The background theory of the resonance wavelength sensor including perturbation, refractive index and polarizability was discussed. The discussion was then expanded to WGM microresonators, in terms of geometries and fabrication, as well as the light coupling into microresonator with a particular focus on a sphere resonator. The discussion was then extended to the extreme sensitivity of the technique over the most common methods, due to its high Q-factor. Chapter 1 continued with more detail from previous works published in this field to elucidate and solidify the concepts and applications of using WGM as sensor detection. A review of WGM based sensing and applications were then presented, including chemical, biological and another WGM-based sensing. The key advantages and disadvantages of the WGM sensor were also summarized. Finally, objectives and aims of the research project were presented in the last section.

Next, Chapter 2 focused on the instrumentation and methodology used throughout the WGM sensor project starting from the purpose of each device and instrumentation in the home-built WGM setup. Then the following section detailed in the fabrication process including the microsphere resonator, the tapered waveguide and then the fluidic cell fabrication process. The experimental set-up for resonant wavelength shift detection was paid particular attention in the following section. Chapter 2 also included parameters used to control the WGM signals then data analysis process, programme and software used for the wavelength-shift analysis. Microsphere Q-factor calculation also was demonstrated in the last section of this chapter. The WGM set-up is considered to be simple and practical, but it does suffer from the fact that the tapered wave-guide is fragile and easy to break. Even the set-up has a potential to apply as a

portable device but temperature controller is still required in order to obtain more accurate results.

In Chapter 3, the relevance of WGM in chemical sensing is clearly supported by our findings in this chapter. As was stated in Chapter 1, the objective in Pb(II) sensor work was to develop a novel detection technique for quantification of the trace amount of Pb(II) in water using the home-built WGM setup mentioned in Chapter 2. There were two main objectives which were set to improve (1) the sensitivity and (2) selectivity of the sensor. The study has shown that the simple Pb(II) sensor based on the WGM detection reached all goals mentioned in Chapter 1 such as LOD of the sensor that can be traced down to extremely low levels which were significantly lower than more conventional detection strategies. One of the most significant findings to emerge from this study was that the Pb(II) WGM sensor integrated with Au NPs plasmonic enhancement permits the project to reach the goal of not only sensitivity but also selectivity of the technique. By combining Au NPs plasmonic enhancement and GSH as a chelator, the WGM-Pb(II) sensor was very sensitive and selective to Pb(II). Au NP-GSH probe for Pb(II) is very selective to Pb(II). Chapter 3 initially described detailed about Pb(II) such as symptoms from acute Pb(II) poisoning and, regulation of Pb(II) exposure limit from different organizations. More importantly, limits of detection from other works were also compared with our work which was an important evidence to prove the success of the WGM-Pb(II) sensor work.

Chapter 3 continued with the experimental set up for Pb(II) based WGM sensor which particularly focused on functionalization of the resonator surface including preparation and characterization of the Au NPs, modification of the particles on the resonator surface. Next section was an explanation of how to detect Pb(II) by the WGM sensor. In this chapter, the results from surface characterization from various techniques such as SEM, AFM, and UV-Visible spectrometry has strongly confirmed the success of attaching Au NPs modified GSH onto the resonator surface with the results in good agreement from each technique. The success of the surface functionalization with GSH-Au NPs increased the sensitivity and selectivity to Pb (II). From hard-soft acid-base (HSAB) principle, predicts that hard acids prefer hard bases, soft acids prefer soft bases, and borderline acids prefer borderline bases. The GSH ligand is a Lewis base which acts as an electron pair donor whereas Pb(II), a Lewis acid, is the electron acceptor. As a result, GSH is very prone to the complex formation by Pb(II). In addition, The GSH act as negatively charged chelating ligands towards Pb(II) by coordinating through $-NH_2$,-SH and the COO^- groups. Herein, GSH was modified onto the surface of Au NPs via -SH and $-NH_2$ is protonated to $-NH_3^+$ so only COO^- groups are available. As described in Chapter 3, the reason behind the selectivity of GSH-AuNP is still not clear. There are, however, other possible explanations why WGM-Pb(II) is very sensitive and selective, Pb(II) binds with carboxylate more strongly than other metals, and kinetics of another heavy metals chelation with GSH is slower

than Pb(II). The detection limit of the sensor is down to ppt or nM levels. The interference study showed that the sensor was very selective to Pb(II) even in the presence of several heavy metals. Apart from the set goals (both sensitivity and selectivity), there were still more benefits gained from the sensor such as rapid but real time detection. Moreover, kinetic data can easily be tracked from the real-time binding curve of Pb(II). Taken together, these findings support strong recommendations for WGM as a chemical sensor for heavy metals.

After the success from the chemical Pb(II) sensor in Chapter 3, we looked for more challenges in the WGM experiment as a biological sensor, therefore, a biological molecule starting from TB in blood plasma was investigated even though the results did not accomplish the set goals but there were many interesting issues. Even though TB's sensor result was not promising, DNA experiment with G-quadruplex was found to be valuable and encouraging for WGM as a biological sensor which will be criticized in the following paragraph.

In Chapter 4, the biosensor based WGM technique was demonstrated with focusing on G-quadruplex DNA study. The chapter started with the overview of G-quadruplex DNA which was presented in order to understand the work including topology and characterization of G-quadruplex structure. The introduction in Chapter 4 then was focused on the methods for investigating G-quadruplex DNA/ligand interaction which was reviewed as follows: UV-visible spectroscopy, CD, fluorescence spectroscopy and SPR technique. Chapter 4 then continued with the experiment section as the project dealt with G-quadruplex DNA, as such functionalization of the DNA on the surface of the resonator and characterization the G-quadruplex topology on the surface was paid particular attention using ATR, AFM and fluorescence. As was mentioned before in Chapter 3, one from many benefits in WGM sensing was the observation of a kinetic fingerprinted, which can be easily tracked from the real-time binding curve. Consequently, kinetic binding of G-quadruplex onto the surface was also presented. The results from this experiment were ordered and ranked by the degree of success, for the interpretation of kinetic fingerprints from ligand binding to G-quadruplex or duplex DNA including dissociation equilibrium constant (K_D) and association and dissociation rate constants (k_{on} and k_{off}), then binding affinities for selected five ligands including TO, MB, MG, NS and CV. The binding mode of the selected five ligands with G-quadruplex was also discussed. Next, the control and competition experiment was demonstrated.

In Chapter 4, limitations of the experimental set-up were detailed, such as the discrimination of different forms of c-myc by WGM, attempting to fold and unfold G-quadruplex on the resonator surface, hybridization c-myc and pre-folded c-myc with complementary strand on the resonator surface. In summary, the G-quadruplex experiments were able to confirm several of the results initially aimed for, however, there were limitations, in addition to some unexpected results. By considering only the positive results, this novel approach opens a door to

investigations of DNA-ligand interaction, and will provide valuable information for future WGM studies of such interactions with various DNA sequences.

In Chapter 5, the aim was to assess the findings of TB sensing experiments, where unexpected results were found, and suggests that the TB-FB is not compatible with WGM sensor. The key problem is that the unsuitable surface functionalization for TB binding starting from using Au NP modified with FB, streptavidin-biotin FB linkage or even simple attaching FB on the MPTMS surface. The most serious disadvantage of this TB-FB method is that the wavelength shift was too complicated to analyse. The main weakness of the study was the failure to control the uniformity of the fibrin structure and the damage to the surface from losing of FB after its cleavage by TB. A much more systematic approach would identify a TB probe which can interact with TB without losing the surface density. Even though the results were not encouraging, and difficulties arose, however, there are still plenty of possible improvement in this work which will be discussed in the next section.

This project was conceived working WGM sensor development. This study makes a major contribution to research on both chemical and biological sensor by demonstrating Pb(II) sensor, G-quadruplex-ligand interaction and finally TB sensor. The findings make an important contribution to the field of the sensor. In this study, WGM offers some important insights into sensor technique such as real-time, label-free, extremely sensitive and selective detection of the target analyte, in addition to the simple setup and low-cost analysis. However, the thesis does not engage with different coupling technique such as a prism. The tapered wave-guide used in this study is the weakness because it is fragile and easy to break. It is also beyond the scope of this study to examine the different geometry of the resonator where it is found to be interesting. The possible improvement and future outlook in each experiment will be presented in the next section.

6.2 Future outlook

WGM is a novel optical technique which is capable of measuring trace levels of analytes within a sample. A large number of sensors which have been presented in recent literature cannot detect analyte without a labelling step in real time; however, the WGM sensor can. With this potential which is infrequently found in common sensors, WGM is one of the best practical sensors, especially in biochemical and biomedical research.

A number of WGM experiments have been conducted using various surface modification methods in order to detect a specific molecule. This technique has been gradually developed over more than two decades but there are still many challenges, for example, microresonator surface modification comes with a multitude of complexity which is still challenge in spite of a number of functionalization methods have been published. Despite the fact that the surface

modification in WGM is difficult, the WGM sensor is still more feasible than common techniques such as fluorescence spectroscopy because of its real time read out and portable potential. This research has thrown up many questions in need of further investigation as will be shown in the next paragraph.

The findings in this project are subject to at least three limitations with the possibility of future works. Firstly, the surface of the WGM microresonator is functionalized for the purpose of protecting the microresonator from non-specific molecules binding onto its surface. For biological molecules such as proteins and DNAs detection, various surface modification techniques have been used with varying degrees of success and compatibility. Until now, the surface functionalization with specific biological molecules of interest has still not been fully achieved in WGM research. The problem relates to when a protein or DNA binds onto a functionalized surface, as a result such a molecule will lose its function due to unfolding or occlusion.

To solve this, a number of modified proteins and DNAs were developed by adding a functional group such as thiol, amino groups or biotin molecules which can adhere to a solid substrate without losing its properties. Such a modified protein is practical but expensive. Not only can the surface modification lead to the interest molecule losing its function, but it also decreases the sensitivity of the sensor. Binding the surface with a functionalized chemical substance can increase the roughness of the surface and make it difficult for the light to circumnavigate the surface, but in the WGM experiment, the functionalization of the surface cannot be avoided in order to make the sensor selective to a molecule of interest. The more modified a sensor, the more selective, while a more greatly modified sensor may suffer from a lack of sensitivity, and so optimization between selectivity and sensitivity is required. To sum up, in this issue, there is still more work required on the functionalization process.

Secondly, the light coupling is one of the crucial steps in the development of WGM sensor and is still a challenge in spite of the number of the light coupling methods which have been published. Despite the fact that the tapered waveguide is the simplest method, but this fragile waveguide seems highly unlikely if the sensor is to be adapted as a portable device. The metrics of the WGM measurement will be very sensitive to the alignment of the tapered fibre optic next to the resonator. Small changes in the gap or position along the taper can affect coupling efficiency, thus reducing the robustness of the approach for high throughput applications. The approach will not be easily multiplexed since each experiment will need a separate fibre/resonator pair. This point of the issue needs further development.

Thirdly will be further works from each application. In the Pb(II) experiment, the work proved successful. Possible future adaptation includes its development as a portable field device.

However, temperature fluctuation outside the laboratory might be a problem. Moreover, the coupling system used in this work, tapered wave-guide is too fragile to be a portable device. Finally, in this part, the possible future work might be improving the sensor to detect a range of heavy metals at the same time by modifying the chelator attached on the surface of the resonator. For the G-quadruplex experiment, there are several possible future works regarding the G-quadruplex experiment detailed in Chapter 4. As is demonstrated, the immobilization of G-quadruplex has not been fully examined. There are many possible functionalization processes which can be applied such as click reaction. This is the first time that WGM was reported for sensing G-quadruplex/ligands interaction. There are a lot of doors to investigate in this work such as folding G-rich DNA to G-quadruplex complex by small molecules and detection of this folding process in real-time. Different sequences of DNA should be examined. A major criticism of the G-quadruplex's work is in the ligand binding experiment where there should be another technique provided in order to verify the result and a different mathematical model to fit the entire curve. However, because of the limit on time, the work has been continued after the thesis and can be found in the appendices "Novel sensing for real-time monitoring of Ligand binding to G-Quadruplex and duplex DNA by the whispering gallery mode (WGM) technique" where the affinities of the ligand were verified with fluorescence technique and the binding curves have been verified with polynomial fitting using math lab program.

Finally, concerning the TB experiment, although extensive research has been carried out on TB-FB interaction as a TB probe, unfortunately, there has been no reliable evidence that can confirm the promise of the TB-WGM sensor. This indicates that TB-FB interaction is not compatible as a probe for WGM so another interaction or bio-recognition elements for TB should be investigated for example TBA or HD 22 which shows good affinity and specificity against TB. TB-FB might not be a good model of protein-protein interaction for WGM as during the generation of fibrin (F) the modified material may be lost from the surface due to cleavage of FB by TB.

Appendices | List of publications

1.Label-Free Pb(II) Whispering Gallery Mode Sensing Using Self Assembled Glutathione-Modified Gold Nanoparticles on an Optical Microcavity (Panich, S., Wilson, K. and Edel, J. B., *Label-Free Pb(II) Whispering Gallery Mode Sensing Using Self-Assembled Glutathione-Modified Gold Nanoparticles on an Optical Microcavity.* Analytical Chemistry, 2014. 86(13): p. 6299-6306.)

2.Real-Time Monitoring of Ligand Binding to G-Quadruplex and Duplex DNA by Whispering Gallery Mode Sensing (Panich, S., Sleiman., M. H., Steer, I., Ladame, S. and Edel, J. B., *Real-Time Monitoring of Ligand Binding to G-Quadruplex and Duplex DNA by Whispering Gallery Mode Sensing.* ACS Sensors, 2016.)

analytical chemistry

Article

pubs.acs.org/ac

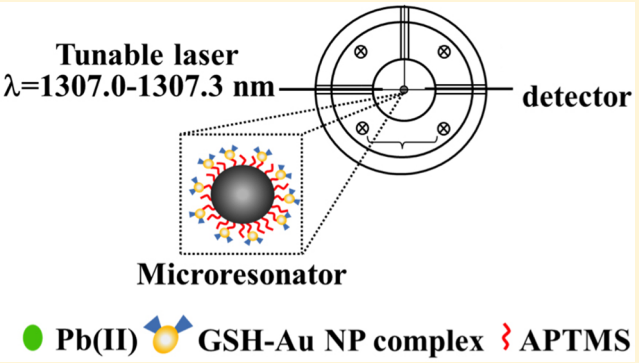
Label-Free Pb(II) Whispering Gallery Mode Sensing Using Self-Assembled Glutathione-Modified Gold Nanoparticles on an Optical Microcavity

Sirirat Panich, Kerry A. Wilson, Philippa Nuttall, Christopher K. Wood, Tim Albrecht, and Joshua B. Edel*

Department of Chemistry, Imperial College London, South Kensington Campus, London SW7 2AZ, United Kingdom

Supporting Information

ABSTRACT: An ultrasensitive assay for the detection of Pb(II) has been developed using whispering gallery mode (WGM) sensing. In this technique a photonic microcavity was decorated with glutathione (GSH)-modified gold nanoparticles (Au NPs). The resonator was functionalized using an aminosilane to promote adhesion of the GSH-modified NPs creating a highly sensitive sensor specific to Pb(II). Upon introduction of Pb(II) solutions via a fluidic cell, Pb(II) ions bind to the GSH−Au NP complex and induce a shift of the resonant wavelength. Using this detection strategy we show that we are able to detect Pb(II) concentrations down to 0.05 nM in the presence of alkaline and heavy metal interferences such as Mg(II), Mn(II), Ca(II), Ni(II), Cd(II), Cr(II), Fe(II), and Hg(II). The signal was found to be proportional to the Pb(II) concentration within the range of 2.40−48.26 nM and was found to have an association constant of 2.15×10^5 M^{-1} s^{-1}. The sensitivity obtained shows unparalleled advantages over currently available technology and satisfies the exposure thresholds set out by world organizations such as International Agency for Research on Cancer (IARC) and the Environmental Protection Agency (EPA). We believe that this sensor has the potential to be made portable for applications in environmental monitoring and in-field applications.



It is well-known that exposure to even trace amounts of heavy metals such as lead (Pb), cadmium (Cd), mercury (Hg), or arsenic (As) can cause disease and even death in humans.[1] As such, many international and national regulatory bodies, including the World Health Organization (WHO), Environmental Protection Agency (EPA), and the International Agency for Research on Cancer (IARC) have established regulations highlighting exposure limits in food and water in order to protect the worldwide population. The symptoms of acute lead poisoning include fatigue, headaches, irreversible learning difficulties, lung tumors, and illnesses related to the nervous system. Moreover, some evidence indicates that lung and stomach cancer can be attributed to Pb(II) exposure. As a result, Pb(II) has been classified as a possible carcinogen to humans by IARC.[2] While the EPA has defined 72.40 nM (15 ppb) to be a safe threshold in drinking water, IARC has a lower threshold of 48.26 nM (10 ppb). On the basis of these low thresholds, it is clear that simple technology needs to be developed to design assays that are addressable at these concentrations.

Several promising analytical techniques have already been developed to detect trace levels of Pb(II) in tap water,[3] paints,[4] food samples,[5] biological,[6] and environmental samples.[7] The majority of these methods are typically based on atomic absorption spectrometry (AAS) or inductively coupled plasma spectroscopy (ICP) where detection limits down to 4.83 μM (1000 ppb) can be achieved.[8] Despite the fact that the detection limits are low, they are still higher than those set out by IARC and sample preconcentration is often required.[9] This makes the techniques time-consuming and complex for in-field applications. ICP is a very promising tool for trace analysis of Pb(II); however, this technique is complicated, and suffers from memory effects and molecular or atomic interferences.[10] In order to overcome these shortcomings, there has been a recent drive to develop simpler and more sensitive assays based around the direct or indirect detection of Pb(II).

Although many alternatives exist, the most promising involves colorimetric-based approaches. For example, gold nanoparticles (Au NPs) are commonly used as they can act as highly adaptable probes that exhibit different optical and electronic properties in the presence Pb(II). The majority of such sensors have been based around the detection of Pb(II) in the presence of binding ligands such as DNA-modified enzymes,[11] gallic acid,[12] or catechin.[13] Detection limits of the latter were shown to be 1.45 nM (300 ppt); however, complex labeling procedures were required. Another example relates to

Received: January 22, 2014
Accepted: May 28, 2014
Published: May 28, 2014

ACS Publications © 2014 American Chemical Society

the work by Chai et al.[14] where they report on a simple colorimetric aggregation-based assay using both glutathione (GSH) and Au NPs with detection limits down to 96.52 nM (20 ppb). Alternatively, Ali et al.[15] demonstrate that GSH-capped CdSe and CdTe quantum dots could be used as a fluorescent probe for the indirect determination of Pb(II) concentration down to 19.30 nM (4 ppb). Other techniques have also been explored with varying degrees of success and complexity.[16,17] However, novel detection strategies are still required to improve acquisition times, portability, and enhance the sensitivity of assays especially when taking into consideration the limits of detection set out by world organizations. To this end, whispering gallery mode (WGM) sensing offers attractive prospects over more conventional technology. These include real-time subsecond acquisitions, label-free, near single molecule sensitivity, and it can be made using CMOS processing methods,[18] used for in-field applications, and is accessible to a nonspecialist user.

The operating mechanism of WGM sensing is simple,[19−21] where resonance modes in dielectric microcavities can be used to detect minute changes in the surrounding local environment. Upon binding of an analyte to the cavity, a shift in the resonance wavelength occurs (Figure 1); as such, the concentration of the analyte can be easily determined. The phenomenon of a whispering gallery in the context of sound waves was first described more than a hundred years ago by John William (Lord Rayleigh).[20] However, only recently has WGM sensing been used to create novel optical, chemical, and biological sensors. The majority of WGM sensors involve the detection of single particles or biological samples such as biomarkers,[22,23] protein,[24] or viruses.[25,26] Generally speaking, smaller molecules or even ions tend to be difficult to detect in part due to the low sensitivity of WGM sensing to dissolved ions, as well as the lack of ability to discriminate between ionic species. As a result, few examples of heavy metal detection using WGM sensing have been reported. An exception is the work by Hanumegowda et al.[27] where they detected Hg(II) by using microsphere optical ring resonators. However, in this case detection limits were still very high (241.30 nM or 50 ppb) due to limitations associated with the spectral resolution and saturation levels. To overcome these limitations and drive the detection limits lower, we have developed a hybrid technology relying on the specific binding of Pb(II) to GSH adsorbed to Au NPs to sensitize the surface of the optical microcavity.

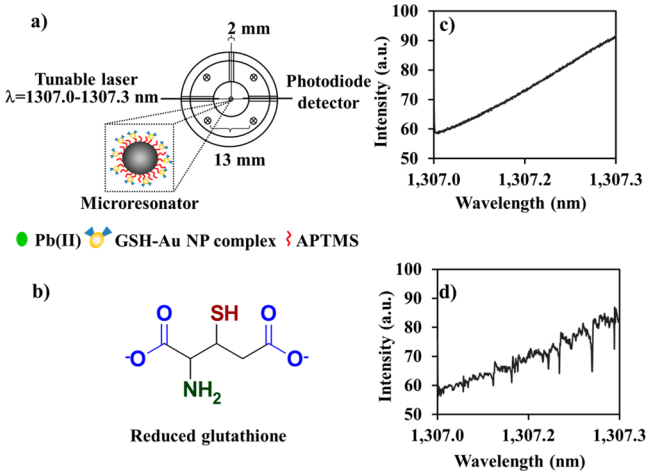


Figure 1. (a) Schematic representation of a WGM platform for the detection of Pb(II). The light, generated by a tunable laser, circumnavigates the surface of a microresonator through a tapered waveguide made from an optical fiber. This light is strongly confined inside the microsphere by total internal reflection. Energy is extracted from the fiber, resulting in a negative peak detected by a photodetector. The surface of the resonator is functionalized with GSH to improve the specificity to Pb(II). When the metal ion binds to the modified resonator a spectra shift is observed which is used to quantify the concentration of the analyte. (b) Chemical structure of reduced glutathione as a chelator in which $-COO^-$ groups were used for chelating with Pb(II). (c) Transmission spectrum before and (d) when coupled to a microsphere resonator.

In this article, we show that GSH−Au NPs adsorbed to an aminopropyl trimethoxysilane (APTMS)-coated glass resonator, incorporated into a microfluidic cell, can be used for efficient sensing of Pb(II). When Pb(II) binds to the surface of the Au NP via the bound GSH, a shift of the resonance wavelength is observed due to the perturbation and the polarization of the bound Pb(II) molecule.[28] This shift is proportional to the amount of Pb(II) bound to the GSH−Au NP complex and can be used for quantifying the amount of analyte present. Furthermore, due to the inherent sensitivity of the technique, we show that real-time kinetics can be determined by fitting the binding to a simple pseudo-first-order binding model. We show that such a sensor can be used to detect Pb(II) down to concentrations of 0.05 nM (10 ppt) in the presence of other ionic interferences. This work represents an important step toward realizing a portable platform for environmental monitoring and biological toxicology assays without the need for purification or preconcentration.

EXPERIMENTAL SECTION

Preparation and Characterization of the Au NPs. Citrate-stabilized Au NPs with an average diameter of 16 nm were synthesized according to the Turkevich method.[29] The synthesis was performed in a 250 mL round-bottom flask connected to a condenser. Gold(III) chloride hydrate (8.86 mg, $HAuCl_4 \cdot 3H_2O$, Aldrich, U.K.) was dissolved in 95 mL of deionized water. The resulting mixture was refluxed for 20 min at 150 °C, and then 5 mL of sodium citrate tribasic dehydrate (20 mg, $HOC(COONa)(CH_2COONa)_2 \cdot 2H_2O$, Sigma-Aldrich, U.K.) was rapidly added. The reaction mixture was then stirred for 15 min and then cooled to room temperature. The size and concentration of the Au NPs was determined using UV−vis spectroscopy (Spectrometer, Thermo), dynamic light scattering (delsaTM, Analyzer), and scanning electron microscopy (SEM, Oxford).

Modification of the Au NP Surface with GSH. The functionalization of Au NPs with GSH was performed according to the protocol previously described by Beqa et al.[16] All modifications were performed in the dark under an N_2 atmosphere due to the sensitivity of the GSH complex to light and oxygen. Au NPs, at a concentration of 0.59 nM and volume of 8 mL, were added to a 100 mL round-bottom flask, after which, 1 mL of 0.59 μM reduced L-glutathione ($H_2NCH(CO_2H)CH_2CH_2CONHCH(CH_2SH)CONHCH_2CO_2H$, Sigma-Aldrich, U.K.) was added. The mixture was stirred for 2 h at room temperature in dark conditions to ensure complete binding of GSH onto the surface of the NPs. The pH of the resulting mixture was adjusted to 8.0 using 0.01 M NaOH. Finally, the mixture was then washed by centrifugation at 10 000 rpm for 20 min and the supernatant aspirated off to remove unbound GSH. The remaining complex was further washed

dx.doi.org/10.1021/ac500845h | Anal. Chem. 2014, 86, 6299−6306

with water three times. The spectrum of the complex with 4.83 μM (10 ppm) Pb^{2+} was checked to confirm the successful functionalization of GSH on the Au NP surface.

WGM Resonance Shift Measurements. The platform for optical detection was based on the work previously described by Wilson et al.[30] and is shown schematically in Figure 1a. A wavelength-tunable distributed feedback laser, DFB (D2304G, 1310 nm isolated DFB laser module, Lucent), was used as an excitation source with a nominal wavelength of 1307 nm and a maximum power output of 10 mW. The laser was mounted on a LM14S2 butterfly laser mount (Thorlabs) and driven using a LDC 201C current controller (Thorlabs) and TED 220C temperature controller (Thorlabs) to control the output wavelength. The laser wavelength was tuned through a narrow range of wavelengths using a sawtooth function generated from an 80 MHz arbitrary waveform generator (model 4086, BK Precision). The laser was scanned at a frequency of 100 Hz for all experiments. The laser output was coupled to a single mode optical fiber (F-SMF-28, Newport). All the fiber-optic cables were connected using a fusion splicer (S123c, Fitel). The output of the optical fiber was then coupled to an InGaAs photodetector (PDA 10cs, Thorlabs). The photodetector was interfaced with a Labview data acquisition card (BNC 2110, National Instrument), and the signal was analyzed using a custom-written Labview script that could track the resonant peak as a function of time.[30] All data was then post processed using statistical software such as Origin 8.6.

Fabrication and Functionalization of the Microresonator. All microresonators were fabricated from single-mode optical fibers (F-SMF-28, Newport) by placing the tip in an oxygen−hydrogen torch flame which produces sufficiently high temperatures to melt the glass. By precisely controlling the orientation, a spheroidal shaped tip was then formed due to the surface tension of the molten glass. It is this tip that was used as the microresonator, which was determined to be 250 ± 100 μm in diameter from both optical and SEM imaging (Supporting Information, Figure S1). The microresonator was then functionalized using an aminosilane in order to increase the adhesion between the glass and the GSH-modified NPs. Briefly, the microresonator was immersed in a 0.1% v/v solution of APTMS and toluene under dry conditions in order to avoid exposure to oxygen and water vapor. The solution was then gently heated to 70 °C for 60 min and allowed to cool for 20 min. The microresonators were then washed in fresh toluene and dried in an oven for 30 min. As a result, a greater deposition of gold particles modified with GSH (Figure 1b) on the surface was possible due to the electrostatic interaction of the negatively charged particles with the positively charged APTMS. The resonator was then aligned to be in close proximity to the tapered waveguide by using a three-axis micromanipulator (PT3/M, Thorlabs). Finally, the resonator and waveguide were inserted into a microfluidic cell in order to efficiently deliver Pb(II); details are described in both Figure 1 and the Supporting Information, Figure S1.

Detection of Pb(II) by WGM Resonance Shift. In order to maximize the sensitivity, the positions of the waveguide and resonator were aligned to maximize the *Q*-factor (a dimensionless parameter which defined as the resonant frequency/bandwidth) obtained as determined from the transmitted spectrum. As an example, differences between transmission spectra from the coupled and uncoupled cases are shown in Figure 1, parts c and d, respectively. Typical *Q*-factors were determined to be 6×10^6, which are comparable to what has been reported in the literature[31] and limited by the optical absorbance of water near 1300 nm. In all experiments, a single resonance line at 1307 nm was used as a reference and tracked over the course the experiments. However, all measurable resonances in the spectrum were also tracked for later analysis. It is this change in wavelength ($\Delta\lambda$), or resonance shift, which can be directly correlated to the Pb(II) concentration. Once the optics were fully aligned, GSH (Figure 1b) modified Au NPs were delivered into the fluidic cell to decorate the surface of the microsphere. Resonance wavelength shifts were recorded until a plateau was reached, indicating that the surface was saturated (Supporting Information, Figure S2). Excess NPs were removed by flushing the cell with deionized water at least five times. In order to quantify Pb(II) concentrations, the fluidic cell was initially filled with 500 μL of DI water followed by allowing the system to stabilize for ∼15 min. Once complete, 50 μL of varying concentrations of Pb(II) or other metal ions was then pipetted into the fluidic cell. Resonance shifts were tracked until saturation. Between runs the fluidic cell was washed with at least 5 vol equiv of water.

RESULTS AND DISCUSSION

Characterization of the GSH-Modified Au NPs. The rationale behind using GSH is that it has excellent specificity when binding to Pb(II) in comparison to other metal ions. In fact, among its many vital biological roles, GSH is designed to protect cellular membranes from unwanted heavy metals via complex formation. GSH contains four functional groups as shown in Figure 1b: two carboxyl (−COOH), one amino ($-NH_2$), and one sulfhydryl (−SH) group. In aqueous solution it has been shown that Pb(II) complexes via the thiol moieties.[32] However, when bound to a Au NP, the −SH group is occupied due to the formation of a strong Au−S bond with the nanoparticle surface. Therefore, the binding is likely to take place via the two free $-COO^-$ groups.[16] This is also supported by the work of Kim et al.[33] where they claim that Pb(II) binds with the two $-COO^-$ units. An interesting consequence of this chelator is that at pH 7 the carboxylic acid is deprotonated to $-COO^-$ and the amine group is protonated to $-NH_3^+$, which protects GSH from binding with Zn(II)and Cd(II). This can enhance the selectivity and the sensitivity of the technique. In addition to GSH acting as a good chelate ligand, it also acts to stabilize the NPs.[16] The motivation for this work was to sensitize a resonator to ensure specificity only to Pb(II). Due to the plasmonic coupling of the NPs, the surface of the resonator can potentially result in enhanced sensitivity by numerous orders of magnitude as proposed recently by Shopova et al.[34] When a nanoparticle approaches the surface of the WGM resonator, it is polarized by the evanescent field, generating from orbiting of the light from the laser, extends into the surrounding medium. This interaction induces a shift in the resonance frequency proportional to the polarizability of the particle. A nearby enhanced field increases the energy required to polarize the particle relative to the total energy in the resonator. This leads to a larger frequency shift. Therefore, the strategy followed was to coat the resonator with GSH-modified Au NPs. Prior to doing so, we also investigated whether GSH could be adsorbed directly to the resonator thereby removing the added complexity associated with NP adsorption. Without NPs, the resonator has much higher *Q*-factors and therefore has the added possibility of improved detection limits. It should be mentioned that, although immobilization of GSH onto a glass or APTMS surface is

dx.doi.org/10.1021/ac500845h | Anal. Chem. 2014, 86, 6299−6306

possible, a catalyst and high temperatures are required (see Supporting Information Figure S2a for an example relying simply on adsorption).[35] Decorating the resonators with the Au NPs is a simple solution, granted at the expense of the *Q*-factor. For all experimental work it was therefore deemed appropriate to utilize the NPs on the resonator to facilitate the measurements.

The GSH−Au NP complex was synthesized prior to decoration onto the surface of the microresonator. GSH bound to NPs on its own does not cause a shift or broadening in the UV−vis spectrum, as shown in Figure 2a, indicating no aggregation takes place. This was performed at a 8:1 volume ratio of NP (0.59 nM) and GSH (0.59 μM) and agrees well with Beqa et al.[16] In fact, the NPs are likely to be stabilized with the complex. It should be noted that the absorbance of the complex increased compared with the absorbance of the unmodified Au NP as shown in Figure 2a and therefore is a good indication that the surface coupling has been successful.[36] The surface modification was also confirmed using dynamic light scattering (DLS) whereby the average diameter for Au NPs without and with GSH was determined to be 25.0 ± 8.2 and 37.3 ± 19.8 nm, respectively. These values are slightly larger than those recorded by SEM (16 ± 0.4 and 21 ± 0.64 nm) and atomic force microscopy (AFM) (15.8 ± 0.21 and 16.77 ± 0.22% nm), which is generally expected as it is the hydrodynamic diameter which is being measured in DLS unlike SEM, where the dehydrated diameter is measured; alternatively, another possibility which cannot be ruled out is dimerization.

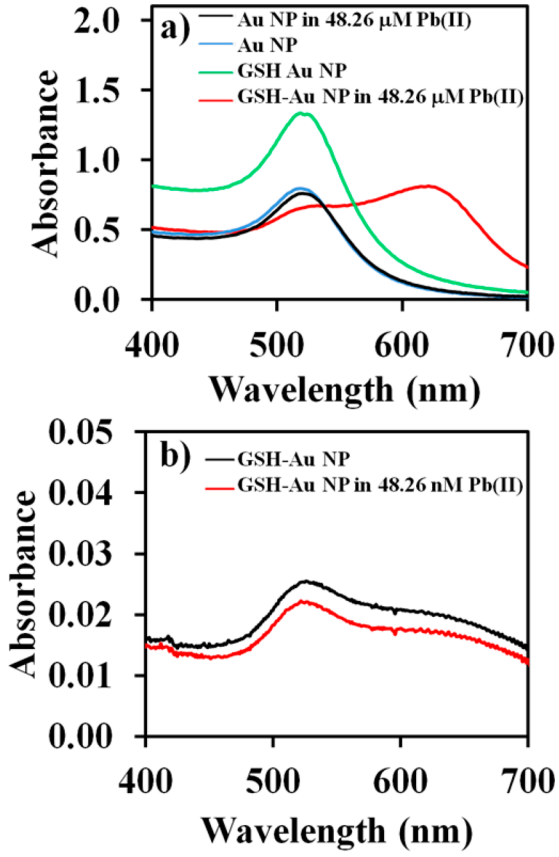


Figure 2. (a)UV−Vis spectra of Au NP and GSH-modified Au NP complex before and after addition of Pb(II) in solution. (b) Example spectra of the GSH−Au NP complex deposited on an APTMS glass-coated surface before and after binding with 48.26 nM Pb(II).

To determine the appropriate GSH concentration, a serial dilution of GSH was performed at a constant NP concentration in bulk solution (Supporting Information, Figure S3). Upon addition of 48.26 μM (10 ppm) Pb(II), aggregation is expected which results in broadening and a red shift of the plasmon resonance as shown in Figure 2a (i.e., the solution color changes from red to blue). As a control, no color change was observed with bare NPs in the presence of 48.26 μM (10 ppm) Pb(II), whereas a clear color change was observed with GSH-modified particles. Unfortunately this colorimetric change is only observable at concentrations of Pb(II) greater than 4.82 μM (1 ppm). Although this technique on its own is elegant and simple, detection limits are well above those designated by the IARC and EPA. To understand the spectral properties on the microresonator surface, a glass coverslide coated with APTMS and the NP complex was used as a model.[29] The spectra with and without the addition of 48.26 nM (10 ppb) Pb(II) is shown in Figure 2b. No spectral shift was observed at 518 nm indicating that the NPs do not aggregate with the addition of Pb(II) when bound to the resonator. This was also consistent with results obtained using SEM and AFM imaging as shown below (Figure 3).

The GSH-mediated Au NP assembly was studied before by Beqa et al.,[16] who calculated that 12 GSH molecules were bound per Au NP with diameter of 10 nm. Using the same ratio between GSH and surface area we estimate that 30 molecules of GSH would bind per 16 nm NP as used in these studies. Assuming 1:1 binding between GSH ligand and Pb(II), approximately 30 Pb(II) ions would bind per NP. Specific details of the binding chemistry between GSH and Au NPs have been nicely documented by Stobiecka et al.[36] They report on several possible mechanisms that could potentially take place for the assembly of *n* GSH-linked NPs (where *n* is the number of Au NPs and can be any number from 3 to 6). More details of the characteristics of the GSH−Au NP complex on the surface of the microresonator will be discussed in the next section. However, it should be noted that the mechanism in our case is likely to be different due to the NPs being immobilized on the surface of a resonator, and no linking is expected.

Surface Characterization of the Resonator. All surface characterization of the resonators was performed using electron backscatter diffraction scanning electron microscopy (EBSD-SEM, Oxford) and AFM (Agilent) as shown in Figure 3. Due to the complexity of the sample associated with the NP dimensions and curvature of the surface, AFM imaging was performed in tapping mode using a supersharp noncoated n^+-silicon tip (Windsor Scientific, U.K.). APTMS-functionalized resonator surfaces with and without a 15 min of exposure to the GSH-modified NPs were analyzed as shown in Figure 3, parts a and b. The results obtained by AFM were analyzed using WsxM.[37] The results in Figure 3 show that an APTMS-coated microresonator is relatively smooth with an rms roughness of 1.9 nm. The roughness was increased to 4.2 and 5.8 for GSH-capped NPs with and without 48.26 nM (10 ppb) Pb(II), respectively. It can be seen that NPs adhere very well to the functionalized resonator surface and results are comparable to that of Liu et al.[38] With Pb(II) added to the resonator at exposure levels of 48.26 nM (10 ppb) or lower, little or no agglomeration of the Au NP was observed as is shown in the AFM and SEM images in Figure 3c. According to the result from AFM, the percentage coverages of GSH−Au NP coated

dx.doi.org/10.1021/ac500845h | *Anal. Chem.* 2014, 86, 6299−6306

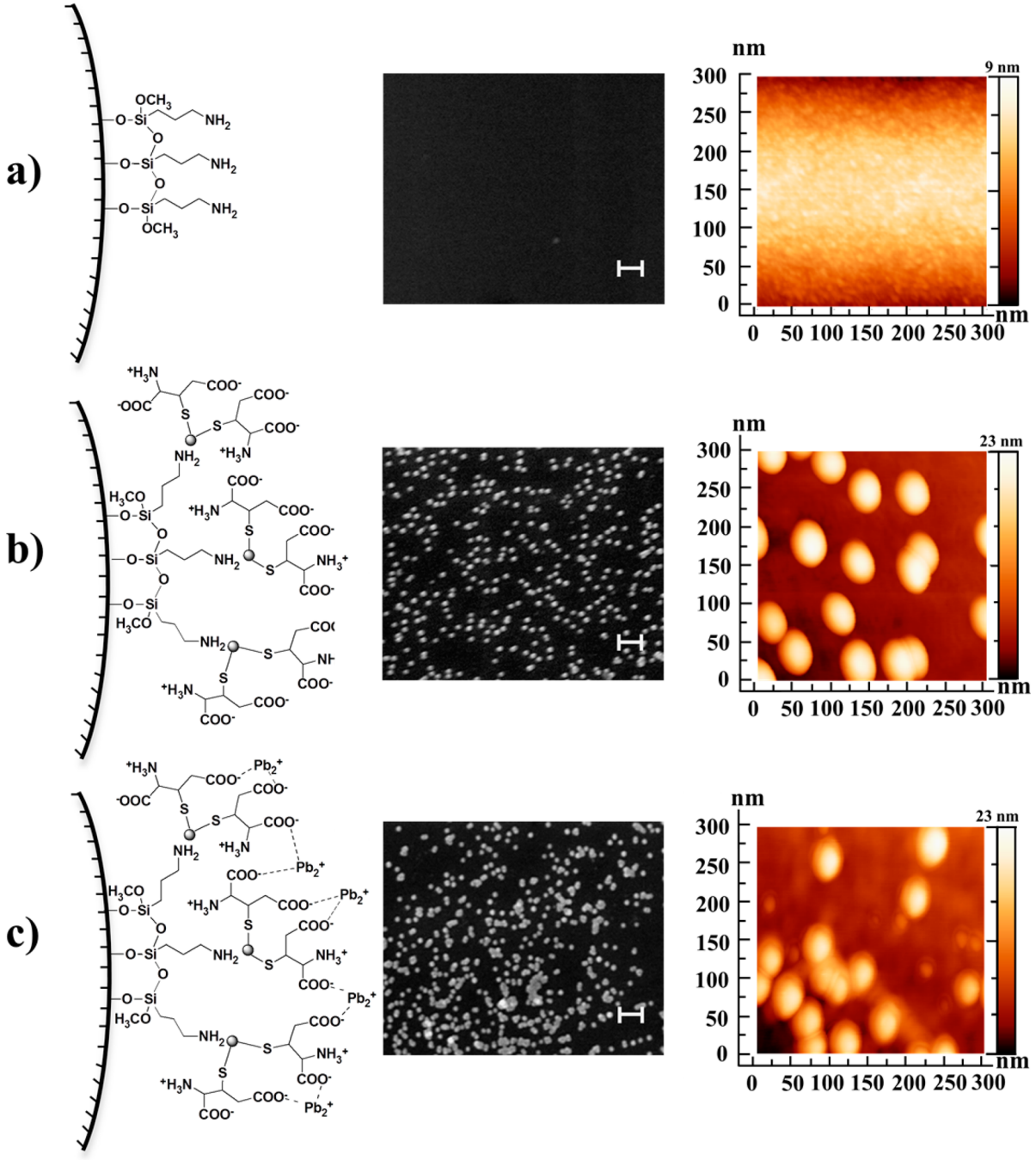


Figure 3. Chemical structure of the molecules used for surface functionalization: (a) APTMS, (b) APTMS coated with the GSH−Au NP complex, and (c) GSH−Au NPs in the presence of Pb(II). Surface coverage was characterized using SEM (middle) and AFM (right). In these experiments, the resonators were soaked in a solution of GSH−Au NPs for 15 min followed by the addition of either 4.82 μM or 48.26 nM Pb(II), respectively. The scale bars for SEM images are 200 nm.

with and without Pb(II) are 40% and 42%. At higher concentrations, minor aggregation was observed and was likely due to rearrangement of the NPs on the resonator surface in the presence of Pb(II). Therefore, under the dynamic range of the WGM measurement, all shifts observed are due to the chelation of Pb(II), which has a high polarizability effect compared with other metals,[39] to the NP without induced aggregation.

Upon NP binding to the resonator surface, the *Q*-factor decreased from 6×10^6 to 4×10^5 as shown in Supporting Information Figure S4 and was due to an increase in surface roughness as a result of the adsorbed Au NPs, which necessarily diminishes the intrinsic *Q*'s of the resonant mode. Addition of Pb(II) to the solution induced no change in the *Q*-factors. As mentioned earlier, the *Q*-factor is lowered upon the addition of NPs and indeed lowers with increased surface roughness or NP surface coverage; therefore, a fine balance needs to be met between ensuring a sufficiently high *Q*-factor and sufficient particles on the surface to sense Pb(II) as shown in Supporting Information Figure S5. Normally, there are four terms which can be considered to affect the *Q*-factor and can be mathematically defined as follows: $Q_0^{-1} = Q_{rad}^{-1} + Q_{mat}^{-1} +$

dx.doi.org/10.1021/ac500845h | *Anal. Chem.* 2014, 86, 6299−6306

$Q_{s.s}^{-1} + Q_{count}^{-1}$.[20,40] Q_{mat}, Q_{rad}, $Q_{s.s}$, and Q_{count} can be described as intrinsic material adsorption, radiation loss, scattering losses, and coupling loses, respectively. In our case, $Q_{s.s}^{-1}$, is the dominating force in decreasing the overall Q-factor due to surface inhomogeneity associated with the NP modification. It was deemed that ∼40% NP coverage (16 nm in size) was a good compromise, which still gave a sufficiently high Q which could be tracked over the measurement time scale.

Quantification of Pb(II) Using WGM Sensing. The wavelength of the resonant mode is highly sensitive to the surrounding local environment. When Pb(II) binds to the surface, the increased polarizability of the Pb(II) with respect to water causes a shift of the resonant mode to longer wavelengths as seen in Figure 4a. The WGM signal upon addition of Pb(II) was found to be nonlinear at low concentration (less than 2.4 nM) and saturated at higher concentration as shown in the Supporting Information, Figure S6a. This trend agrees well with Hanumegowda et al. where Hg(II) was tracked by WGM sensing.[27] The detection limit of the WGM sensor was found to be 0.05 nM (10 ppt), based on setting a threshold of 3 times the standard deviation of a blank signal as shown in the Supporting Information, Figure S6b. Typical resonant shifts range between 1307.0 and 1307.3 nm, which is well within scanning resolution of the laser. This resonance shift can be monitored as a function of time as is shown in Figure 4b with addition of Pb(II). Therefore, it is possible to measure real-time binding curves which reveals not only the concentration of Pb(II) based on the plateau but also the rate of binding between GSH and Pb(II). The binding mechanism can be defined as follows, eq 1.

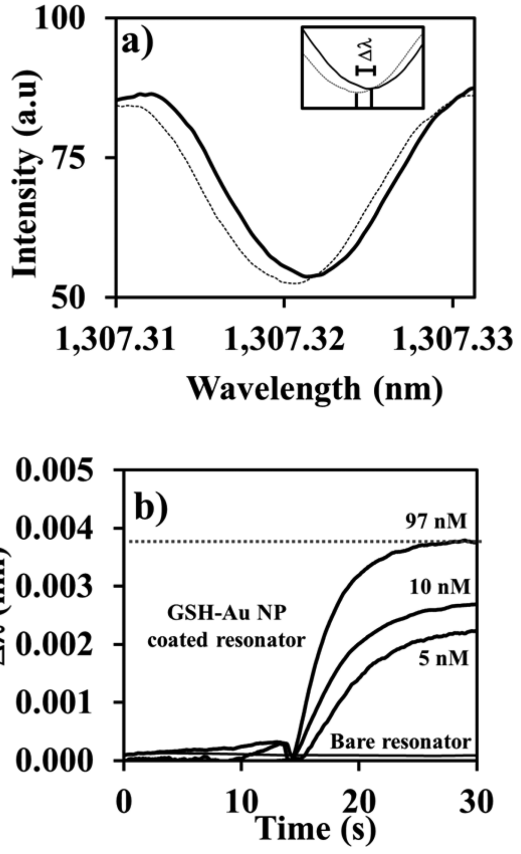


Figure 4. (a) Example wavelength shift due to the binding of Pb(II) at 2.40 nM. (b) Time-dependent binding curves for a bare resonator 5, 10, and 97 nM Pb(II). The baseline from the blank injection is shown in the Supporting Information, Figure S10.

$$m\mathrm{Pb(II)} + n\mathrm{C} \underset{k_{-1}}{\overset{k_1}{\longleftrightarrow}} \mathrm{Pb}_m\mathrm{C}_n \quad (1)$$

Here k_1 and k_{-1} are the association and dissociation rate constants, respectively. The binding between Pb(II) and $-COO^-$ of GSH can be described by a monoexponential growth equation or pseudo-first-order reaction as shown in eq 2.[41,42]

$$\Delta\lambda_t = \Delta\lambda_{max}(1 - e^{-k_{obs}t}) \quad (2)$$

where $\Delta\lambda_t$ is the time-dependent resonance wavelength shift and $\Delta\lambda_{max}$ is the maximum resonance wavelength shift at the plateau. The observed rate constant (k_{obs}) could then be estimated by fitting the curve using a nonlinear least-squares fit as is shown in Figure 5a. The association constant obtained by plotting k_{obs} as a function of Pb(II) concentration (Figure 5b) whereby a linear relationship is expected (eq 3) with a slope equals to k_1 and y-intercept of k_{-1}.

$$k_{obs} = k_1[\mathrm{Pb(II)}] + k_{-1} \quad (3)$$

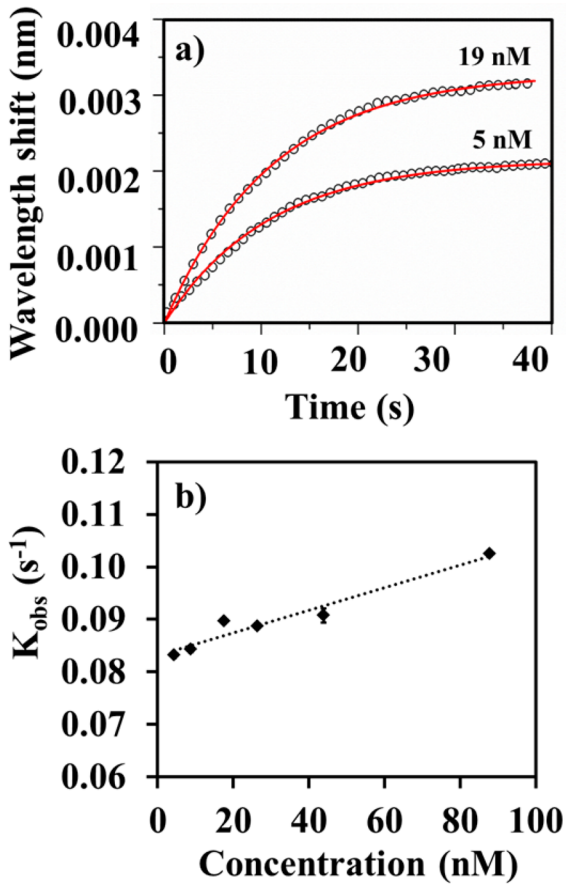


Figure 5. (a) Time-dependent binding curves for 5 and 19 nM Pb(II). A nonlinear least-squares curve fit using an exponential growth model is shown in red. (b) Observed rate constants as a function of Pb(II) concentration with a linear least-squares fit. The association rate constant (k_1) as calculated from the slope was determined to be 2.15 × 10^5 M^{-1} s^{-1}.

dx.doi.org/10.1021/ac500845h | Anal. Chem. 2014, 86, 6299−6306

The association constant was therefore determined to be 2.15×10^5 M^{-1} s^{-1}. This value is comparable to 3.90×10^5 M^{-1} which has already been reported for Pb(II) binding to a similar synthetic ligand by Hatai et al.[43] This is also comparable to what has been reported for Hg(II) binding to 2-mercaptopropyltrimethoxysilane.[27] Unfortunately, until now there has been no report on determining the binding affinity of Pb(II) to GSH.

Using this detection strategy we are able to detect levels of Pb(II) down to 0.05 nM (10 ppt) which is significantly lower than what has previously been reported (Table 1) and well

Table 1. Comparison of the Limit of Detection of Measuring Pb(II) from Our Work and Previous Studies

ref	methods	LOD (nm)
this work	WGM using GSH−Au NPs	0.05
16	DLS with GSH−Au NPs	0.48
13	fluorescence detection using enzyme mimics of catechin-synthesized Au NPs	1.45
5	quenching of the fluorescence of CdTe quantum dots	13.03
15	glutathione-capped quantum dots	38.61
11	colorimetric biosensor using DNAzyme-directed assembly of Au NP	96.52
44	thin-film microsensor based on chalcogenide glasses	96.52
14	colorimetric detection using glutathione-functionalized Au NP	96.52

below the minimum standards as set out by IARC and EPA. Furthermore, our results exhibits a linear range between 2.40 and 48.26 nM with $r^2 = 0.9973$, as shown in Figure 6a. In order to obtain information on the repeatability of the technique, the slopes of the calibration curves were compared from multiple repeat experiments with little or no deviation. Typical standard deviations of the slope were found to be in the range of 0.004−0.019.

In Figure 6, parts a and b, the resonance shift is normalized according to $\Delta\lambda r/\lambda$ where r is the radius of the resonator (μm), λ is the laser wavelength (1.310 μm), and $\Delta\lambda$ is the resonance shift before normalization (as shown in Figure 4, parts a and b). This is required to compensate in differences between resonators with different radii. It should be noted that calibration runs were performed before every set, in order to take into account any potential effects associated with temperature fluctuations (see the Supporting Information, Figure S10). Furthermore, a possible artifact could be the nonspecific interaction of Pb(II) with the APTMS-coated part of the resonator which could result in either irregular shifts or a systematic offset. Control measurements were performed on a bare APTMS-coated resonator in the same Pb(II) concentration range as Figure 6a; however, there was no observable shift. This is likely due to electrostatic repulsion between the APTMS-terminated amine group and the positive charge on the Pb(II). At concentrations greater than 1.45 M (300 ppm), a linear concentration dependence could be observed (Supporting Information, Figure S7a). However, in this mode the surface is nonspecific to Pb(II) and nonspecific binding could easily be washed out using DI water (Supporting Information, Figure S7b). It is worth highlighting that, as the detection limits are well below the minimum recommended concentrations, no preconcentration or other complex sample preparation is necessary. Thus, samples can be taken directly from the field and assayed without manipulation.

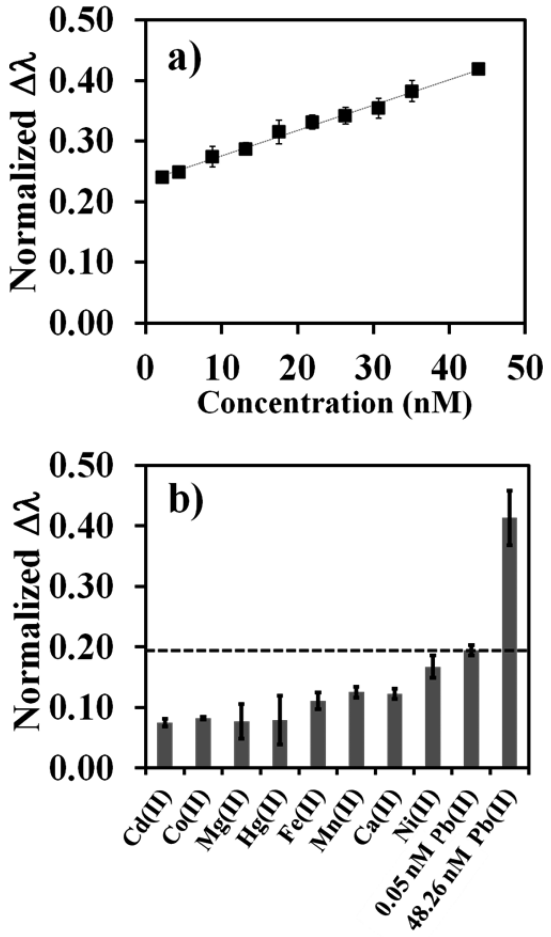


Figure 6. (a) Maximum normalized resonance wavelength shift is plotted as a function of Pb(II) concentration. The dynamic range was determined to be between 2.40 and 48.26 nM with a detection limit of 0.05 nM. (b) A comparison of maximum normalized resonance shift is shown for potential interferences at a concentration of 48.26 μM. For comparison, the signal from 0.05 and 48.26 nM Pb(II) is also shown.

It is interesting to note that such small changes in $\Delta\lambda$ indicate less than 10^{10} ions of Pb(II) bind to the resonator which highlights the sensitivity of this technique. Maintaining high Q-factors within the cavity could potentially bring the detection limit down even further. Potential solutions to increasing the sensitivity would be to decrease the NP size or reduce the surface coverage of the NP on the resonator. Both of these factors would likely increase the Q-factors and decrease the detection limits.

Selectivity of the Resonator. To assess the selectivity of the developed method, various common alkaline and heavy metals were tested as interferences using both UV−vis spectroscopy (Supporting Information, Figure S8) and WGM sensing (Figure 6b). The UV−vis spectra show that only GSH-conjugated NPs with Pb(II) resulted in aggregation of the NPs. Similar measurements utilizing Mg(II), Mn(II), Ca(II), Ni(II), Cd(II), Cr(II), Fe(II), and Hg(II) showed no appreciable spectral shifting and/or aggregation of the particles. Thus, we conclude that the GSH−Au NP complex does not specifically bind to these divalent cations, which is in agreement with Bequa et al.[16] On the other hand the selectivity of the resonator highlights that Pb(II) can be easily detected at concentrations of 0.48 nM (100 ppt) in the presence of the same interferences

dx.doi.org/10.1021/ac500845h | Anal. Chem. 2014, 86, 6299−6306

at much higher concentrations (48.26 μM, 10 ppm). It is interesting to note that unlike in UV−vis spectroscopy, the signal dependence on interferences is unique to each ion, with each ion exhibiting a unique spectral response as shown in Supporting Information Figure S9.

CONCLUSIONS

The detection limit of the WGM sensor was found to be 0.05 nM (10 ppt), based on setting a threshold of 3 times the standard deviation of a blank signal. The sensor is simple to use, has no expensive running costs, and is highly selective to Pb(II). Furthermore, the selectivity is unparalleled for a range of metal ions at much higher concentrations. Importantly, the GSH−Au NP-coated resonator exhibits 10 times greater sensitivity when compared to using DLS with Au NPs modified with GSH. Not only can quantitative information be acquired but kinetic information can also be extracted in real time. We believe that this technique has the potential to be applied for use as a portable device for analysis of Pb(II) for in-field applications due to the sensitivity, selectivity, and portability of the sensor. In addition, a temperature controller for the sensor may be required because of the effect with temperature fluctuations. Finally, it is expected that either changing the ligand or controlling the pH can achieve similar selectivity and detection limits for other metal ions.

ASSOCIATED CONTENT

Supporting Information

Additional information as noted in text. This material is available free of charge via the Internet at http://pubs.acs.org.

AUTHOR INFORMATION

Corresponding Author

*E-mail: joshua.edel@imperial.ac.uk.

Notes

The authors declare no competing financial interest.

ACKNOWLEDGMENTS

S.P. acknowledges Ph.D. funding from the Royal Thai government. J.B.E. acknowledges the receipt of an ERC starting investigator award and an EPSRC basic technology grant.

REFERENCES

(1) Jarup, L. *Br. Med. Bull.* **2003**, *68*, 167−182.
(2) Steenland, K.; Boffetta, P. *Am. J. Ind. Med.* **2000**, *38*, 295−299.
(3) Bakirdere, S.; Yaroglu, T.; Tirik, N.; Demiroz, M.; Fidan, A. K.; Maruldali, O.; Karaca, A. *Spectroscopy (N. Y., NY, U. S.)* **2013**, 824817.
(4) Zhu, W.-y.; Liu, X.-t.; Xue, Q.-h.; Shan, B.-t. *Fenxi Shiyanshi* **2009**, *28*, 95−98.
(5) Wu, H.; Liang, J.; Han, H. *Microchim. Acta* **2008**, *161*, 81−86.
(6) Singh, K. P.; Devender, S.; Sapana, G.; Sonia, V.; Ishwar, S. *Res. J. Chem. Environ.* **2013**, *17*, 53−58.
(7) Yaman, M.; Erel, E. *At. Spectrosc.* **2012**, *33*, 212−217.
(8) Zeeman, P. B.; Butler, L. R. P. *Appl. Spectrosc.* **1962**, *16*, 120−124.
(9) Chen, Z.; He, H. *Guangdong Weiliang Yuansu Kexue* **1995**, *2*, 18−20.
(10) Purdue, L. J.; Enrione, R. E.; Thompson, R. J.; Bonfield, B. A. *Anal. Chem.* **1973**, *45*, 527−530.
(11) Liu, J.; Lu, Y. *J. Am. Chem. Soc.* **2003**, *125*, 6642−6643.
(12) Huang, K.-W.; Yu, C.-J.; Tseng, W.-L. *Biosens. Bioelectron.* **2010**, *25*, 984−989.
(13) Wu, Y.-S.; Huang, F.-F.; Lin, Y.-W. *ACS Appl. Mater. Interfaces* **2013**, *5*, 1503−1509.
(14) Chai, F.; Wang, C.; Wang, T.; Li, L.; Su, Z. *ACS Appl. Mater. Interfaces* **2010**, *2*, 1466−1470.
(15) Mohamed Ali, E.; Zheng, Y.; Yu, H.-h.; Ying, J. Y. *Anal. Chem.* **2007**, *79*, 9452−9458.
(16) Beqa, L.; Singh, A. K.; Khan, S. A.; Senapati, D.; Arumugam, S. R.; Ray, P. C. *ACS Appl. Mater. Interfaces* **2011**, *3*, 668−673.
(17) Jiang, C.; Ma, M.; Wang, Y. *Anal. Methods* **2012**, *4*, 3570−3574.
(18) Luchansky, M. S.; Bailey, R. C. *Anal. Chem.* **2011**, *84*, 793−821.
(19) Fan, X.; White, I. M.; Shopova, S. I.; Zhu, H.; Suter, J. D.; Sun, Y. *Anal. Chim. Acta* **2008**, *620*, 8−26.
(20) Chiasera, A.; Dumeige, Y.; Féron, P.; Ferrari, M.; Jestin, Y.; Nunzi Conti, G.; Pelli, S.; Soria, S.; Righini, G. C. *Laser Photonics Rev.* **2010**, *4*, 457−482.
(21) Baaske, M.; Vollmer, F. *ChemPhysChem* **2012**, *13*, 427−436.
(22) Huckabay, H. A.; Dunn, R. C. *Sens. Actuators, B* **2011**, *160*, 1262−1267.
(23) Dantham, V. R.; Holler, S.; Barbre, C.; Keng, D.; Kolchenko, V.; Arnold, S. *Nano Lett.* **2013**, *13*, 3347−3351.
(24) Santiago-Cordoba, M. A.; Boriskina, S. V.; Vollmer, F.; Demirel, M. C. *Appl. Phys. Lett.* **2011**, *99*, 073701.
(25) He, L.; Oezdemir, S. K.; Zhu, J.; Kim, W.; Yang, L. *Nat. Nanotechnol.* **2011**, *6*, 428−432.
(26) Vollmer, F.; Arnold, S.; Keng, D. *Proc. Natl. Acad. Sci. U.S.A.* **2008**, *105*, 20701−20704.
(27) Hanumegowda, N. M.; White, I. M.; Fan, X. *Sens. Actuators, B* **2006**, *120*, 207−212.
(28) Vollmer, F. *Boehringer Ingelheim Fonds Futura* **2005**, *20*, 239−244.
(29) Chaikin, Y.; Kedem, O.; Raz, J.; Vaskevich, A.; Rubinstein, I. *Anal. Chem.* **2013**, *85*, 10022−10027.
(30) Wilson, K. A.; Finch, C. A.; Anderson, P.; Vollmer, F.; Hickman, J. J. *Biomaterials* **2012**, *33*, 225−236.
(31) Vollmer, F.; Arnold, S. *Nat. Methods* **2008**, *5*, 591−596.
(32) Mah, V.; Jalilehvand, F. *Inorg. Chem.* **2012**, *51*, 6285−6298.
(33) Kim, I.-B.; Dunkhorst, A.; Gilbert, J.; Bunz, U. H. F. *Macromolecules* **2005**, *38*, 4560−4562.
(34) Shopova, S. I.; Rajmangal, R.; Holler, S.; Arnold, S. *Appl. Phys. Lett.* **2011**, *98*, 243104.
(35) Allen, C. L.; Chhatwal, A. R.; Williams, J. M. J. *Chem. Commun.* **2012**, *48*, 666−668.
(36) Stobiecka, M.; Coopersmith, K.; Hepel, M. *J. Colloid Interface Sci.* **2010**, *350*, 168−177.
(37) I. Horcas, R. F.; Gomez-Rodriguez, J. M.; Colchero, J.; Gomez-Herrero, J.; Baro, A. M. *Rev. Sci. Instrum.* **2007**, *78*, 013705.
(38) Liu, F.-K.; Chang, Y.-C.; Ko, F.-H.; Chu, T.-C.; Dai, B.-T. *Microelectron. Eng.* **2003**, *67*−*68*, 702−709.
(39) Evans, B. J.; Peacor, D. R. *J. Solid State Chem.* **1973**, *7*, 36−39.
(40) Gorodetsky, M. L.; Savchenkov, A. A.; Ilchenko, V. S. *Opt. Lett.* **1996**, *21*, 453−455.
(41) Srisa-Art, M.; Dyson, E. C.; deMello, A. J.; Edel, J. B. *Anal. Chem.* **2008**, *80*, 7063−7067.
(42) Goodrich, J. A.; Kugel, J. F. *Binding and Kinetics for Molecular Biologists*; Cold Spring Harbor Laboratory Press: Cold Spring Harbor, NY, 2007.
(43) Hatai, J.; Pal, S.; Jose, G. P.; Sengupta, T.; Bandyopadhyay, S. *RSC Adv.* **2012**, *2*, 7033−7036.
(44) Mourzina, Y.; Schoning, M. J.; Schubert, J.; Zander, W.; Legin, A. V.; Vlasov, Y. G.; Kordos, P.; Luth, H. *Sens. Actuators, B* **2000**, *B71*, 13−18.

ACS SENSORS

Article

pubs.acs.org/acssensors

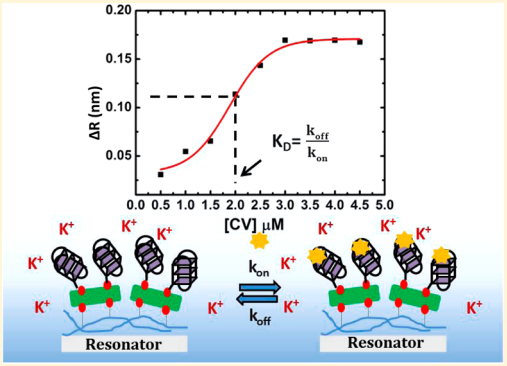
Real-Time Monitoring of Ligand Binding to G-Quadruplex and Duplex DNA by Whispering Gallery Mode Sensing

Sirirat Panich,[†] Mazen Haj Sleiman,[‡] Isobel Steer,[‡] Sylvain Ladame,*[,‡] and Joshua B. Edel*[,†]

[†]Department of Chemistry and [‡]Department of Bioengineering, Imperial College London, South Kensington Campus, London, SW7 2AZ, United Kingdom

Supporting Information

ABSTRACT: The therapeutic potential of small molecules targeting G-quadruplexes has gained credibility since such structures were shown to form in human cells and to be highly prevalent in the human genome, most notably at telomere ends and in oncogene promoters. Herein, we perform whispering gallery mode (WGM) sensing for monitoring DNA−small molecule interactions. Unlike most existing technologies, WGM sensing offers numerous advantages including high sensitivity, real-time analysis, easy access to kinetic parameters, and much lower cost than current gold standards. In this work, interactions of five known DNA-binding ligands with either G-quadruplex or duplex DNA immobilized on a sphere micro-resonator have been assessed. The induced shift of the resonant mode from quadruplex (or duplex)−ligand binding was used to estimate kinetic parameters. Association and dissociation rate constants (k_{on} and k_{off}, respectively) as well as dissociation equilibrium constants (K_D) were measured for these five ligands binding to both duplex and quadruplex DNA.



KEYWORDS: *whispering gallery mode (WGM), G-quadruplex (G4), duplex, kinetic data, ligand interaction, association constant, dissociation constant*

Recently, much effort has been invested in drug discovery strategies that target DNA[1] and there is a growing trend to design small molecules that can bind unique nucleic acid sequences and/or structures with both high affinity and high specificity. Such molecules have great potential as effective anticancer and antitumor chemotherapeutic agents.[2] Initial strategies focused almost exclusively on targeting DNA in its most common form in cells, i.e., as a double helix.[3] However, an increasing number of studies are now targeting alternative secondary structures to regulate specific biological processes. Among them, four-stranded structures, termed G-quadruplexes (or G4) and resulting from the intramolecular folding of guanine-rich oligonucleotides, have been gaining in popularity since it was demonstrated that they were highly prevalent in the human genome and could form in living human cells.[4−6] Severe conditions like cancer, fragile X syndrome, Bloom syndrome, or Werner syndrome have been linked to genomic defects that involve G-quadruplex forming sequences. Therefore, small molecules that can bind and stabilize DNA, especially in its G-quadruplex form, have great therapeutic potential.[7−9]

A key challenge for identifying and selecting DNA-binding ligands that can target specific DNA sequences or structures is the ability to effectively screening large numbers of molecules against individual DNA motifs. In recent years, several basic experimental methods and new technological advances have been developed to monitor and/or characterize interactions between oligonucleotides and small molecules.[10,11] DNA melting techniques where DNA folding/unfolding is typically monitored by UV−visible spectroscopy, fluorescence spectroscopy, or circular dichroism (CD) are among the most commonly used and provide valuable information on the ability of small molecules to stabilize DNA structures.[12−15] However, these assays often require high DNA and ligand concentrations and do not allow easy access to thermodynamic and kinetic parameters. Other techniques such as surface plasmon resonance (SPR),[15−18] nuclear magnetic resonance (NMR),[19] and mass spectrometry[20−23] have all been used with varying degrees of success. SPR in particular has been used for monitoring real-time binding of small molecules to DNA immobilized onto gold surfaces. Upon binding of a ligand of interest to the surface-immobilized DNA, a shift in plasmon resonance is produced that can be used to obtain real-time kinetic information. However, the complexity of the setup and of the functionalization process makes this costly technique unsuitable for large-scale screening.[24] There is therefore a need to develop a novel sensing strategy that is reliable, fast, low-cost, and sensitive, and can be used for real-time DNA-ligand screening.

Herein, we propose the use of whispering gallery mode (WGM) sensing where laser light circumnavigates around a silica sphere by total internal reflection. Changes in optical path length

Received: May 1, 2016
Accepted: September 1, 2016
Published: September 1, 2016

ACS Publications © 2016 American Chemical Society

DOI: 10.1021/acssensors.6b00301
ACS Sens. 2016, 1, 1097−1102

and refractive index occur in response to molecular binding. Briefly, upon binding of small molecules to a DNA target immobilized at the surface of a resonator, the optical path length increases and perturbs the sphere out of resonance. Getting the sphere back into resonance requires compensation by increasing the wavelength of the laser.[25] In addition, these small molecules will interact with the evanescent tail at the resonator surface resulting in a change in the local refractive index also leading to a small, but detectable resonance wavelength shift.[26] Previously, WGM has been integrated in sensors for tracking of biomolecular kinetic parameters[27] such as protein binding,[28,29] enzyme activities,[30] and DNA binding.[31] There are many similarities between WGM and SPR,[26] although versatile functionalization, ease of multiplexing, and significantly lower cost make WGM sensing particularly attractive. It is also noteworthy that nonspecific interactions are commonly observed between small molecules and the carboxymethylated dextran matrix commonly used on SPR chips for DNA binding studies and that such interfering interactions could be avoided when using WGM.[32]

Herein, to overcome this limitation, the surface of the resonator was modified with a biotinylated silane that is stable under a large range of salt concentrations and pH.[33] Modification of the WGM resonator was then achieved by streptavidin grafting followed by immobilization of biotinylated DNA (see SI Figure S1). With such a platform it was possible to differentiate between duplex and G-quadruplex DNA and to extract binding kinetic parameter.

MATERIAL AND METHODS

Chemicals and Materials. HPLC-purified DNA oligonucleotides were purchased from Sigma-Aldrich and used without further purification. Stock solutions (1 mM) were prepared in water and stored at-20 °C. C-myc DNA d(TGAGGGTGGGTAGGGTGGGTAA and a mutated analogue that cannot fold into a G4 structure d(TGAGTGTGTGTAGTGTGTGTAA) labeled with biotin at their 5′-end were prepared at a final strand concentration of 100 μM in 10 mM Tris·HCl buffer (pH 7.4) in the presence of 100 mM KCl. The DNA solutions were heated at 95 °C for 5 min before being slowly cooled down to room temperature overnight. Double-stranded DNA was made by mixing C-myc DNA in 10 mM Tris·HCl buffer (pH 7.4) with a stoichiometric amount of its complementary strand d(TTACCCACCCTACCCAC). The mixture was annealed at 95 °C for 5 min, then slowly cooled down to room temperature overnight.

Characterization. Attenuated total reflectance (ATR) spectra were recorded using an FT-IR spectrometer (UATR Two, PerkinElmer). First, an open beam background spectrum was collected. For the collection of resonator sample spectra, 10 resonators were placed on the ATR crystal, then pressed into the pressure arm over the crystal/sample to collect the spectrum. A confocal microscope (DP71, Olympus) was used to analyze the fluorescence on the functionalized microspheres. Microspheres carrying different DNA structures were examined with a 20× magnification objective, using a Hg lamp. The resonators were immersed in 10 μM Thiazole Orange (TO) for 1 h, and then the image was recorded and the fluorescence signal was further analyzed with analySIS docu software.

WGM Microresonator Fabrication and Functionalization. All microresonators were fabricated from single mode optical fibers (F-SMF-28, Newport) by placing the tip in a fusion splicer (FITEL S123), which produces an electric arc to melt the glass. By precisely controlling the arc shot, a spheroid-shaped tip was then formed due to the surface tension of the molten glass. It is this tip that was used as the microresonator. Typical diameters ranged 190−210 μm. The microresonator was then functionalized using an aminosilane (i.e., 3-Aminopropyl triethoxysilane, APTES) in order to covalently attach biotin to the glass surface. Briefly, the microresonator was immersed in a 2% v/v solution of APTES in ethanol for 1 h. In the following step, the silanized resonator was washed with fresh ethanol and dried in an oven for 30 min. The resonator was then immersed in 1.6 mg/mL sulfo-*N*-hydroxysuccinimide biotin ester sodium salt in 10 mM Tris·HCl buffer pH 7.4 in the presence of 100 mM KCl for 1 h. The biotinylated resonator was finally rinsed with the same buffer and dried with a stream of N_2.

Monitoring DNA−Small Molecule Interactions. The experimental platform used was similar to that published by Panich et al.[34] The biotinylated resonator was aligned to couple to the waveguide and was then secured in a low volume flow cell using epoxy glue. The buffer solution (10 mM Tris·HCl buffer pH 7.4 in the presence of 100 mM KCl) was pumped into the system by a syringe pump at a flow rate of 100 μL/min. The resonance wavelength was recorded as a baseline. Streptavidin (0.025 mg/mL) in the same buffer was then pumped in until the resonance shift reached a plateau. The system was then flushed with buffer and the same process was repeated for immobilization of prefolded biotinylated DNA (quadruplex or duplex). For small molecule screening, solutions of small molecules of varying concentrations were introduced into the flow cell until the signal reached a plateau. Between each measurement, the ligand was washed off with continuous flow of the running buffer.

Fluorescence Titration Experiment. To assess the DNA binding affinity of TO, CV, MB, and MG, fluorescence titration experiments were carried out in 96-well plates. Briefly, increasing amounts of G4 or duplex DNA were titrated in a solution of ligand at fixed concentration (1 μM)[41−44] and fluorescence intensity was then recorded using a CLARIOstar fluorescence plate reader (BMG Labtech) at the relevant excitation and emission wavelengths (485−520 nm TO, 580−625 nm CV, 580−680 nm MB, 615−650 nm MG). Calculated K_D values are presented in Table S2 and graphs are shown in Figure S9.

RESULTS AND DISCUSSION

DNA Immobilization onto the Microresonator. The glass sphere surface of the resonator was first coated with a monolayer of APTES and subsequently reacted with sulfo-NHS-biotin to generate a stable (covalently linked) biotinylated surface. Streptavidin was then immobilized onto the biotin-functionalized glass spheres followed by addition of 5′-biotinylated oligonucleotides (for more detail about functionalization steps, see Figure S1). A schematic representation of the setup highlighting the operational principles is shown in Figure 1. Briefly, a 1307 nm (λ) DFB laser was coupled to the spherical resonator via the use of a single mode ∼2 μm tapered waveguide.

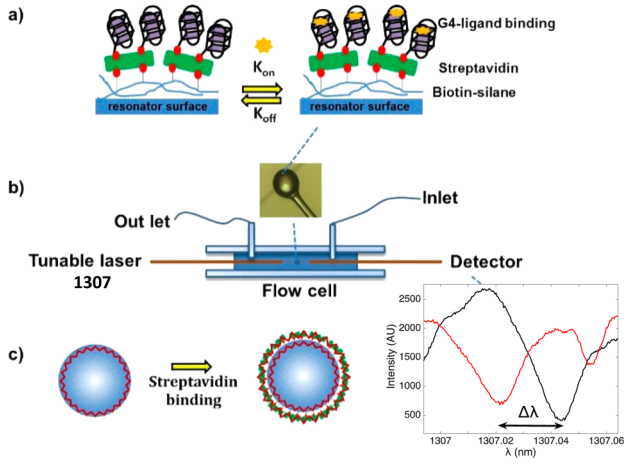


Figure 1. (a) Schematic representation of a typical WGM platform to monitor interactions between G-quadruplex and ligands. (b) Representation of a flow cell. (c) Binding of the molecule of interest increases the laser path length; illustrated here is an example of $\Delta\lambda$ before (red) and during (black) binding of streptavidin.

DOI: 10.1021/acssensors.6b00301
ACS Sens. 2016, 1, 1097−1102

By doing so, the laser light propagates and is confined to the sphere surface. As the radius of propagation is highly dependent on the combined radius of the sphere (R) and the length of surface modification (ΔR), the detected output resonance wavelength will shift to the red ($\Delta\lambda$) as the modification thickness and/or density increases (Figure 1c). It is this effect which can be used to easily quantify binding and kinetics in real time. For example, streptavidin bound to the biotinylated resonator surface will result in an increase of the optical path length causing a loss of resonance. This mechanism is the same for DNA and ligand binding. Gradually, as the number of available binding sites becoming occupied increases, the resonance shift will reach a plateau.

It is therefore possible to determine binding constants by quantifying the rate at which the plateau is reached. The wavelength shift is proportional to the wavelength increase[25]

$$\Delta\lambda/\lambda = \Delta R/R \quad (1)$$

and the thickness of the layer can be calculated as follows:

$$\Delta R = [(\Delta\lambda R)/\lambda] \quad (2)$$

In this study, well-characterized C-myc quadruplex was used as a model system[35] and annealed in 10 mM Tris·HCl buffer pH 7.4 in the presence of 100 mM KCl. Duplex DNA was also prepared under similar conditions to assess quadruplex versus duplex specificity. Representative WGM binding curves for immobilization of quadruplex and duplex biotinylated DNAs onto streptavidin-coated resonators are shown in Figure 2. G4

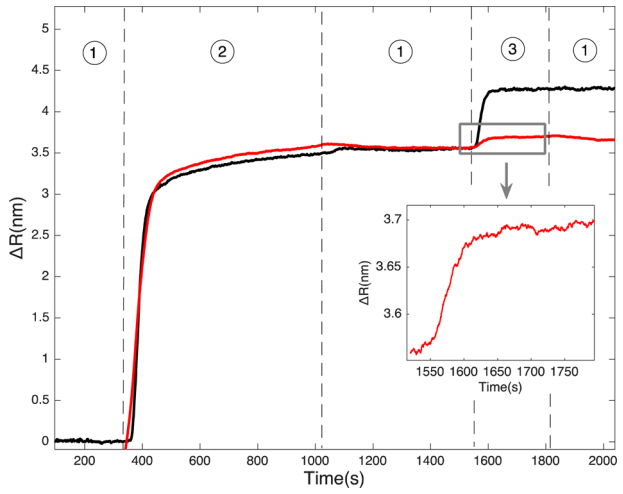


Figure 2. WGM curves for real-time monitoring of binding of biotinytated G-quadruplex (black) and duplex (red) DNA onto a streptavidin-coated resonator. ① 100 mM KCl in 10 mM Tris.HCl buffer pH 7.4; ② 25 μg/mL streptavidin in buffer ①; ③ 1 μM DNA in buffer ①.

structures were found to induce a resonance shift (i.e., largest interaction with the evanescent field close to the surface) 5 times greater than that of duplex DNA, likely due to its compact structure (when compared to double-stranded DNA).

Characterization of Immobilized DNA onto the Microresonator. Characterization of the silanized resonator surface was achieved by attenuated total reflectance (ATR) to confirm successful grafting of APTES as shown in SI Figure S2. Thiazole orange (TO) was used as a fluorogenic probe to demonstrate the successful immobilization of duplex and quadruplex DNA on the surface of the resonator. TO is known to become highly fluorescent upon binding to G-quadruplex and duplex DNA while remaining almost nonfluorescent in aqueous solution, or in the presence of unfolded single-stranded DNA.[36] Resonators functionalized with duplex, quadruplex, and single-stranded DNA were incubated with a solution of TO and them imaged by fluorescence microscopy. As shown in Figure 3, only micro-

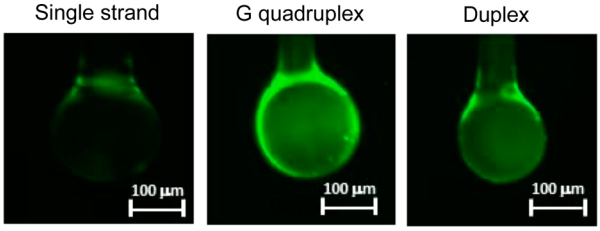


Figure 3. Fluorescence microscopy images of a microsphere coated with various DNA structures in the presence of TO. Fluorescence intensity indicates the presence of a duplex or quadruplex structure on the resonator, while no fluorescence is observed when the DNA is single-stranded.

spheres coated with duplex and quadruplex DNA become strongly fluorescent, while only residual fluorescence was observed with the microsphere coated with single-stranded DNA. These results confirm that both duplex and quadruplex DNA preformed in solution remain in their folded conformation when bound at the resonators' surface. DNA concentrations were then optimized to ensure saturation of the surface (i.e., all available streptavidin binding sites are occupied; see SI Figure S3). From the resonance shift it becomes possible to determine the thickness or length of the adsorbed analyte as previously reported by Vollmer and Arnold.[25] For example, the thickness of streptavidin attached to the biotin surface was found to be ~3.5 nm (Figure. 2) which is comparable with results obtained by AFM at ~3.8 nm.[37] Similarly, the thickness of the C-myc quadruplex at the surface of the resonator was measured as ca. 0.7 nm, which is in very good agreement with data from the X-ray crystal structure of a DNA quadruplex with a similar parallel-stranded topology.[38]

The suitability of this technology for characterizing the interaction between DNA and small molecules was then assessed. During the past decade, a plethora of G4-specific ligands have been developed[39] and had their DNA-binding potential assessed by various sensing techniques. Herein, in order to validate our technology, we determined the association rate constant (k_{on}), dissociation rate constant (k_{off}), and dissociation equilibrium constant (K_D) for five well-known DNA-binding ligands which include Crystal violet (CV), Malachite green (MG), Methylene blue (MB), Thiazole orange (TO), and Netropsin (NS). While NS preferentially binds to duplex DNA[40] and MB binds both duplex and quadruplex with similar affinities, TO, CV, and MG show various levels of selectivity for quadruplex over duplex DNA, mainly through π-stacking interactions with the top G-tetrad.[36,41−44]

G-Quadruplex and Duplex DNA Ligand Binding Kinetics. A typical WGM sensorgram showing the real-time binding of CV to C-myc DNA in its G-quadruplex form is shown in the inset of Figure 4 (top). To ensure the association and dissociation rates are not perturbed by mass transport limitations, a high flow rate (100 μL min^{-1}) was used to minimize the diffusion distance (Figure S4). From these sensorgrams it is possible to estimate the equilibrium constant (K_D), and association (k_{on}) and dissociation (k_{off}) rate constants. K_D is the ratio of the dissociation to the association rate constants

DOI: 10.1021/acssensors.6b00301
ACS Sens. 2016, 1, 1097−1102

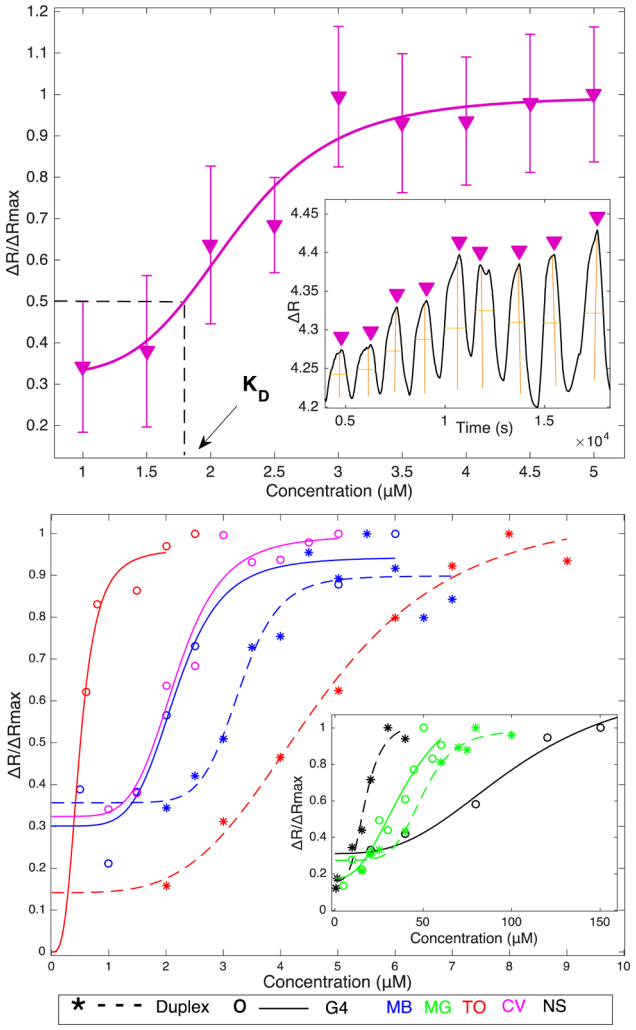


Figure 4. (top) Sigmoid curve illustrating K_D at EC_{50}. Inset picture shows the WGM ΔR response-binding of different concentrations of CV ligand binding to G quadruplex. When the wavelength shift reached a plateau, the ligand was replaced by a continuous flow of buffer before a higher ligand concentration was used. Peak heights are normalized to the maxima (ΔR_{max}) before plotting to the dose response model. Error bars represent the range of signal noise. (bottom) Dose response curves for all five ligands binding to G4 and duplex, in order to estimate K_D at EC_{50} (values presented in Table 1).

(k_{off}/k_{on}).[45] The K_D can also be determined by plotting the response at equilibrium against the ligand concentration, where the K_D equals 50% of the maximum response.

The dose response binding curves of all five ligands with G4 and duplex are shown in Figure. 4 (bottom). Assuming a 1:1 interaction, the binding between DNA and the ligand can be described by a monoexponential growth equation or pseudo-first-order reaction as shown in eq 3.[34]

$$\Delta R_t = \Delta R_{max}(1 - e^{-k_{obs}t}) \quad (3)$$

where ΔR_t is the time-dependent radius shift and ΔR_{max} is the maximum radius shift at the plateau. All ligand binding fits typically exhibited an r^2 of >0.99. The observed rate constant for association (k_{obs}) which was given by the initial binding slope could then be estimated by fitting a two-term polynomial (see insets of Figure 5 and Figure S5).

Association constants were obtained by plotting k_{obs} as a function of ligand concentration whereby a linear relationship is

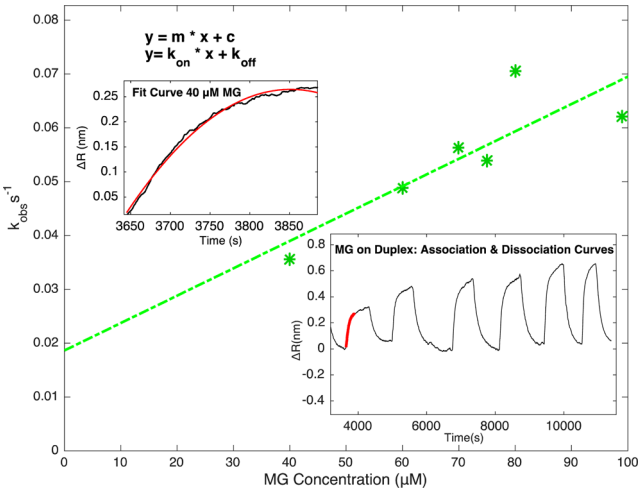


Figure 5. Plot of WGM k_{obs} as a function of ligand concentration, using the example of MG binding to duplex DNA. Inset pictures illustrate an example of polynomial curve fit (in red), with slope taken as k_{on} and intercept as off.

expected with slope equal to the association rate constant, k_{on} and intercept equal to k_{off} (Figure 5, and Figure S6). The dissociation rate constant (k_{off}) can also be calculated through linearization of the dissociation phase peak shift using the following equation:[46−48]

$$\ln(\Delta R(t)/\Delta R_0) = -k_d t \quad (4)$$

where R_0 is the wavelength at the beginning of the dissociation phase and $R(t)$ is the wavelength as a function of time (see Figure S7 and Table S1).

To ensure that the observed binding originates from the specific interactions of the ligand with DNA, control experiments were performed with DNA free resonators. Under these conditions, the wavelength shift was negligible (Figure S8) suggesting minimal nonspecific interactions of the ligand with the surface.

Ligand Binding Affinities. A summary of binding affinities for the five ligands tested is given in Table 1 and shows good agreement with values published in the literature (shown in red) and values from fluorescence titration experiments obtained using the exact same DNA sequences (Figure S9 and Table S2). As expected, TO and MG both exhibit a moderate preference for binding to G4 DNA, MB binds to both duplex and quadruplex DNA with comparable affinities, and NS preferentially binds to duplex DNA. In contrast, CV was shown to bind to quadruplex DNA with high specificity, no binding to duplex DNA being detectable at ligand concentrations up to 12 μM. This result is in agreement with the work performed by Kong et al.[41] Competition experiments are a very efficient way of assessing the ability of small molecules to discriminate between quadruplex and duplex DNA. Herein, experiments were performed where binding of CV and MB to G4 DNA was assessed in the absence and in the presence of double-stranded Calf Thymus (CT) DNA used as a competitor. The results (Figure S10) show that CV binding to the G4 DNA is not affected when competitor DNA is present in the surrounding medium, thus confirming highly specific binding to G-quadruplex DNA. On the other hand, MB binding to the G4-functionalized WGM resonator was completely inhibited in the presence of competitor CT DNA and no wavelength shift could be detected. This result can be explained by the fact that MB, previously shown to bind with

DOI: 10.1021/acssensors.6b00301
ACS Sens. 2016, 1, 1097−1102

Table 1. Summary of Kinetic Parameters of DNA Interaction with Five Ligands Deduced from the WGM Binding Slopes (k_{off}/k_{on}) and Peaks (EC_{50} K_D)[a]

DNA	Ligand	EC50 K_D (μM)	k_{off}/k_{on} K_D (μM)	K_{on} (x10^6 M^{-1} s^{-1})	K_{off} (s^{-1})
G4	CV	1.8	2.19	0.00323	0.00710
	MB	1.9 (4μM)[46]	2.22	0.00441	0.00980
	TO	0.45 (0.3-3)[47]	0.52	0.00286	0.00149
	MG	23.7 (2-35)[47]	8.96	0.00115	0.01031
	NS	62	45.60	0.00025	0.01140
Duplex	CV	*	*	*	*
	MB	2.94	2.62	0.00343	0.00897
	TO	4.2 (0.3-3)[47]	2.83	0.00249	0.00705
	MG	43.1 (>50)[47]	36.56	0.00051	0.01865
	NS	14.5	10.47	0.00072	0.00754

[a](*) values could not be estimated because the transmission spectrum was perturbed by high polarizability. The values in red brackets are extracted from the literature, from homogeneous screenings with different sequences of DNA.

comparable affinities to both duplex and quadruplex DNA, would no longer be available to interact with immobilized G4 DNA when already complexed with a large excess of duplex DNA in solution.

CONCLUSIONS

In conclusion, we report on whispering gallery mode (WGM) sensors being used for real-time monitoring of small molecule binding to either duplex or quadruplex DNA. Five known ligands were tested and showed DNA-binding profiles comparable to data available in the literature and to data from fluorescence titration experiments, thus validating our technology. Comparable K_D values were obtained by fitting either the maximum response at equilibrium or the association rate constant as a function of ligand concentration. When compared to existing technologies we have demonstrated that WGM was highly sensitive, required minimal volumes of DNA and ligand, and was suitable for real-time monitoring of DNA–ligand interactions. It also provides access to the same kinetic parameters as the gold standard SPR for only a fraction of the cost.

ASSOCIATED CONTENT

Supporting Information

The Supporting Information is available free of charge on the ACS Publications website at DOI: 10.1021/acssensors.6b00301.

Details of the experiment, mechanism of surface functionalization, ATR and fluorescent experiment for characterization of resonator surface, WGM binding curve of the prefolded C-myc at different concentrations, mass transfer limited interaction from the different flow rate, examples of curve fitting for K_{obs} control experiment, and competition experiment of CV and MB between G-quadruplex on the surface and duplex in the surrounding medium (PDF)

AUTHOR INFORMATION

Corresponding Authors

*E-mail: s.ladame@imperial.ac.uk.
*E-mail: joshua.edel@imperial.ac.uk.

Author Contributions

The manuscript was written through contributions of all authors.

Notes

The authors declare no competing financial interest.

ACKNOWLEDGMENTS

S.P. acknowledges PhD funding from the Royal Thai government. I.S. acknowledges PhD funding from the BBSRC. J.B.E. acknowledges the receipt of an ERC starting investigator award and an EPSRC basic technology grant.

ABBREVIATIONS

G4, G-quadruplex; WGM, whispering gallery mode; CD, circular dichroism; SPR, surface plasmon resonance; NMR, nuclear magnetic resonance; ATR, attenuated total reflectance; TO, thiazole orange; APTES, 3-aminopropyl triethoxysilane; CV, crystal violet; MG, malachite green; MB, methylene blue; NS, netropsin; CT, Calf Thymus

REFERENCES

(1) Holt, P. A.; Buscaglia, R.; Trent, J. O.; Chaires, J. B. A discovery funnel for nucleic acid binding drug candidates. *Drug Dev. Res.* **2011**, *72*, 178–186.
(2) Ali, A.; Bhattacharya, S. DNA binders in clinical trials and chemotherapy. *Bioorg. Med. Chem.* **2014**, *22*, 4506–4521.
(3) Baraldi, P. G.; Bovero, A.; Fruttarolo, F.; Preti, D.; Tabrizi, M. A.; Pavani, M. G.; Romagnoli, R. DNA minor groove binders as potential antitumor and antimicrobial agents. *Med. Res. Rev.* **2004**, *24*, 475–528.
(4) Biffi, G.; Tannahill, D.; McCafferty, J.; Balasubramanian, S. Quantitative visualization of DNA G-quadruplex structures in human cells. *Nat. Chem.* **2013**, *5*, 182–186.
(5) Lam, E. Y. N.; Beraldi, D.; Tannahill, D.; Balasubramanian, S. G-quadruplex structures are stable and detectable in human genomic DNA. *Nat. Commun.* **2013**, *4*, 1796.
(6) Rhodes, D.; Lipps, H. J. G-quadruplexes and their regulatory roles in biology. *Nucleic Acids Res.* **2015**, *43*, 8627–8637.
(7) Ohnmacht, S. A.; Neidle, S. Small-molecule quadruplex-targeted drug discovery. *Bioorg. Med. Chem. Lett.* **2014**, *24*, 2602–2612.
(8) Balasubramanian, S.; Hurley, L. H.; Neidle, S. Targeting G-quadruplexes in gene promoters: a novel anticancer strategy? *Nat. Rev. Drug Discovery* **2011**, *10*, 261–275.
(9) Müller, S.; Rodriguez, R. G-quadruplex interacting small molecules and drugs: from bench toward bedside. *Expert Rev. Clin. Pharmacol.* **2014**, *7*, 663–679.
(10) Murat, P.; Singh, Y.; Defrancq, E. Methods for investigating G-quadruplex DNA/ligand interactions. *Chem. Soc. Rev.* **2011**, *40*, 5293–5307.
(11) Jaumot, J.; Gargallo, R. Experimental methods for studying the interactions between G-quadruplex structures and ligands. *Curr. Pharm. Des.* **2012**, *18*, 1900–1916.
(12) De Cian, A.; Guittat, L.; Kaiser, M.; Saccà, B.; Amrane, S.; Bourdoncle, A.; Alberti, P.; Teulade-Fichou, M.-P.; Lacroix, L.; Mergny, J.-L. Fluorescence-based melting assays for studying quadruplex ligands. *Methods* **2007**, *42*, 183–195.
(13) De Rache, A.; Mergny, J.-L. Assessment of selectivity of G-quadruplex ligands via an optimized FRET melting assay. *Biochimie* **2015**, *115*, 194–202.

DOI: 10.1021/acssensors.6b00301
ACS Sens. 2016, 1, 1097–1102

(14) Paramasivan, S.; Rujan, I.; Bolton, P. H. Circular dichroism of quadruplex DNAs: Applications to structure, cation effects and ligand binding. *Methods* **2007**, *43*, 324−331.
(15) Hacht, A. V.; Seifert, O.; Menger, M.; Schütze, T.; Arora, A.; Konthur, Z.; Neubauer, P.; Wagner, A.; Weise, C.; Kurreck, J. Identification and characterization of RNA guanine-quadruplex binding proteins. *Nucleic Acids Res.* **2014**, *42*, 6630−6644.
(16) Redman, J. E. Surface plasmon resonance for probing quadruplex folding and interactions with proteins and small molecules. *Methods* **2007**, *43*, 302−312.
(17) McLuckie, K. I. E.; Waller, Z. A. E.; Sanders, D. A.; Alves, D.; Rodriguez, R.; Dash, J.; McKenzie, G. J.; Venkitaraman, A. R.; Balasubramanian, S. G-Quadruplex-Binding Benzo[a]phenoxazines Down-Regulate c-KIT Expression in Human Gastric Carcinoma Cells. *J. Am. Chem. Soc.* **2011**, *133*, 2658−2663.
(18) Pillet, F.; Romera, C.; Trévisiol, E.; Bellon, S.; Teulade-Fichou, M.-P.; François, J.-M.; Pratviel, G.; Leberre, V. A. Surface plasmon resonance imaging (SPRi) as an alternative technique for rapid and quantitative screening of small molecules, useful in drug discovery. *Sens. Actuators, B* **2011**, *157*, 304−309.
(19) Adrian, M.; Heddi, B.; Phan, A. T. NMR spectroscopy of G-quadruplexes. *Methods* **2012**, *57*, 11−24.
(20) Beck, J. L.; Colgrave, M. L.; Ralph, S. F.; Sheil, M. M. Electrospray ionization mass spectrometry of oligonucleotide complexes with drugs, metals, and proteins. *Mass Spectrom. Rev.* **2001**, *20*, 61−87.
(21) Brodbelt, J. S. Evaluation of DNA/Ligand Interactions by Electrospray Ionization Mass Spectrometry. *Annu. Rev. Anal. Chem.* **2010**, *3*, 67−87.
(22) Nagesh, N.; Krishnaiah, A.; Dhople, V. M.; Sundaram, C. S.; Jagannadham, M. V. Noncovalent Interaction of G-Quadruplex DNA with Acridine at Low Concentration Monitored by MALDI-TOF Mass Spectrometry. *Nucleosides, Nucleotides Nucleic Acids* **2007**, *26*, 303−315.
(23) Rosu, F.; Nguyen, C.-H.; De Pauw, E.; Gabelica, V. Ligand Binding Mode to Duplex and Triplex DNA Assessed by Combining Electrospray Tandem Mass Spectrometry and Molecular Modeling. *J. Am. Soc. Mass Spectrom.* **2007**, *18*, 1052−1062.
(24) Dash, J.; Waller, Z. A. E.; Pantoş, G. D.; Balasubramanian, S. Synthesis and Binding Studies of Novel Diethynyl-Pyridine Amides with Genomic Promoter DNA G-Quadruplexes. *Chem. - Eur. J.* **2011**, *17*, 4571−4581.
(25) Vollmer, F.; Arnold, S. Whispering-gallery-mode biosensing: label-free detection down to single molecules. *Nat. Methods* **2008**, *5*, 591−596.
(26) Soteropulos, C. E.; Hunt, H. K. Attaching Biological Probes to Silica Optical Biosensors Using Silane Coupling Agents. *J. Visualized Exp.* **2012**, *63*, 1−6.
(27) Wu, Y.; Vollmer, F., Whispering Gallery Mode Biomolecular Sensors. In *Cavity-enhanced Spectroscopy and Sensing*, 1st ed., Gagliardi, G.; Loock, H. P., Eds.; Springer, 2014; Vol. *179*, chapter 9, pp 323−349.
(28) Dahmen, J.; Soteropulos, C.; Stacey, G.; Hunt, H. Using microscale optical biosensors to elucidate binding kinetic parameters between the plant defense response elicitor chitin and chitin binding proteins; 245th ACS National Meeting & Exposition; American Chemical Society, New Orleans, United States, 2013; AGFD-298.
(29) Pasquardini, L.; Berneschi, S.; Barucci, A.; Cosi, F.; Dallapiccola, R.; Insinna, M.; Lunelli, L.; Conti, G. N.; Pederzolli, C.; Salvadori, S.; Soria, S. Whispering gallery mode aptasensors for detection of blood proteins. *J.Biophotonics* **2013**, *6*, 178−187.
(30) Wilson, K. A.; Finch, C. A.; Anderson, P.; Vollmer, F.; Hickman, J. J. Combining an optical resonance biosensor with enzyme activity kinetics to understand protein adsorption and denaturation. *Biomaterials* **2015**, *38*, 86−96.
(31) Wu, Y.; Zhang, D. Y.; Yin, P.; Vollmer, F. Ultraspecific and Highly Sensitive Nucleic Acid Detection by Integrating a DNA Catalytic Network with a Label-Free Microcavity. *Small* **2014**, *10*, 2067−2076.
(32) Read, M.; Harrison, R. J.; Romagnoli, B.; Tanious, F. A.; Gowan, S. H.; Reszka, A. P.; Wilson, W. D.; Kelland, L. R.; Neidle, S. Structure-based design of selective and potent G quadruplex-mediated telomerase inhibitors. *Proc. Natl. Acad. Sci. U. S. A.* **2001**, *98*, 4844−4849.
(33) Marttila, A. T.; Laitinen, O. H.; Airenne, K. J.; Kulik, T.; Bayer, E. A.; Wilchek, M.; Kulomaa, M. S. Recombinant NeutraLite Avidin: a non-glycosylated, acidic mutant of chicken avidin that exhibits high affinity for biotin and low non-specific binding properties. *FEBS Lett.* **2000**, *467*, 31−36.
(34) Panich, S.; Wilson, K. A.; Nuttall, P.; Wood, C. K.; Albrecht, T.; Edel, J. B. Label-Free Pb(II) Whispering Gallery Mode Sensing Using Self-Assembled Glutathione-Modified Gold Nanoparticles on an Optical Microcavity. *Anal. Chem.* **2014**, *86*, 6299−6306.
(35) Siddiqui-Jain, A.; Grand, C. L.; Bearss, D. J.; Hurley, L. H. Direct evidence for a G-quadruplex in a promoter region and its targeting with a small molecule to repress c-MYC transcription. *Proc. Natl. Acad. Sci. U. S. A.* **2002**, *99*, 11593−11598.
(36) Lubitz, I.; Zikich, D.; Kotlyar, A. Specific High-Affinity Binding of Thiazole Orange to Triplex and G-Quadruplex DNA. *Biochemistry* **2010**, *49*, 3567−3574.
(37) Li, H.; Park, S. H.; Reif, J. H.; LaBean, T. H.; Yan, H. DNA-Templated Self-Assembly of Protein and Nanoparticle Linear Arrays. *J. Am. Chem. Soc.* **2004**, *126*, 418−419.
(38) Parkinson, G. N.; Lee, M. P. H.; Neidle, S. Crystal structure of parallel quadruplexes from human telomeric DNA. *Nature* **2002**, *417*, 876−880.
(39) Monchaud, D.; Teulade-Fichou, M.-P. A hitchhiker's guide to G-quadruplex ligands. *Org. Biomol. Chem.* **2008**, *6*, 627−636.
(40) Randazzo, A.; Galeone, A.; Esposito, V.; Varra, M.; Mayol, L. Interaction of distamycin A and netropsin with quadruplex and duplex structures: a comparative 1H-NMR study. *Nucleosides, Nucleotides Nucleic Acids* **2002**, *21*, 535−545.
(41) Kong, D.-M.; Ma, Y.-E.; Wu, J.; Shen, H.-X. Discrimination of G-quadruplexes from duplex and single-stranded DNAs with fluorescence and energy-transfer fluorescence spectra of crystal violet. *Chem. - Eur. J.* **2009**, *15*, 901−909.
(42) Kong, D.-M.; Guo, J.-H.; Yang, W.; Ma, Y.-E.; Shen, H.-X. Crystal violet-G-quadruplex complexes as fluorescent sensors for homogeneous detection of potassium ion. *Biosens. Bioelectron.* **2009**, *25*, 88−93.
(43) Kong, D.-M.; Ma, Y.-E.; Guo, J.-H.; Yang, W.; Shen, H.-X. Fluorescent Sensor for Monitoring Structural Changes of G-Quadruplexes and Detection of Potassium Ion. *Anal. Chem.* **2009**, *81*, 2678−2684.
(44) Bhasikuttan, A. C.; Mohanty, J.; Pal, H. Interaction of Malachite Green with Guanine-Rich Single-Stranded DNA: Preferential Binding to a G-Quadruplex. *Angew. Chem., Int. Ed.* **2007**, *46*, 9305−9307.
(45) Núñez, S.; Venhorst, J.; Kruse, C. G. Target−drug interactions: first principles and their application to drug discovery. *Drug Discovery Today* **2012**, *17*, 10−22.
(46) Zhang, F.-T.; Nie, J.; Zhang, D.-W.; Chen, J.-T.; Zhou, Y.-L.; Zhang, X.-X. Methylene Blue as a G-Quadruplex Binding Probe for Label-Free Homogeneous Electrochemical Biosensing. *Anal. Chem.* **2014**, *86*, 9489−9495.
(47) Vummidi, B. R.; Alzeer, J.; Luedtke, N. W. Fluorescent Probes for G-Quadruplex Structures. *ChemBioChem* **2013**, *14*, 540−558.
(48) Soteropulos, C. E.; Hunt, H. K.; Armani, A. M. Determination of binding kinetics using whispering gallery mode microcavities. *Appl. Phys. Lett.* **2011**, *99* (10), 103703.

DOI: 10.1021/acssensors.6b00301
ACS Sens. 2016, 1, 1097−1102